ISBN 978-82-471-3127-5 (printed ver.)
ISBN 978-82-471-3128-2 (electronic ver.)
ISSN 1503-8181

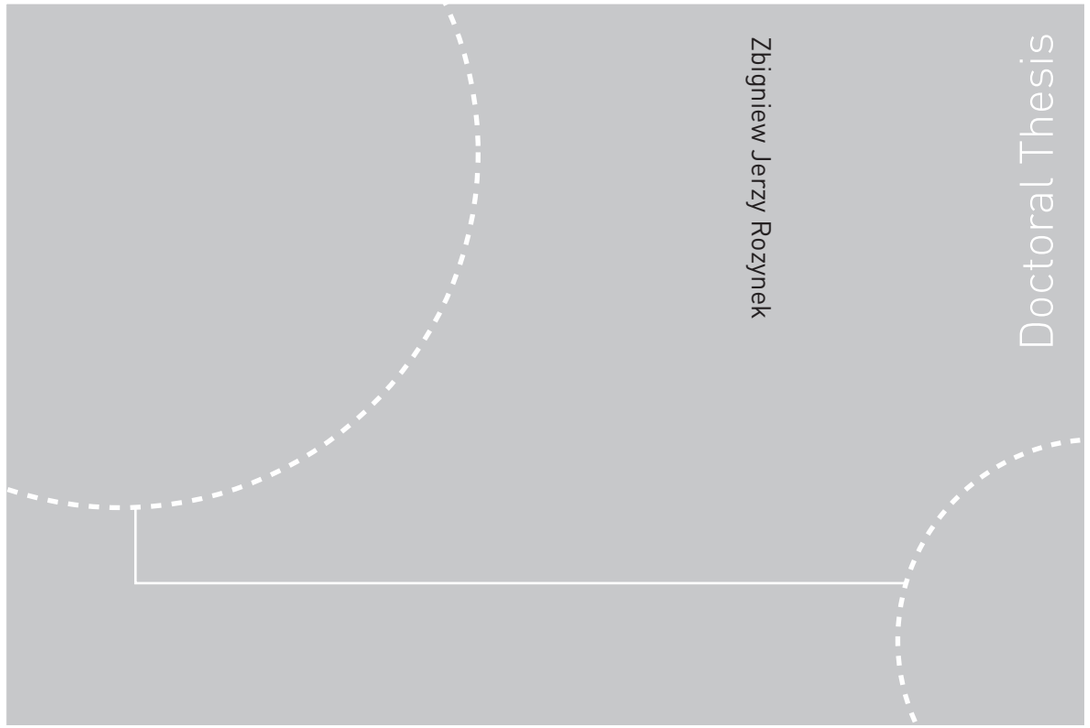

Doctoral theses at NTNU, 2011:279

Zbigniew Jerzy Rozynek

Experimental Studies of Self-organization from Electrically Polarized Clay Particles

NTNU
Norwegian University of
Science and Technology
Thesis for the degree of
Philosophiae Doctor
Faculty of Natural Sciences and Technology
Department of Physics

NTNU
Norwegian University of
Science and Technology

Doctoral theses at NTNU, 2011:279

NTNU

NTNU
Norwegian University of
Science and Technology

Zbigniew Jerzy Rozynek

Experimental Studies of Self-organization from Electrically Polarized Clay Particles

Thesis for the degree of Philosophiae Doctor

Trondheim, October 2011

Norwegian University of
Science and Technology
Faculty of Natural Sciences and Technology
Department of Physics

NTNU
Norwegian University of
Science and Technology

NTNU
Norwegian University of Science and Technology

Thesis for the degree of Philosophiae Doctor

Faculty of Natural Sciences and Technology
Department of Physics

ISBN 978-82-471-3127-5 (printed ver.)
ISBN 978-82-471-3128-2 (electronic ver.)
ISSN 1503-8181

Doctoral Theses at NTNU, 2011:279

Printed by Tapir Uttrykk

Acknowledgements

I would like to acknowledge professor Jon Otto Fossum. Primarily, for his encouragement, comments and guidance that fulfilled the major expectations one could have from a good university supervisor. Secondarily, for his managing skills, concerning a time-consuming writing of different proposals for financial grants and scientific supports, such as allocations of a synchrotron beamtime, etc. The latter one I have also found to be important for my scientific development.

Special thanks go to professor Kenneth Dahl Knudsen from IFE, who has helped me in countless ways over the four years it has taken to finish the thesis.

I could not have completed this project without several kinds of help. In particular, I would like to express my gratitude to all co-authors. Most of my time inside and outside a laboratory (including day and night shifts) I have spent with Baoxiang Wang, Min Zhou, Rene Castberg, Henrik Mauroy and Tomas Plivelic.

Warm thanks go to my colleagues and friends at the Department of Physics for creating a friendly environment. Elisabeth Lindbo Hansen, Davi de Miranda Fonseca and Henrik Hemmen must be explicitly mentioned here, and their contribution both to my scientific progress and to my personal development.

I also thank the technical staff, which would include persons working in the electronic workshop, glass workshop, and the main mechanical workshop. Ole Tore Buset is our group technician, and I thank him for his invaluable help throughout my whole work.

I am utterly grateful to my friends and family whose encouragement and loving presence enabled me to write this dissertation.

I especially want to thank Wioletta for believing in me and being patient. She carefully minded what I was doing in order to prevent me from becoming a workaholic person.

I acknowledge the Research Council of Norway for their financial support. This PhD scholarship was granted through the FRINAT Program: NFR project number 171300.

Preface

The clay based systems studied here belong to the field of science called complex matter physics. One can define a complex system as consisting of many independent entities ("particles" in a broad sense) coupled via various interactive connections. Descriptions of such complex systems are in general simplified by focusing on the "right level of description"[*], thus reducing the unnecessary factors (e.g. studying only the mechanisms of aggregation of clay particles). This may lead to extraction of the essential descriptive elements of interest from such a complex system (e.g. dipole-dipole particle interactions in the present case).

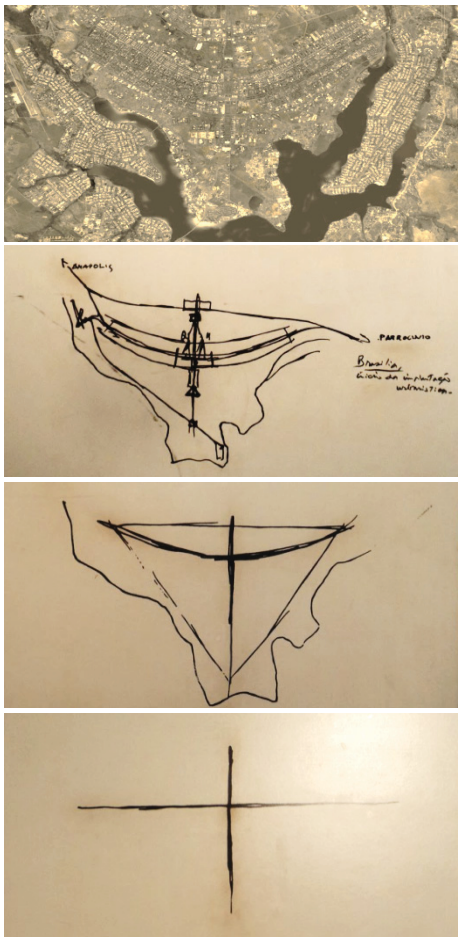

During one of my conference travels I visited the "Espaço Lúcio Costa" museum and took pictures of the famous pilot plan for Brasilia drawn by Lucio Costa. These pictures may serve here as a good example of how things can be taken apart to find an essence of the design. It is not possible to guess the shape of the city by looking at the top most image. A vast number of details may hide the essential pattern. Once the redundant features are removed, the contours start appearing. After further reduction the major curves are revealed, and finally two simple crossing segments are obtained. Now depending on the level of description of interest, different levels of hierarchical complexity leading towards the final essential simplistic description at the bottom panel, may be found in all of these stages.

This way of reducing complexity can in general be utilized to understand general physical processes and phenomena in materials science, for example for the clay based systems we study here.

In my general view, and for my own work in particular, it is important to include such a philosophical base into the research in any field of science[†].

Figure 1. The famous pilot plan for Brasilia drawn by Lucio Costa. The sketch shows how one can extract the essence from a complex matter system (as in this example the real city of Brasilia), and focus on the right level of description reducing the unnecessary factors for the description. The top most image is reprinted from Google Maps.

[*] N. Goldefeld and L. Kadanoff, Science vol. 284, p. 87 (1999)

[†] These philosophical reflections are based on the discussions by E. G. Flekkøy and J. O. Fossum on *Complexity - Systems and Interplays in Nature*, in the book „Naturens kode", E. Newt and G. Einevoll, eds., Gyldendal 2005. For an english translation see: http://www.complexphysics.org

List of papers

1. **Dynamic column formation in Na-FLHC clay particles: Wide angle X-ray scattering and rheological studies**
   Z Rozynek, B Wang, M Zhou and J O Fossum
   J. Phys.: C.S. **149** (2009) 012026

2. **Electric field induced structuring in clay–oil suspensions: new insights from WAXS, SEM, leak current, dielectric permittivity, and rheometry**
   Z Rozynek, K D Knudsen, J O Fossum, Y Méheust, B Wang and M Zhou
   J. Phys.: Condens. Matter **22** (2010) 324104

3. **Electrorheological properties of organically modified nanolayered laponite: influence of intercalation, adsorption and wettability**
   B Wang, M Zhou, Z Rozynek and J O Fossum
   J. Mater. Chem. **19** (2009) 1816-1828

4. **E-field Induced Alignment from Organically Modified Fluorohectorite Clay Particles**
   Z Rozynek, B Wang, J O Fossum and K D Knudsen
   Submitted to Eur. Phys. J. E

5. **Different Aspects of Electrically Activated PP/Clay Nanocomposites**
   Z Rozynek, T S Plivelic, S M L Silva, J O Fossum, E N de Azevedo and G J da Silva
   In preparation.

6. **Characterisation of Paraffin/Clay Composites.**
   Z Rozynek, R Castberg, J O Fossum and A Mikkelsen
   In preparation.

7. **Electric Field Induced Structuring and Rheological Properties of Kaolinite and Halloysite Clays**
   Z Rozynek, T Zacher, M Janek, M Čaplovičová and J O Fossum
   In preparation.

Other papers (included in this thesis in the Appendix)

8. **Structuring from nanoparticles in oil-based ferrofluids**
   Z Rozynek, A Józefczak, K D Knudsen, A Skumiel, T Hornowski, J O Fossum, M Timko, P Kopčanský and M Koneracká
   Eur. Phys. J. E **34** (2011) 28

9. **Wide angle scattering study of nanolayered clay/gelatin electrorheological elastomer**
   B Wang, Z Rozynek, M Zhou and J O Fossum
   J. Phys.: C.S. **149** (2009) 012032

Other papers (not included in this thesis)

10. **Carbonate-Assisted Hydrothermal Synthesis of Nanoporous CuO Microstructures and Their Application in Catalysis**
    M Zhou, Y Gao, B Wang, Z Rozynek and J O Fossum
    Eur. J. Inorg. Chem. (2010) 729-734

11. **Minute synthesis of extremely stable gold nanoparticles**
    M Zhou, B Wang, Z Rozynek, Z Xie, J O Fossum, X Yu and S Raaen
    Nanotechnology **20** (2009) 505606

It has been decided that two scientific articles (P.8 and P.9) should be included in the thesis as appendices, since they are partially related to the main subject regarding both the self-assembly phenomena and clay science.

The two last papers (P.10 and P.11) are mentioned only in the list of papers. They are not a part of this dissertation nor directly related to the subject of this thesis, but they were also completed with my contributions in the laboratory during the time of my PhD work.

My contribution to the papers

1. **Dynamic column formation in Na-FLHC clay particles: Wide angle X-ray scattering and rheological studies**
   My contribution to this scientific article includes: sample preparation, involvement in all performed experiments, data analysis, writing and handling the submission process.

2. **Electric field induced structuring in clay–oil suspensions: new insights from WAXS, SEM, leak current, dielectric permittivity, and rheometry**
   My contribution to this scientific article includes: sample preparation, involvement in all performed experiments, data analysis, writing and handling the submission process.

3. **Electrorheological properties of organically modified nanolayered laponite: influence of intercalation, adsorption and wettability**
   My contribution to this scientific article includes experimental part, namely wide angle X-ray scattering and energy dispersive spectrometry. I participated in discussions over the results, analysed part of the data in the paper, and helped in writing.

4. **E-field Induced Alignment from Organically Modified Fluorohectorite Clay Particles**
   My contribution to this scientific article includes: sample preparation, involvement in most of the performed experiments, namely wide angle X-ray scattering, zeta potential measurements, optical microscopy observations, sedimentation tests, and electric current measurements. Most of the data analysis and writing was conducted by me. I also handled the submission process.

5. **Different Aspects of Electrically Activated PP/Clay Nanocomposites**
   My contribution to this scientific article includes: designing of the heating cell and the experimental set-up and participation in the synchrotron studies. The data analysis and part of writing process were conducted by me. I also participated in all discussions concerning the results and research development.

6. **Characterisation of Paraffin/Clay Composites.**
   My contribution to this scientific article includes: sample preparation, involvement in all performed experiments, namely wide angle X-ray scattering, rheology and optical microscopy observations. The data analysis and writing was conducted by me. I will handle the manuscript submission process.

7. **Electric Field Induced Structuring and Rheological Properties of Kaolinite and Halloysite Clays**
   My contribution to this scientific article includes: involvement in major part of the performed experiments, namely wide angle X-ray scattering rheometry, optical observation measurements and electrical current measurements. The data analysis and part of writing process were conducted by me. I also participated in all discussions concerning the results and research development. I will handle the manuscript submission process.

Contents

1. Introduction

The research presented here has been performed at the Department of Physics, in the Laboratory for Soft and Complex Matter Studies. The scientific work included primarily experimental studies of nano-structured soft and complex materials, in particular clay minerals. The title of the project is: *Experimental Studies of Self-organization from Electrically Polarized Clay Particles*, and the assignment involved studies of general physical processes and phenomena in such systems by means of experimental methods such as x-ray scattering (SAXS/WAXS), atomic force microscopy (AFM), scanning and transition electron microscopy (SEM/TEM), rheometry, zeta potential measurements, energy dispersive analysis (EDS), optical microscopy observations, electric current and dielectric properties measurements, and other methods. In addition to working with these techniques at laboratories at NTNU, experiments were performed at X-ray synchrotron sources, and in collaboration with researchers at those laboratories (ESRF in France and MAX-lab in Sweden).

In the present studies, the final structure is self-organized *from/by* particles. It should not be confused with the term self-assembly *of* particles, which refers to more general meaning of building a nanoscale structure molecule by molecule

The project was initially planned as a continuation of the research started by previous PhD candidate K.P.S. Parmar, in which guided self-organization from non-modified clay particles was studied by means of some of the experimental techniques mentioned above [1]. However, many new ideas blossomed a few months after the startup of my PhD employment and led to: studies of modified laponite and fluorohectorite assemblies in oil suspensions; investigation of clay/paraffin composites; observation of structural changes in clay/polymer melted composites; and finally rheological properties and *E*-field induced structuring of kaolinite and halloysite clays.

To provide a background for the scientific papers, the introductory part of the thesis has the following layout: firstly, detailed information about different non-modified clay particles used during the studies, namely fluorohectorite, laponite, montmorillonite, kaolinite and halloysite, is provided in section 1.1; their modified counterparts are presented in section 1.2 together with short explanations on the modification routines; the clay particle behaviour in *E*-fields is explained in 1.3, and descriptions of the experimental techniques used within the whole research project are given in section 1.4. The summary of the main results and the thesis development are presented in section 2, while section 3 covers the last comments and future outlook. The main research results of this thesis start in section 4, and that includes published scientific articles and manuscripts either submitted or in preparation. In the appendix one can find other experiments, conducted during the PhD study period, that are related to the subject of particle alignment, but should not be considered as the part of the thesis.

1.1. Clay and clay minerals

An often used definition of nomenclature for clay and clay minerals, given by the joint nomenclature committees (JNCs) of the Association Internationale pour l'Etude des Argiles (AIPEA) and Clay Minerals Society (CMS), describes *clay* as: "a naturally occurring material composed primarily of fine-grained minerals, which is generally plastic at appropriate water contents and will harden when dried or fired". Likewise, the term *clay mineral* is difficult to describe. The definition proposed by the JNCs is: "… phyllosilicate minerals and minerals which impart plasticity to clay and which harden upon drying and firing" [2,3].

According to the author, the definitions above do not provide explicit and sufficient information and are included rather as a matter of a form. Instead, the characteristic properties of *clay* and *clay minerals* presented in Table 1 are believed to deliver a more intuitive understanding.

Table 1. Characteristic properties of clay minerals

Property	Explanation
Layered structure	Particle consists of thin (0.65-1 nm) crystalline sheets that usually stack up one another forming a "deck of card" like structure[‡].
Swelling	An increase in particle thickness due to water[§] intercalation between the crystalline sheets (platelets).
Particle size	Thickness/radius in nanometres range, width/length < few μm (aggregates can take sizes up to mm).
Specific surface area	The total surface area per unit of mass – can be as high as hundreds of m^2/g. Important in case of adsorption, gas permeability and other reactions on surfaces.
Charge	The net layer charge (e^-) arises when tetrahedral and octahedral sheets are joined to form a single crystalline layer. For 1:1 phyllosilicates: $\xi \sim 0$ (e.g. kaolinite, halloysite) For 2:1 phyllosilicates: $\xi \sim 0.2$ to 1.2 (e.g. hectorite, laponite)
Intercalation	Ability to host extraneous substances such as surfactant molecules, polymeric chains and other macromolecules.
Modification	The ease with which both an external and an internal surface can be modified. For example, adding surfactant molecules onto the clay particle external surface changes its hydrophilic properties.
Plasticity	Defined as the ability of a clay material to be moulded into a certain shape without rupturing when stress is applied, and for this shape to be retained after the stress is removed.
Hardening	When fired or dried becomes firm and permanent physical and chemical changes may occur.

[‡] Applies to a disc/flake-like particle. In case of e.g. halloysite, formed by rolling up a platy structure, the layer repetitions can be found across the two dimensional spiral.

[§] Intercalation of other spieces may also change the characteristic distance along stacking direction.

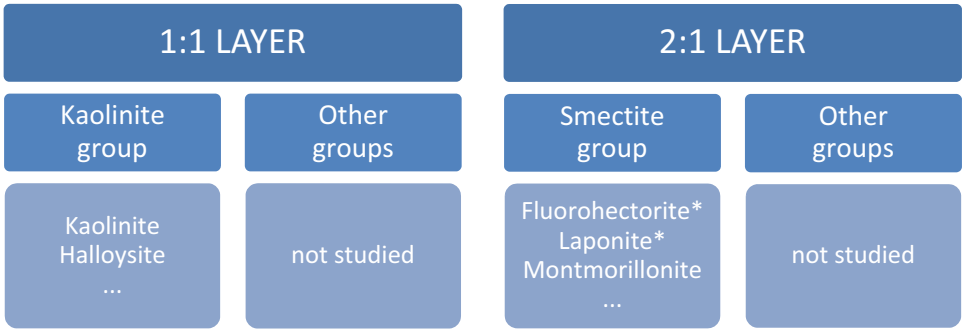

Figure 2. Diagram showing a classification of clay minerals used in the thesis. Asterisk (*) denotes synthetic materials.

There is a distinction between the terms *clay* and *clay mineral.* The two major differences are the material's origin and its size. *Clay mineral* can be natural or synthetic with no size criterion, whereas *clay* is defined as a natural, fine-grained (<2 μm or 4 μm) phyllosilicates. Since the expression *clay mineral* encompasses both natural and also synthetic clays, it will be used throughout this thesis wherever mentioned clay, clay particle or clay mineral[**].

There are many ways of classifying clay minerals based on different criterions. Firstly, they are divided into two groups called one-to-one (1:1) and two-to-one clays (2:1), which refers to their crystalline sheet structure. Clays are fundamentally built of tetrahedral (T) and octahedral (O) sheets. Thus 1:1 clay particle (TO) consists of the repetition of one tetrahedral and one octahedral sheets, while the 2:1 notation (TOT) signifies that the host layers contains one octahedral sheet sandwiched between two tetrahedral sheets. The schematic examples of these two configurations are shown in Figure 3. Clay minerals are arranged in groups as shown in Figure 2, where clay minerals used in this research are highlighted.

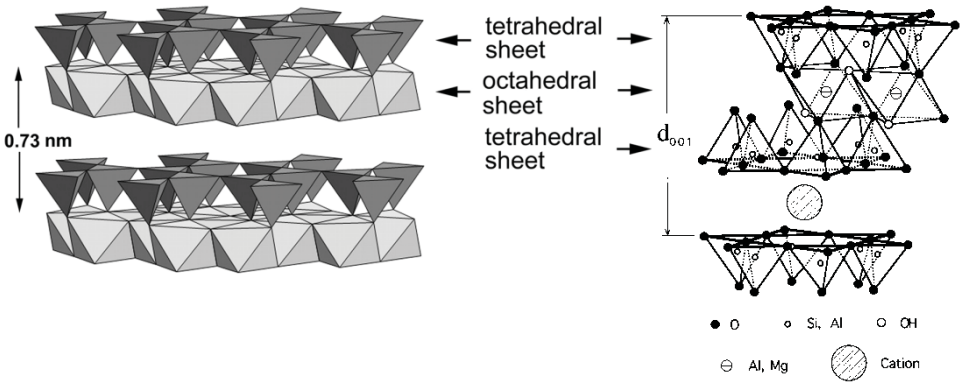

Figure 3. Typical 1:1 structure of kaolinite (left) [4] and a 2:1 layered silicate clay (right) [5]. The basal spacing d_{001} is the smallest c-axis repeat distance. Note: there is no gallery cation for 1:1 clay.

[**] Many researchers do not (consciously or not) differentiate between those two terms and simply use *clay* when writing about *clay minerals.*

1.1.1. Kaolinite and halloysite

Both kaolinite and halloysite belong to the kaolin group of minerals having essentially similar chemical composition with the nominal chemical formula $Al_4Si_4O_{10}(OH)_8$ per unit cell, but each have important structural and stacking differences. It is a 1:1 layer silicate mineral, with one tetrahedral sheet linked through oxygen atoms to one octahedral sheet of alumina octahedral [6]. Kaolinite has been described as a non-expandable clay. However, when treated with aqueous solutions containing molecules such as urea, or potassium acetate, kaolinite undergoes expansion through the insertion of the molecules between the kaolinite layers [7-11].

Halloysite has a single layer of water molecules in each interlayer space which increases d_{001} from characteristic 7.2 Å of kaolinite to about 10 Å. Dehydrated halloysite had $d_{001} \sim 7$ Å. There is a marked tendency for layers of halloysite to roll up into cylinders or scrolls or to adopt spheroidal shapes. This, and layer disorder, leads to broad and asymmetric rather than sharp X-ray reflections. There are, however, examples of platy halloysites [6].

Kaolinite characteristic features:

- Interlayer space $d_{001} \sim 7.2$ Å,
- Net charge $\xi \sim 0$,
- Disc-shaped, form "a deck of card" structure (see Figure 4 left),
- No swelling with water, but can swell with a few organic compounds.

Halloysite characteristic features:

- Interlayer space $d_{001} \sim 10$ Å or
- Interlayer space $d_{001} \sim 7.2$ Å, when heated ~ 200 ºC,
- Net charge $\xi \sim 0$,
- Tend to roll up into cylinders, spheroidal shapes, etc. (see Figure 4 right).

Common applications: paper coating and filling, used in the manufacturing of bricks and ceramics, paint, plastics, textiles, gaskets, adhesives, sealants, caulks, fertilizers, rubber, ink, fiberglass, cracking catalysts and many other uses [12].

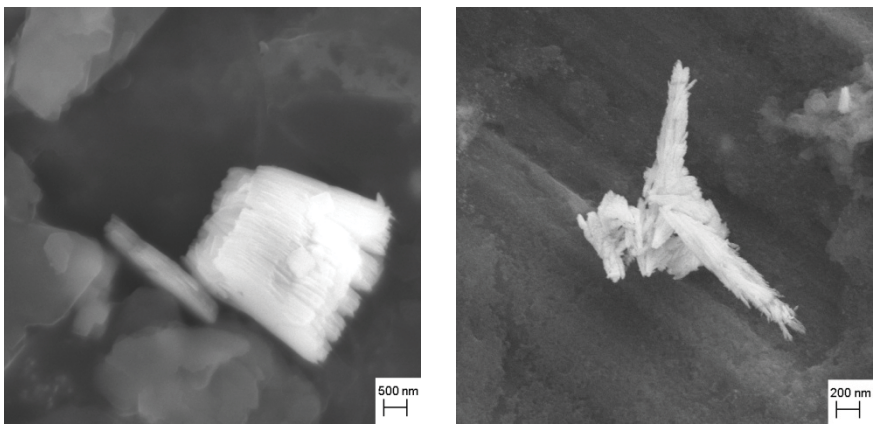

Figure 4. SEM image of kaolinite (left) and halloysite (right) clay particles.

1.1.2. Fluorohectorite (Fh), laponite (Lp) and Montmorillonite (Mmt)

Fluorohectorite, laponite and montmorillonite clay minerals belong to the smectite group. Smectites are 2:1 phyllosilicates that possess a net negative charge. Counter ions are located between clay lamellar sheets to balance for that charge. The exchangeable cations such as sodium, calcium, lithium, iron or magnesium are common. In this thesis, two samples with different cations were used, i.e. Na-Fh and Li-Fh.

All of smectites take up water which results in expendability. The interlayer hydration complexes of these clays arise from intercalation of a discrete[††] number of water layers (WL), that is: 0WL, 1WL, 1.5WL[‡‡] and 2WL. The swelling of layered smectite clay particles consists of a change in the interlayer repetition distance (*d*-spacing) as a function of temperature and humidity [13]. Apart from intercalated water, organic molecules may be present when exchanged with inorganic cations. The surface of smectites particles is hydrophilic, i.e. it has a tendency for binding water. This property can be altered by chemical modification (see section 1.2). Thus when the non-modified clay minerals are suspended in polar medium (such as water) they disperse very well, whereas in a non-polar medium (such as silicone oil) they form agglomerates and tend to sediment out.

Fluorohectorite has the following chemical formula: $M_x(Mg_{6-x}Li_x)F_4Si_8O_{20}$, where M denotes either Li or some other monovalent cation. It is a silicate where a fraction of Mg^{2+} ions is substituted by Li^+ in trioctahedral sites resulting in a structural negative charge of 1.2 e^- per unit cell [14]. The surface charge density of fluorohectorite is very high when compared to that of laponite (0.4-0.7 e^- per unit cell). Fluorohectorite has been reported from x-ray data to retain a stacked structure of lamellar particles composed of between 20 and 100 unit layers when dispersed in water, whereas laponite is known to exfoliate into single unit layers in aqueous suspensions [15].

The chemical composition of montmorillonite is $M_x(Al_{4-x}Mg_x)Si_{8-y}Al_yO_{20}(OH)_4$. The structure of montmorillonite exhibits a substitution for Si^{4+} by Al^{3+} in the tetrahedral layer and for Al^{3+} by Mg^{2+} in dioctahedral sites that gives rise to the net negative charge of 0.8 e^- per unit cell [16].

Laponite is a synthetic clay mineral having the smallest dimensions of all species mentioned above. In a dilute aqueous suspension, the individual laponite clay particle resembles a disc of thickness 1 nm and of average diameter ~25 nm. Laponite clay is a particularly interesting model system due to both the small size and monodispersity of the colloidal platelets, in contrast to natural and other synthetic clays which in general are polydisperse and micrometer sized [17]. When dissolved in water, H_2O molecules enter the interlayer space to hydrate the sodium ions. This breaks the particle-stacks apart (formed when laponite in a form of powder), resulting in separated Laponite discs, or separated groups of discs.

[††] It was recently reported by Hemmen at el. [13] that the sudden transition step from a monohydrated state (1 WL) to a dehydrated state (0 WL) as well as between the monohydrated and dihydrated (2 WL) state, is preceded by a continuous change in the interlayer space.

[‡‡] The existence of an intermediate regime (1.5 WL) was found recently by Tenorio et al. for Li-Fh clay mineral kept at RH~60 % [18]. Also the molecular simulation of Tambach et al. [19] in Li-montmorillonite hydrates shows existence of a basal spacing 13.5 Å.

Because laponite discs have a negatively charged faces and positively charged edges, the individual particles interact, forming three-dimensional networks [20]. This property of forming a clear gel is utilized in various applications. Laponite's empirical chemical formula is $Na^{0.7+}[Si_8Mg_{5.5}Li_{0.3}O_{20}(OH)_4]^{0.7-}$, where Na is an interlayer exchangeable cation. Laponite is a synthetic trioctahedral hectorite clay composed of two tetrahedral silica sheets and a central octahedral magnesia sheet. The negative surface of the laponite particle contains positively charged sodium ions. These can be shared by several laponite sheets forming aggregates [21].

In Figure 5 the scanning/transmission electron microscopy (SEM/TEM) images of sodium fluorohectorite (left) and laponite (right) particles are shown. Note that the micrographs were taken with different magnifications. One can see that fluorohectorite particles can be more than 100 times larger than those of laponite. Fh particles resemble more hexagonal platy structures, whereas laponite particles display more rounded shapes.

Smectite clay minerals characteristic features:

- Interlayer space d_{001} ~10, ~12.5, ~15.5 Å, for 0WL, 1WL and 2WL
- Exchangeable cations (e.g. Na^+, Li^+, Fe^{2+}) balance the negative charge,
- Swelling occurs in a stepwise fashion,
- Net charge $\xi \sim 1.2$ for Fh, $\xi \sim 0.8$ for Mmt and $\xi \sim 0.4$ for Lp,
- Mmt is a natural clay mineral, whereas Fh and Lp are synthetic,
- Can sorb cationic species from solution, high cation exchange capacity.

Common applications of clay from the smectite group: can be also used in the manufacturing of bricks and ceramics, drilling muds, paper, rubber, paints and many other applications. Since various organic molecules can be accommodated in interlayer spaces, the smectite clays are extensively used as decolorizing agents, for purifying fats and oils, and also in the refinement of petroleum. Their ion exchange properties lead to possible use in treating radioactive waste [6]. In addition, laponite can be used in conventional toothpastes and mouthwash liquids [22].

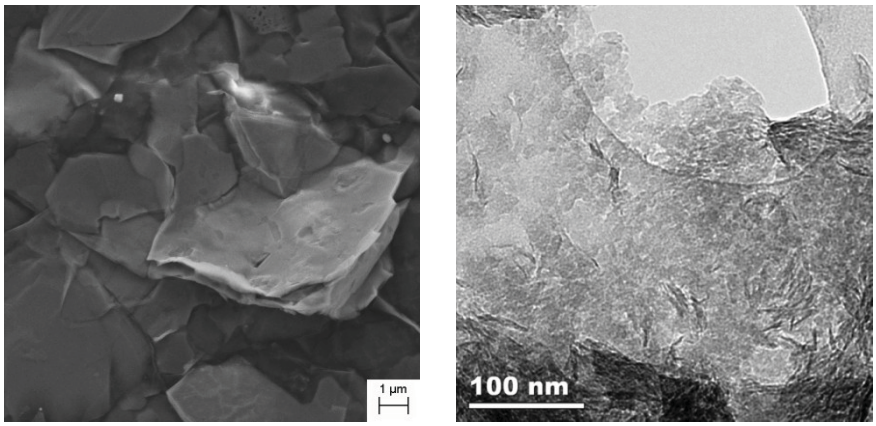

Figure 5. SEM image of Fh (left) and TEM image of Lp (right) particles. Note different scale bars.

1.2. Modification of clay particles

Clays, in their natural forms, are hydrophilic, or depending on the discussed context one could say organophobic. When suspended in a non-polar medium, such as silicone oil, they tend to form large agglomerations and sediment. In order to make use of clay particles for example as a basis for an ER fluid one needs to avoid the tendency for particles in suspension to sediment. The general methods to counteract the sedimentation include controlling both size and shape of particles, preparing hollow or porous particles, and matching of densities between particles and solution [23,24]. Addition of surfactants is commonly used to prevent the particle agglomeration, which then slows down particle sedimentation, or if the particles are small enough (i.e. magnetic particles in ferrofluids), ensures that they are held in suspension by Brownian motions [25]. By exchanging the original interlayer cations for organocations (typically quaternary alkylammonium ions) an organophilic surface is generated, consisting of covalently linked organic moieties.

Another reason for modifying clays is the ease of uniform dispersion in an apolar polymer matrix. Since the aspect ratio of the clay layers and the interfacial contact area between the clay and matrix are high, the incorporation of small amounts of such inorganic filler into a polymer medium can significantly improve the properties of the resulted polymer/clay nanocomposites [26,27]. However, the chemical affinity between the inorganic filler and apolar polymers is quite reduced. To promote compatibility, it is necessary to chemically modify the inorganic filler with intercalation of organophilic character cations, which expand the interlamellar space of the clay, decreasing the interaction among the silicate sheets, and facilitating the diffusion and accommodation of the polymeric matrix [28].

The layered silicate polymer nanocomposites can also attained a great degree of stiffness and strength. Furthermore, the presence of the dispersed phase results in additional properties, such as flame retardancy, enhanced barrier properties, increased degradability of biodegradable polymers, as well as ablation resistance, compared to either component [29,30,31]. All these improvements depend heavily on the structure and properties of the organoclays. Hence, understanding the microstructure of the organoclays themselves is essential for many industrial applications.

Three types of clay minerals belonging to the smectite group have been organically modified. The obtained organoclays' new physical and chemical properties, and also behaviour in presence of an external electric field were investigated and compared to that of their non-modified counterparts. In particular, changes in the electrorheological properties of organically modified clays, the surfactant intercalation type and its adsorption, particle wettability, nature of aggregation, and also an *E*-field induced structuring were studied.

1.2.1. Modified fluorohectorite and laponite

The synthetic laponite clay was purchased from Laponite Inc. as a fine white powder, and the synthetic fluorohectorite clay was delivered by Corning Inc. with lithium being an exchangeable cation. Both clay types were modified using a surfactant called cetyltrimethylammonium bromide (CTAB, which has the chemical formula $[CH_3(CH_2)_{15}]NBr(CH_3)_3$. Most of surfactants consist of a hydrophobic tail and a hydrophilic head. Depending on the composition of their head, they are classified as: non-ionic, anionic, cationic and amphoteric. The CTAB is a cationic surfactant with a positively charged head group. Therefore the head of the molecule tend to adsorb onto the clay particle face carrying a negative net charge. Depending on the concentration of the CTAB used during the modification, the cation exchange and intercalation occur – the cations (e.g. Li^+ or Na^+) are replaced by the surfactant molecules. This can also increase the characteristic interlamellar distance between clay crystalline sheets as it is shown in Figure 6.

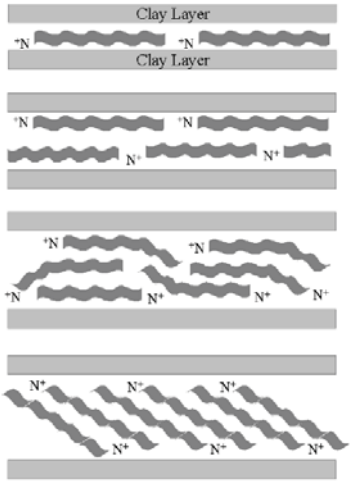

The surfactant molecules can adopt monolayer, bilayer, pseudotrimolecular, paraffin-type or other arrangements. It may require long time of exchanging process to obtain a fully developed structure. For sake of example the results published by He et al. [32] are provided. They showed that arrangements of the surfactant in the smectite clay interlayer were fairly distinctive and varied from lateral-bilayer (0.7CEC, 1.48 nm), then to paraffin-type monolayer (1.5CEC, 2.45 nm) and finally to paraffin-type bilayer (5CEC, 4.03 nm). For more detailed studies and examples of the development of the lamellar structure due to increase of the surfactant concentration, the following references are recommended [32-35].

Figure 6. Potential conformations of interlayer cations: (from top to bottom) monolayer, bilayers, pseudo-trimolecular layer, and paraffin complex. Reprinted from [33]

Both types of organoclays can be made according to a procedure that can be simplified as follows. The appropriate amount of cationic surfactant is mixed with DI water. In another beaker the clay powder is stirred in DI water in a similar way. After some time both solutions are mixed together and stirred for a long time (hours-days) at around 80 ºC. Rinsing is needed to remove any free surfactant from the solution. The filtered clay can be then (i) dried at 110 ºC and dispersed in a non-polar liquid or (ii) transferred directly to such medium using the liquid-liquid phase transfer method. The obtained cationic surfactant exchanged modified laponite/fluorohectorite clays can be labelled according to the CTAB concentration used, e.g. 0.5CEC-clay, 1CEC-clay or 4CEC-clay (xCEC means x times the cation exchange capacity).

1.2.2. Modified montmorillonite

Modified montmorillonite was purchased from Southern Clay Products, Inc. It has a brand name Cloisite® 20A. It is a natural montmorillonite purified and modified with a quaternary ammonium salt ion-exchanging sodium cations. Cloisite® 20A is commercially used as an additive for plastics and rubber to improve various physical properties, such as reinforcement, coefficient of linear thermal expansion, synergistic flame retardant and barrier. Its characteristic interlamellar distance d_{001} is around 2.42 nm [36]. This distance can change when particles suspended in polymeric matrix [37].

To summarize, organically modified clay particles can be used when a non-polar environment is used as the hosting medium. The figures below show two important examples of sample improvement with regards to particle anti-sedimentation properties and dispersion. There is currently a great deal of interest in the development of new techniques of particle dispersion in, for example, PP/clay nanocomposites this includes particle alignment and also delamination, where the silicate layers are fully separated and dispersed homogeneously throughout the polymer matrix [38].

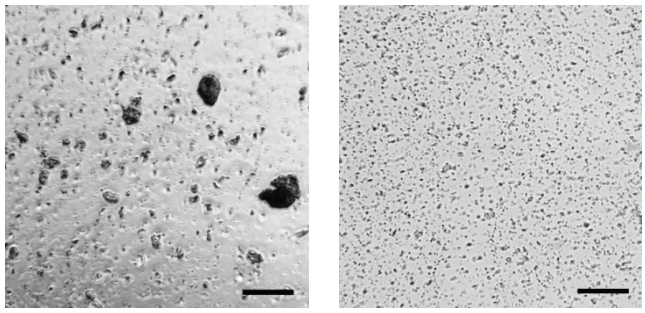

Figure 7. Microscope images of non-modified Na-Fh (left) and organically modified Fh (right) clay particles suspended in silicone oil. The length of the bar corresponds to 200 μm.

Figure 8. All non-modified clay particles (top row) sedimented just after 1 day, whereas for organoclay particles (bottom row) it took around 2 weeks.

1.3. Clay particles in E-fields

Since a substantial part of the present research includes the electric-field induced structuring from clay particles, it is necessary to explain physical aspects behind this behaviour.

Application of an electric field induces polarization of the suspended dielectric particles. They consequently orient in the field and aggregate, which results in the formation of a columnar structure parallel to the electric field direction [39]. The final[§§] particle organization is shown in Figure 9a, where the electric field is applied horizontally to the clay/silicone oil suspension. Figure 9b presents a sketch of an X-ray experiment in which the particle orientation distribution is inferred from the two dimensional diffraction patterns.

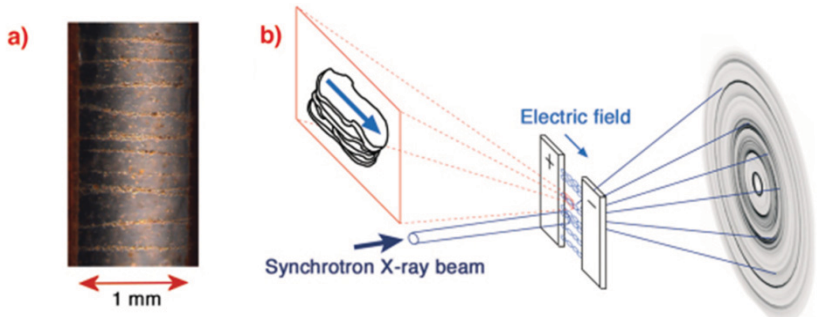

Figure 9. a) Optical microscope image of ER chain formation under an *E*-field applied in the horizontal direction. b) Sketch of the reported X-ray scattering experiments. Reprinted from [39].

The formation of a column-like structure consists of four stages and these need to be considered separately in order to describe different physical processes that lead to the final particle assembly.

(i) Clay particles polarization

Application of an external electric field induces particle polarization. The clay particles polarise along their silica sheets, i.e. their stacking direction in normal to the polarisation direction. Fossum et al. [40] suggest that the intercalated ions and water, which are movable, could play a central role in particle electrical polarisation. The resulting induced dipole is attached structurally to the clay particle, and this causes clay particles to reorient and interact. However, a detailed description was not provided in ref. [40] and the mechanisms of the polarization in clays are still under discussion. It is not a trivial task to perform an experiment[***] which could confirm or disprove some of the hypotheses. Normally clay particles contain water molecules that can

[§§] Within a given time scope, in this case an optical microscopty image was taken few minutes after the application of an *E*-field.

[***] There is actually an ongoing experiment which may help to shine light on the subject of clay polarization. Differently prepared clay particles suspended in silicone oil are submitted to an *E*-field. Their rotation (very diluted system to avoid particle-particle interactions) is recorded and then the rotation time is estimated. It is believed that this approach could be utilized to define the polarization mechanism and quantify the particle charge.

occur in four modes: intercalated water either associated with intercalated cations, internal surfaces in the clay stacks, adsorbed on the external surfaces of the stacks, or free water molecules that are trapped in micropores between stacks by capillary forces. This increases the system complexity. In addition the role of exchangeable ions and clay surface ions has to be taken into account.

The rheological data provide an approximate time scale τ_1 for polarisation, which is in a range of 10^{-5} to 10^{-7} seconds. This is a rapid process and the application of an AC fields in low and middle range frequencies has no influence on the particle rotation. However, the usage of the AC fields can be advantageous since the effect of electrophoresis[†††], which is often observed in a clay/oil suspension, can be avoided.

(ii) Particle rotation / alignment

When polarized, a clay particle starts to rotate and orient along the E-field direction. The rotation time is proportional to the carrier fluid viscosity and inversely proportional to: firstly the difference in the dielectric constants between particle and medium; and secondly the electric field squared. The time scale τ_2 for particle rotation is in a range of 10^{-3} to 10^{1} seconds, for E-field strengths between 50 and 2000 V/mm and viscosity of silicone oil between 100 and 500 mPa.s. This allows for optical microscopy observation when a high-speed camera is used or when E-field strength is low and viscosity high[‡‡‡].

(iii) Chain formation

If particle concentration is high enough and a minimum critical E-field is applied[§§§] a chain formation occurs via a particle dipole-dipole interaction.

The potential energy can be expressed as [41]:

$$V_{d-d} = \frac{1}{4\pi\varepsilon_o} \cdot \frac{\vec{p}_1 \cdot \vec{p}_2 - 3(\hat{n} \cdot \vec{p}_1)(\hat{n} \cdot \vec{p}_2)}{|\vec{r}_1 - \vec{r}_2|^3} \qquad (1)$$

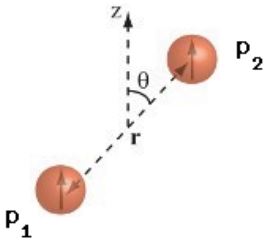

[†††] Electrophoresis may also be a desired effect, for example the electrophoretic mobility can be measured to study the role of exchangable cations.

[‡‡‡] Numbers taken from a recent ongoing experiments, not published yet.

[§§§] Critical field and critical particle concentration are coupled one to another.

where: p is the electric dipole moment and p_1=p_2=p for the same particles, r is the distance between particles, $\hat{n}$ is the unit vector, and θ is the angle between the vector connecting the two particles and the electric field direction.

$$\vec{p}_1 \cdot \vec{p}_2 = p^2$$

$$\hat{n} \cdot \vec{p}_1 = \mathrm{p} \cdot \cos\theta, \quad \hat{n} \cdot \vec{p}_2 = \mathrm{p} \cdot \cos\theta \quad thus$$

$$V_{d-d} = \frac{p^2}{4\pi\varepsilon_o} \cdot \frac{1 - 3\cos\theta \cdot \cos\theta}{r^3} \qquad (2)$$

Assuming finite values for p and r, V_{d-d} reaches zero when

$$1 - 3\cos^2\theta = 0 \ \ which\ gives\ \theta_{zero} \approx 54.7°$$

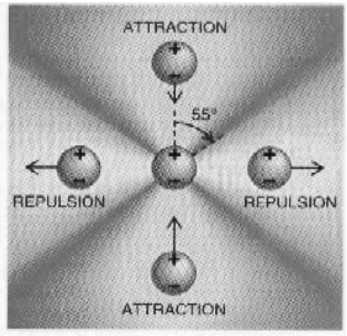

If the position of two particles is that the angle θ>54.7º they will repel each other, whereas when the angle θ<54.7º the attractive interaction will occur. That is the reason why particles form single chains. The time scale for particle bridging $\tau_3 \propto E^{-2}$ is between 10^{-1}-10^{1} s (for parameters as in (ii)). When time passes the structure may coarsen into thicker column-like assemblies (see further discussions).

Figure 10. The sketch of the dipole-dipole particle interaction. If two particles located within the theta angle of 54.7º, the attractive interaction will cause aggregation, otherwise they will repel one another. Reprinted from [42].

If the simple dipole moment is express as: $\vec{p} = \beta r_d^3 \vec{E}$ where β is an effective polarizability of the particle, r_d is its radius, and $\vec{E}$ is the electric field, the Eq.2 describing the interaction energy between two polarizable particles is given by:

$$V_{d-d}(r,\theta) \propto \frac{\beta^2 r_d^6 E^2}{r^3}(1 - 3\cos^2\theta) \qquad (3)$$

The force between these particles, which can be obtained by differentiating Eq.3, has three important features: it is a long-range interaction, decaying as a power law r^{-4}; and it is strongly anisotropic; and is proportional to E^2.

In real electrorheological fluids the situation may be more complex and some modifications should be taken into consideration. There exists no solvent being a perfect insulator, thus it will move charges to the particle surfaces in an attempt to screen the induced charge [43,44]. In addition, higher order multipolar interactions might play an important role. Thus, one needs to be careful when trying to describe the system in quantitative terms.

(iv) Chain coarsening into column-like structures

In the last step, which is characterized by a time scale $\tau_4 >> \tau_3$ the chain-like structures slowly drift together and coarsen. After an arbitrary long time, all of the chains (and thus all of the particles) in the fluid would be seen as a large aggregated mass. The force that drives the coarsening cannot solely originate from the electric field, since this interaction is weak (arises from the **periodic dipole moment** along each chain) and has a short-range nature. For perfectly aligned chains this interaction dies off exponentially with distance and is very weak when chains are separated by a distance greater than the size of their constituents.

However, the chains will never be perfectly ordered and will fluctuate thermally. When they do so, they develop **local concentrations of dipole moments**. The result is that the root mean square electric field dies off as power 2 of distance x from a chain (in direction normal to the chain axis) and is proportional to radius of dipolar particle.

$$E(x) \propto k_B \mathrm{T} \frac{a}{x^2} \qquad (4)$$

This leads to a power-law induced force between two chains, arising from the coupling between these dipole fluctuations in different chains. The effective free energy of interaction between such chains (of length L) separated by a distance l is

$$F(l) \propto -2k_B T \frac{La^4}{l^5} \qquad (5)$$

Interestingly this field does not depend on the strength of the induced dipole moment itself (provided that the external electric field is strong enough to form chain-like structures). This is due to the fact that stiffness of a chain increases with dipole moment reducing proportionally the strength of the fluctuations.

There is the third force contributing to the chain coarsening, namely **Keesom interaction**, which arises from the coupling between thermal fluctuations in the dipole moment of the individual particles. The interaction energy between lines is actually similar to that of the fluctuation coupling (eq.5)

$$U_{vdW}(l) \propto -A \frac{La^4}{l^5} \qquad (6)$$

where A is the Hamaker constant. For electrorheological fluids, A varies over about (0.2-2.5) $k_B T$, so that this coupling is in the same order of magnitude but normally smaller than the fluctuation coupling described before. For more detailed discussion the reader is referred to the following literature [45-47].

The time scale during which columns will collide with one another under the influence of the fluctuating forces $\tau_4 \propto E^{-4/5}$ is longer compared to $\tau_3 \propto E^{-2}$. The development of thick aggregated assemblies is shown in Figure 11. Initially clay particles are distributed randomly in silicone oil (left). When electric field is applied many single chain-like bridges are formed (middle), followed by larger structure formation.

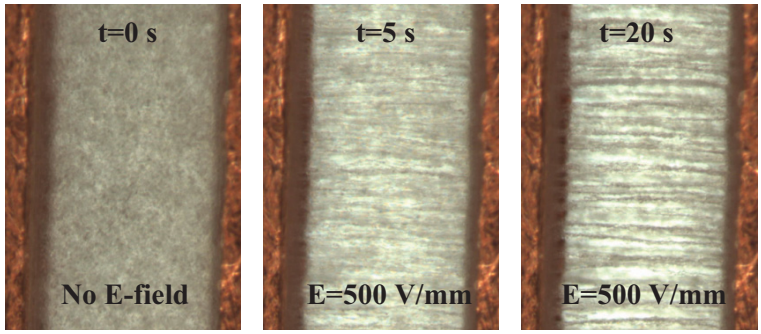

Figure 12. The development of thick columnar structures from Na-Fh clay particles suspended in silicone oil. Electric field is applied in a horizontal direction between electrodes spanned by 1 mm.

While investigating the whole process of the structuring or each phase separately, one should decide on type of electric fields used, since the behaviour of particles under a DC field may differ from that found in presence of an AC field. The electrophoretic particle motion is an important effect, dominating in a low frequency range between 0 and 30 Hz. This electrokinetic phenomenon was actually first time observed in 1807 using clay particles dispersed in water [48]. The dispersed clay particles have an electric surface charge that is screened by a diffuse layer of ions with the same absolute magnitude of charge but opposite sign. An external electric field exerts the electrostatic Coulomb forces (of different directions) on both the clay surface charge and the ions. In addition the particle experiences the friction force due to motion in a liquid. The total resulting force is then

$$F_{tot} = F_{el} + F_f + F_{ret} = 0 \quad (6)$$

where F_{el} is the electrostatic force, F_f is the friction force, and F_{ret} is the retardation force originating from the viscous stress caused by ions located at some distance from the particle surface. If the diffuse layer is small compared with the radius of the particle the viscous stress is

$$F_{ret} = 4\pi a^2 \eta \frac{dv(r)}{dr}, boundary\ condition: v = v_e \quad (7)$$

where η is the dynamic viscosity of the dispersion medium, a is the particle radius, and r is the distance from the particle surface. Now, the electrical force is the charge multiplied by the field strength, and the total charge on the particle is the charge density at the shear plane multiplied by the area of the particle:

$$F_{el} = -E \times 4\pi a^2 \epsilon \frac{d\psi(r)}{dr}, boundary\ conditions: r = 0\ and\ \psi(r) = \xi \quad (8)$$

where ε is the relative permittivity of the dispersion medium, μ_e is the electrophoretic mobility, and ξ is the zeta potential. When friction force is small $F_{tot} = -F_{el}$, which gives [49]

$$E\varepsilon\xi = \eta v_e \quad (10)\ and\ v_e = \mu_e \cdot E \quad (11), \qquad thus\ \mu_e = \frac{\varepsilon\zeta}{\eta} \quad (12)$$

The above is valid for low Reynolds numbers and moderate electric field strengths, under the condition that the diffuse layer is small compared with the radius of the particle. Note that there is no size term in equations 10 and 12 as the surface area terms cancelled out. For detailed discussions on the particle mobility in the electric field (Smoluchowski vs. Huckel model, correction terms, etc.) the reader is referred to the literature [50,51].

If a colloidal particle has a charged surface, a layer of counter-ions will be formed close to its surface (assuming presence of such ions in a solution). The population of this monolayer is a function of the electrostatic potential and the ionic content of the solution phase (plus specific chemical interactions). It is assumed that the surface of a particle has a uniform charge distribution and the layer of counter-ions is adjacent to this surface. At the outer edge (viewed from the interface) of the counter-ions plane, the adsorbed ions change charge and sign of the potential ξ relative to ground (i.e. infinite distance from the particle surface). This quantity is difficult to measure on a routine basis, since ions in this layer do not move when a particle is forced to move, e.g. by electric field. But one can relatively easily estimate a zeta-potential from electrokinetic measurements (theory discussed above) where the motion between the fluid and the interface is detectable. The zeta-potential is a characteristic potential found at some distance from the particle surface ions, where ions start to displace when the particle is in a motion. This plane is called the slipping plane or shear plane, its position is not well-defined, and the value of ξ can be a little be uncertain. A sketch of a model of the so-called the double layer is shown in Figure 13.

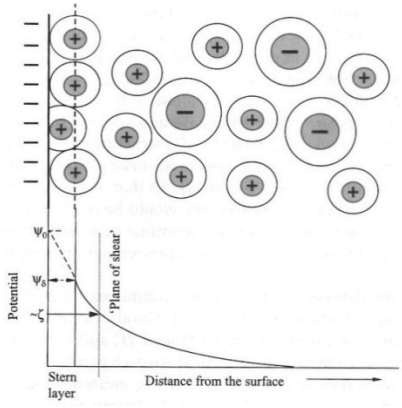

Figure 13. Illustration of a simple model for electrical double layer at the surface of a clay particle. Reprinted from [51]

The above phenomenon can be utilized to define the surface of clay particles by measuring the zeta-potential (e.g. changes in zeta-potential sign and magnitude are expected for organoclays when compare that of their non-modified counterparts). The particle motion, on the other hand, is unfavourable when one tries to study the clay particle alignment (second phase) using an optical microscope. The application of AC fields is more beneficial. However, one should take into consideration the appropriate frequency range, since the dielectric properties of such dielectric particles change as frequency changes. The example is shown in

Figure 14, where oxidized polyacrylonitrile/silicone oil ER fluid was investigated under an AC field with frequencies up to 10 kHz [52]. Further increase of the frequency values may lead to complete disappearance of the ER effect when approaching the time scale of particle polarisation.

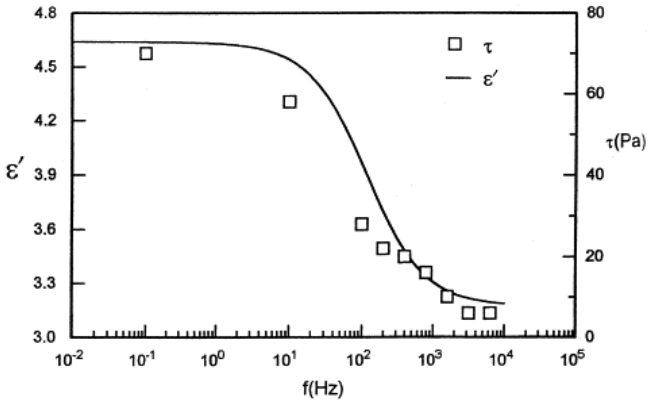

Figure 14. The shear stress obtained at 300 V/mm and dielectric constant predicted using Wagner model (solid line) are showed again electric field frequency. Reprinted from [52]

Considering the ER effect itself, three common and in most cases valid theories should be presented here, namely polarization, conduction and dielectric loss models.

- Polarization model
  The objective of the polarization models is to relate the material parameters, such as the dielectric properties of solid particles and a liquid medium, the particle volume fraction, the electric field strength, etc., to the rheological properties of the whole suspension. Using an idealized physical model ER system — a uniform, hard dielectric sphere (real dielectric constant ε_p, diameter $2r$) dispersed in a Newtonian continuous medium (real dielectric constant ε_m), the derived electrostatic force is found to be dependent on the dielectric constant mismatch between the particle and continuous medium [53-56]. A universal form can be written as:

$$F \propto \varepsilon_m (2r)^2 \left(\frac{\varepsilon_p/\varepsilon_m - 1}{\varepsilon_p/\varepsilon_m + 2} \right)^2 E^2 \quad (13)$$

  where F is the electrostatic force, r is the particle radius, and ε_p and ε_m are the dielectric constants of particle and medium, respectively. The shear modulus increases linearly with the dielectric constant ratio $\varepsilon_p/\varepsilon_m$, indicating that a high particle dielectric constant gives a strong ER effect. There are, however, examples of particles possessing very large dielectric constants (e.g. $BaTiO_3$, ε_p ~ 2000), but showing weak ER effects [57]. The polarization model fails to describe other important ER experimental observations, such as the rheological property dependence on the electric field frequency and the particle conductivity [56].

- Conduction model

  The conduction model can successfully explain ER phenomena that are unexplainable by using the polarization model. It can predict the current density, the yield stress and the temperature dependence of the ER suspension. However, the conduction model can only be used for the situation where the suspension microstructure has been fully formed. The conduction model only considers the particle interaction, regardless of the microstructure change after an electric field is applied. It therefore cannot give an explanation of the dynamic phenomena, such as the response time of ER fluid. The conductivity mismatch between particle and liquid medium, rather than the dielectric constant mismatch, is thought to be a dominant factor for DC and low frequency AC excitation [58,59].

- Dielectric loss model

  Two dynamic processes are emphasized in this model. The first step is the particle polarization process, in which the particle dielectric constant is dominant. The second step is particle rotation determined by the particle dielectric loss. The second step is the most important one, which distinguishes the ER particle from non-ER particle. In other words, both the ER particle and non-ER particle can be polarized under the influence of an electric field, however, only the ER particle can re-orientate along the electric field direction, building the fibrillated bridges between two electrodes. The non-ER particle does not have such ability. The possible reason is that the ER particle has a comparatively high dielectric loss tangent, which can generate a large amount of bounded surface charge. The particle turns even under a weak electric field. The non-ER particle cannot gain enough surface charge due to its low dielectric loss. Although they are still able to be polarized, the total inter-particle force would be cancelled out owing to the diversity of particle dipole vectors. Derivation of the general equation for this model is rather long and troublesome, thus the reader is referred to [56] for more detailed explanations.

1.4. Experimental techniques

A considerable part of the research was dedicated to investigating particle alignment in presence of electric fields, the ER response, thermal properties, etc. In order to understand physics behind these phenomena it was also very important to characterize the samples themselves by, for example, collecting information about particle shape and size, morphology, or surface and bulk properties. Therefore many different experimental techniques had to be employed, and these are briefly explained below. The focus is put more on the information (parameters) that can be obtained (measured) from each method and the justification for their use, rather than a description of technical details.

AFM / SEM / TEM / Optical microscopy

All of these microscopy techniques were used to characterize clay minerals. Atomic force microscopy (AFM) is very practical when high magnification images are needed and it has a few advantages over other high magnification methods. Unlike the electron microscope which provides a 2-D projection, the AFM provides a 3-D surface profile. Additionally, samples viewed by AFM do not require any special treatments (such as metal/carbon coatings) that would irreversibly change or damage the sample. The AFM method can be used to monitor the clay mineral surface, its roughness and thickness. Due to its very high vertical resolution it is possible to see even a single crystalline layer of a clay particle.

Scanning electron microscope (SEM) is more convenient than AFM when more general overview on average size, distribution and shape of both a single particle and an aggregated structure are needed. The magnification and the imaged area can be freely controlled ranging from hundreds of mm^2 to few μm^2, whereas the standard AFM probe can only image a maximum area of about 150×150 μm. This technique was very beneficial for studying aggregates, particle shapes and arrangement in the agglomerations (see Figure 4). Normally the EDS detectors are coupled to the SEM instrument allowing for elemental analysis.

Transmission electron microscope (TEM) is designed for a very high magnifications. It is capable of imaging at even higher resolutions than SEM. However, the sample preparation can be a complex and time-consuming procedure. It can be used for studying the smallest clay minerals, such as laponite particles having only several nm sizes.

Optical microscopy can be employed for observations of structuring from aggregated clay particles. Together with cameras capable for fast imaging, the particle rotation, chaining and also column formation can be readily investigated.

EDS

Energy dispersive X-ray spectrometry (EDS) is an analytical technique used for the elemental analysis or chemical characterization of a sample. It can be very useful when clay minerals are chemically modified. One can easily check whether certain exchangeable cations were fully replaced by other species, e.g. other cations, surfactant molecules, etc. In addition, it can be used as a cross-check method providing information on sample purity.

ξ- potential

The zeta potential was measured using Malvern Zetasizer Nano-ZS (Malvern Instruments, UK) with a folded capillary [86] cell. Measurements can be performed on non-modified and modified clay minerals to check whether the modification is successful or not (sign of Ψ_ξ). For example, Na-Fh clay particles carry a net negative charge due to the negative charges on their surfaces dominating over the positive charges at the edges. The zeta potential of non-modified Na-Fh is expected to have negative values. With the addition of CTAB molecules (positively charged head group) the zeta potential becomes positive. In addition, the absolute magnitude of zeta-potential gives an indication on the stability of colloidal suspension being measured. For the absolute values of the zeta-potential in range between 0 and 30, colloidal solutions are considered to be unstable, since the repulsive forces between particles are weak and they tend to aggregate, which leads to fast sedimentation. For the absolute values of the zeta-potential in range between 30 and 60, colloidal solutions are considered to be moderately stable. This is the case for system studied in this research. Particle sedimentation time is in range of hours, days. Finally, for $|\Psi_\xi|>60$ the solution is very stable.

Electric current and dielectric properties measurements

The electric current and dielectric properties measurements are complementary, in particular to rheological measurements. The obtained information can shine the light on the mechanisms of the electrorheological responses. In addition, one can also monitor water content in clay particles.

Because of the difficulty of directly measuring the dielectric properties of the particles, clay/silicone oil suspensions can be used to carry out dielectric investigations. The dielectric constant can be estimated indirectly via measurements of the capacitance in a configuration of a parallel-plate capacitor.

TGA/DTG

Thermal gravimetric analysis (TGA) is used to determine sample thermal properties such as degradation and decomposition points, and also to investigate adsorbed moisture content or inorganic/organic components in materials. Sample weight is measured with a very high precision (~μg) against temperature as shown in the example below. Figure 15 shows TGA curves of Na-Fh and dehydrated kaolinite samples. This type of analysis can be used to determine water content. It can be seen that there is a significant loss of mass for Na-Fh sample at temperature range between 50 and 200 ºC, whereas no such behaviour is found for kaolinite sample. The TGA curves, however, require transformation to see more detailed features and this is done by taking the 1st derivative resulting in DTG curves.

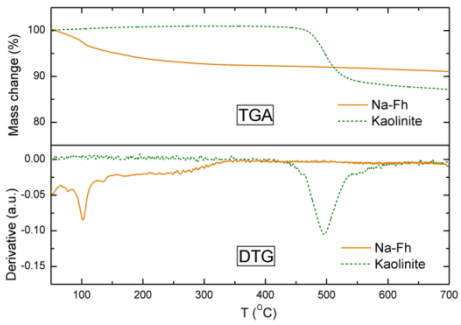

Figure 15. TGA and DTG analysis (25-800 ºC) of Na-Fh and Kaolinite clay samples.

Rheology

The electric field induced liquid-to-solid transition in ER fluids (due to a chain formation) is manifested by changes in the ER properties, such as viscosity, yield stress, elastic (storage) and viscous (loss) moduli, etc. All these properties can be measured by rheometeters, being very advanced and sensitive tools. There are different rheological cells and geometries that allow measuring a broad range of samples from ER fluid, through MR fluids, Newtonian and non-Newtonian fluids, gels, very viscous and low viscosity solutions. Two types of tests can be performed in order to measure different parameters, and these include rotational tests (viscosity η or static yield stress τ_y can be obtained) and oscillatory tests (loss $G^{'}$ and storage $G^{''}$ moduli can be obtained). All the parameters measured are directly or indirectly related to the following factors: temperature, water content, *E*-field strength and frequency, particle dielectric properties, liquid medium, concentration, shape, size or surface, etc.; and the influence of these factors can be determined by means of rheometry. In particular, the difference in ER response between non-modified and organically modified particles was of high importance. Even though the present studies have a basic-research oriented nature, the proximity of studied samples to potential applications should be also taken into consideration. Thus, measurements of the increased ER properties observed for modified clay particles were of high importance.

WAXS/SAXS

Finally, both wide- and small-angle X-ray scattering (WAXS and SAXS) techniques are essential when studying clay minerals. The Bragg diffraction pattern allows to determine the chemical composition or phase composition of the sample. When studying clay minerals, the measurements of the characteristic interlamellar distance between clay crystalline sheets may be of importance (changes when water or organic species intercalates) and this featured can be monitored by means of the X-ray technique. In powdered samples (of for example synthetic fluorohectorite) several aspects of the structure and dynamics of intercalated water molecules can be studied e.g. water diffusion as a function of relative ambient humidity or temperature. Examples of studies utilizing scattering methods can be found in the following articles [60,61,62] (X-ray scattering) and [63,64] (neutron scattering). In addition, the alignment of crystallites (or particle orientational distribution in the case of clay particles suspended in solution) can be found and quantify using a 2-D detector. When the studied system is anisotropic, i.e. clay particles have their preferential orientation (see Figure 16b) due to: presence of an external electric field, magnetic field, gravity, etc.; the 2-D Bragg patterns (rings) become anisotropic in their intensity distribution along the azimuthal angle φ (see Figure 16c). These patterns (rings) can be represented as 1-D plots (scattering intensity versus azimuthal angle) and then fitted to the desired function. In the present study, the classical Maier–Saupe functional form (see Figure 16d) was used. Although in the clay system studied here, the interaction energy is different from that used by Maier and Saupe in their mean field model for liquid crystalline order, the latter functional form was found to be well suited to the raw data, as discussed in [65, 66]. The angular 'width' of the function $f(\varphi)$ is a quantification of the orientational order of the particles in the suspension. This is contained in the *m*

parameter, and is conveniently expressed using the global nematic order parameter S_2. In short, the fitting parameter m is related to the full width at half maxima i.e. the smaller its value the higher the degree of anisotropy. The nematic order parameter S_2 ranges from -1/2 to 1. The nematic state is expected for S_2>0, anti-nematic when S_2<0, whereas S_2 = 0 denotes no orientational order.

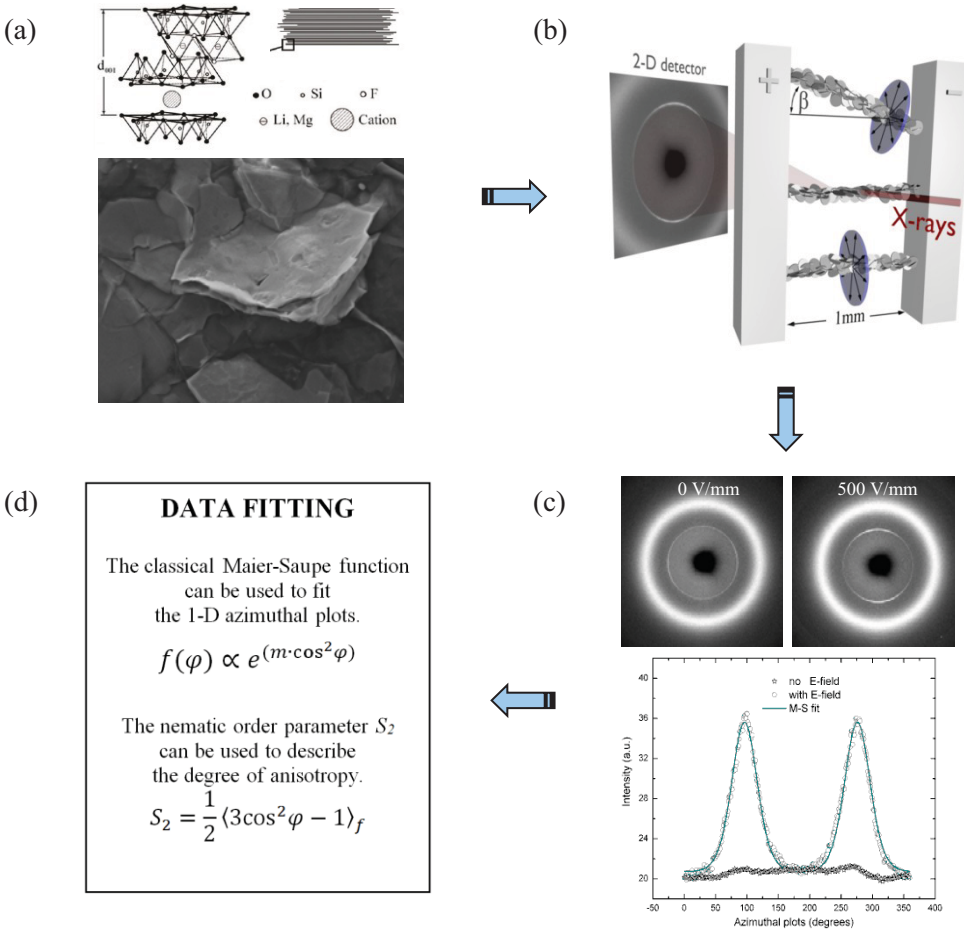

Figure 16. Sketch showing the Na-Fh clay particles (a) aligned between electrodes and X-rayed using WAXD with 2-D detector (b). The obtained 2-D patterns are azimuthally integrated (c) and fitted to the Maier-Saupe model in order to describe the degree of anisotropy in the system (d).

The system geometry is described within this thesis as antinematic. That is the particle's stacking direction is, on average, in a plane normal to the reference direction which is chosen to be along the electric field, since this is the only unique axis in the problem (see Figure 17b - blue disc indicates the plane normal to the reference direction represented by large black arrow). Figure 17 shows the normal nematic (a) and antinematic (b) configurations. The first impression one may have is that the particles in the nematic geometry are nearer to the perfect nematic arrangement than those in the antinematic geometry are to the perfect anti-nematic arrangement. In fact, S_2=-1/2 for particles shown on the right panel of the figure,

since the plane normal direction of each particle is perpendicular to the reference direction $\mathbf{n_o}$; and therefore the perfect antinematic state is achieved.

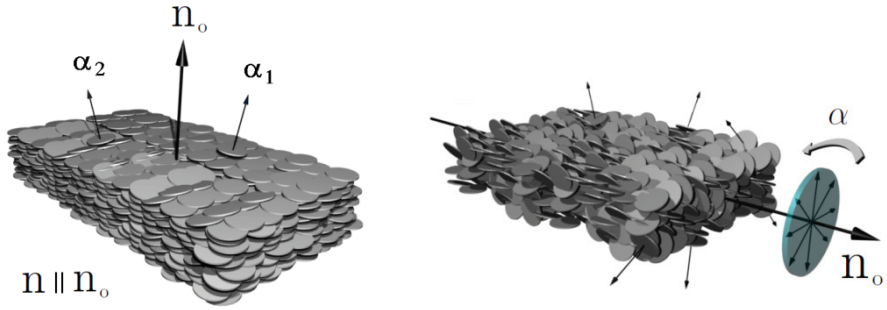

Figure 17. Nematic (a) and antinematic (b) configurations.

Some confusion may arise when searching literature for the definition of the nematic order parameter and names for the set-up geometry that is called *antinematic* in this study. To give few examples:

> Hemmen et al [67] use the classical nematic order parameter (S_2) ranging from -1/2 to 1, where -1/2 denotes perfectly oriented particles in the *antinematic* configuration, 0 refers to complete lack of any orientational order, whereas 1 denotes perfectly oriented particles in the *nematic* geometry. The *antinematic* term is used when clay platelets, on average, are oriented with their normals perpendicular to the director of order, which is parallel to the symmetry axis of the cylindrical tube.
> (they use S_2 in range between (0 and -1/2) when describing antinematic systems)

> Meheust et al. [65], use the same naming as Hemmen et al. but re-define the range of S_2 values (from -1/2–0 → 0–1) simply by multiplying it by -2.
> (they use S_{an} in range between (0 and 1) when describing antinematic systems)

> It might be even more confusing when introduced to work of Dozov et al. [68] They suggest different name to what is called here as the *antinematic* state, the *para-antinematic*. They distinguish between the situations where particles, on average, align with their stacking direction normal to the reference direction without any preferred azimuthal direction (i) and with a preferred azimuthal direction, i.e. particles parallel to each other (ii). They propose to name the latter antinematic.
> (they use S_2 in range between (0 and -1/2) for para-antinematic systems)

Initially, I followed the description given by Meheust et al. (Paper 1, Paper 2, and Paper 3). However, in order to be consistent with commonly acceptable definition of the antinematic configuration (e.g. used by Hemmen et al.) I decided to use the nematic order parameter S_2 which lies in range between 0 and -1/2 (other manuscripts).

2. Thesis development – introduction to the Articles

As mentioned in the introduction, this thesis work represents a continuation of previous research focused mainly on guided self-assembly from non-modified clay particles. My first efforts were put into understanding various features related to this subject such as particle alignment. That is their orientational distribution as a function of time and electric field strength; electric current development during the chain/column formation, and complementarily the rheological properties were measured. The main results on these topics are presented in **Paper 1** and **Paper 2**, and they are:

(i) many of thin chains are formed initially (~1-20μm) and they attract one another resulting in creation of thicker (~50-200μm) columns within the given limited evolution time of ~ 6 min;
(ii) the particles mean orientational distribution does not seem to change as the *E*-field strength increases from 350 to 750 V/mm;
(iii) the value of current density increases and saturates at a different characteristic time, both being *E*-field strength dependent;
(iv) there is a qualitative indication that chain formation and coarsening can be distinguished by comparison of electrical current and the dynamical development of WAXS diffractograms (though additional measurements are needed to be more conclusive on that point); leak current density J is related to particle concentration Φ and E-field strength as: $J \propto \Phi^{0.74} E^{2.12}$;
(v) dependence of the yield stress on the E and Φ is shown to scale as: $\tau_y \propto \Phi^{0.87} E^{1.66}$;
(vi) the dielectric constant is *E*-field or particle orientation dependent (though additional measurements are needed to be more conclusive on that point).

The PhD work, branched out into related directions with a somewhat differing motivation in each case. It was decided to organically modify two types of synthetic clay minerals, namely laponite and fluorohectorite, in order to find their new and improved properties, and to avoid formation of agglomerates, improving anti-sedimentation properties that made previous measurements difficult to conduct. The results of the chemical treatment of laponite particles are described in **Paper 3**, whereas the comparison between non-modified and organically modified fluorohectorite clays is presented in **Paper 4**. The main results are:

(i) the resulting materials show different structures and surface properties – particles became lipophilic and formed smaller aggregates when suspended in non-polar medium;
(ii) not only surfactant adsorption but also intercalation occur – exchangeable cations are replaced by CTAB molecules;
(iii) the modified laponite ER fluids exhibit improved sedimentation properties;
(iv) rheological properties are improved, possibly due to change of both the dielectric constant and the dielectric loss tangent;
(v) the organic modification results in a better overall alignment of the clay particles in presence of *E*-field;
(vi) zeta-potential measurements confirm the successful modification.

Paper 5 and **Paper 6** can be considered as a third group, since both of them include studies of the clay-based polymer composites, although the motivations for launching these two projects were somewhat different. In the **Paper 5**, the structural changes in modified MMT/polymer composites were investigated and confronted with two recently published articles by Park et al. [37] and Kim et al., [69]. They observed a very interesting phenomenon of clay delamination (exfoliation) due to application of AC electric fields. This could potentially open up a new chapter in the field of clay based nanocomposites, since such material in principle should possess superior mechanical properties when compared to conventional filler-based composites. These interesting phenomena were the main motivation for conducting similar experiments, understand the mechanisms behind the electric field induced exfoliation better, and contribute to this fascinating field of polymer/clay science. The main collaborating partners are: Suedina M L Silva (Fed. University Campina Grande, CG-Brazil) responsible for sample preparation; and Tomas S Plivelic (Max-Lab, Lund University, Lund, Sweden) a synchrotron X-ray and polymer science expert. Our group has provided expertise in clay alignment and was responsible for the experimental part and data analysis. The samples, provided from the collaborator (Campina Grande, Brazil) in the form of solid blocks, were investigated in melted state (T between 25-195 ºC). The main results are:

(i) DC electric fields are found to have noticeable but little effect on the clay particle structure and the basal spacing has increased by around 5 %, whereas the application of AC electric fields resulted in the alignment of clay particles only;
(ii) despite many efforts, no clay particle exfoliation is observed (seems to be more challenging than described by other authors);
(iii) the polymer crystallization prevents better particle orientation;
(iv) the degree of anisotropy decreases during crystallization;
(v) application of either DC or AC electric fields resulted in very similar particle alignment and none of them should be considered as privileged.

The research carried out in the **Paper 6** was focused more on time and E-field strength dependent development of the anisotropy from fluorohectorite clay particles suspended in paraffin-wax matrix. The main results are:

(i) the nematic order S_2 depends on the E-field strength;
(ii) thermal effects oppose the electrical forces and prevent from perfect particle alignment, stronger electric fields are required to achieve higher degree of anisotropy;
(iii) on average, the *final* clay particle orientation (i.e. after heating, aligning in the E-field for long time, and solidifying) is not of the highest order, and it is believed that particles lose their most optimal arrangement due to chaining;
(iv) the dehydration of clay particles takes nearly 10 h for clay particles in melted paraffin, re-hydration process in crystalized paraffin is very slow due to very low water penetration through the oligomer matrix, and the pure 1 WL state is not achieved even after 6 months of exposure to 55 % relative humidity and room temperature.

Towards the end of my PhD work period, I met M. Janek (Slovak Academy of Science, Bratislava) and was asked to measure halloysite samples. The rheological measurement appeared to be interesting and further investigations were performed. Those led to origin of the manuscript presented here as **Paper 7,** which consists of comparison of ER responses between kaolinite and halloysite clay/silicone oil suspensions; and differences in the *E*-field induced structuring from both types of clays. The main results are:

(i) since kaolinite and halloysite are natural clays, it is important to verify if the purification is successful, which can be confirmed by means of XRD and FTIR techniques

(ii) SEM/TEM images confirms that the kaolinite sample is a well-crystallized mineral with platy particles of hexagonal symmetry, whereas the morphology of halloysite particles is very different consisting of irregularly shaped particles including flakes and tubular particles

(iii) the overall alignment of the kaolinite particles is significantly better compared to that of halloysite particles, this is mainly a result of the different form of aggregates, which in both cases in the presence of an external *E*-field are columnar structures;

(iv) the disc-like kaolinite particles stack up on each other and align along the electric field direction, i.e. the stacking direction perpendicular to the electric field direction, whereas the halloysite samples is found to give no rise to anisotropy on the 2-D WAXS diffraction patterns, indicating no basal plane preferential orientation for this system;

(v) the electrorheological response is considerably stronger for kaolinite suspensions compared to those of the halloysites, this cannot be explained by a simple polarization model, since the dielectric constants are similar for both samples, thus it is suggested that the way particles aggregate is the dominant factor;

(vi) electric currents are measured and they scale as: $I_K \propto E^{4.1}$ and $I_H \propto E^{2.0}$ for kaolinite and halloysite, respectively;

(vii) electrochemical behaviour of the suspensions and consumption of electrochemical species (water molecules) mediating the current flow is different for kaolinite and halloysite, and this was confirmed by TGA analysis;

3. Final comments of this work and future outlook

In this section, the possible directions for future studies are given. These have arisen together with the thesis development, i.e. during the literature review, and as a result of the experimental measurements.

At the beginning of the PhD study period, I found it surprising (and interesting) that in the field of clay science, studied intensively for nearly 80 years, there were still so many unanswered fundamental questions. Later on, I realized that some of the experimental tasks were non-trivial and challenging. To give a few examples I will start with the problem related to the polarization phenomena.

There are potentially many effects contributing to the clay particle induced polarization, which leads to its re-orientation in presence of an electric field. Since the clay particle is anisotropic in its shape, the electronic polarization (on the atomic scale) existing in each material may contribute to particle rotation. In addition, the polarization of intercalated water, surface water and water stored in material micropores can play an important role. Also the role of displacements of cations must also be considered. Possibly one of these mechanisms is dominant. There is an on-going project within our group which may "shine light" on the subject of clay polarization. Differently prepared clay particles suspended in silicone oil are exposed to an *E*-field. Their rotation is recorded and then the rotation time is estimated. It is believed that this approach could be utilized to understand the polarization mechanism and quantify the particle dipole moment and thus the magnitude of the displaced charge.

Another question is related to the charge transport mechanism in synthetic clays. The complete understanding of that phenomenon is essential and may potentially lead towards new application-oriented studies. There are two major proposed mechanisms describing the charge transport in clays: (i) proton exchange mechanism [70-73] and (ii) the influence of intercalated cations predominantly being responsible for the electrical conduction [74,75]. The latter mechanism was investigated by Kaviratna et al. [76], whereas the former one was addressed by Tenorio et al. [77]. However, the subject remains open for further discussion and revisions.

Another problem is related to the measurements of electrical currents of clay particles during the structuring. It was observed that for some types of clays the current increases, while for others it decreases in time. In principal, there are two effects that can be explained qualitatively, but the quantitative analysis seems to be troublesome. The electrical current grows when the number of conducting bridges increases. On the other hand, it was reported that if a constant current is injected though a water containing clay minerals, the voltage measured between two electrodes decays over time. This is due to the storage of electrical charges that accompany the electromigration of charge carriers (electrons and ions) in porous materials and electrochemical activity at interfaces between various phases [78]. These two effects may have different characteristic time decays and may also vary with clay type, water content, *E*-field applied and its frequency, etc.

References

1. K. P. S. Parmar, *"Oil dispersions of nano-layered silicates in an external electric field: An experimental study"*, Doctoral thesis at NTNU, 2006:218.
2. F. Bergaya, B. K. G. Theng and G. Lagaly, *"Handbook of Clay Science"*, Elsevier (2006) 3-8.
3. S. Guggenheim and R. T. Martin, *"Definition of clay and clay mineral – joint report of the AIPEA nomenclature and CMS nomenclature committees"*, Clays and Clay Minerals, **43** (1995) 255-256.
4. T. Kogure and E. Okunishi, J. Electron Microsc. **59** (2010) 263-271.
5. S. A. Solin, Ann. Rev. Materials Science **27** (1997) 89–115, 1997.
6. W. A. Deer, R. A. Howie and J. Zussman, "*An introduction to the rock-forming minerals*", Harlow: Longman, 2nd ed. (1992) 357-376.
7. R.L. Ledoux and J.L. White, J. Colloid & Interface Sci. **21** (1966) 127.
8. G.J. Churchman, J.S. Whitton, G.G.C. Claridge and B.K.G. Theng, Clays Clay Miner. **32** (1984) 241.
9. G. Lagaly, Phil Trans. Roy. Soc. Lond. **A311**, (1984) 315.
10. K. Tsunematsu et al., Nendo Kagaku. **34** (1995) 228.
11. R. L. Frost, J. Kristof, J. T. Kloprogge and L. Rintoul, Spectrochimica Acta Part A **56A** (2000) 1681-1691.
12. H. H. Murray, Applied Clay Science, **5** (1991) 379-395.
13. H. Hemmen, L. R. Alme, J.O. Fossum and Y. Meheust, Phys.Rev. E **82** (2010) 036315.
14. P. D. Kaviratna, T. J. Pinnavaia and P.A. Schroeder, J. Phys. Chem. Solids **57** (1996) 1897.
15. E. DiMasi, J. O. Fossum, T. Gog and C. Venkataraman, Phys.Rev. E **64** (2001) 061704.
16. G. Sposito, N. T. Skipper, R. Sutton, S. Park, A. K. Soper, J. A. Greathouse, J. A. Proc. Natl. Acad. Sci. U.S.A. **96** (1999) 3358.
17. J. O. Fossum, Physica A **270** (1999) 1-2.
18. R. P. Tenorio, M. Engelsberg, J. O. Fossum and G. J. da Silva, Langmuir **26 (**2010) 9703–9709.
19. T. J. Tambach, P. G. Bolhuis, E. J. M. Hensen and B. Smit, Langmuir **22 (**2006) 1223.
20. E. Balnois, S. Durand-Vidal and P. Levitz, Langmuir, **19** (2003) 6633-37
21. B. Wang, M. Zhou, Z. Rozynek and J. O. Fossum, J. Mater. Chem. **19** (2009) 1816.
22. Internet source: http://www.scprod.com/pdfs/LaponiteBrochureE.pdf, [accessed 05.07.2011], Southern Clay Production, Inc.
23. J. X. Li, X. G. Gong, S. Y. Chen, W. J. Wen and P. Sheng P, J. Appl. Phys. **107** (2010) 093507.
24. J. Lu and X. P. Zhao, J. Mater. Res. **17** (2002) 1513-1519.
25. Z. Rozynek et al., Eur. Phys. J. E **34** (2011) 28.
26. K. S. Santos, E. Bischoff, S. A. Liberman, M. Oviedo and R. S. Mauler Ultrasonics Sonochemistry **18** (2011) 997-1001.
27. A.C.C. Esteves, A.B. Timmons and T. Trindade, Quim Nova **27** (2004) 798–806.
28. K.S. Santos, S.A. Liberman, M.A.S. Oviedo and R.S. Mauler, J Polym. Sci.: Part B: Polym. Phys. **46** (2008) 2519–2531.
29. E. P. Giannelis, Adv. Mater. **8** (1996) 29-35.

30. P. Podsiadlo, A. K. Kaushik, E.M Arruda et al., Science **318** (2007) 80-83.
31. S. Letaief and C. Detellier, J. Mater. Chem **17** (2007) 1476-1484.
32. H. P. He, R. L. Frost, F. Deng, J. X. Zhu, X. Y. Wen and P. Yuan, Clay Clay Miner. **52** (2004) 350-356.
33. J. L. Bonczek, W. G. Harris and P. Nkedi-Kizza, Clay Clay Miner. **50** (2002) 11–17.
34. P.H. Massinga, W.W. Focke, P.L. de Vaal and M. Atanasova, Appl. Clay Sci. **49**, 142 (2010).
35. G. Lagaly, Solid State Ionics 22, 43 (1986).
36. Internet source, http://www.scprod.com/product_bulletins, [accessed 09.07.2011], Southern Clay Production, Inc.
37. J. U. Park, et al., Polymer **47** (2006) 5145–5153.
38. E. P. Giannelis, Adv. Mater. **8** (1996) 29.
39. J. O. Fossum, Y. Meheust, K. P. S. Parmar, K. D. Knudsen, K. J. Maloy and D. M. Fonseca, Europhys. Lett. **74** (2006) 438-444.
40. J. O. Fossum, Y. Meheust, K. P. S. Parmar, K. D. Knudsen, K. J. Maloy and D. M. Fonseca, ESRF Scientific Highlights (2006) 23-24.
41. J. D. Jackson, *"Classical Electrodynamics"*, 2nd ed., Wiley (1962) 143
42. T. C. Halsey and J. E. Martin, Sci. Am. **269** (1993) 58-64.
43. D. L. Klass and T. W. Martinek, J. Appl. Phys. **38** (1967) 67.
44. Y. F. Deinega and G. V. Vinogradov, Rheol. Acta **23** (1984) 636.
45. T. C. Halsey and W. Toor, J. Stat. Phys. **61** (1990) 1257-1281.
46. T. C. Halsey and W. Toor, PRL **65** (1990) 2820-2823.
47. T. C. Halsey, Science **258** (1992) 761-766.
48. F. F. Reuss, Mem. Soc. Imperiale Naturalistes de Moscow **2** (1809) 327.
49. J. Goodwin, *"Colloids and Interfaces with Surfactants and Polymers"*, 2nd ed., Wiley (2009) 289-294.
50. R. J. Hunter, *"The Zeta Potential in Colloid Science"*, Academic Press, London (1981).
51. J. Goodwin, *"Colloids and interfaces with surfactants and polymers"*, 2nd ed., Chichester: Wiley (2009) 134-137.
52. T. Hao, J. Colloid Interface Sci. **206** (1998) 240.
53. R. A. Anderson, Langmuir **10** (1994) 2917.
54. L. C. Davis, J. Appl. Phys. **73** (1993) 680.
55. D. J. Klingenberg, S. Frank and C. F. Zukoski, J. Chem. Phys. **94** (1991) 6160.
56. T. Hao, Adv. Colloid Interfac. **97** (2002) 1-35.
57. Y. Otsubo and K. Watanabe, J. Soc. Rheol. Jpn. **18** (1990) 111.
58. L. C. Davis, Appl. Phys. Lett. **60** (1992) 319.
59. L. C. Davis, J. Appl. Phys. **72** (1992) 1334.
60. G. J. da Silva, J.O. Fossum, E. DiMasi, K. J. Maloy and S. B. Lutnæs, Phys.Rev. B **67** (2003) 094114.
61. N.I. Ringdal, D. M. Fonseca, E.L. Hansen, H. Hemmen, and J.O. Fossum, Phys.Rev. E **81** (2010) 041702.
62. G. J. da Silva, J.O. Fossum, E. DiMasi, K. J. Maloy and S. B. Lutnæs, Phys.Rev. E **66** (2002) 011303.
63. K. D. Knudsen, J. O. Fossum, G. Helgesen and V. Bergaplass, J.Appl. Cryst. **36** (2003) 587.

64. R. P. Tenorio, L. R. Alme, M. Engelsberg, J. O. Fossum, F. Hallwass, J. Phys. Chem. C **112** (2008) 575.
65. Y. Meheust, K. D. Knudsen and J. O. Fossum, J. Appl. Cryst. **39** (2006) 661-670.
66. Z. Rozynek, K. D. Knudsen, J. O. Fossum, Y. Méheust, B. Wang and M. Zhou J. Phys.: Condens. Matter **22** (2010) 324104.
67. H. Hemmen, N. I. Ringdal, E. N. De Azevedo, M. Engelsberg, E. L. Hansen, Y. Meheust, J.O. Fossum and K. D. Knudsen, Langmuir **25** (2009) 12507–12515.
68. I. Dozov, E. Paineau, P. Davidson, K. Antonova, C. Baravian, I. Bihannic and L. J. Michot, J. Phys. Chem. B **115** (2011) 7751-7765.
69. D. H. Kim et al., Polymer **47** (2006) 5938-5945
70. D. M. Stamires, J. Chem. Phys., **36** (1952) 3174.
71. J. Barriol, C. C. Cabrera and A. M. Robert, J . Chem. Phys., **59** (1962) 154.
72. J. D. Bernal and R. H. Fowler, J . Chem. Phys., **1** (1933) 515.
73. B. Rosenberg, J. Chem. Phys., **36** (1962) 816.
74. J. J. Fripiat, A. Jelli, G. Poncelet and J. Andre, J. Phys. Chem. **69** (1965) 2185.
75. H. Bidadi, P. A. Schroeder and T. J. Pinnavaia, J. Phys.Chem. Solid **49** (1988) 1435.
76. P. D. Kaviratna, T. J. Pinnavaia, T. J and P. A. Schroeder, J. Phys. Chem. Solids **57** (1996) 1897.
77. R. P. Tenorio, M. Engelsberg, J. O. Fossum, and G. J. da Silva, Langmuir **26** (2010) 9703–9709.
78. P. Leroy and A. Revil, J. Geophys. Res. **114** (2009) B10202.

Paper I

Dynamic column formation in Na-FLHC clay particles: Wide angle X-ray scattering and rheological studies

Z Rozynek, B Wang, M Zhou and J O Fossum

J Phys.: C.S. 149 (2009) 012026

Journal of Physics: Conference Series **149** (2009) 012026 doi:10.1088/1742-6596/149/1/012026

Dynamic Column Formation in Na-FLHC Clay Particles: Wide Angle X-ray Scattering and Rheological Studies

Z Rozynek, B Wang, M Zhou, and J O Fossum

Department of Physics, NTNU, Høgskoleringen 5, NO-7491, Trondheim, Norway

E-mail: zbigniew.rozynek@ntnu.no

Abstract. The dynamic chain and column formation of 5wt.% clay particles suspended in silicone oil has been studied using synchrotron Wide Angle X-Ray Scattering (WAXS) technique and rheometry. The anisotropic arrangement of particles described by the global order parameter S has been investigated. The WAXS data have also allowed distinguishing between the chain and column formation processes by comparison of the change of WAXS angular plots maxima with the current density growth in function of time. The saturation time t_s (after which there was no change in the system observed) was estimated. In addition, the rheological properties of the ERF have been measured including the static yield stress.

1. Introduction

Electrorheological fluids (ERFs) are liquids that solidify, or become very viscous, under an electric field. The transition from liquid into a solid-like state indicates that there is an inner ordering of the ER-constituents, which leads to a change in the rheological properties. Application of an electric field induces polarization of the suspended dielectric particles and a chain-like structure can be formed along the electric field direction [1-3]. Recently, the Giant Electrorheological (GER) fluid was discovered and it differs from the conventional ER fluids by exceeding the theoretical upper bound [4,5] of the yield stress, reaching 250 kPa at 5 kV/mm [6,7]. That discovery opens new horizons in the field of ER systems and inspires rheologists for working on further developments of such systems. In order to predict the response and behavior of ERFs under an applied electric field, it is important to gain an understandable knowledge of the physical mechanism of the chain and column formation and its dynamics. In the present study, synthetic clay particles Na-fluorohectorite (Na-FLHC) suspended in insulating, non-polar silicone oil form with time chain-like structures when subjected to an external electric field. The time needed to create columns of aggregated particles varies as the electric field (0.35, 0.5 and 0.75 kV/mm) increases. Wide Angle X-Ray Scattering (WAXS) diffraction patterns reveal changes of the direction of the dipolar moment induced in clay particles when the electric field is applied. The anisotropic arrangement of particles forming the chain can be described by the global order parameter S. The detail description of the system geometry, fitting procedure and calculations of S parameter can be found in the report of Meheust Y, et al. [8]. In-depth analysis of the system measured can be obtained using rheometry. The shear stress τ as a function of a shear rate $\dot{\gamma}$ can reveal the type of ER fluid and in case of samples of this study the shear stress is represented by the Bingham plastic rheological model [9,10]

2. Sample preparation and characterization methods

The synthetic Na-FLHC clay was purchased from Corning Inc. (New York) in a form of powder. According to supplier, its chemical formula is given as $Na_{0.6}(Mg_{2.4}Li_{0.6})Si_4O_{10}F_2$ per unit cell, where Na is an interlayer exchangeable cation. A silicone oil Dow Corning 200/100 Fluid (dielectric constant of 2.5, viscosity of 100 mPa·s and specific density of 0.973 g/cm^3 at 25°C) was used as a suspending liquid as a relatively non-polar and non-conductive medium, with a DC conductivity of the order of magnitude of 10^{-12} S/m. The preparation of the ER fluid was undertaken by the following procedure. Clay powder was crushed with a pestle and mortar, and then dried in vacuum oven for 12h at 90°C. At

the same time the silicone oil was heated at 110°C for 12h. After that, the clay powder and silicone oil were mixed in glass tubes and vigorously hand-shaken for ~2min, then placed in an ultrasonic bath for 1h and again vigorously shaken for 1h in an orbital shaker. The clay concentration was assumed to be ~5 wt.% and it sedimented rather slow, however for rheological data collection the sample needed to be pre-shaken each time before measurement.

The wide angle x-ray scattering experiment (WAXS) was carried out at the European Synchrotron Radiation Facility (ESRF) in Grenoble, France. The X-ray beam with wavelength of 0.72Å and 0.3x0.3mm^2 beam size at sample was used. On the beamline BM01A a two-dimensional MAR 345 image plate detector with diameter of 345mm and a read-out time of around 40s was installed. The WAXS experiment was performed at RT for sample at rest (no liquid flow through a custom-made scattering cell). Electric fields from 0.35 to 0.75kV/mm have been chosen as a result of the following observations: for the electric filed above 0.75kV/mm the chain and column formations are too fast to be distinguished; electric fields below 0.35kV/mm however are too week for particles to form any chains.

The rheological properties of the clay suspensions were measured at RT, under DC electric fields using a Physica MCR300 rheometer.

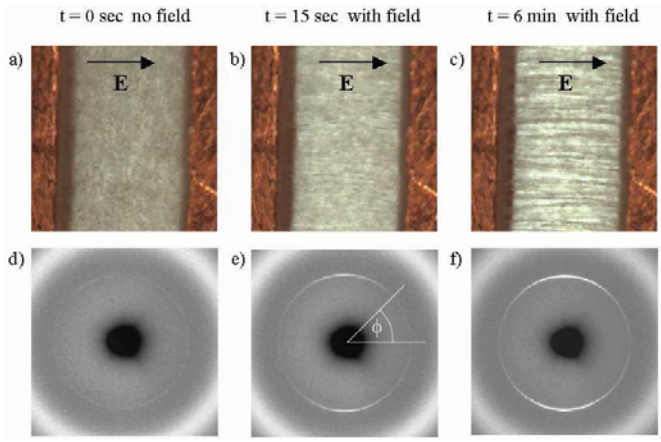

Figure 1. Optical microscope (a,b,c) and WAXS data (d,e,f)

3. Results and discussion

Normally, the Na-FLHC particles are randomly dispersed into the silicone oil (fig.1a). Microscopy images of the sample experiencing an electric field for different time are shown in fig.1b, 1c. The formation of column-like structures aligning parallel to the field is clearly observed. Many of thin chains are formed first (~1-20μm) and they attract each other resulting in creation of thicker (~50-200μm) columns. After the time t_s (which will be called here the saturation time) no major changes in the system are noticeable. Figure 1d is obtained prior to the application of an electric field and isotropic pattern can be observed, since particles are distributed randomly with not specified orientation. The two-dimensional WAXS patterns in figures 1e and 1f are becoming gradually more intensive in time, and the dependence of intensity for azimuthal angle ϕ is pronounced. This change of the 1st Bragg peak intensity in time is plotted as function of the azimuthal angle ϕ and presented in figures 2a and 2b for different electric (DC) fields.

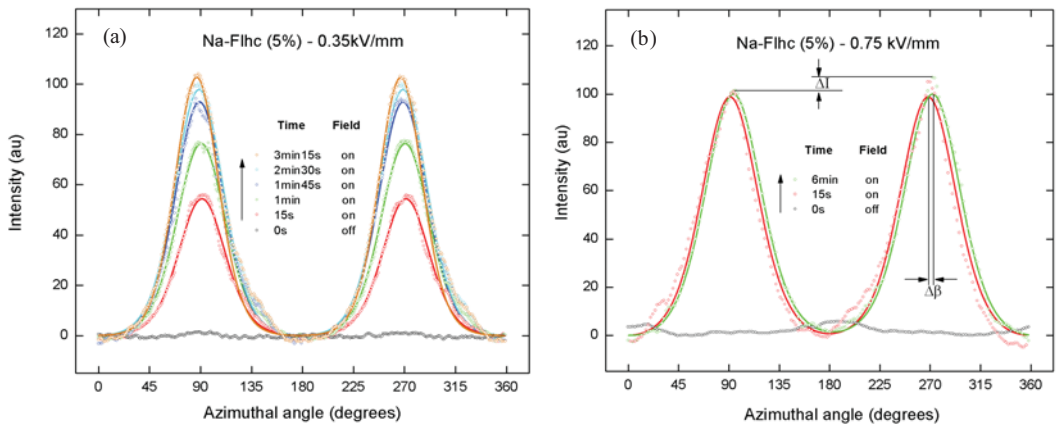

Figure 2. Angular plots of the 1st Bragg peak changing with time under an electric field

There are three possible events which can influence these WAXS pattern changes while time passes by: either clay platelets are being more orientated along the electric field or/and clay particles are forming chains or/and chains are coarsening into column-like structures in a range of the X-ray beam. These three situations can occur in different time range or they may overlap in time. By looking at figures 2 and also taking into account the calculations of S parameter (tab.1) one can conclude that the intensity does not changes due to particle orientation and it is rather dependent on the dynamic chain or/and column formation. The mean orientation distribution hardly changes and S oscillates around 0.63, 0.65 and 0.60 under applied fields of 0.35 kV/mm, 0.50 kV/mm and 0.75 kV/mm, respectively.

	Time	15s	1min	1min45s	2min30s	3min15s	6min	**Avr.**
0.35 kV/mm	**S**	0.63	0.61	0.62	0.62	0.67	0.65	0.63
0.50 kV/mm	**S**	0.62	0.62	0.64	0.64	0.68	0.67	0.65
0.75 kV/mm	**S**	0.53	0.64	0.65	0.58	0.60	0.59	0.60

Table 1. Calculated order parameters for Na-FLHC clay suspension under an electric fields of 0.35, 0.50 and 0.75 kV/mm.

The current density increases when chains are being formed. However, it does not change while chains coarsen into the column. Therefore by comparison between the current density growth and the change of WAXS angular plots maxima versus time (fig.3), both chain and column formation processes can be distinguished. This information might be of importance when one needs a self-assembly from particles to lead into the single chain formation rather than aggregated column creation. For 0.75 kV/mm and 0.50 kV/mm electric fields the current density curves overlap with WAXS data indicating the chain formation is followed by rapid column aggregation. However, for the lowest electric field current density increases faster than the WAXS records for the same field pointing out that the column formation occurs slower comparing to higher electric fields. That follows the thermal theory of coarsening [11,12], which describe the collision time of two chains as follows: $t_c \sim \rho^{3/2} \cdot k_B T^{-1/2} \cdot E^{-1}$, where ρ is a distance between two chains. Thus, when the electric field E increases (more rapid chain formation entails both the decrease of distances between chains and the increase of current resulting in the temperature T rise) the coarsening occurs more rapidly. For the different field strength, the intensity for azimuthal angle and integrated q values becomes saturated at the different time t_s which was estimated as: ~195s, ~150s and ~60s for electric fields of 0.35kV, 0.50kV and 0.75kV, respectively. One can see that the data and its fitted curves in fig. 2b are left- or right-shifted. This is due to the movement of a columnar structure that can be tilted in respect to the reference orientation while being formed.

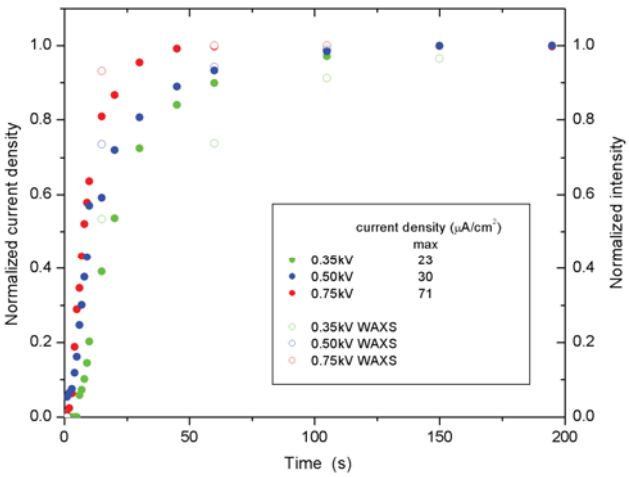

Figure 3. Leaking current density and maxima of angular plots versus time.

Fig.4 shows the yield stress τ_y of different clay particle concentration Θ as a function of electric field E. The power law with exponent α of 1.57, 1.77, 1.67 and 1.64 was used to fit the results for the samples with 5, 10, 20 and 40 wt.% of clay particles, respectively. The exponent α is commonly found in the range between 1 and 2 [13]. The yield stress for the sample with 5wt.% of clay particle was estimated as 16 Pa at 1kV/mm. whereas the yield stress of 102 Pa was measured for the sample with 40wt.% of clay particles. As one can see the yield stress τ_y and what follows the apparent viscosity η of the ER suspension is largely dependent on the particle concentration Θ and the

relationship is nearly linear. Similar results have been found by many researchers [9] and the fibrillation model was used to derive that dependence. However simple and very limited, the fibrillation model can be also suggested here as the mechanism of the ER effect. In this model particles can be polarized and aligned as a dipole along the direction of the electric field. The interaction between the polarized particulates would be increased, resulting in the obvious ER effect. The particle could bear some net charge, arising from the non-uniform polarization or ionic adsorption, thus electrophoresis could contribute to the particle motion. This particle migration was observed using optical microscope and also confirmed by the experiment described below. Steady shear stress for a DC electric field was compared with a low-frequency (50Hz) periodic AC field of the same RMS voltage values. The results are shown in the inset of figure 4. The shear stress is higher when the AC power supply is used. This is due to the fact that electrically induced particle migration is minimized.

4. Conclusion

The dynamic chain and column formation of 5wt.% clay ER suspension has been studied by means of WAXS technique and rheometry. It was shown that the mean orientation distribution hardly changes in time (15sec – 6min) and the order parameter oscillates around 0.63, 0.65 and 0.60 under applied fields of 0.35 kV/mm, 0.50 kV/mm and 0.75 kV/mm, respectively. The WAXS experiments have also allowed distinguishing between the chain and column formation processes by comparison of the change of WAXS angular plots maxima with the current density growth versus time. For the lowest electric field (0.35 kV/mm) there was clear evidence that coarsening of chains into the thicker columns occurs much slower comparing to the samples at higher fields, where column formation takes place immediately after chains are being formed. The saturation time t_s (after which there was no change in the system observed) was estimated as: ~195s, ~150s and ~60s for electric fields of 0.35kV, 0.50kV and 0.75kV, respectively. The formation of chains and columns is more rapid when an applied voltage is higher. Steady shear stress for a DC electric field was compared with a low-frequency periodic field and a slight increase in the shear stress was observed due to the minimization of particle migration. In addition, the most important electrorheological properties have been measured which included both the electric field and also particle concentration dependent yield stress tests.

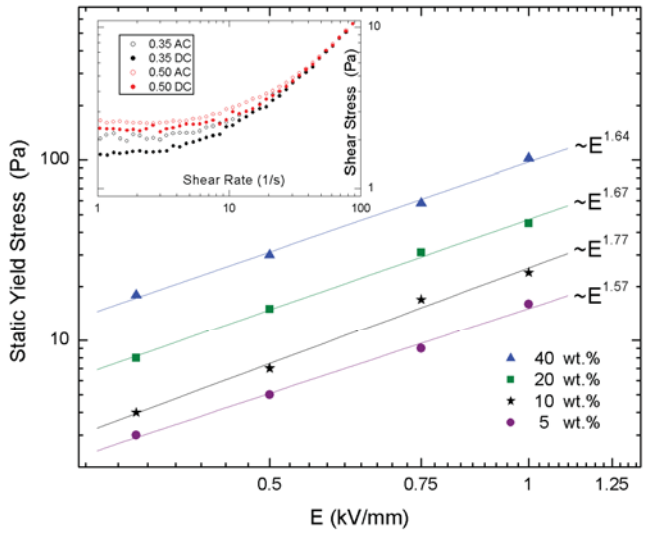

Figure 4. Log-log plot of the static stress for different clay concentrations as a function of E. Inset shows that the shear stress is higher when AC field is used due to minimizing of particle migration.

Acknowledgments

The authors acknowledge assistance from K.D.Knudsen, O.T.Buset and D.Chernyshov while performing experiments at the Swiss-Norwegian Beam Lines at ESRF. Special thanks to Y.Méheus for his interesting comments. This work was supported by the Research Council of Norway through the FRINAT Program: NFR project number 171300.

References

[1] Tao R 1991 *Physical Review Letters* **67**(3): 398-401.
[2] Espin M, et al. 2005 *Langmuir* **21**(11): 4896-4903.
[3] Fossum J, et al. 2006 *Europhysics Letters* **74**: 438-444.
[4] Ma H, et al. 1996 *Physical Review Letters* **77**: 2499-2502.
[5] Ma H, et al. 2003 *Advances in Physics* **52**: 343-383.
[6] Wen W, et al. 2003 *Nature Materials* **2**: 727-730.
[7] Huang X, et al. 2006 *Solid State Communications* **139**: 581-588.
[8] Meheust Y, et al. 2006 *Journal of applied crystallography* **39**(5): 661-670.
[9] Klingenberg D, et al. 1990 *Langmuir* **6**: 15-24.
[10] Gast A, et al. 1989 *Advances in Colloid and Interface Science* **30**: 153-202.
[11] Halsey T 1992 *Science* **258**: 761-766.
[12] Martin J, et al. 1998 *Phys. Rev. E* **57**(1): 756-775.
[13] Parmar K, et al. 2008 *Langmuir* **24**(5): 1814-1822.

Paper II

Electric field induced structuring in clay–oil suspensions: new insights from WAXS, SEM, leak current, dielectric permittivity, and rheometry

Z Rozynek, K D Knudsen, J O Fossum, Y Méheust, B Wang and M Zhou

J. Phys.: Condens. Matter 22 (2010) 324104

IOP Publishing Journal of Physics: Condensed Matter

J. Phys.: Condens. Matter **22** (2010) 324104 (8pp) doi:10.1088/0953-8984/22/32/324104

Electric field induced structuring in clay–oil suspensions: new insights from WAXS, SEM, leak current, dielectric permittivity, and rheometry

Z Rozynek[1], K D Knudsen[2], J O Fossum[1], Y Méheust[3], B Wang[1] and M Zhou[1]

[1] Department of Physics, NTNU, Høgskoleringen 5, NO-7491, Trondheim, Norway
[2] Physics Department, IFE, Kjeller, Norway
[3] Geosciences Rennes, UMR CNRS 6118, University of Rennes 1, Rennes, France

E-mail: zbigniew.rozynek@ntnu.no and jon.fossum@ntnu.no

Received 3 August 2009, in final form 14 January 2010
Published 15 July 2010
Online at stacks.iop.org/JPhysCM/22/324104

Abstract

The electric field induced structuring in clay–oil suspensions has been studied by means of wide angle x-ray scattering (WAXS), rheometry, scanning electron microscopy (SEM), as well as leak current density and dielectric constant measurements. The clay particles' orientation distribution was inferred from the azimuthal changes of the clay diffraction peak intensity. The angular width of that distribution was quantified through an orientational order parameter. Chain and column formation processes were distinguished by comparison of the time evolution of the diffraction peak amplitude with that of the current density. Leak current density was measured for different electric field strengths E and clay particle concentrations Φ. The following scaling relation was found: $J \propto \Phi^{0.74} E^{2.12}$. In addition, the dependence of the yield stress on the electric field and on the particle concentration was measured and shown to scale as: $\tau_y \propto \Phi^{0.87} E^{1.66}$.

(Some figures in this article are in colour only in the electronic version)

1. Introduction

The fast rheological response to an applied electric field, which is the characteristic behavior of electrorheological fluids (ERFs), has attracted attention from both engineers and scientists since Winslow discovered this phenomenon in 1947 [1]. ERFs are complex fluids that solidify, or become very viscous, when submitted to an applied electric field. The transition from a liquid to a solid-like state indicates that an internal ordering of the electrorheological (ER) constituents has appeared, leading to dramatic changes in the rheological properties. Application of an electric field induces polarization of the suspended dielectric particles. They consequently orient in the field and aggregate, which results in the formation of a chain-like structure parallel to the electric field direction [2–4]. The most common ERFs are suspensions of 1- to 100 μm polarizable particles at volume fractions of 0.05–0.50 dispersed in an inert insulating liquid. For an electric field E in the range 50–5000 V mm^{-1} the particles form chains that span the gap between the electrodes [5].

Recently, the giant electrorheological (GER) effect was discovered: an ERF was made that differs from the conventional ERFs in that it exceeds the theoretical upper bound [6, 7] of the yield stress, reaching 250 kPa at 5 kV mm^{-1} [8, 9]. That discovery opens new horizons in the field of ER systems and inspires scientists working on further developments of such systems. With such large yield stresses within reach, ERFs provide the possibility of rapid-response (of the order of milliseconds) coupling between mechanical devices and electronic control systems. Fast liquid–solid transition and high yield stress make ERFs attractive for many future technologies.

In order to predict the response and behavior of ERFs under an applied electric field, it is important to

Table 1. Expressions of the order parameter as defined for a nematic and anti-nematic geometry.

Nematic	Anti-nematic
$S_n = \frac{1}{2}\langle 3\cos^2\alpha - 1\rangle_f$ i.e.,	$S_{\text{an}} = \langle 3\cos^2(\frac{\pi}{2} - \alpha) - 2\rangle_f = \langle 3\sin^2\alpha - 2\rangle_f$ i.e.,
$S_n = \pi \int_0^{\pi/2} (3\cos^2\alpha - 1) f(\alpha) \sin\alpha \, \mathrm{d}\alpha$	$S_{\text{an}} = 2\pi \int_0^{\pi/2} (3\sin^2\alpha - 2) f(\alpha) \sin\alpha \, \mathrm{d}\alpha$

gain an understanding of the physical mechanism of the chain and column formation and its dynamics. The present study is focused on these points rather than on the rheological properties of the systems themselves. Synthetic Na fluorohectorite (Na-Fh) clay particles suspended in insulating, non-polar silicone oil form chain-like structures when subjected to an external electric field. The time needed to create columns of aggregated particles decreases as the electric field increases. WAXS diffraction patterns can reveal changes (if any) in the orientation of the clay particles when the electric field is applied. WAXS therefore allows us to monitor the orientational order in the suspensions during ER chain and column formation. The method is briefly explained in section 2, while the results are presented in section 4. The chain formation is associated with an increase in the leak currents through the fluid; we monitor these currents and observe that they allow us to discriminate between chain and column formation (section 4.3). The evolution of the effective dielectric properties of the material is presented in section 4.4. Rheometry measurements provide the corresponding changes in the mechanical properties of the suspensions (section 4.5).

2. Theoretical background of the study

2.1. What symmetry does the orientational order have in our system?

As a coarse approximation, the Na-Fh clay platelets forming the chain can be represented as disk-shaped aggregates, whose orientation is completely defined by a unit normal vector (**n**) (the director). Thus, the anisotropic arrangement of these particles can be described by an orientation distribution f that is a function of the platelet director (**n**)s orientation. Given that the chain/column is parallel on average to the direction, denoted by unit vector ($\mathbf{n}_o$) (which we shall denote 'reference director'), of the applied electric field, the orientation distribution function f only depends on one characteristic angle α: the angle between the director (**n**) of a given platelet and the reference director ($\mathbf{n}_o$) [10]. Moreover, WAXS measurements reveal that the particles have their directors lying on average in a plane perpendicular to ($\mathbf{n}_o$) (see figure 1).

Following many other authors [10, 11], we denote this orientational configuration as an *anti-nematic* configuration. It relates to the better known *uniaxial nematic* geometry, for which the orientation distribution function also depends on the angle between a platelet's director and a reference director, but with all directors on average parallel to each other. In other words, in the uniaxial nematic configuration, the reference director is also the mean director, and $f(\alpha)$ is peaked around $\alpha = 0$, while in the present anti-nematic configuration, $f(\alpha)$ is peaked around $\alpha = \pi/2$.

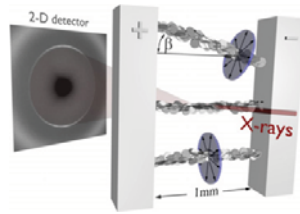

Figure 1. Experimental geometry for the WAXS measurements. Particles are forming chains along the E-field.

We use the classical Maier–Saupe functional form, $f(\alpha) \propto \exp(m\cos^2\alpha)$ for the orientation distribution. Although in our system the interaction energy is different from that used by Maier and Saupe in their mean field model for liquid crystalline order, the latter functional form was found to be well suited to our data, as discussed previously by Méheust, *et al* [10].

2.2. Determination of the orientational distribution from two-dimensional WAXS images

In the Maier–Saupe functional form for f, m is the only adjustment parameter; since the orientation distribution probability (ODP) function is normalized to 1, its peak amplitude is related to its peak width, so that the value of m completely defines f. This value is obtained from one-dimensional plots of the peak amplitude of a given clay diffraction peak as a function of the azimuthal angle ϕ. We fit to these azimuthal profiles the following formula:

$$I = I_o + C\exp\{m[\sin\theta\sin\Theta_o + \cos\theta\cos\Theta_o\cos(\varphi - \Phi_o)]^2\} \quad (1)$$

for which the five fitting parameters are m, the base line I_o, the amplitude C, and the two angles Φ_o and Θ_o that define ($\mathbf{n}_o$) with respect to the laboratory frame. Details of the method can be found in [10].

2.3. Order parameter

The angular dispersion of the function f is a quantification of the orientational order of the suspension. It is contained in the m parameter as defined above, but is more conveniently measured using a global order parameter S. The order parameter was first defined for uniaxial nematics so as to possess values between 0 and 1, to vanish for an isotropic phase ($S = 0$), and to reach the maximum value of $S = 1$ [12] for a fully anisotropic state, where particles/crystallites are perfectly aligned with each other. The corresponding expression for S is given in the left column of table 1 as S_n. In different physical systems, depending on the orientational

geometry, an adequate choice of the method for calculating the order parameter is required. For example, the nematic order parameter S_n computed from an anti-nematic geometry has values between -0.5 and 0. Changing the mathematical formulation of the order parameter to the anti-nematic order parameter S_{an} (see right column of table 1) in effect simply amounts to multiplying the nematic order parameter S_n by a factor of -2. All calculations are made accordingly, which is why the S_{an} order parameter values reported in the present work are positive and lie within the numerical range 0–1 in magnitude, while the corresponding S_n lie in the range 0.5–0.

2.4. Model for the rheology of the suspensions

Rheometry has been used to measure the shear stress τ as a function of a shear rate $\dot{\gamma}$. For samples in this study, and under application of an electric field, this dependence is well described by the Herschel–Bulkley rheological model: $\tau = \tau_y + b\gamma^p$, where τ_y, b, p are constants named the yield stress, consistency index, and power-law index, respectively. The effective viscosity of Herschel–Bulkley fluids upon deformation is not constant but follows a power-law type behavior in contrast to the constant viscosity found in Bingham fluids [13, 14]. The yield stress typically scales as $E^\alpha \Phi^\beta$, where E is the applied electric field and Φ is the particle fraction, with $1 < \alpha < 2$ and $\beta \approx 1$ when derived on the basis of the so-called fibrillation model, where chains are formed in the ER suspension. In this model particles become polarized and aligned as a dipole along the direction of the electric field. Consequently, the interaction between the polarized particles increases, resulting in the ER effect. The particle could bear some net charge, arising for example through the ionic adsorption, thus electrophoresis could contribute to the particle motion (that is observed in the case of this study) for particle re-arrangement [15–17].

3. Experimental methods

3.1. Sample preparation

Synthetic fluorohectorite clay was purchased from Corning Inc. (New York) in the form of powder, and cation exchanged into sodium fluorohectorite (Na-Fh) in our laboratory. Its final chemical formula is given as $Na_{0.6}(Mg_{2.4}Li_{0.6})Si_4O_{10}F_2$ per half unit cell, where Na is an interlayer exchangeable cation.

A silicone oil Dow Corning 200/100 fluid (dielectric constant of 2.5, viscosity of 100 mPa s, and specific density of 0.973 g cm^{-3} at 25 °C) was used as a suspending liquid, providing a relatively non-polar and non-conductive medium, with a DC conductivity of the order of magnitude of 10^{-12} S m^{-1}.

The preparation of the ERF was undertaken by the following procedure: clay powder was crushed with a pestle and mortar, and then dried in a vacuum oven for 12 h at 90 °C. At the same time the silicone oil was heated at 110 °C for 12 h. Subsequently, the clay powder and the silicone oil were mixed in glass tubes and vigorously hand-shaken for ∼2 min, then placed in an ultrasonic bath for 1 h and again vigorously shaken for 1 h in an orbital shaker. The sample was centrifuged for 1 min at 500 rpm to filter out large aggregates of clay particles >50 μm. The final clay concentrations were approximately 1, 5, 10, 20, and 40 wt%, respectively.

3.2. Clay particle characterization

SEM was employed in order to characterize both the general clay aggregate sizes/shapes and the size/shape of *individual* particles formed from multi-layer stacking of silica sheets held together by cations and water molecules. A field emission scanning electron microscope (model S-4300SE from Hitachi) was used in these studies. The samples were gold coated and attached to an SEM stub using double-sided conductive carbon tape.

3.3. Diffraction experiments

The WAXS experiment was carried out at the European Synchrotron Radiation Facility (ESRF) in Grenoble, France. An x-ray beam with a wavelength of 0.72 Å and a 0.3 × 0.3 mm^2 beam size at the sample was used. The beamline BM01A is equipped with a two-dimensional MAR345 image plate detector with a diameter of 345 mm and a read-out time of about 40 s. The sample to detector distance was set to 350 mm and calibrated using a standard LaB_6 sample, resulting in a maximum diffraction angle 2θ of about 26° that enabled detection of scattering in a q-range of approximately 0.2–2 Å^{-1}.

The experimental geometry is shown in figure 1. The custom-made sample cell consisted of an electrically insulating acrylic glass in the form of a cubic cuvette, where the top part can be opened for inserting two identical 1 mm × 1 mm × 50 mm thick copper electrodes separated by a gap of 1 mm. Two openings were made on the sides of the cuvette and these were sealed by thin transparent Scotch tape that gave very little attenuation of the x-ray beam. The sample (<0.5 ml) was placed between the electrodes from above. The WAXS experiment was performed at ambient temperature for samples at rest (no liquid flow through the scattering cell). Electric fields from 0.35 to 0.75 kV mm^{-1} were chosen as a result of the following observations: for electric fields above 0.75 kV mm^{-1} the chain and column formations are too fast to be followed experimentally, and electric fields below 0.35 kV mm^{-1} are too weak for particles to form any chains.

3.4. Rheometry

The rheological properties of the clay suspensions were measured under DC electric fields using a Physica MCR300 Rotational Rheometer. All the rheological measurements were performed at a constant temperature of 25 °C. These included controlled shear rate tests for measuring shear stress as a function of shear rate (flow curves), static yield stress determination by means of the controlled shear stress measurements, and leak current of the ERF versus time.

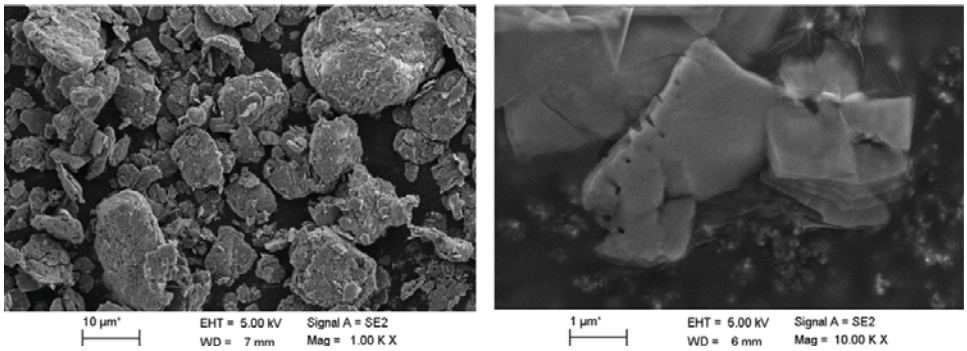

Figure 2. SEM images of Na-Fh clay particles with magnifications of 1000 (left) and 5000 (right), respectively.

3.5. Leak density current and dielectric constant measurements

One of the many serious concerns in ER applications is to minimize the power consumption and, thus, to determine the unwanted current called the leak current. For clay-based ER fluids an electric current can appear via the water containing clay particles. A conductivity cell was designed to study the current leakage through ERFs at different electric field strengths and particle volume fractions. A pair of parallel electrodes made out of copper sheets of surface area 100 cm^2 was sealed on two sides using an insulating 1.2 mm thick spacer. The bottom of the cell was sealed with a non-conductive rubber that could be removed after the measurement was finished in order to enable a proper cleaning of the cell. The sample (12 ml) was applied from the top of the cell. The DC leak current was measured using a standard ammeter. The dielectric constant was estimated indirectly via the measurement of a capacitance using an Agilent LCR meter 4263B and the same conductivity cell.

The dielectric constant was measured as follows: an electric field was applied for 5 min just after an ERF had been introduced into the conductivity cell. Next, the electric field was switched off and the LCR meter started measuring the capacitance at four different frequencies. Shortly after, the decay of the dielectric constant was measured for 10 min. Each measurement was repeated three times and the results are shown as a mean value.

4. Results

4.1. SEM imaging

Figure 2 shows two SEM images of the Na-Fh clay powder with magnifications of 1000 (left) and 5000 (right), respectively. One can see that clay particles form aggregates of different sizes varying from a fraction of a micrometer up to tens of micrometers in both length and width. The aggregates differ also in shapes; hence the polydispersity is high in terms of both size and shape. In figure 2 (right) an *individual* particle can be seen; it consists of a multi-layer stacking of silicate sheets held together by cations and water molecules. The *individual* idealized Na-Fh clay particle is typically considered to be a disk-like structure consisting of tens/hundreds of silica sheets (thus having thickness of tens/hundreds of nm) with a μm-sized diameter [18, 19]. The fact that the clay particles form rather large aggregates cannot be disregarded when one tries to understand the value of the order parameter, which is described in section 4.2. One should not expect the order parameter to be as high as, for example, reported by Hemmen *et al* [18], where the clay particles were generally separated from each other and in some cases the *individual* clay particles were exfoliated into platelets. However, one should be able to observe changes in order parameter values between randomly dispersed and E-field polarized clay aggregates.

4.2. Orientational order from WAXS measurements

Prior to the application of the electric field, the Na-Fh particles are randomly dispersed into the silicone oil. The formation of chain-like structures aligning parallel to the E-field is observed after its application. Many thin chains are formed first (with thickness in the range 1–50 μm) and they subsequently attract each other, resulting in thicker (in the range 50–200 μm) columns. After a time t_s (the saturation time), no major changes in the system are noticeable by optical microscopy [20].

The E-field-induced self-assembly of the clay aggregates can be further investigated by x-ray scattering methods. Dynamic changes in the clay orientational order can be observed from two-dimensional WAXS patterns, as explained in section 2.2. Figure 3 shows WAXS patterns from a suspension, without (a) and with (b) an E-field of 750 V mm^{-1} applied. The inner diffraction ring lies at 0.51 $Å^{-1}$ and is attributed to the (001) Bragg diffraction from the layered silicate sheets within clay particles. Typically, the distance d_{001} is close to 12 Å when one layer of water is intercalated between silicate sheets [10]. The outer peak at 0.83 $Å^{-1}$ is due to the silicone oil, i.e. the maximum in its radial distribution function. It is a broad and relatively strong peak that shields the second order (001) Bragg peak from the clay particles. The first Bragg peak intensity changes in time after the electric field has been applied. This change can be better appreciated when

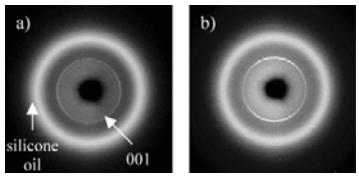

Figure 3. WAXS patterns of clay particles without (a) and with (b) E-field applied. The 001 clay diffraction peak and the oil diffuse scattering peak are present in both images.

Table 2. Calculated values of the anti-nematic order parameters S_{an} under different E-field strengths. The corresponding nematic order parameter is $S_{an} = -2S_n$.

E-field (V mm^{-1})	S_{an} (average)
350	0.63 ± 0.01
500	0.64 ± 0.02
750	0.60 ± 0.05

the intensity of the (001) Bragg diffraction peak is plotted as a function of the azimuthal angle φ, as shown in figure 4. There are three possible events that can provoke changes in these WAXS patterns with increasing time: (i) clay particles become polarized and orient individually in the external field; (ii) the polarized particles attract each other and form chains; (iii) the chains coarsen into column-like structures. These three processes can occur in different time ranges or they may overlap in time.

Table 2 shows values of the order parameter calculated for different E-fields (according to [10]). Since it was found that the order parameter did not change in time (15 s–6 min), the averaged value of S is only presented with its estimated error. The mean orientation distribution is also observed not to display any significant differences, within estimated error, for the different applied fields of 350, 500, and 750 V mm^{-1}, respectively.

Hence, there seems to be no evidence of E-field dependence, nor time dependence on the order parameter S, for the E-field range (350–750 V mm^{-1}) and timescale (15 s–6 min) addressed in this study. One can conclude that the clay aggregates rotate and align along the E-field much faster (probably in ms timescale) than chains (seconds) and columns (seconds/minutes) are formed.

The amplitude of the WAXS azimuthal profiles is a measure of the average particle orientation in the scattering volume, but it also scales with the number of particles existing within this volume. Since we find that the order parameter is nearly constant with time, the amplitude change seen in figure 4 is a demonstration of how the number of particles contributing to the scattering increases in time. This observation is a sign of the progressing chain and bundle formation inside the scattering volume, where (1) already formed chains are attracted to each other and/or (2) particles being still in motion (electrophoresis) finally attach to an existing chain. Both effects can increase the lateral dimensions of chains. The two processes, namely particle orientation and chain formation, may affect each other to some extent, but the

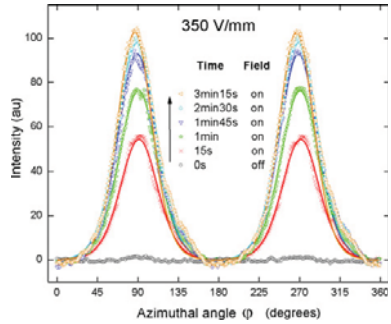

Figure 4. Azimuthal plots of the changes with time of the first Bragg peak amplitude under an E-field of 350 V mm^{-1}. The corresponding azimuthal plots from the model are shown as continuous lines.

particle orientation is the initial step and is largely finished when the chain formation takes over, as illustrated by the order parameter values along with the data in figure 4.

4.3. Chain formation versus column formation from leak current measurements

The leak current density increases when chain bridges spanning two electrodes are being formed. However, it is not expected to change when chains coarsen into columns as described at the end of section 4.2. In this case, the total cross sectional area of all chain bridges, thus the total number of particles that contribute to the leak current, remains unchanged (the leak current can increase with the moisture content increment in the system, but it is not relevant here, since this process is relatively slow). In other words, the leak current measurement can provide information about the chain formation only. In contrast, as discussed in section 4.2, the increase of the scattering intensity is associated with the progressing chain and bundle formation due to an increased average particle density within the scattering volume. Therefore, by comparing rates of the normalized current density growth in time with the normalized time-dependent change in the WAXS azimuthal plot maxima (figure 6), chain and column formation processes can be qualitatively distinguished from each other. This information may be of importance when one needs a self-assembly from particles to lead to single chain rather than aggregated column formation.

Figure 6 shows both types of data plotted in logarithmic scale as a function of time. Note that the WAXS data at a given time are obtained as the normalized maximum value for the azimuthal variations of the first Bragg peak intensity, for three different E-fields: 350, 500, and 750 V mm^{-1}. In particular, the corresponding azimuthal plots are shown in figure 5 at $t = 15$ s. A characteristic time τ was estimated by fitting straight lines to the data in figure 6. For electric fields of 750 and 500 V mm^{-1}, the current density curves nearly coincide with the WAXS data ($\tau_{750\text{WAXS}} = 9.26$ versus $\tau_{750\text{CURRENT}} = 9.9$ and $\tau_{500\text{WAXS}} \approx \tau_{500\text{CURRENT}} = 22.7$), indicating that the chain formation is followed by rapid column formation. However, for the lowest electric field, current density (which

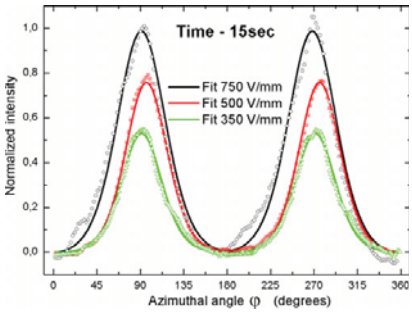

Figure 5. Azimuthal plots of the first Bragg peak amplitude at fixed time $t = 15$ s for different E-fields. The corresponding azimuthal plots from the model are shown as continuous lines.

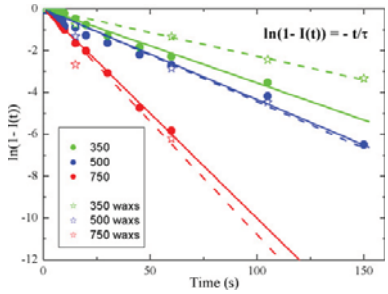

Figure 6. Leak current density and maxima of azimuthal plots versus time.

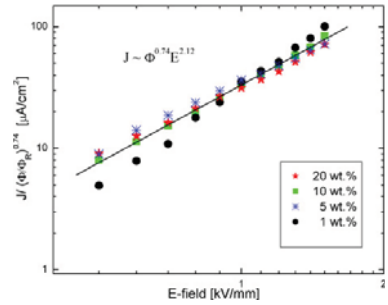

Figure 7. Log–log plot of the current density, normalized by $\Phi/\Phi_R^{0.74}$ ($\Phi_R = 20$ wt% is an arbitrarily chosen reference value), versus the applied electric field for different clay particle concentrations. The power law fitted to the whole data, in the form $E^{2.12}$, is also plotted.

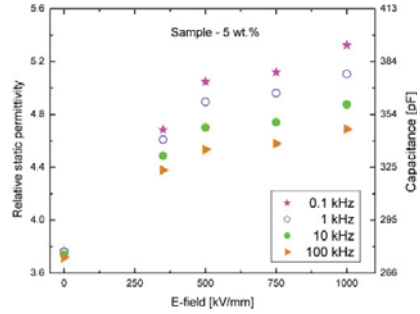

Figure 8. Relative static permittivity and capacitance versus E-field strength, for various frequencies.

witnesses the single chain formation) increases faster than the WAXS azimuthal plot maximum (which changes not only when chains but also when the thicker columnar structures are being formed) for the same field ($\tau_{350\text{WAXS}} = 43.5$ versus $\tau_{350\text{CURRENT}} = 28.6$). This indicates that single chains are formed first followed by the columnar growth. Under the low electric field these processes occur slower than for higher electric fields and it can be concluded that the chain formation and the chain aggregation into columns are two phenomena that occur on significantly different timescales. This was also observed under the optical microscope.

The leak current density of ERF was found to rise with increasing strength of the applied electric field, and observed to nearly follow a second-order power law (figure 7) of E, thus a clay-based ERF does not obey Ohm's law, $V = IR$. Other power laws were found by different researchers and the power-law relationship can be represented in a more general way as $J \propto E^n$, where the exponent n has been found to vary between 1 and 5 [21]. The mechanism for the effect of electrical field strength on the current leaking through ER fluids is still poorly understood. However, it is expected that intercalated water plays an important role in activating the current leakage [22]. The clay concentration dependence on the current density was measured and found to follow a power law with an exponent 0.74 on average for four different clay particle concentrations. Figure 7 shows the current density data normalized by $\Phi/\Phi_R^{0.74}$ (where $\Phi_R = 20$ is an arbitrarily chosen reference value) as a function of the applied electric field. The overall data (that collapsed onto each other after normalization) were fitted with a power law with an exponent 2.12. Therefore, the current density scales with the particle fraction and electric field as $J \propto \Phi^{0.74} E^{2.12}$.

4.4. Measurements of dielectric constant

The dielectric constant was derived from the measured capacitance C according to the conventional relation $\varepsilon = Cd/(\varepsilon_o A)$, where ε_o is the dielectric constant of a vacuum, d is the thickness of the gap between the electrodes, and A is the contact area of the electrodes. The dielectric properties, such as dielectric constant and leak current play important roles in relation to the performance of ER materials. As can be seen from figure 8, the larger the electric field strength, the larger the dielectric constant of the ERF. As the overall capacitance stems from the joined capacitances of all individual dipoles within the ER chains/columns, this means that each of these individual capacitances, resulting from clay aggregate's induced polarization, corresponds to a polarization charge that increases non-linearly (and faster than linearly) with the external electric field strength (but with a saturation at very large E-field strengths).

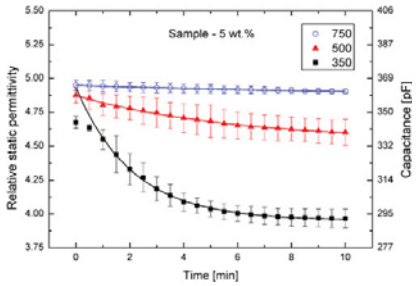

Figure 9. Relative static permittivity decays in time after switching off an E-field (sample with 5 wt% clay concentration).

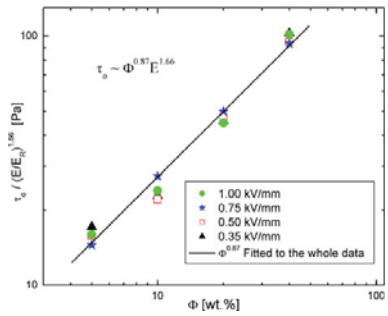

Figure 11. Log–log plot of the static yield stress, normalized by $(E/E_R)^{1.66}$ (the arbitrarily chosen reference value is $E_R = 1$ kV mm^{-1}), versus the volume fraction at different strengths of the applied electric field. The power law fitted to the whole data set, in the form $\Phi^{0.87}$, is also plotted.

It is interesting to note that the dielectric constant goes down rapidly after 350 V mm^{-1} is switched off (see figure 9). That field strength is rather small (just above the critical field needed for a chain formation), and chains/columns are not coarsened tightly enough to not break apart. The time needed to break them apart is short. On the other hand, for a high field strength of 750 V mm^{-1}, the dielectric constant falls down very slow, and chains remain after the field has been switched off. The data were fitted with an exponentially decaying function that provided characteristic decay times of 11.5, 5.8, and 2.1 s for electric field strengths of 350, 500, and 750 V mm^{-1}, respectively.

4.5. Rheological behavior

The yield stress point can be found using different methods and these include: controlled shear rate (CSR) measurements followed by adequate fitting procedures, controlled shear stress (CSS) tests, the bifurcation method, oscillatory test, etc. One may discuss which method is the most appropriate to use, since the value of the yield stress can vary with different methods. However, in the case of our study the two methods used, namely CSR and CSS, give very similar results as presented below. Figure 10 shows a log–log plot of the flow curves fitted with the Herschel–Bulkley model (left) and the yield stress determination via controlled shear stress tests (right) for a suspension of 10 wt% of clay under different applied electric field strengths. The yield stress values obtained from CSR tests by fitting with Herschel–Bulkley are 4.49, 7.37, 12.2, and 27.1 Pa for the electric field strengths of 350, 500, 750, and 1000 V mm^{-1}, respectively. These values coincide with the results acquired from the CSS method (see figure 10, right). Since the power-law index p (see section 2.4) lies in the range of 1.3–1.9 the usage of the Herschel–Bulkley model is justified.

Figure 11 shows the dependence of the yield stress τ_y on both the clay particle concentrations and the applied electric field (based on values obtained from the CSS tests). A power law of average exponent 1.66 was found, and this is in good agreement with earlier results [23, 24]. The yield stress shown here was normalized by $E/E_R^{1.66}$ ($E_R = 1$ kV mm^{-1} is a reference value) and plotted as a function of the clay concentration Φ. The collapsed data were fitted with a power law with an exponent 0.87. Thus, the static yield stress scales as $\tau_y \propto \Phi^{0.87} E^{1.66}$, in general agreement with the fibrillation model described in section 2.4 that can be used here to explain the mechanism of the ER effect.

5. Conclusion

The electric field induced structuring from clay particles suspended in silicone oil has been studied by means of WAXS,

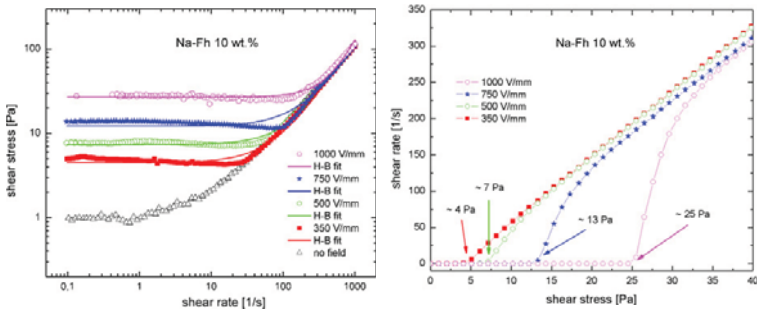

Figure 10. Log–log plot of the flow curves fitted with the Herschel–Bulkley model (left) and the yield stress determination via controlled shear stress tests (right) for a suspension of 10 wt% of clay under different applied electric field strengths.

rheometry, SEM, leak current density, and dielectric constant measurements.

Firstly, SEM was employed in order to characterize both the general clay aggregate sizes/shapes and the size/shape of individual particles. It was observed that clay particles form aggregates of different sizes varying from a fraction of a micrometer up to tens of micrometers in both length and width. The aggregates also differ in shapes; hence the polydispersity is high in terms of both size and shape.

The 001 scattering peak intensities from two-dimensional WAXS diffractograms were plotted as a function of the azimuthal angle and then fitted according to the model from [10] in order to obtain the particles' orientational distributions. In this way, an orientational order parameter S could be calculated; the obtained values showed that S does not change much with time (15 s–6 min) after a fast initial buildup of the orientational order. The reference orientation of the distribution was also observed not to display any significant differences, within the estimated error, for the different applied fields of 350, 500, and 750 V mm^{-1}, respectively. One concludes that the clay aggregates rotate and align along the E-field much faster (probably on a ms timescale) than chains (seconds) and columns (seconds/minutes) are formed.

Particle orientation distributions from WAXS data show that particle orientation occurs very fast with respect to chain formation and aggregation. In addition, a comparison of the characteristic times for column formation by chain aggregation (from the evolution of the amplitude of WAXS azimuthal maxima) and for chain formation (from leak current monitoring) shows that the two processes happen at the same time and on a similar timescale for all applied electric fields, except the lowest one, for which chain aggregation into columns is a significantly slower process than their formation. For the lowest electric field (0.35 kV mm^{-1}) there was clear evidence that coarsening of chains into the thicker columns occurs much slower than at higher fields, where column formation takes place immediately after chains are formed.

The leak current density of ERF was measured for different electric field strengths and clay particle concentrations. It was found that the leak current density depends on electric field and clay concentration as follows: $J \propto \Phi^{0.74} E^{2.12}$. The dielectric constant was derived from the measured capacitance.

In addition, the most important rheological properties of our ER fluid have been measured, which includes the dependence of the yield stress both on the electric field and on the particle concentration. The following scaling behavior was observed: $\tau_y \propto \Phi^{0.87} E^{1.66}$.

Future prospects for this work include (i) extending the study of characteristic times for chain versus column formation in order to see if such a behavior is a general feature of this type of system, (ii) investigating fluctuations in the leak current, and (iii) carrying out a more detailed study of the dielectric properties of the system.

Acknowledgments

The authors acknowledge assistance from O T Buset and D Chernyshov while performing experiments at the Swiss–Norwegian Beam Lines at ESRF, and A P Hammersley, creator of the Fit2D program. This work was supported by the Research Council of Norway through the FRINAT Program: NFR project number 171300, as well as through the Aurora French-Norwegian collaboration program for travel between France and Norway (French Aurora Grant No. 18810 WC, NFR Grant No. 187697/V11).

References

[1] Winslow W M 1947 *US Patent Specification* 2517850
[2] Wang B, Zhou M, Rozynek Z and Fossum J 2009 *J. Mater. Chem.* **19** 1816–28
[3] Fossum J O, Meheust Y, Parmar K P S, Knudsen K D, Måløy K J and Fonseca D M 2006 *Europhys. Lett.* **74** 438–4
[4] Espin M J, Delgado A V and Płocharski J 2005 *Langmuir* **21** 4896–903
[5] Larson R G 1999 *Struct. Rheol. Complex Fluids* **8** 368
[6] Ma H, Wen W, Tam W Y and Sheng P 1996 *Phys. Rev. Lett.* **77** 2499–502
[7] Ma H, Wen W, Tam W Y and Sheng P 2003 *Adv. Phys.* **52** 343–83
[8] Wen W, Huang X, Yang S, Lu K and Sheng P 2003 *Nat. Mater.* **2** 727–30
[9] Huang X, Wen W, Yang S and Sheng P 2006 *Solid State Commun.* **139** 581–8
[10] Méheust Y, Knudsen K D and Fossum J O 2006 *J. Appl. Crystallogr.* **39** 661–70
[11] Wensink H H and Vroege G J 2005 *Phys. Rev.* E **72** 031708
[12] Gennes G P and Prost J 1993 *Phys. Liq. Cryst.* **41/42** 2
[13] Vishwanath K P and Kandasamy A 2010 *Appl. Math. Mod.* **34** 219–27
[14] Alexandrou A N, McGilvreay T M and Burgos G 2001 *J. Non-Newton. Fluid Mech.* **100** 77–96
[15] Klingenberg D and Zukoski C F 1990 *Langmuir* **6** 15–24
[16] Hao T 2002 *Adv. Colloid Interface Sci.* **97** 1–35
[17] Gast A and Zukoski C F 1989 *Adv. Colloid Interface Sci.* **30** 153–202
[18] Hemmen H, Ringdal N I, Azevedo E N, Engelsberg M, Hansen E L, Méheust Y, Fossum J O and Knudsen K D 2009 *Langmuir* **25** 12507–15
[19] Fonseca D M, Méheust Y, Fossum J O, Knudsen K D and Parmar K P S 2009 *Phys. Rev.* E **79** 021402
[20] Rozynek Z, Wang B, Zhou M and Fossum J O 2009 *J. Phys. Conf. Ser.* **149** 012026
[21] Conrad H, Chen Y and Sprecher A F 1990 *Proc. 2nd Int. Conf. on ER Fluids* (Lancaster: Technomics) p 252
[22] Chen T Y and Luckham P F 1994 *J. Phys. D: Appl. Phys.* **27** 1556–63
[23] Parmar K P S, Meheust Y, Schjelderupsen B and Fossum J O 2008 *Langmuir* **24** 1814–22
[24] Méheust Y, Parmar K P S, Schjelderupsen B and Fossum J O 2010 arXiv:1002.0242v1

Paper III

Electrorheological properties of organically modified nanolayered laponite: influence of intercalation, adsorption and wettability

B Wang, M Zhou, Z Rozynek and J O Fossum

J. Mater. Chem. 19 (2009) 1816-1828

Electrorheological properties of organically modified nanolayered laponite: influence of intercalation, adsorption and wettability†

Baoxiang Wang,* Min Zhou, Zbigniew Rozynek and Jon Otto Fossum*

Received 21st October 2008, Accepted 5th January 2009
First published as an Advance Article on the web 11th February 2009
DOI: 10.1039/b818502f

Cetyltrimethylammonium bromide (CTAB) modified synthetic laponite is synthesized by an ion exchange method and characterized by simultaneous small-angle X-ray scattering (SAXS) and wide angle X-ray scattering (WAXS), field emission scanning electron microscopy (FESEM), transmission electron microscopy (TEM), energy dispersive spectrometry (EDS), atomic force microscopy (AFM), thermal analysis and rheometry. Through the formation of the organoclay, the properties of clay change from hydrophilic to hydrophobic. Morphology results show that the hydrophilic particles are aggregating easily, whereas the suitable CTAB modified laponite can get near monodispersed nanoparticles due to its hydrophobic properties. It is proposed that CTAB is intercalated and adsorbed onto the laponite partially depending on the substituted concentration of the surfactant cation exchange capacity (CEC) (0.5CEC to 6CEC). The electrorheological (ER) effect is investigated for suspensions of CTAB modified laponite dispersed in silicone oil. The two-dimensional SAXS images from ER bundles of CTAB modified laponite exhibit markedly anisotropic SAXS patterns, giving a measure for laponite particle alignment within the ER structure. An optimum electrorheological effect can be attained at a particular CEC substituted concentration. On the basis of the structure analysis and dielectric measurements, we attribute the enhancement of ER activity to the improvement in the dielectric properties that showed an increase in the dielectric constant and the dielectric loss at low frequency and their regular optimum change with CTAB modification.

1. Introduction

Smart structures and materials are a subset of functional structures and materials, with adaptability as their main characteristics. They can be defined as materials with an ability to respond in a pre-designed useful and efficient manner to changes in environmental conditions, including any changes in their own condition. Transducers that have piezoelectric, pyroelectric, electrostrictive, magnetostrictive, piezoresistive, electroactive, or other sensing and actuating properties are good examples of smart materials.[1,2] Electrorheological fluids (ERFs) are a kind of smart material consisting of suspensions of dielectric particles dispersed in a nonconducting liquid. ERFs exhibit drastic changes in their rheological properties, including a large enhancement in apparent viscosity and yield stress under an applied electric field. Application of an electric field can induce polarization of the suspended particles and a chainlike structure can be formed along the electric field direction in a few milliseconds.[3–9] The transition to a solid-like state is due to chain formation and the liquid-to-solid transition indicates that there is an inner ordering of the ER constituents which leads to a change in the rheological properties. This phenomenon is reversible when the external electric field is removed. Because of their controllable viscosity and short response time, ER materials are potential materials for use in active devices, brakes, clutches, shock absorbers and actuators.[10–18]

The wettability of the particle with respect to silicone oil is very important for enhancing the ER effect. Moreover, anti-electric breakdown, stability and strong polarization are closely related to the wettability of particles.[19] Wen *et al.*[20] demonstrated that the particle wetting surface in a liquid could induce ER effects, and they found that nanoparticles of barium titanyl oxalate coated with urea suspended in hydrocarbon oil give no measurable ER effect. Interestingly, by adding a small amount of oleic acid to the hydrocarbon oil, Shen *et al.* achieved a high yield stress.[20c] The addition of the surfactant changes the non-wetting particles into wetting ones which induce the so-called giant electrorheological (GER) effect. Fang *et al.*[21] investigated theoretically the effects of zero-field dispersity of colloidal particles, and particle wettability, on the ER effect, and found that well dispersed particles resulting from particle wettability have much stronger attraction than those aggregated into different clusters. These authors found that the surface tension between particles and oil can be greatly reduced due to the mediating effect of the surfactant molecules, thus allowing particles to disperse very well in zero field and then form a better particle structure upon application of an electric field. Bare laponite particles as described below are hydrophilic and their wettability with silicone oil is poor. However, when organic modified clay surfaces are formed, the wettability may be transformed from non-wetting to wetting.

Clay minerals are layered silicates, whose primary particles are platelet shaped. The "unit cell" structure of a single clay platelet

Department of Physics, Norwegian University of Science and Technology (NTNU), Høgskoleringen 5, NO-7491 Trondheim, Norway. E-mail: baoxiang.wang@ntnu.no; jon.fossum@ntnu.no

† Electronic supplementary information (ESI) available: DTG traces of CTAB and 6CEC-Lp; 2D anisotropic scattering patterns; evidence for the change of wettability. See DOI: 10.1039/b818502f

is made of tetrahedral sheets and octahedral sheets joined in a face-to-face configuration in three dimensions.[22–27] A 2:1 clay mineral is classified as di-octahedral when two thirds of the octahedral sites are occupied by cations in its unit cell. Laponite is a synthetic nano-layered silicate and has the empirical chemical formula $Na^{0.7+}[Si_8Mg_{5.5}Li_{0.3}O_{20}(OH)_4]^{0.7-}$, where Na is an interlayer exchangeable cation. Laponite is a synthetic tri-octahedral hectorite clay composed of two tetrahedral silica sheets and a central octahedral magnesia sheet. The negative surface of the laponite particle contains positively charged sodium (Na^+) ions. These can be shared by several laponite sheets forming aggregates. Isomorphic substitutions of the divalent magnesium atoms by monovalent lithium leads to the formation of negative charges within the lattice, which is balanced by the sodium ions located at the surface. Laponite is a synthetic nanoclay, which consists of disc-like particles with a thickness of 1 nm and an average diameter of 30 nm. In contrast to pristine mica-type silicates which contain alkali metal and alkali earth charge-balancing cations, organically modified layered silicates (OLS) contain alkylammonium or alkylphosphonium cations.[28,29] The presence of these organic modifiers in the galleries renders the originally hydrophilic silicate surface organophilic. Depending on the functionality, packing density, and length of the organic modifiers, the OLSs may be engineered to optimize their compatibility with a given polymer.[30–32] Depending on the packing density, temperature, and chain length, the chains are thought to lie either parallel to the host layers forming lateral mono- or bilayers or radiate away from the surface forming extended (paraffin-type) mono- or bimolecular arrangements.

In this study, we demonstrate the influence of intercalation and adsorption on the wettability and electrorheological properties of organic modified nanolayer laponite. Our CTAB-modified laponite organoclays have been carefully characterized by atomic force microscopy (AFM), field emission scanning electron microscopy (FESEM), transmission electron microscopy (TEM), energy dispersive spectrometry (EDS), simultaneous small-angle X-ray scattering (SAXS) and wide angle X-ray scattering (WAXS), and thermal gravimetric analysis (TGA). Experimental results confirmed that CTAB can be intercalated and adsorbed onto the laponite depending on the concentration of the surfactant. Surface modified laponite clay is lipophilic and thus disperses much easier in oil in comparison to unmodified laponite. An optimum electrorheological effect could be attained due to the good wettability of CTAB modified laponite.

2. Materials and characterization

2.1. Materials

The synthetic laponite clay was purchased from Laponite Inc. as a fine white powder. Laponite is a trioctahedral clay with lithium substituting for magnesium in the octahedral layers. Its cation exchange capacity (CEC) is 47 mequiv/100 g. Its surface area (BET) is 370 m^2/g. The surface charge density of individual discs is 0.4 e^-/unit cell, and the specific particle density is 2.65 g/cm^3. The surfactant (cetyltrimethylammonium bromide, $[CH_3(CH_2)_{15}]NBr(CH_3)_3$, CTAB) used was of analytical grade. A silicone oil (a Newtonian liquid) Dow Corning 200/100 Fluid (dielectric constant of 2.5, viscosity of 100 mPa·s and specific density of 0.973 g/cm^3 at 25 °C) was used as a suspending liquid because it is relatively non-polar and non-conductive, with a DC conductivity of the order of magnitude of 10^{-12} S/m.

2.2. Preparation of the organoclay and its ER suspension

The synthesis of organoclay nanohybrids was undertaken by the following procedure. In the present work, the stoichiometric amount (based on the CEC) of cationic surfactant was added to a solution of powdered clay. To 400mL of distilled water, 8.0 g of laponite was added, and this solution was stirred and heated to 80 °C. At the same time, a second solution of the stoichiometric amount of CTAB and 100mL distilled water was prepared. Both solutions were stirred for 10h. Finally, the surfactant solution was added carefully to the hot clay solution forming flocs immediately. Then the mixture was stirred at 80 °C for 24h. The stirring solution was covered and cooled to room temperature overnight. The flocs were filtered, redispersed in 250 mL of water for 2 h, and filtered again. This process was repeated four times to remove any free surfactant and checked by an $AgNO_3$ solution. The filtered treated clay was dried at 100 °C in a vacuum oven overnight, then crushed with a pestle and mortar, and returned to the vacuum oven for 3 h at 100 °C and kept in a sealed container until use. The obtained cationic surfactant-exchanged laponites were labelled as 0.5CEC-Lp, 1CEC-Lp, 2CEC-Lp, 4CEC-Lp, and 6CEC-Lp. In this research, xCEC means x times the cation exchange capacity and how many surfactants are used for the ion exchange method.

The ER suspensions of organoclay in silicone oil were prepared by the following steps. 10 wt% of CTAB modified laponite powder and silicone oil suspension were prepared. The silicone oil was heated at 110 °C for 24 h. The heated organoclay powder and silicone oil were immediately mixed in glass tubes which were then sealed and left to cool to room temperature. The glass tubes were vigorously hand-shaken for ~5 min and placed in an ultrasonic bath for 1h and again vigorously shaken for 1h in an orbital shaker before the rheology measurements.

2.3. Characterization

Thermal gravimetric analysis (TGA) was performed on a TGA/SDTA851^e TGA instrument (Mettler Toledo As.) under N_2 flow (100 mL/min) with a heating rate of 10 °C/min. Furnace temperature and time were adjusted by using the software STAR^e.

The X-ray scattering experiment was carried out at room temperature using a sealed-tube CuKα source with a wavelength of 1.5418Å utilizing NanoSTAR, a small-angle X-ray scattering (SAXS) system, from Bruker AXS. It uses a two dimensional detector and the size of collected beam is 0.4mm. The possibility of different sample–detector distances make it possible to perform both SAXS and WAXS experiments with the same equipment. The sample-to-detector distance was calibrated using a silver behenate standard, and the scattering data were averaged over the whole detector. The SAXS experiments were performed making the ER suspension in a custom-made scattering cell. The scattering cell consists of an insulating plastic material, whose top part was open, while both the (front and back) sides and the

bottom part were closed by gluing a standard kapton film. Two parallel and identical 1/2 mm thick copper electrodes separated by a gap of 1 mm are inserted from the top of the sample cell. The sample to be studied (<2 mL) is placed between the electrodes from the top part. After application of an electric potential difference (such as 2 kV) between the copper electrodes, the organoclay particles are first observed to form chain-like structures parallel to the applied electric field. Small-angle scattering is a useful tool to study disordered structures and porous media. In a small angle X-ray scattering (SAXS) experiment, the dependence of the scattered intensity on the scattering angle 2θ is controlled by the size of the colloidal particles, their tendency to aggregate, the porosity of the disperse system, the magnitude of the specific surface area, and more generally, by the inhomogeneities characterizing the structure of the disperse system. The scattered intensity $I(q)$, as a function of the momentum scattering vector q

$$q = 4\pi\sin(2\theta/2)/\lambda$$

where λ is the wavelength of the incident beam and 2θ is the scattering angle, is proportional to the Fourier transform of the geometric correlation function of the electron density. The scattering vector q has the dimension of inverse length (*i.e.* Å^{-1}), so that the length d in real space corresponding to a certain q-value is given by:

$$d = 2\pi/q$$

The AFM images were taken using a MultiMode™ Atomic Force Microscope from Veeco Instruments, operating in normal room air. Small samples originating from different CTAB modified laponite solutions were deposited onto cleanly cleaved mica surfaces. To prepare a sample, a freshly cleaved piece of mica was fastened on top of a 1cm radius metal disk. Using a micropipette, a 10 μL drop of the solution was placed on the mica surface. The drop was dispersed over the available area, and was then left to air dry for at least an hour, leaving dehydrated assembled rough films covering the mica surface. These surfaces were imaged using a DI AFM Multimode TM SPM with a Nanoscope V controller and a *J* scanner in contact mode. Our AFM images consist of the standard 512 × 512 pixels. The images were corrected for scanning curvature instrumental artifacts using the DI Nanoscope software flattening procedure.

Electron micrographs were acquired using a field emission scanning electron microscope (Zeiss Ultra, 55 Limited Edition, accelerated voltage 15kV) and a TEM (JEOL JEM 2010, operated at 200 kV). For the TEM samples, a suspension of a small amount of sample in ethanol was given an ultrasonic treatment for 5 min and then dropped onto a copper grid. The scanning microscope was equipped with an energy dispersive X-ray spectroscopic detector. Energy dispersive spectrometry (EDS) patterns were obtained by a Link ISIS (Oxford Co., England), using a SiLi detector. It was used to do elemental analyses (starting with boron, since for elements of lower atomic weight large errors are incurred).

The rheology of our organoclay suspensions was measured under DC electric fields using a Physica MCR 300 Rotational Rheometer equipped with a coaxial cylindrical cell Physica CC27/ERD, specially designed for ER measurements. The cell has an outer cylinder diameter of 14.46 mm and an inner cylinder diameter of 13.33 mm. The immersion length of the inner cylinder is 40 mm, and the corresponding sample volume is 19.35 ml. Two grounding brushes connected to the internal cylinder's axis induce an artificial ~1 Pa yield stress in all data, but this value is negligible compared to all yield stress values addressed here. All rheological measurements were carried out at constant temperature (25 °C). Four types of rheology tests were performed: controlled shear rate (CSR) tests for measuring shear stress; two different methods for measuring the static yield stress (controlled shear stress (CSS) and the so-called bifurcation method); and finally oscillation tests were performed to determine the elastic properties.

- controlled shear rate (CSR): before reading the shear stress, we initially applied the electric field to a suspension for 300s and then sheared it from 0.01 to $1000s^{-1}$.
- controlled shear stress (CSS): to determine the static yield stress a linearly increasing shear stress (in steps of 2 Pa) was imposed on suspensions after they had been subjected to the external electric field for 300 s.
- bifurcation tests: firstly, the ER suspension were pre-sheared at a constant shear rate $\dot{\gamma} = 100\ s^{-1}$ for 200 s, then the electric field was applied and the suspension was sheared at a constant shear stress for 300 s while observing the viscosity changes with time. The sample was then poured back into its container and hand shaken again before the test was repeated with a slightly higher shear stress. This procedure was carried out until the yield point was determined.
- oscillation experiments: a sinusoidal strain was applied to the ER fluid by driving the cylindrical bob. The viscoelastic parameter of the storage modulus was then measured at different electric fields. Using the Physica universal measuring system and US200 software, two different experiments were performed. First, strain amplitude was swept from 0.001 to 100% at a fixed driving frequency. Second, the driving frequency was swept from 0.001 to 100 Hz at a fixed strain 0.01.

Dielectric measurements. Because of the difficulty of directly measuring the dielectric properties of the particles, we used suspensions to carry out dielectric investigations. Having considering the influence of the particles' arrangement induced by an external electric field on the dielectric properties, we kept the ER suspensions in a random dispersal system whose structure would not be disturbed by the bias field of 2 V/mm. The capacitance C and dielectric loss tangent ($\tan\delta$) of suspensions were measured by an automatic Agilent 4263B LCR meter (Agilent Technologies, Malaysia) with a 16089E test fixture at room temperature and frequencies of 100Hz, 120Hz, 1kHz, 10kHz and 100kHz. The dielectric constant was derived from the measured C according to the conventional relation $\varepsilon = Cd/(\varepsilon_0 S)$, where ε_0 is the dielectric constant of a vacuum, *i.e.*, 8.85×10^{-12} F m^{-1}, d is the thickness of gap between electrodes, and S is the contact area of the electrodes.

3. Results and discussion

3.1. Thermal properties

The thermal decomposition temperatures and stability of the CTAB modified laponite can be obtained by TGA/DTG.

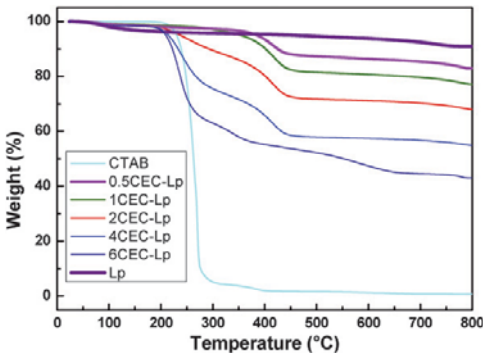

Fig. 1 TGA curves (25–800 °C) of laponite, CTAB and a series of CTAB modified laponites.

Thermal gravimetrical analysis (TGA) indicates a mass loss of below 4 wt% before 200 °C for unmodified laponite, and this is attributed to the loss of water from the sample. The second loss of about 5wt% in the case of dehydroxylation occurred between 650–800 °C (see Fig. 1 and 2). For CTAB, the complete decomposition took place in the range of 200–400 °C and the maximum peak is at 270 °C (see Fig.1 and Fig. S1†). For the CTAB modified laponite, the weight loss at 800 °C is increased with the enhancement of CEC-relative CTAB substitution, which means that the organic content in the organoclay is also increased simultaneously. From room temperature to 800 °C, the complete weight losses for different CTAB modified laponites 0.5CEC-Lp, 1CEC-Lp, 2CEC-Lp, 4CEC-Lp, 6CEC-Lp are 17.2%, 22.9%, 32%, 45.1%, 57.1% respectively.

The differential thermogravimetric analysis (DTG) patterns of laponite, CTAB and CTAB modified laponite are shown in Fig. 2 and Fig. S1.† The laponite shows two thermal decomposition steps at 85 and 722 °C, corresponding to the loss of adsorbed water and the dehydroxylation of the clay. For the 4CEC-Lp sample, four DTG peaks are observed at about 80, 243, 416 and 780 °C, which are attributed to the loss of water, the combustion and loss of the surfactant molecule adsorbed on the clay external surface, the decomposition of the surfactant molecule

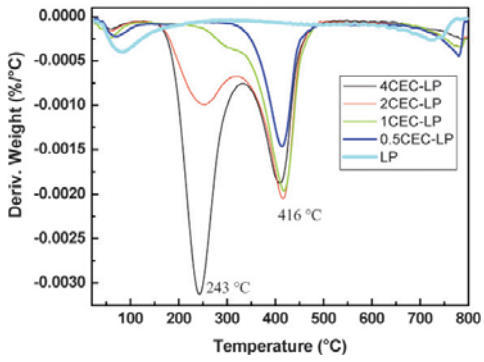

Fig. 2 DTG traces (25–800 °C) of laponite and CTAB modified laponites. The maxima are indicated.

intercalated between the clay sheets and the dehydroxylation of laponite respectively. DTG is particularly useful to judge the state of intercalation or adsorption. For pure CTAB, complete decomposition took place in the range of 200–400 °C and the maximum peak is at 270 °C. For adsorption of CTAB on the surface of laponite, the combustion and loss of the surfactant molecule adsorbed on the clay external surface took place at about 243 °C. For intercalation of CTAB into the interlayer of laponite, the decomposition of the surfactant molecule intercalated between the clay sheets took place at about 416 °C. In the intercalated condition, the CTAB molecules are bonded strongly in the interlayer of the laponite and its decomposition temperature is higher than that of adsorbed CTAB. At low CEC concentrations, such as 0.5 and 1CEC, only intercalated peaks can be observed but not absorbed ones. The surfactant molecules are not lost until 416 °C compared with the loss of the pure surfactant at 270 °C which shows that the CTAB molecules are bonded strongly in the interlayer of the laponite. With the increase of CEC-relative CTAB substitution, the adsorbed peak is apparent and its strength is also increased. Up to 6CEC, it is much larger than the intercalated peak.

3.2. SAXS/WAXS

Fig. 3 shows different two-dimensional SAXS diffractograms of 4CEC-Lp particles dispersed into silicone oil. Fig. 3(a) is obtained from a suspension of 4CEC-Lp particles prior to the application of a DC electric field. The particles are randomly oriented in the suspension without the electric field, so the image is isotropic and the intensity is also low due the low organoclay concentration in the scattering volume. If the electric field exceeds a certain threshold, the 4CEC-Lp particles attract each other and assemble into chains and columns that are aligned along the field direction. The chain or column structures are formed under the combined effects of applied field and inter-particle repulsions. In the presence of an electric field (Fig. 3(b–d)), the pattern become anisotropic due to particle orientation in the field. Furthermore, with the increase of electric field, the anisotropic pattern is clearer and stronger. The anisotropic strength of 4CEC-Lp particles is more evident than that of 0.5CEC-Lp particles (shown in Fig. S2†), which means that the ER effect of 4CEC-Lp particles is more pronounced. Fig. 4 shows how the intensity of circular scattering rings such as those presented in Fig. 3 and Fig. S2† evolves as a function of the azimuthal angle Φ, between 0 and 360°. For $E = 0$, the intensities are independent of Φ and the two-dimensional scattering pattern

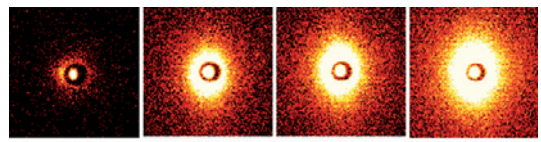

Fig. 3 The two-dimensional anisotropic SAXS scattering pattern obtained from chains of 4CEC-Lp particles initially dispersed in silicone oil, in the presence of a DC external electric field of magnitude equal to (a) 0 kV/mm, no chain, isotropic scattering pattern; (b) 1 kV/mm, (c) 2kV/mm, (d) 3kV/mm, strong chain, strong anisotropic scattering pattern.

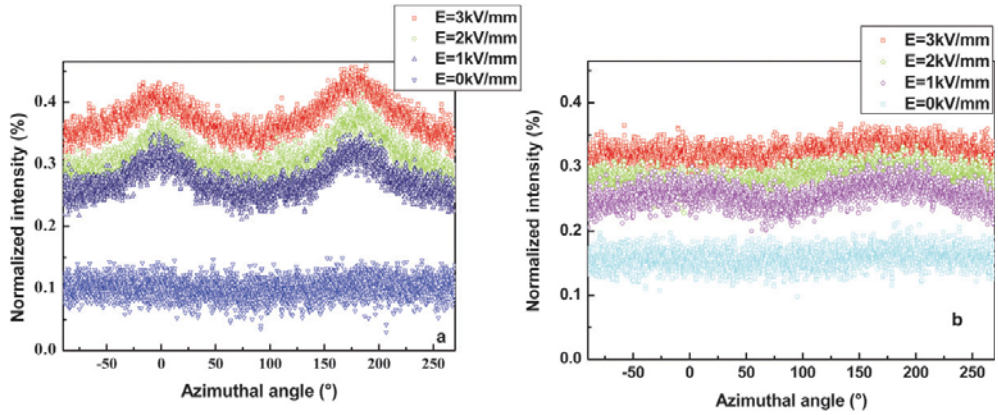

Fig. 4 Dependence of the intensity of circular scattering rings on the azimuthal angle Φ at the different electric field: (a) 4CEC-Lp; (b) 0.5CEC-Lp.

is isotropic. For $E = 1$, 2, 3 kV/mm, respectively, the azimuthal positions of the maxima along the plots in Fig. 4 demonstrate that the preferred orientation of the organic modified laponite nanoparticles is with the lamellar stacking plane parallel to the direction of the electric field. The anisotropic maxima intensities are also increased with the enhancement of electric field.

Laponite is a synthetic trioctahedral 2:1 layered silicate. In aqueous solutions, water molecules are intercalated into the interlamellar space of laponite, leading to an expansion of the mineral due to the hydration of the metal ions. The ions can be thus replaced by other cations by simple ion exchange reactions. The wide angle X-ray diffraction (WAXS) patterns of Na-laponite and a series of CTAB-exchanged laponites are plotted in Fig. 5. A broad peak attributable to a low degree of ordering is observed for pure laponite ($d_{001} = 12.5$ Å, $d = 2\pi/q$). The diffraction peak was shifted to a lower angle after ion exchange, indicating an increase of the interlayer distance of the clay sheets of 2 Å for the different CTAB concentrations. Similar variations of the basal spacing for different organic loadings are observed ($d_{001} = 14.5$ Å). The swell interlayer was attributed to the formation of single-layer complexes, with the alkyl chains being oriented parallel to the clay sheets. In the low scattering vector range, the intensity of the curve is moved towards the pure CTAB curve with the enhancement of CTAB concentration which means that more CTAB is adsorbed on the surface of laponite. The slope of −2 is typical for scattering from a randomly particles.

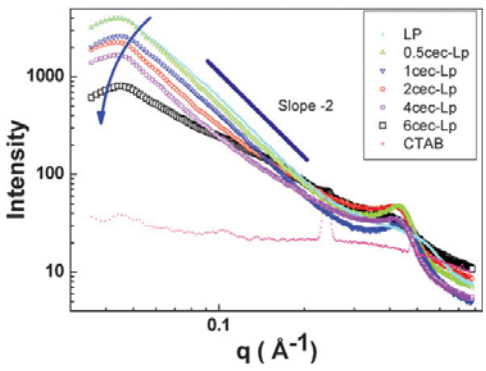

Fig. 5 The WAXS data of laponite and CTAB-exchanged laponite powders.

3.3. AFM, SEM, TEM study

The pure laponite particles, due to their hydrophilic properties, easily aggregate and the aggregate size distribution is polydisperse, from hundreds of nanometers to near tens of micrometers (shown in Fig. 6a). At low concentrations of CTAB substitution (0.5CEC or 1CEC), CTAB intercalates into the laponite interlayer after the ion exchange reaction, which only increases the hydrophobic properties of the laponite interlayer, whereas the particle surface of laponite is still hydrophilic. This can lead to the aggregation of 0.5CEC-Lp particles due to the heat treatment during the synthesis, so the aggregate size distribution of intercalated sample 0.5CEC-Lp is also polydisperse and can not be decreased compared with that of pure laponite (shown in Fig. 6b). However at higher concentrations of CTAB substitution (4CEC or 6CEC), the CTAB surfactant is not only intercalated into the interlayer of laponite, but also adsorbed on the surface of laponite stacks. So both the interlayer surface and the particle surface of laponite are modified from hydrophilic to hydrophobic. The hydrophobic tails of CTAB molecules adsorbed onto the surface of laponite can prevent the aggregation of particles during heat treatment procedures. Through organic modification at very high concentrations of CTAB substitution, smaller aggregate sizes and narrow size distribution can be obtained for the sample of 4CEC-Lp (shown as Fig. 6c and d). The aggregate size of 4CEC-Lp particles is around 200–400nm.

SEM images of pure laponite (a), 0.5CEC-Lp (b) and 4CEC-Lp (c) particles are shown in Fig. 7. From these images, we can see that for the samples of pure laponite and 0.5CEC-Lp, their aggregate sizes are very large and the aggregate size distribution is polydisperse, from hundreds of nanometers to a few tens of micrometers due to their surface hydrophilic properties. However through organic modification at high concentration of CTAB, smaller aggregate sizes and narrow size distribution can

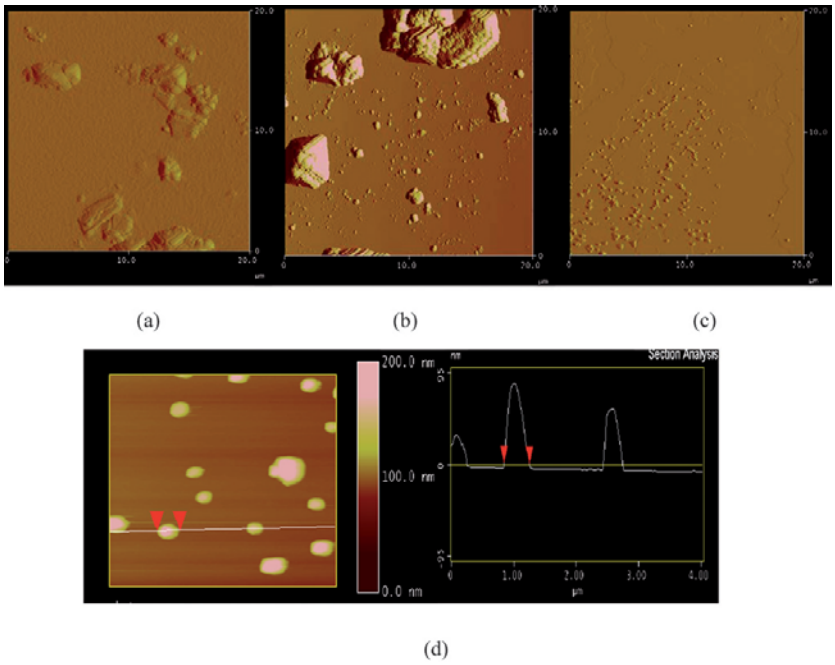

Fig. 6 AFM deflection images for different samples: a) laponite; b) 0.5CEC-Lp; c) 4CEC-Lp. d) Section analysis of 4CEC-Lp particles: size distribution 200–400nm; scale 4 × 4 μm.

be obtained for the sample of 4CEC-Lp. From Fig. 7(c), smaller particles (from 200nm to 400nm) with a narrow size distribution can be found. Furthermore, typical transmission electron microscopy (TEM) measurement was employed to demonstrate the nanostructure of 4CEC-Lp particles. At low magnification (Fig. 8a), dark particles around few hundreds nanometer can be found. At high magnification (Fig. 8b), smaller size particles (about 30nm) can be seen. Laponite, as a synthetic clay, consists of disc-like particles with a thickness of 1 nm and an average diameter of 30 nm. So in this case, single crystals of laponite are observed in the sample of 4CEC-Lp and these single crystals aggregate together to form the particles. The ions play an important role in the ER effect. Ions not only can increase the conductivity, but also can enhance the polarization ability of particles. All these can enhance the ER effect effectively. Energy dispersive spectroscopy (EDS) was employed to determine the elemental compositions of different samples and the results are shown in Fig. 9. From Fig. 9, we can see that for pure laponite, Na, Mg, Si etc. elements are observed from the EDS pattern. However, for 1CEC-Lp and 4CEC-Lp, C, Mg, Si etc. elements are observed and elemental Na is not observed for these modified samples. So this may mean that Na^+ which originally existed in the interlayer of laponite can be fully exchanged in the modified laponite, both for 4CEC-Lp and for 1CEC-Lp.

3.4. ER effect

Flow curves were measured using the CSR mode for CTAB modified laponite ERFs under different electric field strengths, as shown in Fig. 10. In the absence of an electric field, the ERF behaves as a Newtonian fluid, whose shear stress increases linearly with shear rate. When a DC electric field is applied, as the shear rate increases, the behaviour of shear stress only decreases slightly even at very high shear rate and shows Bingham fluid behaviour, which is the typical rheological characteristic of ERFs.[33–36] This behaviour is described by the Bingham fluid model,

$$\begin{cases} \tau = \tau_y + \eta\dot{\gamma} & \text{if } \tau \geq \tau_y \\ \dot{\gamma} = 0 & \text{if } \tau < \tau_y \end{cases} \quad (1)$$

Here, τ_y is the yield stress and is a function of an electric field strength, τ is the shear stress, $\dot{\gamma}$ is the shear rate, and η is the shear viscosity. From Fig. 10, we can see that the 4CEC-Lp suspension (Fig. 10a) shows more pronounced ER properties than 0.5CEC-Lp (Fig. 10b) in the same range of shear rate. The ER efficiency $((\tau_E - \tau_0)/\tau_0$, where τ_0 is the shear stress without electric field and τ_E is the shear stress with electric field) is close to 150 and 29 (3.5kV/mm) at a shear rate of $10s^{-1}$ for the 4CEC-Lp and 0.5CEC-Lp ER suspensions respectively. Under application of a sufficiently large electric field, ER fluids show well-defined yield stresses, beyond which they tend to be shear-thinning. At low shear rate, the suspensions exhibit a dynamic yield stress that increases with the electric field; the typical shear behaviour of an ER fluid under these conditions is most often characterized as a Bingham-like solid given by the expression (1). In Fig. 10d, a simple Bingham model has been fitted to the data of 4CEC-Lp ER fluid. The leaking current density for the 4CEC-Lp ER fluids

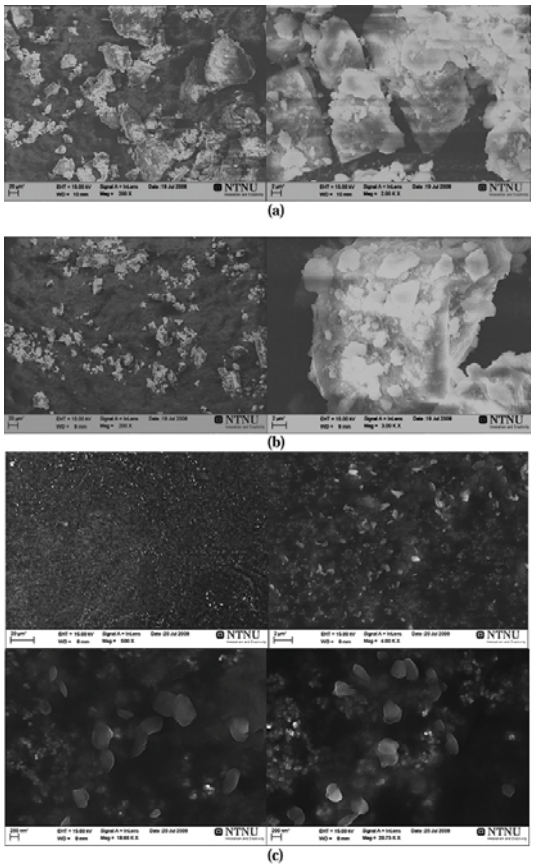

Fig. 7 SEM images of pure laponite (a), 0.5CEC-Lp (b) and 4CEC-Lp (c) particles.

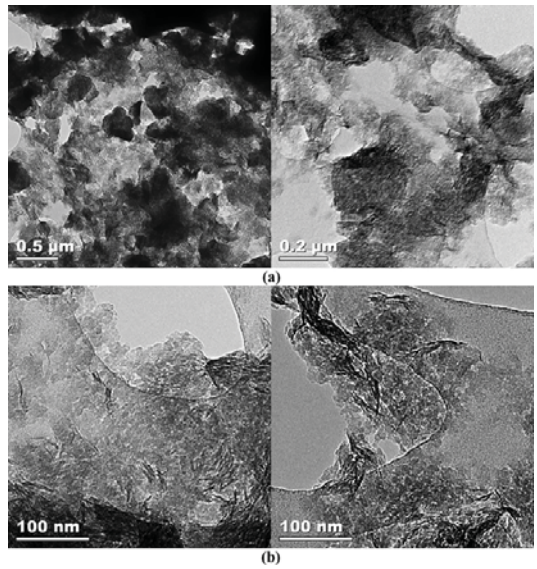

Fig. 8 TEM images of 4CEC-Lp particles.

was measured at different electric field strengths (see Table 1). The leaking currents are useful to judge the potential applications of ER fluids. Smaller leaking currents mean smaller energy consumption and more safety for the application. It is known that the rheological behaviour of an ER suspension is the result of a change of fibrous-like structures. This structure change is mainly dominated by the electric-field induced electrostatic interaction and the shear-field-induced hydrodynamic force. Large polarizability and sufficient polarization response of ER particles are important to produce stronger and faster electrostatic interactions that can maintain structures and rheological properties stable under shear flow. As we increase the shear rate, the fibrillar structure of particles aligned in the applied electric field direction is distorted and destroyed. However, the shear stress remains approximately constant (plateau region) as the shear rate is increased, where the electrostatic force still dominates to form the chain structure.[37,38] The stable shear stress level for the 4CEC-Lp organoclay ERF means that the electrostatic interaction and the polarization response are still dominating even if the shear rate is increased, and thus, particles make fibrous structures fast enough to maintain the structure under shear flow. In the present work, it can be seen that the ER effect has a strong dependence on the CEC substitution, which is associated closely with the state of intercalation and adsorption. For the sample of 4CEC-Lp, CTAB surfactant is not only intercalated into the interlayer of laponite, but also adsorbed on the surface of laponite stacks. So both interlayer surface and particle surface are modified. However for high CEC substitution, such as 5CEC-Lp and 6CEC-Lp, dissociative or separated CTAB should appeared. So the ER effect of mixtures of laponite and CTAB was investigated to reflect the influence of dissociative or separated CTAB. Different mixtures of laponite and CTAB ($Weight_{laponite}$:$Weight_{CTAB}$ adopted as 7:3, 8:2, 9:1) were prepared and dispersed into silicone oil at a weight fraction of 10%. Fig.10 c shows the shear stress of mixtures of laponite and CTAB (10wt% in silicone oil) ERF as a function of shear rate under various electric fields. The ER efficiency $(\tau_E - \tau_0)/\tau_0$ is close to 50, 58, and 63 (3.5kV/mm) at a shear rate of $10s^{-1}$ for the mixtures of laponite and CTAB (7:3, 8:2, 9:1, respectively) ERFs. These values are lower compared with that (150) of 4CEC-Lp ERF. This means that dissociative or separated CTAB are not beneficial for the enhancement of ER effect. In our samples, suitable adsorption of CTAB on laponite surface may cause strong surface polarization, which may increase the ER activity. This result of mixtures of laponite and CTAB can further explain that the ER effect has a strong dependence on the CEC substitution and why high CEC substitution (5CEC and 6CEC) can decrease the ER effect. The Bingham fluid model has often been used for the prediction of ER dynamic. The Bingham flow exhibits a non-vanishing yield stress, which is defined as a stress where the suspension behavior changes from solid-like to fluid-like at a zero shear rate limit. While the Bingham model clearly captures an essential element of the ER dynamic, it fails to account for the often-observed shear-thinning behavior and

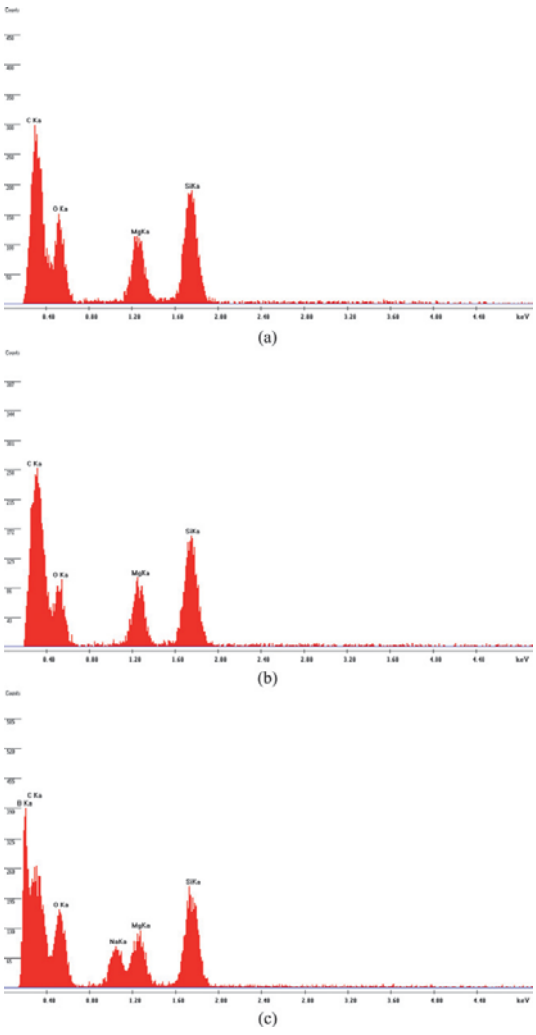

Fig. 9 EDS patterns of 4CEC-Lp (a), 1CEC-Lp (b) and pure laponite (c) particles.

other behavior like the decrease of shear stress in the low shear rate region.[39,40] Recently, the Cho–Choi–Jhon model was proposed for the ER fluids especially useful in the low shear rate.[40,41]

$$\tau = \frac{\tau_y}{1 + (t_2\dot{\gamma})^{\alpha}} + \eta_\infty\left(1 + \frac{1}{(t_3\dot{\gamma})^{\beta}}\right)\dot{\gamma} \qquad (2)$$

Here, τ_y is the dynamic yield stress defined as the extrapolated stress from low shear rate region, α is related to the decrease in the stress, t_2 and t_3 are time constants, and η_∞ is the viscosity at a high shear rate and is interpreted as the viscosity in the absence of an electric field. The exponent β has the range $0 < \beta < 1$, since $d\tau/d\dot{\gamma} \geq 0$. The flow curves of the 0.5 and 1.0kV/mm, shown in Fig. 10(c), have been fitted with the Cho–Choi–Jhon model, see Fig. 10(e). The results show that this model is useful especially for the decrease of shear stress in the low shear rate region and fits the flow curves more accurately than the Bingham model.

Fig.11 shows the yield stress of 4CEC-Lp ERFs as a function of electric field strength using the CSS mode. One of the most common ways of measuring the yield stress of ER fluids is to apply an increasing shear stress to the sample initially at rest, and observe at which stress the fluid starts to flow. The maximum stress that makes ER fluid start to flow is named yield stress. The yield stress of 4CEC-Lp measured by the CSS mode is 375Pa at E = 3.5kV/mm (10wt%) and its evident yield point is shown by arrows.

Theoretically the yield stress is defined to be the stress at which the fluid starts/stops flowing, *i.e.* where the viscosity changes between being finite and infinite. To determine the yield stress experimentally has proven to be very difficult. Different values for the yield stress have been obtained depending on which geometry and experimental procedure used. As well as the CSS mode, the yield stress of the 4CEC-Lp suspensions under application of an electric field was also measured using the bifurcation procedure described by Bonn *et al.*, which may be considered as a more precise method to determine the yield stress of ER fluids.[42–44] This method has given reproducible results for the "true" yield stress for different systems, *e.g.* gels and clay suspensions. It also is a novel method for measuring yield stresses of ER fluids. Each sample is first pre-sheared at a constant shear rate $\dot{\gamma} = 100\ s^{-1}$ for 200 s, and this is done to makes sure that all samples have the same initial condition (shear history). Then the electric field was applied and the suspension was sheared at a constant shear stress for 300 s while observing the viscosity change with time. The viscosity of the sample either went directly to high viscosity or toward a low constant viscosity, depending on the magnitude of the applied shear stress. Since the electric field was applied to the sample when it is sheared, chain- and column-like particle structures are formed across the gap in the cylinder. These structures have to be broken down in order for the ER fluid to start flowing, so this procedure is somewhat analogous to the static yield stress. For shear stresses smaller than the yield point we can see a yield change in the viscosity over time.

When we shear the sample at a constant low shear stress, the viscosity immediately becomes high due to the formation of column-like structures in the direction of the electric field. While increasing the shear stress the gradual build-up in the viscosity to high levels takes longer and longer. At a certain shear stress, depending on the organoclay concentration in the sample and the electric field strength, the viscosity does not increase during the shearing. For shear stresses higher than the yield point we can see a decrease in the viscosity over the time period. So a gradual transition between the two states for stresses around a critical shear stress is observed. Fig. 12 shows the viscosity as a function of time for a 4CEC-Lp ER suspension of particle weight fraction 10% at E = 1kV/mm sheared at different shear stresses. The bifurcation in the rheological behaviour is evident. For shear stresses slightly lower than the critical stress, the sample shows a gradual build-up in the viscosity, suddenly going to high viscosity. At applied shear stresses slightly above the critical shear stress the viscosity is almost constant over the whole time period. At an applied stress corresponding to 66Pa the viscosity

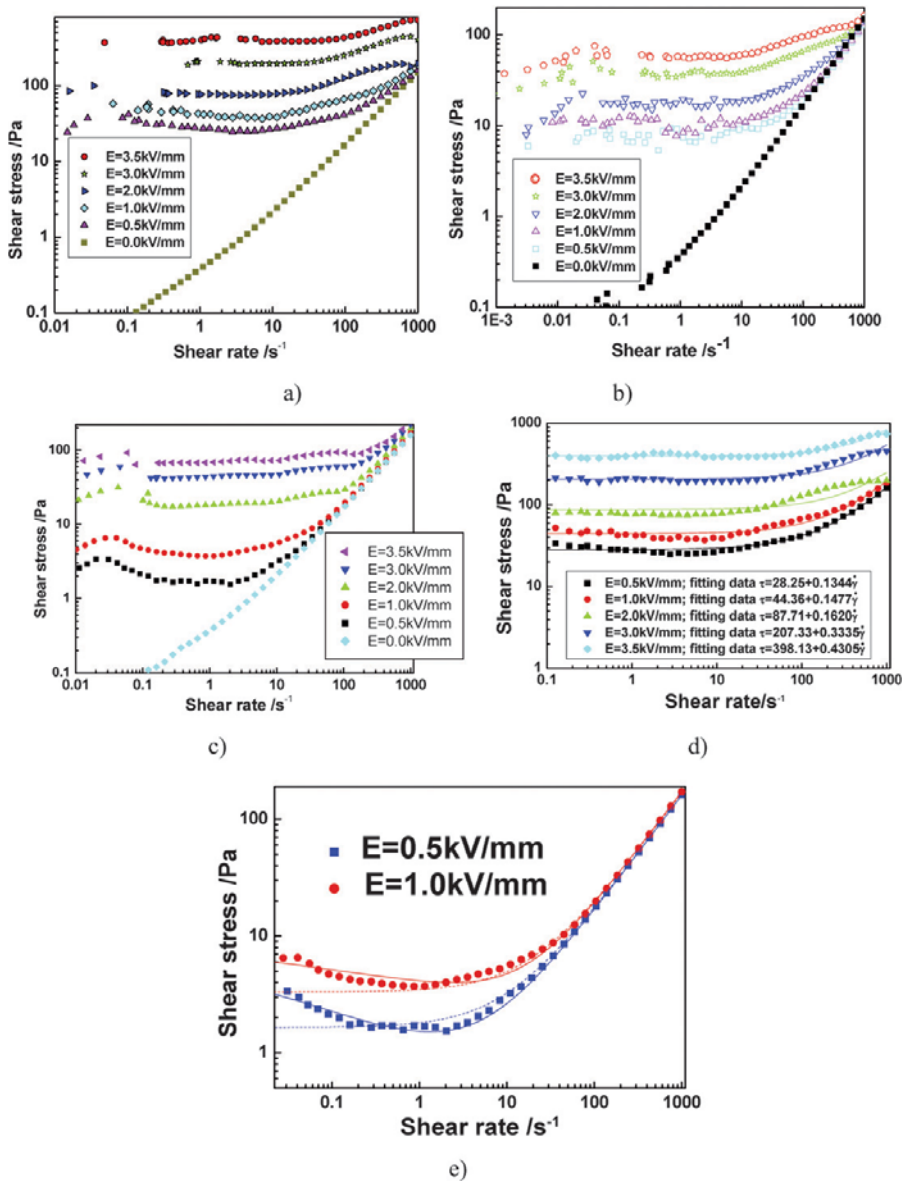

Fig. 10 Shear stress of different CTAB modified laponite (10wt% in silicone oil) ERFs as a function of shear rate under various electric fields: a) 4CEC-Lp, b) 0.5CEC-Lp. c) mixture of laponites and CTAB ($Weight_{laponite}$:$Weight_{CTAB}$ = 7:3), d) Fitting of the data of Fig. 10(a) using the Bingham model under different electric field strengths. The fully drawn line represents the fitting curves of the Bingham model. e) Fitting of the data of (c) using the Bingham model (dashed line) and the Cho–Choi–Jhon model (solid line) under E = 0.5 and 1.0kV/mm.

Table 1 The leaking currents of the 4CEC-Lp ER fluid under different electric field strengths

Electric field strength (kV/mm)	0.5	1	2	3	3.5
Leaking current density (μA/cm^2)	1	2	4	10	18

does not diverge before about 150 seconds. At 67.5 Pa the viscosity curve has completely changed its shape: instead of increasing toward high viscosity it is almost constant or slightly decreasing during the time of shearing. For this test, the critical yield stress is precisely determined between 66 Pa and 67.5 Pa. This bifurcation shear stress is taken to be the yield stress of the

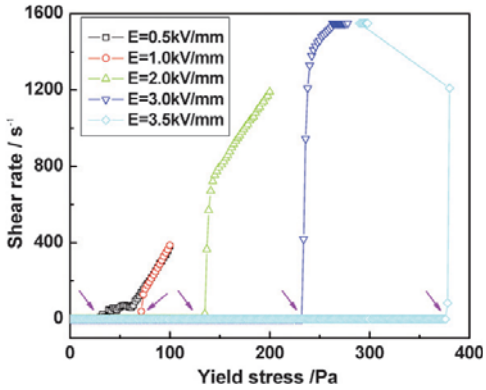

Fig. 11 The yield stress of 4CEC-Lp ERFs as a function of the electric field strength, the yield point is shown by arrows.

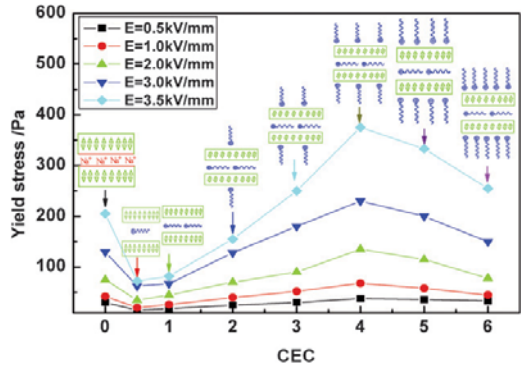

Fig. 13 The yield stress of ERFs as a function of CEC value, the inserts indicate the different intercalation and adsorption states of CTAB modified laponites.

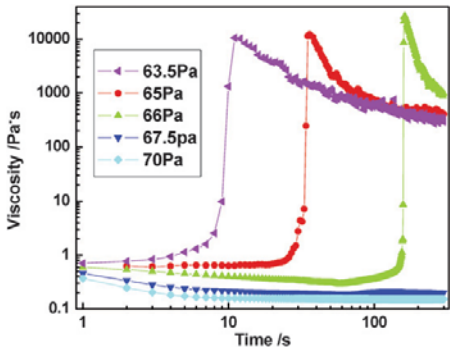

Fig. 12 Viscosity as a function of time for a 4CEC-Lp suspension of particle weight fraction 10% under E = 1 kV/mm.

sample and the value is also similar to that measured by the CSS mode.

Fig.13 shows the yield stresses of different CTAB modified laponite ERFs as a function of CEC value based on the CSS mode. The inserts also indicate the schematic explanation for the different intercalation and adsorption states of CTAB modified laponites. It can be seen that the ER effect has a strong dependence on the CEC, which is associated closely with the state of intercalation and adsorption. With the decrease of aggregate size, the ER effect is increased: Smaller size can induce better ER effect. The effect of the organo-modification is to increase the platelet–platelet separation, decrease the interlayer attraction and make the clay more compatible with the organic host (such as polymer). Intercalation can change the hydrophilic environment of the clay interlayer. Furthermore, the adsorption of surfactant on the surface of the clay nanolayer may increase the hydrophobicity. The hydrophobic tail of the surfactant on the surface of the laponite nanoplatelet can enhance the wettability towards silicone oil and achieve good oleophilicity. However more adsorption of CTAB surfactant on the clay surface can also decrease the ER effect, so suitable organo-modification should be chosen. Here we provide new evidence for the change of wettability. A liquid–liquid phase transfer can verify the change of hydrophilicity of laponite to hydrophobicity of CTAB modified laponite (Fig. S3†). After phase transfer, a 4CEC-Lp organoclay/silicone oil suspension can be obtained from the upper phase by separating the two phases successfully. Meanwhile pure laponite aqueous solution is also used for phase transfer, but no laponite particles can be transferred into the silicone oil. From pure laponite to CTAB modified laponite the wettability of the clay is changed from hydrophilic to hydrophobic, and only CTAB modified laponite can be successfully transferred from the aqueous phase to the organic phase (silicone oil) due to the change of wettability. Pure laponite could not transfer from the aqueous phase to the organic phase due to its hydrophilicity. This new evidence can verify the change of hydrophilicity to hydrophobicity. In recent research, a new type of ER fluid with the giant electrorheological (GER) effect was discovered. The GER fluids consist of coated nanoparticles ($BaTiO(C_2O_4)_2$ + NH_2CONH_2) suspended in silicone oil. In the core/shell structure, the urea coating serves as an ER promoter. Although the dielectric constant of bulk urea is relatively small (about 3.5), urea in the form of thin coatings has a significantly larger dielectric response due to the existence of interfaces that cause saturation surface polarization, which are responsible for the observed GER effect.[4,45,46] In our samples, suitable adsorption of CTAB on laponite surface may also cause strong surface polarization, which may increase the ER activity, thus the effects of enhanced yield stress that we observe (at 4CEC in Fig. 13) could possibly be due to the same mechanism as is responsible for the GER effect. The change of wettability reflects the surface properties of particles, the intrinsic reason for the enhancement of the ER effect is associated with the dielectric properties.

Here, by investigating the dielectric properties of a series of CTAB modified laponite ER suspensions, we find a significant influence of CTAB modification on the dielectric properties of laponite. These improvements in dielectric properties by modifying the internal structure of laponite were responsible for the improvement of the ER properties. The dielectric properties, such as dielectric constant (ε), conductivity (σ) and dielectric loss ($\tan\delta$), play an important role for high performance ER materials. The dielectric constant is connected to the polar strength,

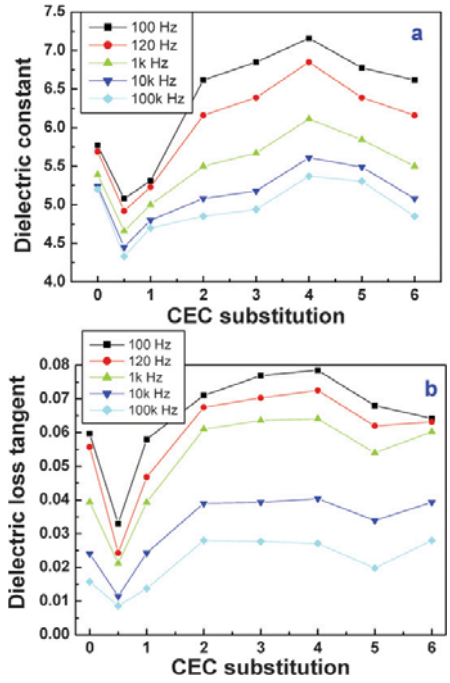

Fig. 14 Dielectric constant and loss tangent of CTAB modified laponite (10wt% in silicone oil) ERFs with different CEC substitutions at five frequencies: 100Hz, 120Hz, 1kHz, 10kHz and 100kHz.

but dielectric loss and conductivity are associated with stability of polar response and steady ER effects between particles. Fig. 14 shows the typical measured dielectric constant and loss tangent of CTAB modified laponite (10wt% in silicone oil) ERFs with different CEC substitutions at five frequencies: 100, 120, 1k, 10k and 100kHz. It is found that the CTAB modification not only increases dielectric loss but also increases dielectric constant at low frequency. Interestingly, there is also a regular change in dielectric constant and loss tangent with the change of CTAB substitution compared with the rheological properties. The dielectric constant and loss tangent initially increase with CTAB substitution but decline when the CEC substitution is beyond 4CEC, at which point dissociative CTAB separation may appear. According to the dielectric mismatch theory, the static force between particles is in direct proportion to the dielectric mismatch coefficient β (eqn. (3)):

$$\beta = (\varepsilon_p - \varepsilon_f)/(\varepsilon_p + 2\varepsilon_f) \quad (3)$$

where ε_P and ε_f are the bulk dielectric constants of the particles and oil respectively. Therefore, a large β value is required to enhance the mechanical strength of the ER fluid. The larger the β value of the particles, the better the ER effect. A large increase of ε as the frequency decreases ($\Delta\varepsilon = \varepsilon_{100} - \varepsilon_{100k}$) and enhancement of dielectric loss are observed, which reflects that CTAB modification increases the proportion of slow polarization, especially the interfacial polarization. This is expected to induce strong ER activity according to the present ER mechanisms. According to the widely accepted studies, not only large polarization ability relating to high dielectric constant but also good polarization response and stability relating to suitable loss factor or loss tangent ($\tan\delta > 0.1$ at 10^3 Hz) or conductivity (10^{-7}–10^{-8} S/m) mainly dominate the high ER effect. Comparing the dielectric properties with the rheological properties, we can consider that the improvement of dielectric properties due to CTAB modification is responsible for the enhancement of the ER activity of laponite. Furthermore, recent studies have shown that smaller size and narrow size distribution can increase the ER effect markedly.[20,46] For example, a comparison of the measured yield stress for two samples consisting of two different particle sizes was made. One example is $BaTiO(C_2O_4)_2$ nanoparticles (particle size around 50nm) suspended in silicone oil. Another one is Rb-doped $BaTiO(C_2O_4)_2$ nanoparticles (particle size around 20nm) suspended in silicone oil. It is observed that the Rb-doped nanoparticle ER fluids exhibit very strong yield stress—up to 250 kPa at 5 kV/mm compared with 120kPa at 5 kV/mm for pure $BaTiO(C_2O_4)_2$ nanoparticle ERFs. Thus particles about 1/2 the size led to a doubling of the maximum attainable yield stress.[2,20,45] Similarly, for series modified titanium oxide nanoparticles, it was also found that the smaller particle size can lead to an improved wettability and higher ER activity. However for both of these samples, the change of yield stress can be attributed to the improvement in the dielectric properties.[47] In this study, the change of yield stress can be attributed to the improvement in the dielectric properties that showed an increase in the dielectric constant and the dielectric loss at low frequency and their regular optimum change with CTAB modification. Only when organic modification or the change of the particle size distribution can enhance the dielectric properties of particles, can the ER effect (include yield stress) be increased. When organic modification or the change of the particle size distribution decrease the dielectric properties of particles, the ER effect (include yield stress) should be decreased. For example, at high concentration of CTAB substitution (5CEC or 6CEC), smaller aggregate sizes and narrow size distribution of particles can also be obtained, however the yield stress is decreased compared with that of 4CEC-Lp ER fluid. This is caused by the decrease of dielectric properties of 6CEC-Lp ER fluid compared with those of 4CEC-Lp ER fluid, so suitable organo-modification should be chosen. The particle size distribution effect on the variance of yield stress only happens when the dielectric properties of particles can be varied by the change of particle size distribution.

Dynamic oscillation tests were used to study the viscoelastic properties of organic modified laponite based ER suspensions under various electric fields. Fig. 15a shows a log-log plot of the storage modulus G' for the 4CEC-Lp particle based ER fluid as a function of strain γ at a fixed angular frequency $\omega = 10$ rad/s under various electric fields. It is seen that G' increases with the electric field and the linear viscoelastic region becomes wider because the chain structure formed in the ER fluid becomes stronger to sustain larger strains. As the strain is increased, the deformation starts to break the chain and G' decreases rapidly. Fig. 15b shows a log-log plot of storage modulus G' for the 4CEC-Lp particle based ER fluids as a function of frequency with a fixed strain of 0.01 in the linear viscoelastic region. The storage modulus was slightly increased as the frequency was

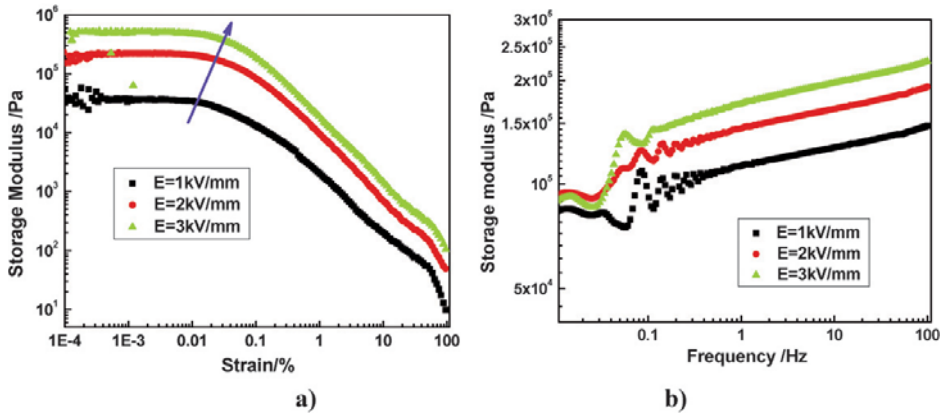

Fig. 15 a) Strain amplitude versus dynamic moduli at a fixed angular frequency $\omega = 10$ rad/s under various electric field strengths; b) frequency f versus dynamic moduli under different electric field using a strain of 0.01.

increased up to 100 Hz. The linear viscoelastic region shows a wider region and higher G' with induced high electric field strength. This phenomenon was also observed in cross-linked rubbers and other ER systems.[37] The inter-particle interactions due to polarization contribute to the enhancement of the dynamic modulus and the steady shear viscosity to a great extent. The polarization forces between the particles increase with increasing electric field strength resulting from increasing particle chain length and magnitude of G'.

3.5. The sedimentation properties of ER suspensions

One of the greatest challenges for applications of ER fluids is the problem of particle sedimentation. The sedimentation properties of ER materials are the main criterion used to evaluate whether the materials can be commercialized or not, because the properties of ERF will weaken rapidly along with the sedimentation of the particle phase. The general methods to enhance the anti-sedimentation of ERFs include controlling the size of particles (nanoparticles, nanorods, nanofibers, nanotubes etc.), preparing hollow or porous particles, changing the match of density between particles and oil, adding surfactant etc. Fig. 16 show ER suspensions of 6CEC-Lp, 4CEC-Lp, 0.5CEC-Lp, and pure laponite, which were deposited for a month. The results show that the antisedimentation of 6CEC-Lp or 4CEC-Lp is better than those of 0.5CEC-Lp or pure laponite. Furthermore, ER suspensions of the former also easily adhered to the bottle wall unlike the latter. Due to the change of wettability, surface modified laponite clay is lipophilic and thus disperses much easier in oil than pure laponite.

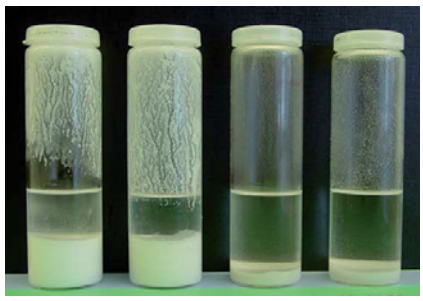

Fig. 16 The sedimentation state of ER suspensions for 6CEC-Lp, 4CEC-Lp, 0.5CEC-Lp and Lp (from left to right); they were all at 10wt% and deposited for a month.

4. Conclusions

A seriaes of CTAB modified nanolayer laponite samples have been synthesized by an ion exchange method. The resulting materials show different structures and surface properties compared to pure laponite. Through suitable organo-modification, near monodisperse organic modified laponite can be made and characterized *via* AFM and SEM measurements. WAXS and TGA results show that CTAB can be intercalated and adsorbed onto the laponite interlayer or surface depending on the concentration of the surfactant. Two-dimensional SAXS images from bundles of 4CEC-Lp ER sample exhibit a clear anisotropy. The modified laponite ER fluids exhibit improved sedimentation properties. Furthermore, one application of such systems of functionalized laponite particles could be in guided self-assembly or orientation of nanoparticles in composite materials, especially for hydrophobic polymer matrices.

Acknowledgements

This work was supported by the Research Council of Norway (RCN) through the NANOMAT Program and the FRINAT Program. The authors also acknowledge the help of Dr Yingda Yu for the SEM and TEM measurements.

References

1 T. C. Halsay, *Science*, 1992, **258**, 761–766.
2 W. J. Wen, X. X. Huang, S. H. Yang, K. Q. Lu and P. Sheng, *Nature Mater.*, 2003, **2**, 727–730.
3 D. Gamota and F. E. Filisko, *J. Rheol.*, 1991, **35**, 399–415.

4 D. J. Klingenberg and C. F. Zukoki, *Langmuir*, 1990, **6**, 15–24.
5 H. Block and J. P. Kelly, *J. Phys. D: Appl. Phys.*, 1988, **21**, 1661–1677.
6 T. Hao, *Adv. Mater.*, 2001, **13**(24), 1847–1857.
7 M. Parthasarathy and D. J. Klingenberg, *Mater Sci. Eng. R*, 1996, **17**(2), 57–103.
8 R. Tao and J. M. Sun, *Phys. Rev. Lett.*, 1991, **67**(3), 398–401.
9 I. S. Sim, J. W. Kim, H. J. Choi, C. A. Kim and M. S. Jhon, *Chem. Mater.*, 2001, **13**, 1243–1247.
10 Y. H. Hyun, S. T. Lim, H. J. Choi and M. S. Jhon, *Macromolecules*, 2001, **34**(23), 8084–8093; H. J. Jin, H. J. Choi, S. H. Yoon, S. J. Myung and S. E. Shim, *Chem. Mater*, 2005, **17**(16), 4034–4037; J. W. Kim, S. G. Kim, H. J. Choi and M. S. Jhon, *Macromol. Rapid Comm.*, 1999, **20**(8), 450–452.
11 J. G. Cao, J. P. Huang and L. W. Zhou, *J. Phys. Chem. B.*, 2006, **110**(24), 11635–11639.
12 T. Hao, A. Kawai and F. Ikazaki, *Langmuir*, 2000, **16**, 3058–3066; T. Hao, A. Kawai and F. Ikazaki, *Langmuir*, 1998, **14**, 1256–1262; T. Hao, A. Kawai and F. Ikazaki, *Langmuir*, 1999, **15**, 918–921.
13 J. O. Fossum, Y. Méheust, K. P. S. Parmar, K. D. Knudsen, K. J. Maløy and D. M. Fonseca, *Europhys. Lett.*, 2006, **74**(3), 438–444.
14 A. Lengalova, V. Pavlinek, P. Saha, O. Quadrat, T. Kitano and J. Steiskal, *Eur. Polym. J.*, 2003, **39**(4), 641–645.
15 M. J. Espin, A. V. Delgado and J. Plocharski, *Langmuir*, 2005, **21**(11), 4896–4903.
16 J. B. Yin and X. P. Zhao, *Chem. Mater.*, 2002, **14**, 4633–4640.
17 B. X. Wang and X. P. Zhao, *Langmuir*, 2005, **21**, 6553–6559.
18 X. P. Zhao and J. B. Yin, *Chem. Mater.*, 2002, **14**, 2258–2263.
19 B. X. Wang and X. P. Zhao, *Adv. Funct. Mater.*, 2005, **15**, 1815–1820.
20 (*a*) W. J. Wen, X. X. Huang and P. Sheng, *Soft Matter*, 2008, **4**(2), 200–210; (*b*) W. J. Wen, X. X. Huang and P. Sheng, *Appl. Phys. Lett.*, 2004, **85**, 299–301; (*c*) C. Shen, W. J. Wen, S. H. Yang and P. Sheng, *J. Appl. Phys.*, 2006, **99**(10), 106104.
21 Z. N. Fang, H. T. Xue, W. Bao, J. P. Huang and L. W. Zhou, *Chem. Phys. Lett.*, 2007, **441**, 314–317.
22 A. B. Bourlinos, S. R. Chowdhury, D. D. Jiang, Y. U. An, Q. Zhang, L. A. Archer and E. P. Giannelis, *Small*, 2005, **1**(1), 80–82.
23 J. W. Gilman, C. L. Jackson, A. B. Morgan, R. Harris, E. Manias, E. P. Giannelis, M. Wuthenow, D. Hilton and S. H. Phillips, *Chem. Mater.*, 2000, **12**(7), 1866–1873.
24 E. P. Giannelis, *Adv. Mater.*, 1996, **8**(1), 29–35.
25 Y. Fujimoto, A. Shimojima and K. Kuroda, *Chem. Mater.*, 2003, **15**(25), 4768–4774.
26 A. Shimojima and K. Kuroda, *Angew. Chem. Int. Edit.*, 2003, **42**(34), 4057–4060.
27 A. Shimojima, N. Umeda and K. Kuroda, *Chem. Mater.*, 2001, **13**(10), 3610–3616.
28 E. N. De Azevedo, M. Engelsberg, J. O. Fossum and R. E. De Souza, *Langmuir*, 2007, **23**(9), 5100–5105; G. J. Da Silva, J. O. Fossum, E. DiMasi and K. J. Maloy, *Phys. Rev. B*, 2003, **67**(9), 094114.
29 Q. Zhou, H. P. He, R. L. Frost and Y. F. Xi, *J. Phys. Chem. C*, 2007, **111**(20), 7487–7493; Q. Zhou, R. L. Frost, H. P. He, Y. F. Xi and L. W. Liu, *J. Colloid Interf. Sci.*, 2007, **307**(2), 357–363.
30 Y. F. Xi, R. L. Frost and H. P. He, *J. Colloid Interf. Sci.*, 2007, **305**(1), 150–158; Y. F. Xi, R. L. Frost, H. P. He, J. T. Kloprogge and T. Bostrom, *Langmuir*, 2005, **21**, 8675–8680.
31 H. Heinz, R. A. Vaia, R. Krishnamoorti and B. L. Farmer, *Chem. Mater.*, 2007, **19**(1), 59–68; H. Heinz, H. Koerner, K. L. Anderson, R. A. Vaia and B. L. Farmer, *Chem. Mater.*, 2005, **17**(23), 5658–5669.
32 H. J. M. Hanley, C. D. Muzny, D. L. Ho and C. J. Glinka, *Langmuir*, 2003, **19**, 5575–5580; D. L. Ho, R. M. Briber and C. J. Glinka, *Chem. Mater.*, 2001, **13**, 1923–1931.
33 B. X. Wang and X. P. Zhao, *J. Mater. Chem.*, 2002, **12**(6), 1865–1869; B. X. Wang and X. P. Zhao, *J. Mater. Chem.*, 2002, **12**(10), 2869–2871; B. X. Wang and X. P. Zhao, *J. Mater. Chem.*, 2003, **13**(9), 2248–2253.
34 A. Lengalova, V. Pavlinek, P. Saha, J. Stejskal and O. Quadrat, *J. Colloid Interf. Sci.*, 2003, **258**(1), 174–178.
35 M. J. Espin, A. V. Delgado and F. Gonzalez-Caballero, *Phys. Rev. E*, 2006, **73**(4), 041503; M. J. Espin, A. V. Delgado and J. D. G. Duran, *J. Colloid Interf. Sci.*, 2005, **287**(1), 351–359.
36 A. Krzton-Maziopa, H. Wycislik and J. Plocharski, *J. Rheol.*, 2005, **49**(6), 1177–1192.
37 M. S. Cho, H. J. Choi and W. S. Ahn, *Langmuir*, 2004, **20**, 202–207; M. S. Cho, Y. H. Cho, H. J. Choi and M. S. Jhon, *Langmuir*, 2003, **19**, 5875–5881; J. H. Sung, D. P. Park, B. J. Park, H. J. Choi and M. S. Jhon, *Biomacromolecules*, 2005, **6**(4), 2182–2188.
38 J. B. Yin and X. P. Zhao, *J. Phys. Chem. B*, 2006, **110**(26), 12916–12925.
39 J. W. Zhang, X. Q. Gong, C. Liu, W. J. Wen and P. Sheng, *Phys. Rev. Lett.*, 2008, **101**, 194503.
40 C. H. Hong, H. J. Choi and M. S. Jhon, *Chem. Mater.*, 2006, **18**, 2771–2772.
41 M. S. Cho, H. J. Choi and M. S. Jhon, *Polymer*, 2005, **46**, 11484–11488.
42 P. Coussot, Q. D. Nguyen, H. T. Huynh and D. Bonn, *J. Rheol.*, 2002, **46**, 573–589.
43 P. Coussot, Q. D. Nguyen, H. T. Huynh and D. Bonn, *Phys. Rev. Lett.*, 2002, **88**, 175501.
44 K. P. S. Parmar, Y. Méheust, B. Schjelderupsenand and J. O. Fossum, *Langmuir*, 2008, **24**, 1814–1822.
45 X. X. Huang, W. J. Wen, S. H. Yang and P. Sheng, *Solid State Commun.*, 2006, **139**(11–12), 581–588.
46 X. Q. Gong, J. B. Wu, X. X. Huang, W. J. Wen and P. Sheng, *Nanotechnology*, 2008, **9**(16), 165602.
47 B. X. Wang, X. P. Zhao, Y. Zhao and C. L. Ding, *Compos. Sci. Technol.*, 2007, **67**, 3031–3038; B. X. Wang, Y. Zhao and X. P. Zhao, *Colloid Surface A*, 2007, **295**, 27–33.

Paper IV

E-field Induced Alignment from Organically Modified Fluorohectorite Clay Particles

Z Rozynek, B Wang, J O Fossum and K D Knudsen

Submitted to Eur. Phys. J. E

EPJ manuscript No.
(will be inserted by the editor)

E-field Induced Alignment from Organically Modified Fluorohectorite Clay Particles

Z. Rozynek[1], B. Wang[1,3], J. O. Fossum[1], and K. D. Knudsen[2]

[1] Department of Physics, NTNU, Høgskoleringen 5, NO-7491 Trondheim, Norway

[2] Physics Department, IFE, 2027 Kjeller, Norway

[3] College of Materials Science and Engineering, Qingdao University of Science and Technology, Qingdao 266042, China

Received: date / Revised version: date

Abstract. The electric field induced alignment of organically modified fluorohectorite (Fh) clay particles suspended in silicone oil was studied by means of synchrotron wide angle X-ray scattering (WAXS). This report focuses on the comparison between the anisotropic arrangement of organically modified clay particles and that of their previously studied non-modified counterparts. The degree of anisotropy was quantified by fitting one-dimensional azimuthal WAXS plots to the Maier-Saupe model and the results are expressed in terms of the anti-nematic order parameter S_{an}. It is shown that organic modification results in a better overall alignment of the clay particles, with $S_{an} \sim 0.71$, which is higher than for the non-modified particles, $S_{an} \sim 0.62$. This behaviour is mainly a result of the formation of smaller and more uniform aggregates, in contrast to the large aggregate structures formed by non-modified clay particles. Thermal decomposition temperatures of the surfactant molecules adsorbed on the clay surfaces and those being intercalated between clay crystalline layers were measured by thermal gravimetric analysis (TGA). Zeta potential measurements confirmed the successful modification of clay surfaces. Optical microscopy observations showed that the sedimentation of modified particles was much slower compared to that of non-modified samples. In addition, the electric field dependent yield stress was measured, revealing improvement of the electro-rheological properties for modified clay particles.

1 Introduction

If a clay particle is brought into an electric field it becomes polarized. The electric polarization will induce a moment of force, which tends to orient the particles towards the field direction [1]. This alignment has been observed for many different particles possessing an electric field induced dipole moment, including: carbon-based nanotubes [2] or fibers [3]; non-spherical polystyrene latex particles [4]; doublet-shaped polymeric particles [5]; anisotropic titania particles [6]; and also the clay family of particles such as laponite [7] and synthetic Na-Fh clays [8,9].

The alignment of particles in either solid or liquid matrices is of considerable importance from the point of view of applications. At present, polymers reinforced by nanoscale dispersed organically modified layered silicates are attracting more and more attention because of the unprecedented suite of new and enhanced properties compared with conventional fillers [10]. These layered silicate polymer nanocomposites can attain a great degree of stiffness and strength with substantially less inorganic content than conventional glass- or mineral-reinforced polymers. Furthermore, the presence of the dispersed phase results in additional properties, such as flame retardancy, enhanced barrier properties, increased degradability of biodegradable polymers, as well as ablation resistance, compared to either component [11,12,13]. The use of organoclays as precursors to nanocomposite formation has been extended into various polymer systems including epoxys, polyimides, polystyrene, nitrile rubber and polysiloxanes [14]. These improvements depend heavily on the structure and properties of the organoclays. Hence, understanding the microstructure of the organoclays themselves is essential for many industrial applications.

This report focuses on the comparison between the anisotropic arrangement of organically modified clay particles and that of their non-modified counterparts studied previously [8], with particular attention towards the potential for use of such modified particles in electro-rheological (ER) systems. The layout of the present work is as follows. Firstly, the sample preparation is explained in section 2.1. The thermal decomposition analysis providing information about surfactant adsorption and the nature of intercalation is presented in section 2.2. Zeta potential measurements supporting the conclusions drawn from the TGA (regarding CTAB adsorption) are described in section 2.3. Descriptions of both the WAXS experimental set-up and the anti-nematic geometry are followed by the WAXS investigation of the E-field induced structuring from modified clay particles (section 3.1). Sedimentation tests and the optical microscopy observations of clay particles suspended in both water and silicone oil are given in section 3.2. Finally, the E-field dependent yield stress measured by controlled shear stress rheometry is presented in section 3.3. Conclusions are presented at the end in section 4.

2 Sample preparation and characterization

2.1 Samples

The purchased material for our experiments was synthetic Li-Fh (Corning Inc., New York) from which Na-Fh was prepared according to the ionic exchange procedure for example described in [15]. Na-Fh is a synthetic 2:1 smectite clay having the nominal chemical formula $Na_{0.6}(Mg_{2.4}Li_{0.6})Si_4O_{10}F_2$ per half unit cell, where Na^+ is an interlayer exchangeable cation. Na-Fh has a surface charge of 1.2 e^-/unit cell [16,17] and is a polydispersed clay with platelet diameters ranging from a few hundred nm up to several μm.

The surfactant used (Cethyl Trimethyl Ammonium Bromide, $[CH_3(CH_2)_{15}]NBr(CH_3)_3$, Sigma) was of analytical grade. A silicone oil, Dow Corning 200/100 Fluid (dielectric constant of 2.5, viscosity of 100 mPa.s and specific density of 0.973 g/cm^3 at 25 °C) was used as the suspending liquid. The oil is relatively non-polar and non-conductive, with a DC conductivity of the order of 10^{-12} S/m. For the synthesis of the organoclay oil-based suspension, 100 mL of distilled water and 2.5 g of Na-Fh were mixed, and the solution was stirred and heated to 80 °C. In parallel a second solution with the stoichiometric amount of CTAB (0.43, 0.86, 1.72 g) and 25 mL distilled water was prepared. Both solutions were stirred for 10 h. Finally, the surfactant solution was added carefully to the heated clay solution, resulting in an immediate flocs formation. The mixture obtained was stirred at 80 °C for 24 h and then cooled to room temperature. Subsequently, the liquid-liquid phase transfer method was used to obtain the organoclay/silicone solution, which was prepared as follows: 50 mL of silicone oil was added to the aqueous solution and stirred for 48 h. The mixed solution was then centrifuged 15 min at 4000 rpm to accelerate the phase separation. The organoclay/silicone oil suspension was subsequently collected from the upper phase and heated at 110 °C for 24 h. Figure 1 gives an illustration of the phase transfer from the aqueous phase to the organic phase.

Before the rheology measurements, the electro-rheological suspensions of organoclay in silicone oil was vigorously hand-shaken for ∼1 min and placed in an ultrasonic bath for 3 h and again vigorously shaken for 1 h in an orbital shaker. The obtained organoclay ER suspension were labelled as 1CEC-Fh, 2CEC-Fh, and 4CEC-Fh, where CEC refers to the cation exchange capacity.

2.2 TGA/DTG

Thermal gravimetric analysis (TGA) was performed on a TGA/SDTA851^e instrument (Mettler Toledo AS) under N_2 flow (10 mL/min) with a heating rate of 10 °C/min.

TGA data indicated a mass loss of below 10 wt.% until 200 °C for non-modified Na-Fh (see Figure 2), and this was

attributed to the loss of water from the sample. The dehydroxylation of Na-Fh occurs normally at temperatures higher than 800 °C [18]. For pure CTAB, the complete decomposition took place in the range of 200-400 °C and the maximum peak was at 270 °C (see supporting figure S1). From room temperature to 800 °C, the complete weight loss for different CTAB modified Fh: 1CEC-Fh, 2CEC-Fh, and 4CEC-Fh were 21.2 %, 34.4 %, 51 %, respectively (Figure 2). The weight loss at 800 °C increased with the amount of CTAB substitution, which confirms that the organic content in the clay was effectively proportional to the degree of substitution.

The differential thermogravimetric analysis (DTG) patterns of non-modified and CTAB modified Fh are presented in Figure 3. The Na-Fh showed one major thermal decomposition step at around 90 °C, corresponding to the loss of water, as also shown in connection with Figure 2. For the CTAB modified Fh samples, three DTG steps were observed at about 50-150, 200-300 and 350-450 °C. These are attributed to: the loss of water; the release and loss of the CTAB surfactant molecule adsorbed on the clay external surface; and the decomposition of the surfactant molecule intercalated between the clay sheets, respectively. More specifically, for the 1CEC-Fh, the first DTG peak is observed at 83 °C attributed to the loss of *adsorbed* water. The next peak is found at 140 °C and is assigned to the loss of *bound* water. The third peak, corresponding to the loss of the CTAB surfactant molecules adsorbed on the clay external surface is observed at 270 °C. The last major peak, assigned to the decomposition of the surfactant molecule intercalated between the clay sheets, is observed at 360 °C.

Analogously, for the 2CEC-Fh, a DTG peak attributed to the loss of water is observed at 80 °C. A second peak is observed at 270 °C and is assigned to the loss of the CTAB surfactant molecule adsorbed on the clay external surface. However, the peak related to the decomposition of the surfactant molecule intercalated between the clay sheets is not observed until 430 °C, compared to 270 °C for the pure surfactant. This shows that the CTAB molecules are now bonded strongly in the interlayer of the fluorohectorite.

With an increase of the surfactant substitution, the peak related to the CTAB molecules adsorbed on the clay surface becomes more pronounced, and is the largest for the 4CEC-Fh (see arrow in Figure 3). This clearly indicates that more surfactant molecules are adsorbed on the surface of fluorohectorite clay.

The results described above agrees well with the x-ray diffraction data presented later (section 3.1). The x-ray data show the development of the clay lamellar structure due to increase of the surfactant concentration, which corroborates the information from the TGA/DTG curves.

2.3 Zeta potential measurements

The zeta potential was measured using Malvern Zetasizer Nano-ZS (Malvern Instruments, UK) with a folded capillary cell. Measurements were performed on the non-modified clay suspension as well as one of the organoclay samples (4CEC-Fh). The pH was equal to 9.6±0.3 for both 4CEC-Fh and Na-Fh deionized water solutions (0.1 wt.% clay). The zeta potential value was the average of 2 parallel trials consisting of 4 measurements. Fluorohectorite clay particles carry a net negative charge due to the negative charges on their surfaces dominating over the positive charges at the edges. The zeta potential of non-modified Na-Fh particles is -79.0±1.5 mV, which makes them well dispersed and moderately stable in aqueous medium. With the addition of CTAB (4CEC-Fh), the zeta potential becomes positive +59.0±7.2 mV. This is an indication of the CTAB adsorption on the clay surface, thus the organoclay particles possess a good stability behaviour and can be easily dispersed in silicone oil due to both the strong particle-particle repulsive interactions and the lipophilic nature of the surfactant tail. The values of conductivity for both samples were measured to be: 155±2 μS/cm and 382±6 μS/cm for Na-Fh and 4CEC-Fh, respectively.

3 Results

3.1 WAXS

The wide angle x-ray scattering experiment (WAXS) was carried out at the European Synchrotron Radiation Facility (ESRF) in Grenoble, France. An x-ray beam with a wavelength of 0.72 Å and a 0.3x0.3 mm^2 beam size at the sample was used. The beamline BM01A is equipped with a two-dimensional MAR345 image plate detector with diameter of 345 mm. The experimental set-up is shown in Figure 4a. The custom-made sample cell consisted of an electrically insulating acrylic glass in the form of a cuvette, where the top part is opened for inserting two identical 1 × 1 × 50 mm thick copper electrodes separated by a gap of 1 mm (see [8] for further details).

Prior to the application of the electric field, both non-modified and modified particles were randomly dispersed into the silicone oil. The formation of chain-like structures aligning parallel to the E-field was observed shortly after its application. The 2-D WAXS patterns in Figure 5 are from a suspension, without (left) and with (right) an E-field of 500 V/mm applied, for non-modified (top) and organically modified clay particles (bottom), respectively. The 001 Bragg ring obtained from non-modified particles (here indicated by 001*) lies at q=5.11 nm^{-1}. The corresponding distance $d_{001^*}=2\pi/q$ is close to 1.2 nm when one layer of water is intercalated between silicate sheets [8]. The outer broad ring is located at q=8.3 nm^{-1}, and is due to the silicone oil, i.e. the maximum in the radial distribution function of this molecular liquid. The position of Bragg rings changes when surfactant is intercalated. They appear at lower

q-range (smaller scattering angle) showing that the characteristic distance d_{001} between clay's crystalline sheets has increased.

Radially integrated 2-D WAXS patterns are shown in Figure 6, as *I(q)* plots. The left panel in Figure 6 shows development of the clay lamellar structure due to increase of the surfactant concentration. He et al. [19] showed that arrangements of the HDTMA surfactant in the montmorillonite clay interlayer were fairly distinctive and varied from lateral-bilayer (0.7CEC), then to paraffin-type monolayer (1.5CEC) and finally to paraffin-type (5CEC). In the present studies the two former transition phases are not seen. Instead, a mixture of different clay populations is observed for sample 1CEC-Fh, and these include: (i) non-modified particles (peak at q=5.11 nm^{-1}), (ii) a paraffin-type bilayer (peak around q=1.57 nm^{-1}), and very broad peak (with its maximum in the radial distribution function at $\sim$ 3 nm^{-1}) that may correspond to paraffin-type monolayer. Higher concentration of CTAB molecules is thus needed to modify all clay particles. For the 2CEC-Fh and 4CEC-Fh samples, the peak at q=5.11 nm^{-1} vanishes and the peak that corresponds to the formation of the paraffin-type bilayer structure becomes very sharp and intense for the sample with the highest CTAB concentration used.

A comparison between 4CEC-Fh modified and non-modified clay particles is shown in Figure 6 (right). The 001 Bragg peak for 4CEC-Fh modified clay is found at q=1.57 nm^{-1}, which corresponds to the distance d_{001}=3.99 nm in the real space. A second and a third peak is found at q=3.15 nm^{-1} and q=4.73 nm^{-1} and occur at 2x and 3x the q-value of the first peak, thus are identified as 002 and 003 Bragg reflections, respectively. The peaks have high intensities and are relatively sharp indicating that the lamellae have attained a well-defined parallel arrangement.

The expected basal spacings for bilayer paraffin-type intercalation is given by the following approximate expression [20]: d_L=2$\times$0.127$n_c\times\sin\beta$ + 1.66 nm where n_c denotes the number of C-C bonds. Here 1.66 nm is the sum of the size of the terminal CH_3 groups, the length of the polar head groups $N(CH_3)_3$ and the thickness of the clay crystalline sheet of 0.656 nm [15]. For CTAB (n_c=14) this gives d_L=4.61 nm for the surfactant intercalating as a paraffin-type bilayer (Figure 7) when the the maximum tilt angle β between the surfactant chains and the crystalline interlamellar silicate sheet is 56 °. There is a mismatch between the calculated lamellar distance d_L and experimentally found distance d_{001}. It is proposed here that CTAB arrangement is a paraffin-type bilayer with an angle of 41 °, which might be due to incomplete ion exchange process even after 1 day of reaction time. This suggestion is supported by the other researchers conclusions [19,20,21,22]. However, it is difficult to obtain detailed information on the conformation of surfactant molecules in the interlayer of fluorohectorite from the x-ray results only, and other complementary techniques (such as FTIR) are needed to make conclusions on this.

When the 2-D WAXS pattern (demonstrated in Figure 5) is integrated azimuthally, a so-called azimuthal plot is made

(Figure 8). The latter may then be fitted by the classical Maier-Saupe function of a functional form $f \sim \exp(m\cos^2\alpha)$ that can be used to calculate the order parameter [23].

The interaction energy in our system is different from that used by Maier and Saupe in their mean field model for liquid crystalline order, but the functional form is found to be well suited to our data. The angular 'width' of the function f is a quantification of the orientational order of the particles in the suspension. This is contained in the m parameter as defined above, but is more conveniently measured using a global order parameter S, see [24].

In the case of our system, the so called *anti-nematic* geometry has to be employed, since the particle stacking direction is, on average, in a plane normal to the reference direction (see Figure 4b - blue disc indicates the plane normal to the E-field direction represented by large black arrow). The order parameter values reported in the present work are defined in a representation where they are positive and lie within the numerical range 0-1 in magnitude, where 1 denotes a perfectly aligned clay particles with their faces being parallel to the E-field direction.

As can be seen, the organically modified sample 4CEC-Fh shows very large anisotropic particle arrangement ($S_{an} \sim$ 0.72) upon application of an electric field. The anisotropy is insignificant without E-field ($S_{an} \sim$ 0.04). Table 1 shows the calculated time-average values of S_{an} (6 measurements) for both modified 4CEC-Fh and non-modified [8] clay suspension at different E-field strengths. The S_{an} grows slightly with increasing E-field for organically modified samples, whereas no such correlation was found for non-modified clay particles. It should be noted here that a relatively narrow range of electric field strength was used during this experiment, thus one cannot make final conclusions about the dependence of S_{an} on the E-field. However, there is a clear difference in magnitude of S_{an}. The degree of anisotropy was higher for the system with organoclay particles ($S_{an} \sim$ 0.71) than for non-modified clay particles ($S_{an} \sim$ 0.62) as described in [8]. This can be explained by the fact that the modified clay particles do not form large aggregates as is the case with non-modified particles, leading to structures that are more easily and uniformly aligned along the E-field. Optical microscopy images presented in the next section support for that conclusion.

Table 1. Calculated average values of S_{an} for both modified 4CEC-Fh and non-modified clay suspension at different E-field strengths

	E-field	4CEC-Fh	Na-Fh[8]
S_{an}	for 350 V/mm	0.70±0.01	0.63±0.01
S_{an}	for 500 V/mm	0.71±0.01	0.64±0.02
S_{an}	for 750 V/mm	0.72±0.01	0.60±0.05

3.2 Optical observations

In order to make use of clay particles as a basis for an ER fluid one needs to challenge the tendency for particles in suspension to sediment. The particle sedimentation properties are often the major criterion used to evaluate whether the ER fluid can be commercialized or not. The general methods to counteract the sedimentation of ER fluids include controlling both size and shape of particles, preparing hollow or porous particles, and matching of densities between particles and solution [25,26]. Addition of surfactants is commonly used to prevent the particles from agglomeration, which then slows down particle sedimentation, or if the particles are small enough (i.e. magnetic particles in ferrofluids), ensures that they are held in suspension by Brownian motions [27]. Figure 9 shows ER suspensions of non-modified Na-Fh (top) and 4CEC-Fh organically modified (bottom) clay particles suspended in silicone oil and deposited for 12 days. The results show that the sedimentation of 4CEC-Fh is much slower than the non-modified sample. It can be seen that almost all non-modified clay particles sedimented after just 12 h, whereas only a small fraction of modified clay particles settled out. The surface modified fluorohectorite clay is lipophilic and thus disperses much easier in oil than its non-modified counterpart. Figure 10 shows that the CTAB modification prevented particles from forming large aggregates when suspended in a non-polar liquid. The size of particle (aggregates) in silicone oil is in the range of 1-30 μm for this organoclay, whereas much larger aggregates are formed in the case of the non-modified clay particles, reaching the size of 200 μm.

3.3 Rheology

The electric field induced yield stress of both the organically modified and the non-modified clay particles suspended in silicone oil was measured using a Physica MCR 300 Rotational Rheometer equipped with a coaxial cylindrical cell Physica C27/ERD. All rheological measurements were carried out at constant temperature of 25 °C and DC electric field. The values of the static yield stress were obtained via the controlled shear stress (CSS) method, in which a linearly increasing shear stress (in steps of 2 Pa) was imposed on suspensions subjected to the same electric field prior (for 300 s) and during the measurement.

Figure 11 shows the yield stress of non-modified (left) and organically modified (right) 10 wt.% samples as a function of electric field strength using the CSS mode. The yield stresses of modified (non-modified) samples are: 54 (13), 120 (62) and 145 (76) Pa for the E-field strengths of 1, 2 and 3 kV/mm, respectively. It can be seen that the yield stress nearly doubled when clay particles are organically modified. The mechanism of the ER effect is not the focus of the

present work and the authors do not intend to draw any firm conclusions. However, we suggest that the increase of the yield stress values can be related to the increase of the particle dielectric loss (see [7,28]).

4 Conclusions

The primary objective of this research was to investigate the electric field induced alignment of organically modified fluorohectorite clay-based ER fluids by means of x-ray studies. However, other methods, namely TGA/DTG, zeta potential measurements and optical observations were employed to understand the differences in chemical and physical properties of modified clay particles when compared to their previously studied non-modified counterparts [8].

A set of samples have been synthesized by an ion exchange method using different concentrations of CTAB. The Na^+ cations intercalated between the clay platelets were exchanged by the surfactant molecules, increasing the characteristic lamellar distance d_{001} from 1.21 to 3.99 nm, which indicates that the intercalated CTAB chains formed a paraffin-type bilayer with a tilt angle of 41 °. The surfactant molecules were also adsorped on the particles' surfaces. The resulting materials became lipophilic, and therefore disperses well in a non-polar liquid, such as a silicone oil.

The TGA/DTG measurements provided data supporting the successful modification of the clay particles. Characteristics of water loss; the release and loss of the CTAB surfactant molecule adsorped on the clay external surface; and the decomposition of the surfactant molecule intercalated between the clay sheets was found for all modified samples in temperature ranges 50-150, 200-300 and 350-450 °C, respectively. The optical microscopy observations and the sedimentation tests showed that the 4CEC-Fh sample dispersed well in oil. Modified clay particles formed much smaller aggregates and sedimented significantly slower than non-modified ones.

The electric field induced alignment from organically modified clay was found to more well-defined. It was shown that the anti-nematic parameters were $S_{an} \sim 0.71$ and $S_{an} \sim 0.62$ for modified and non-modified particles, respectively. The conjecture is that the improved particle organization is due to both the particle-particle repulsive interactions and surfactant adsorption on clay's surface, leading to formation of smaller aggregates in contrast to large aggregated structures formed by non-modified clay particles. The data clearly show that the yield stress increases as much as a factor of 2 for modified clays compared to the unmodified counterpart. The dielectric loss model [28,29] is suggested to explain the mechanism of this ER effect. It is also believed that the larger number of contact points created when unmodified particles self-organize in chains (compared to the unmodified particle chains) can contribute to an enhancement of the effect. Thus both from the point of view of ER fluids with higher yield stress, and also from the point of view of alignment of clay particles inside clay nano-composite materials [30], the modified particles are more

promising in terms of applications. More work is needed and is under way in our group in order to be more conclusive on these points.

The authors acknowledge assistance from D. Chernyshov while performing experiments at the Swiss-Norwegian Beam Lines at ESRF, and A. P. Hammersley, creator of the Fit2D program. This work was supported by the Research Council of Norway through the FRINAT Program: NFR project number 171300.

References

1. M. Grzelczak, J. Vermant, E.M. Furst, L.M. Liz-Marzan, Acs Nano **4**, 3591 (2010)
2. Y.F. Zhu, C. Ma, W. Zhang, R.P. Zhang, N. Koratkar, J. Appl. Phys. **105**, 054319 (2009)
3. T. Prasse, J.Y. Cavaille, W. Bauhofer, Compos. Sci. Technol. **63**, 1835 (2003)
4. T.G.M. Ven, M.K. Baloch, J. Colloid Interf. Sci. **136**, 494 (1990)
5. K. Shin, S. Lee, J.J. Kim, K.D. Suh, Macromol Rapid Comm **31**, 1987 (2010)
6. M. Mittal, E.M. Furst, Adv. Funct. Mater. **19**, 3271 (2009)
7. B. Wang, M. Zhou, Z. Rozynek, J.O. Fossum, J. Mater. Chem. **19**, 1816 (2009)
8. Z. Rozynek, K.D. Knudsen, J.O. Fossum, Y. Méheust, B. Wang, M. Zhou, J. Phys.: Condens. Matter **22**, 324104 (2010)
9. J.O. Fossum, Y. Meheust, K.P.S. Parmar, K.D. Knudsen, K.J. Maloy, D.M. Fonseca, Europhys. Lett. **74**, 438 (2006)
10. W. Xie, Z.M. Gao, W.P. Pan, D. Hunter, A. Singh, R. Vaia, Chem. Mater. **13**, 2979 (2001)
11. E.P. Giannelis, Adv. Mater. **8**, 29 (1996)
12. P. Podsiadlo, A.K. Kaushik, E. Arruda, et al., Science **318**, 80 (2007)
13. S. Letaief, C. Detellier, J. Mater. Chem. **17**, 1476 (2007)
14. P.C. LeBaron, Z. Wang, T.J. Pinnavaia, Appl. Clay Sci. **15**, 11 (1999)
15. G.J. da Silva, J.O. Fossum, E. DiMasi, K.J. Måløy, S.B. Lutnæs, Phys. Rev. E **66**, 011303 (2002)
16. N.I. Ringdal, D.M. Fonseca, E.L. Hansen, H. Hemmen, J.O. Fossum, Phys. Rev. E **81**, 10 (2010)
17. P.D. Kaviratna, T.J. Pinnavaia, P.A. Schroeder, J. Phys. Chem. Solids **57**, 1897 (1996)
18. H.P. He, J. Duchet, J. Galy, J.F. Gerard, J. Colloid Interf. Sci. **288**, 171 (2005)
19. H.P. He, R.L. Frost, F. Deng, J.X. Zhu, X.Y. Wen, P. Yuan, Clays and Clay Minerals **52**, 350 (2004)
20. P.H. Massinga, W.W. Focke, P.L. de Vaal, M. Atanasova, Appl. Clay Sci. **49**, 142 (2010)
21. J.X. Zhu, H.P. He, J.G. Guo, D. Yang, X.D. Xie, Chinese Science Bulletin **48**, 368 (2003)
22. G. Lagaly, Solid State Ionics **22**, 43 (1986)
23. Y. Meheust, K.D. Knudsen, J.O. Fossum, J. Appl. Crystallogr. **39**, 661 (2006)

24. H. Hemmen, N.I. Ringdal, E.N.D. Azevedo, M. Engelsberg, E.L. Hansen, Y. Meheust, J.O. Fossum, K.D. Knudsen, Langmuir **25**, 12507 (2009)

25. J.X. Li, X.G. Gong, S.Y. Chen, W.J. Wen, P.S. P, J. Appl. Phys. **107**, 093507 (2010)

26. J. Lu, X.P. Zhao, J. Mater. Res. **17**, 1513 (2002)

27. Z. Rozynek, A. Józefczak, K.D. Knudsen, A. Skumiel, T. Hornowski, J.O. Fossum, M. Timko, P. Kopčanský, M. Koneracká, Eur. Phys. J. E **34**, 28 (2011)

28. T. Hao, Adv. Colloid. Interfac. **97**, 1 (2002)

29. T. Hao, A.Kawai, F. Ikazaki, Langmuir **16**, 3058 (2000)

30. J.U. Park, Y.S. Choi, K.S. Cho, D.H. Kim, K.H. Ahn, S.J. Lee, Polymer **47**, 5145 (2006)

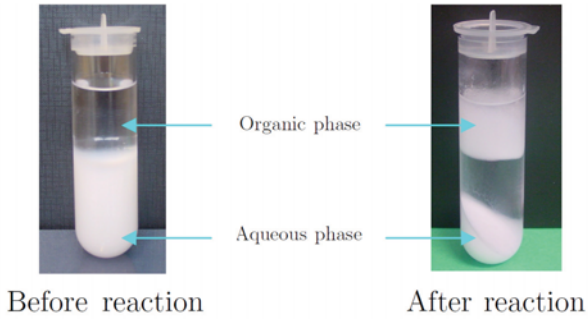

Fig. 1. Illustration of the phase transfer from the aqueous phase to the organic phase.

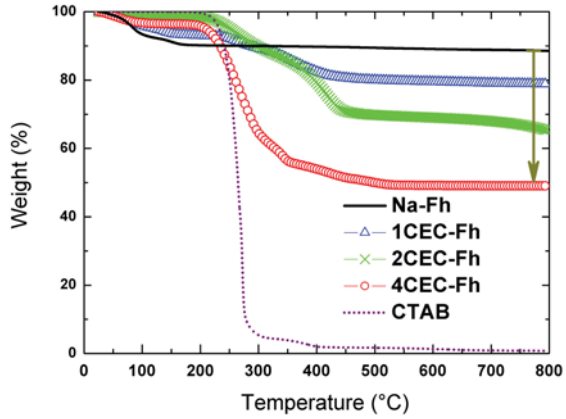

Fig. 2. TGA curves (25-800 °C) of Na-Fh, CTAB and series of CTAB modified Fh. xCEC means that x times the stoichiometric amount of CTAB surfactant was used.

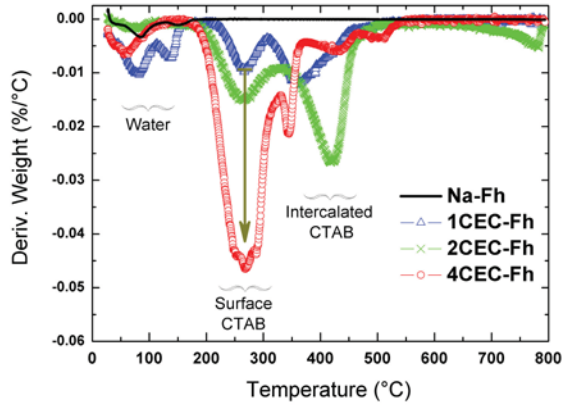

Fig. 3. DTG traces (25-800 °C) of non-modified and CTAB modified Fh.

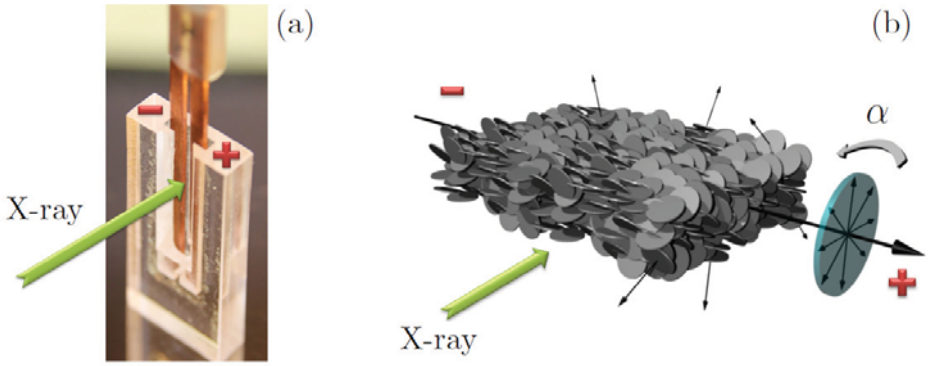

Fig. 4. Image of the sample cell (a) and anti-nematic configurations (b).

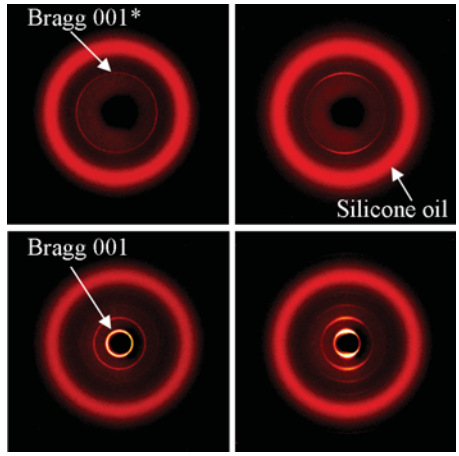

Fig. 5. WAXS patterns of Na-Fh (top) and 4CEC-Fh (bottom) clay particles without (left) and with (right) E-field applied.

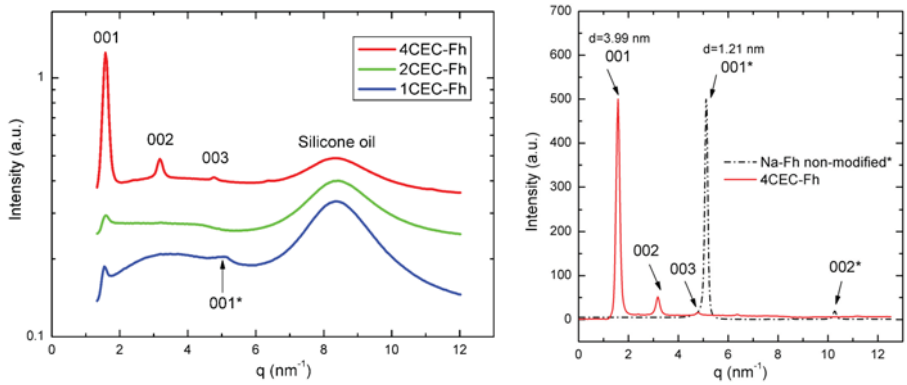

Fig. 6. Integrated WAXS patterns illustrate the CTAB concentration dependent development of lamellar structure (left). Comparison between 4CEC-Fh modified (solid line) and non-modified (dashed line) clay particles with silicone oil peak subtracted (right).

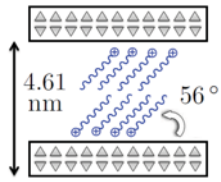

Fig. 7. Orientation of CTAB molecules in paraffin-type bilayer structure. The maximum tilting angle is 56 °, and the distance between clay crystalline layers is d_{max}=4.61 nm.

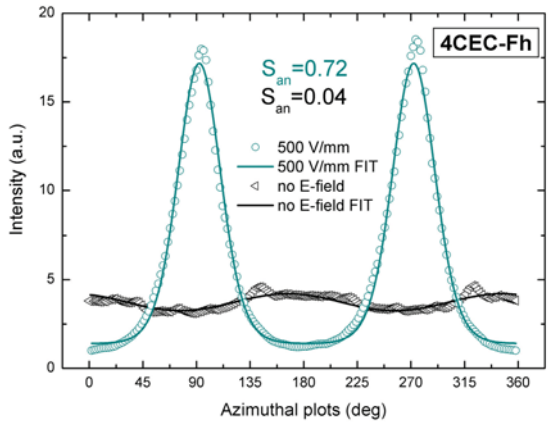

Fig. 8. Azimuthal plots of the first Bragg peak amplitude under an E-field of 350 V/mm (○) and no E-field (▷).

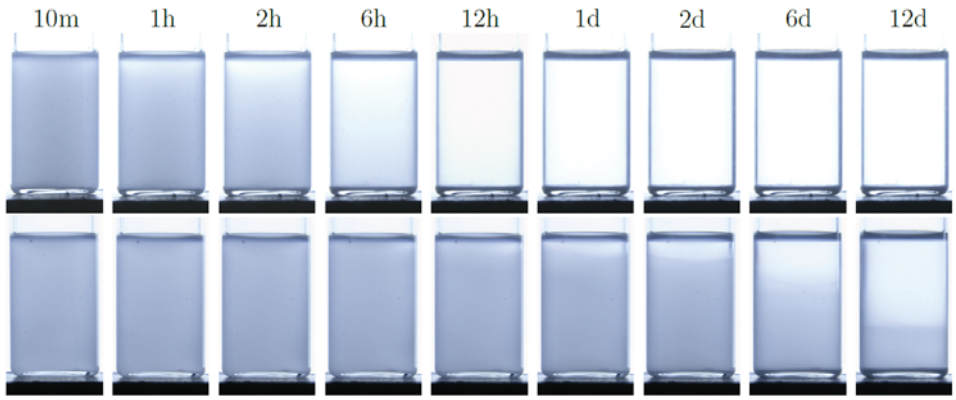

Fig. 9. Sedimentation of non-modified Na-Fh (top) versus 4CEC-Fh (bottom) clay particles in silicone oil. From left, pictures taken at time 10 min, 1-2-6-12 h and 1-2-6-12 days after the solution had been ultrasonicated and shaken.

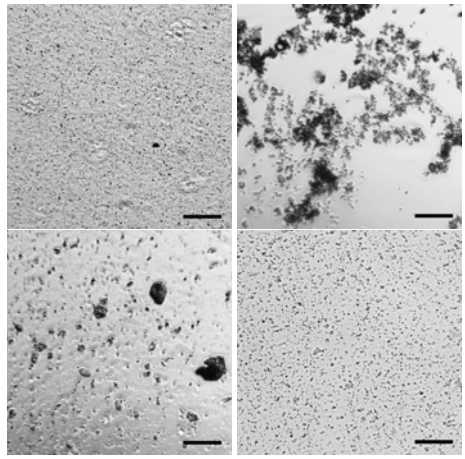

Fig. 10. Microscope images of non-modified Na-Fh (left) and organically modified 4CEC-Fh (right) clay particles suspended in water (top) and silicone oil (bottom). The length of the bar corresponds to 200 μm.

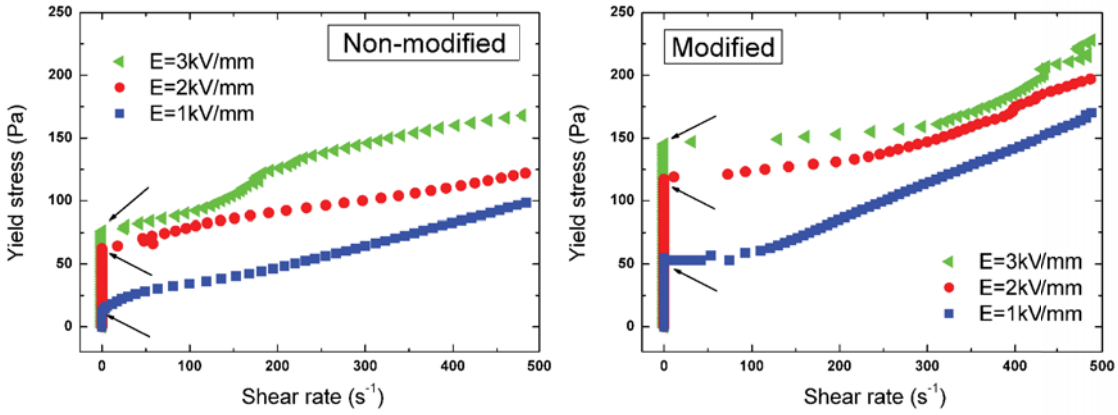

Fig. 11. Flow curves for non-modified (left) and organically modified (right) clay samples suspended in oil as a function of the electric field strength, the yield stress points are indicated by arrows.

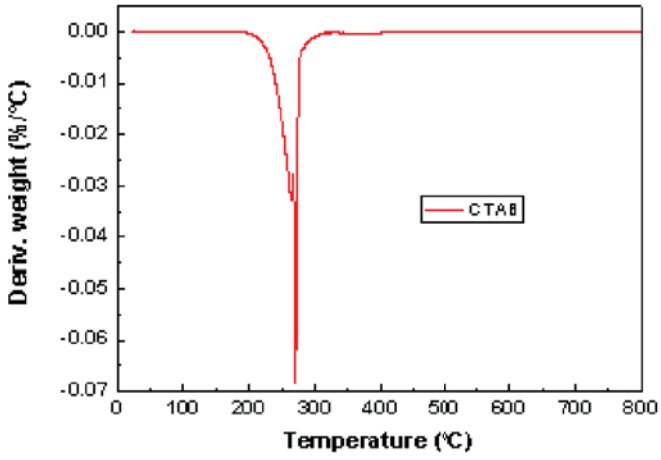

Fig. 12. Supporting figure S1.

Paper V

Different Aspects of Electrically Activated PP/Clay Nanocomposites

Z Rozynek, T S Plivelic, S M L Silva, J O Fossum, E N de Azevedo and G J da Silva

In preparation.

Different Aspects of Electrically Activated PP/Clay Nanocomposites

Z Rozynek,[1] T S Plivelic,[2] J O Fossum,[1] S M L Silva,[3] E N de Azevedo[4] and G J da Silva[5]

[1] Department of Physics, NTNU, Trondheim, Norway
[2] Max-Lab, Lund University, Lund, Sweden
[3] Fed. University Campina Grande, Campina Grande, Brazil
[4] Fed. University Pernambuco, Recife, Brazil
[5] University of Brasilia, Brasilia, Brazil

Abstract

In this work, polypropylene/organoclay nanocomposites were prepared by melt intercalation in an extruder and studied by means of synchrotron X-ray scattering techniques, both at room temperature, and in the melted state (195 ºC) in an applied electric field (*E*). Structural changes and time evolution of the alignment of the layered silicates at different *E*-field strengths, as well as, the final degree of their orientation is discussed. Despite many efforts, structural changes of clay particles, such as clay particle exfoliation was not observed, indicating that this is more challenging to achieve than described by other authors previously.

Keywords: Clay, alignment, polymer, composite, electric field, exfoliation

1. Introduction

In this work we study clay particles added to polymer matrices. The increase in separation of the laminate structure of clay in part or whole, called intercalation and exfoliation respectively (see Figure 1), produces plates that possess a high specific surface area, which theoretically allows for efficient load transfer from the matrix. Dispersed plates also act as barriers to diffusion, inhibiting the flow of gases. Increases in stiffness, strength, and the tortuosity for entering gases have been reported for clay–polymer nanocomposites.[1] Several chemical approaches and diverse polymeric matrices/silicates have been utilized to prepare polymer-clay nanocomposites (PCN), and these include: in-situ polymerization that requires the modification of catalysts as well as of the process itself [2]; or direct melt intercalation, where PP is modified with maleic anhydride (MAPP) or hydroxyl groups (HOPP) to increase the compatibility between PP and the clay surface.[3,4] Although the degree of exfoliation and the correlated physical properties from in-situ polymerization are slightly greater than that

[1] J Wang, S J Severtson and A Stein, *Adv. Mater.***18**,467 1585-1588 (2006)
[2] T Sun and J M Garces, *Adv. Mater.***14**, 128 (2002)
[3] X Liu and Q Wu, *Polymer***42**, 10013 (2001)
[4] P H Nam, P Maiti, M Okamoto, T Kotaba, N Hasegawa and A Usuki, *Polymer***42**, 9633 (2001)

from the melt intercalation process,[5] the cost of composite production is still high and may prohibit commercial applications.

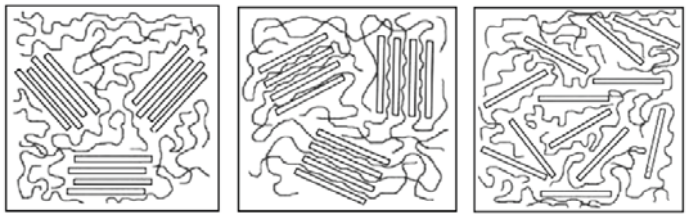

Figure 1. No reaction between clay platelets and polymer chains (a), intercalation of polymer molecules into clay galleries changes their characteristic *d*-spacing (b), clay exfoliation (c).

Controlling the microstructure of polymer/clay materials and in particular the clay exfoliation and the platelets arrangement, i.e. positional and orientational alignment, is an additional issue.[6]The alignment can be achieved by for example biaxial or elongational flow,[7,8] or application of an external electric field.[9]A novel idea was explored by Kim et al.[10] using the effect of an external electric field to assist the penetration the polymer chains into the silicate galleries that led to clay exfoliation. In ref. 10 an electric field is applied on PP/clay melts between the parallel plates of a rheometer resulting in the increase of the rheological properties and exfoliation. However, the explanation for this behaviour was not provided within this article.[9] Further measurements performed by the same group led to the conclusion that the exfoliation process prevails in the AC field due to the imbalance between the van der Waals attraction and the electrostatic repulsion, originating from the dissociation of the bound ions from the clay surfaces.[11,12]In these two reports[11,12] the PP/clay nanocomposites were investigated by means of X-ray scattering in presence of both DC and AC electric fields, without any shearing (sample sits between two electrodes). Thus the clay exfoliation was reported to be purely due to the electric effects, and it developed with time. The clay alignment was also studied by the same group, and they found a very strong DC electric field dependence on the clay alignment, while for the AC electric fields the particle alignment was considerably smaller and was decreasing with time, as exfoliation progresses.

---

5 D H Kim, J U Park, K S Cho, K H Ahn and S J Lee, *Macromol.Mater.Eng.***291**, 1127–1135 (2006)

6 J Collister, in "*Polymer nanocomposites: synthesis, characterization, and modelling*" by R A Vaia and R Krishnamoorti, London: Oxford university press; Ch.2. (2002)

7 M Okamoto, P H Nam, P Maiti, T Kotaka,T Nakayama, M Takada, M Ohshima, A Usuki, N Hasegawa and H Okamoto, *Nano Lett*. **1**, (2001)

8 M Okamoto, P H Nam, P Maiti, T Kotaka, N Hasegawa and A Usuki, *Nano Lett*. **1**, (2001)

9 Z Rozynek, R Castberg, J O Fossum and A Mikkelsen, manuscript in preparation

10 D H Kim, J U Park, K H Ahn and S J Lee, *Macromol. Rapid***24**, 388 (2003)

11 J U Park, Y S Choi, K S Cho, D H Kim, K H Ahn and S J Lee, *Polymer***47**, 5145–5153 (2006)

12 D H Kim, K S Cho, T Mitsumata, K H Ahn and S J Lee, *Polymer***47**, 5938-5945 (2006)

These interesting phenomena were the main motivation for conducting similar experiments, understand the mechanisms behind the electric field induced exfoliation better, and contribute to this fascinating field of polymer/clay science.

This report focuses on the comparison between previously reported electrically activated PP/clay composites in respect to the *E*-field induced alignment of clay particles inside the polypropylene matrix, and also the structural changes in clay particles. The layout of this work is as follows. First, the sample preparation, characterization and the experimental set-upare explained in section 2. Second, the small angle X-ray scattering results are presented in section 3 and these include: monitoring of structural changes (section 3.1), and time dependent development of the system anisotropy during melting and crystallization (section 3.2). Conclusions are presented at the end in section 4.

2. Sample preparation, characterization and experimental set-up

2.1. Sample preparation

A commercial grade of isotactic polypropylene PP H103 (Braskem, Brazil), with melt flow index 40 g/10 min at 230 °C/2.16 kg and density 0.905 g/cm3, was used as polymer matrix for nanocomposites preparation. This grade is appropriated for injection moulding of thin walls products and, according to the manufacturer, contains heat stabilizers to protect against thermal degradation during compounding and processing. The organoclay used in this study (Cloisite® 20A) is obtained from Southern Clay Products (Gonzales, TX). It is a Na+ - montmorillonite, chemically modified with dimethyl dihydrogenated tallow quaternary ammonium chloride, where N+ denotes quaternary ammonium chloride and HT denotes hydrogenated tallow. PP/organoclay master batches were prepared in an intensive internal mixer (Haake Rheocord 90) at 50 rpm for 10 min after organoclay feeding at 210 ºC. Polymer and organoclay C20A were dried in a vacuum oven at 80 ºC for 24h before melt mixing. The masterbatches were pelletized and dried for 2h in the same conditions described above before being added to PP in order to obtain compounds with 5 wt.% organoclay. These compounds were extruded in a counter-rotating twin screw extruder accessory (TW 100) coupled to a Haake operating at 60 rpm and with a temperature profile in the 150-210 ºC range. After extrusion, the materials were air cooled, ground and then injection moulding. Samples were injection moulded in a Ray Ran machine at 210 °C, 100 Pa/cm^2 of pressure for 5 seconds.

2.2. Sample characterization

As the control test the thermal gravimetric analysis (TGA) was performed first. The TG curves (Figure 2) show that the thermal stability of the nanocomposites is enhanced relative to that of virgin PP, and the typical the onset temperature of the degradation is about 50 ºC higher for the nanocomposites. Clay particles protected the polymer matrix with a noticeable increase in thermal stability. The final fraction of mass at 500 °C was found to be around 1 % and 4 % for PP and PP/clay composite, respectively. From the TGA data one can conclude that the maximum temperature of the sample in the melted state should stay below 200 °C.

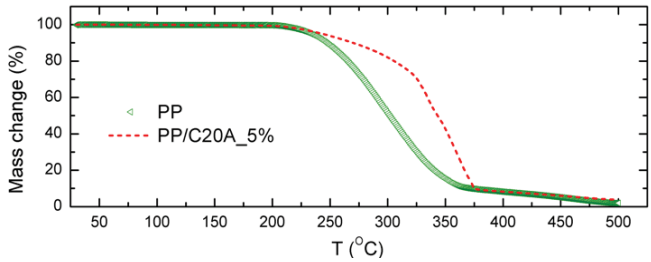

Figure 2. TG curves for PP (green triangle) and PP/C20A with 5 wt. % of the organoclay content (red dashed line).

2.3. Experimental set-up

Initial synchrotron small-angle X-ray scattering (SAXS) experiments were performed at LNLS in Campinas Brazil. These initial experiments serve as a base for the SAXS results reported here, which all were performed at the I711 beamline at MAX-lab, Sweden. The beamline was equipped with a CCD detector with 165 mm active area. The SAXS patterns were recorded using a two-dimensional detector located ~67 cm from the sample. An X-ray beam with a wavelength of 1.1 Å was used, which enabled detection of scattering in a q-range (d-range) of approximately 0.02-0.6 $Å^{-1}$ (1-30 nm). An AC electric field of 1 kV/mm and frequency of 100 Hz, and a DC electric field of 1 kV/mm were applied using a function generator (TG215 ThurlbyThandar Instruments) and a high voltage amplifier (AS-3B1 Matsusada Precision Inc.). Two copper electrodes have a height of 7 mm and a width of 2 mm, and they were separated by 2 mm gap. An electric field was applied horizontally, perpendicular to the direction of the X-ray beam. Figure 3 shows a schematic of the experimental set-up. A custom-made heating cell consisted of two-wall heating unit used to ensure the smallest temperature gradient between sample and environment. The sample chunks were placed in between copper electrodes and thin mica elements glued to the flat sides of the electrodes using high temperature resistant glue.

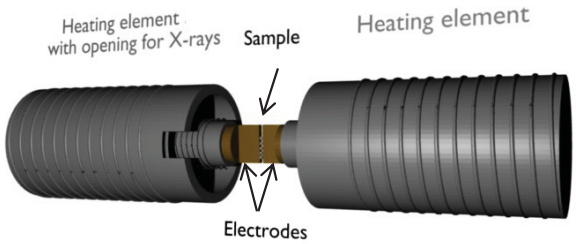

Figure 3. Experimental set-up for SAXS measurements. Sample is placed between two copper electrodes. Two heating units are used to ensure the smallest temperature gradient between sample and environment.

3. Results

3.1. SAXS – structural changes

The structural changes of two samples exposed to DC (Sample 1) and AC (Sample 2) electric fields were monitored during melting and crystallization. Samples were kept in the melted state for 145 min (Sample 1) and 66 min (Sample 2) at around 195 ºC before application of the *E*-fields.

3.1.1. SAXS patterns and the azimuthal integration

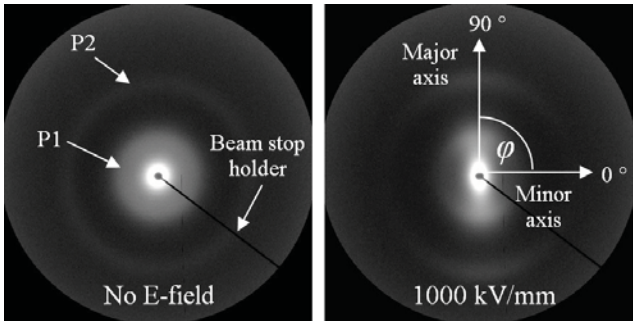

Figure 4. 2-D SAXS images of PP/organoclay composite in melted state (around 195 °C) under AC electric field of 1 kV/mm, 100 Hz. Very strong anisotropy can be seen (right) after 5 min of *E*-field application. The direction of the AC *E*-field is horizontal.

The example of the 2-D SAXS patterns is shown in Figure 4. These were collected from PP/organoclay sample without (left) and with (right) an AC E-field of 1000 V/mm applied, respectively. Prior to the application of the electric field, the organoclay particles are randomly dispersed into the polymer matrix. The alignment of clay particles with their stacking direction being normal to the *E*-field direction (horizontal) is observed after its application. Both the scattering at small angles and diffraction rings (P1 and P2) become anisotropic, i.e. the lowest scattering intensity is found at $\varphi \sim 0$ º and 180 º, whereas it peaks at $\varphi \sim 90$ º and 270 º, which is indicated as the minor and the major axes, respectively.

All the 2-D SAXS patters have been processed prior the integration, i.e. SAXS images of both the PP/organoclay sample inside the sample cell and the background image of the empty sample cell were divided by their transmissions followed by the background subtraction, and then the contributions from the beam stop and its holder were masked out.

The azimuthal integration was performed for φ ± 10 º of the major and the minor axes determined by the orientation of clay particles, i.e. the major axis is drawn along the particle stacking direction. For the example shown in Figure 4 (right) the boundary angles are +80º and +100º for the major axis; and -10º and +10º for the minor axis.

Figure 5 shows azimuthally integrated 2-D SAXS patterns of the PP/organoclay composites during melting (left panel) and exposure to the electric fields (right panel). The scattering intensities were plotted against the momentum transfer $q=4\pi\sin\theta/\lambda$, where 2θ denotes the scattering angle and λ is the wavelength of the X-rays. The real space distance can be calculated as $d=2\pi/q$.

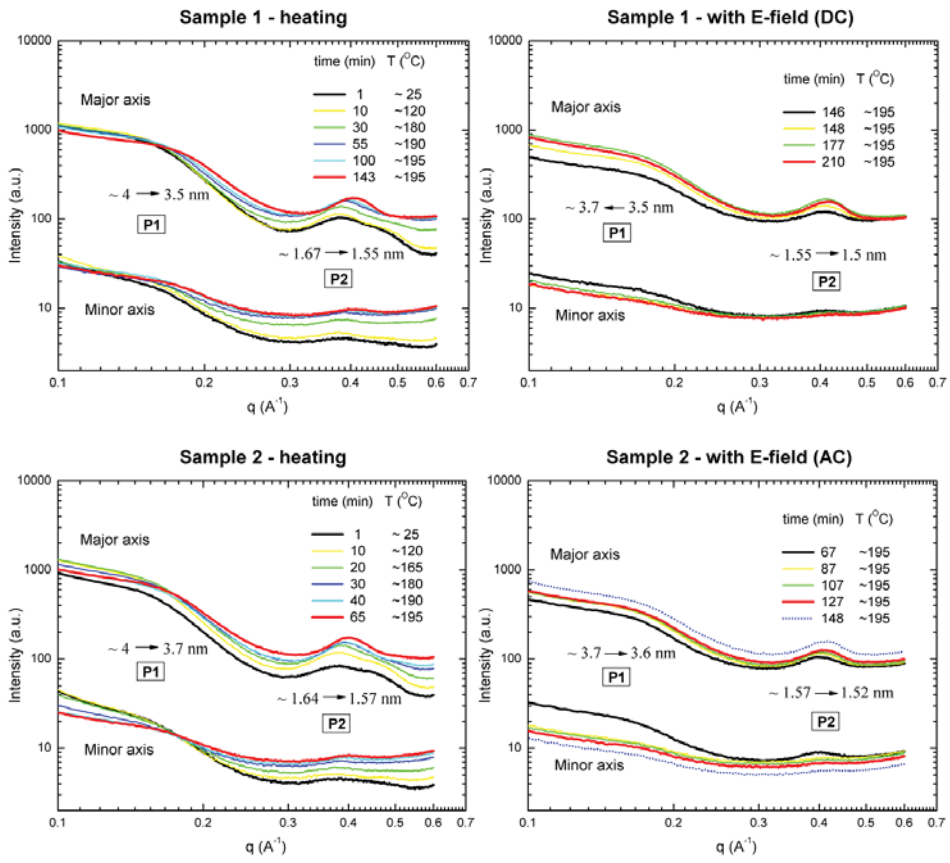

Figure 5. Azimuthally integrated 2-D SAXS patterns of samples 1 (top) and 2 (bottom) during melting and temperature stabilizing (left) and *E*-field application (right).

3.1.2. Samples at RT

Three broad peaks are observed with their centres located at around q_1=0.16, q_2=0.38, and q_3=0.47 Å^{-1}, for both samples in a solid form at RT~25ºC (the initial state: t=1 min), and these correspond to the real space distances around d_1=4.03, d_2=1.67, and d_3=1.33 nm. The former peak (P1) is attributed to the *polymer chains intercalation* between the layers organoclay that increased the initial interlayer spacing d_{100}=2.42 nm of pure Cloisite®20A organoclay[13,14]. The reduction of attractive forces between the clay layers due the chemical treatment of clay particles (surfactant intercalation) and the presence of polar functional groups (maleic anhydride) in PP enable the polymer chains to intercalate into the clay galleries and changed the basal spacing d_{100} from 2.42 to 4.03 nm The structures with some degree of disorder were obtained, but it is not possible the existence of structures exfoliated. It should be noted that the distribution of the d_{100} values is very broad. Two other peaks (P2 and P3) can be assigned to either the presence of a small amount of non-modified montmorillonite particles acting as an impurity in a commercial product[15] or another (more likely) explanation could be that the initial Cloisite®20A structure collapsed to the bilayer and monolayer arrangement of the alkyl chains during melt processing (*surfactant molecule intercalation*). Similar observations were found by Yoon et al.[16] Another hypothesis was suggested by Mandalia et al.[17] and also Zhang et al.[18]. They observed the presence of three diffraction peaks in X-ray patterns of organoclay and nanocomposites of polyethylene and polypropylene and those were attributed to the (001), (002) and (003) basal reflections of one intercalation state, respectively. This suggestion is less probable in present case, since P1 and P2 shift different direction when E-field is applied (see further discussion) and in addition P2 is much narrower when compared to P1. In order to be more conclusive at this point, one would need to employ other experimental techniques, namely FTIR and DSC. However, this is not the main subject of the current study.

3.1.3. Melting of the samples

During the first phase (temperature rise and stabilization) positions of peaks P1 and P2 clearly shift towards higher q-values indicating the decrease in basal spacing of two different populations of clay particles, namely organoclays with polymer (d1) and surfactant (d2)

[13] Supplier web-page: http://www.scprod.com/product_bulletins/ [accessed: 14.06.2011], Southern Clay Products, Inc.
[14] B U Nam and Y Son, *Polym. Bull.***65**, 837–847 (2010)
[15] A Riva, M Zanetti, M Braglia, G Camino and L Falqui, *Polym. Degrad. Stab.* **77**, 299 (2002)
[16] J T Yoon, W H Jo, M S Lee and M B Ko, *Polymer* **42**, 329-336 (2001)
[17] T Mandalia and F Bergaya, *J. Phys.Chem. Sol.* **67**, 836-845 (2006)
[18] J Zhang, D D Jiang and C A Wilkie, *Thermochim. Acta* **430**, 107-113 (2005)

intercalated structures, respectively. In case of Sample 1, these changes are $\Delta d1 \sim 0.53$ nm and $\Delta d2 \sim 0.12$ nm. Sample 2 was monitored for shorter time and therefore the changes are smaller $\Delta d1 \sim 0.3$ nm and $\Delta d2 \sim 0.07$ nm. Since the initial values (sample at RT) of basal spacings recover rapidly during cooling (see the discussion in section 3.1.5), it is believed that collapse comes from the exudation of the surfactant molecules and the polymer chains out from the gallery during heating.[19] Priya et al.[20] and Riva et al.[15] have also stated that, thermodynamically, at high temperatures (>180 °C), when the entropy gain due to exudation is greater than the columbic interaction energy between modifier and silicate layer, organic modifiers can be exudated from the organosilicate interlayer.

3.1.4. Samples exposed to E-fields (DC and AC)

During the second phase a DC *E*-field of 1 kV/mm was applied to Sample 1 for all the time, i.e. around 1h for sample at melted state and also during the cooling. Sample 2, however, was exposed to an AC (100 Hz) *E*-field of 1 kV/mm for 30 min and then the electric field strength was increased to 2 kV/mm for 10 min. The higher *E*-field was maintained during the cooling.

For Sample 1 (DC) the P2 continue shifting the same direction and the value of the d_2 decreases by around 0.05 nm, whereas the shift of the P1 changes its direction and d_1(146min)=3.5 → d_1(210min)=3.7 nm. The distance between the clay crystalline sheets has increased by 0.2 nm in around 1 h. The change of the direction of the shift of P1 is evidently due to the electric field application and is time dependent. The difference of the value of d_1 is, however, very small and cannot be identified as exfoliation. Different behaviours of peaks P1 and P2 may indicate either the intercalation of different species into clay galleries (i.e. surfactant molecules behave differently than polymer chains in presence of electric fields) or the intercalated species are of the same kind but move around and reorient more freely for certain intercalation type.

For Sample 2 (AC) both peaks P1 and P2 continue shifting the same direction and the values of d_1 and d_2 decrease by around 0.1 nm and 0.05 nm, respectively. There is no electric field influence on the basal spacings observed, and the process is rather time-dependent. The increase of the electric field strength (from 1 to 2 kV/mm) seems to have no effect on the *d*-spacings either (blue dotted line in Figure 5).

3.1.5. Cooling of the samples

[19] S M L Silva, M A Lopez-Manchado and M Arroyo, J. *Nanosci. Nanotechnol.* **7**, 4456 – 4464 (2007)
[20] L Priya and J P Jog, *J. Polym. Sci. B* **41**, 31 (2003)

In the last phase samples are cooled down while still exposed to *E*-fields. In case of Sample 1, the P2 recovers to the same initial position and d_2(232min)=d_2(1min)=1.67 nm, whereas d_1(232min)=4.25 and is bigger than d_1(1min)=4.03 by around 0.2 nm, which is similar to Δd_1 produced by the application of the DC electric field.

3.1.6. Summary

Figure 6 illustrates the results described above and it shows a development of the two basal spacings (d_1 and d_2), as a function of time, temperature and *E*-field. The dotted line shows temperature inside the heating cell (2 mm from the sample). Filled symbols represent changes in the values of the characteristic distances d_1 and d_2 for samples not exposed to *E*-field. The application of the electric fields (open symbols) effects d_1 only when the DC electric field is applied, as already discussed. Half-filled symbols denote changes in the values of d_1 and d_2 for samples being cooled down (and still exposed to *E*-fields).

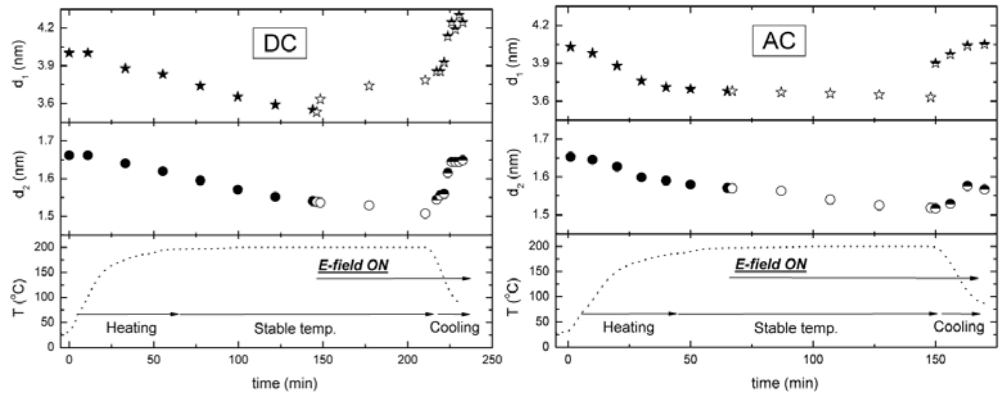

Figure 6. Development of basal spacings related to populations of clay particles with polymer (d_1) and surfactant intercalated (d_2) structures, respectively, as a function of time, temperature and *E*-field presence.

Unfortunately due to the synchrotron time restrictions it was not possible to measure a long time dependence on the change of d_1. It would be also interesting to investigate this phenomenon during several heating and melting cycles.

The observations described above differ clearly from those presented by Kim and Park[11,12]. They showed that the exfoliation was due to electric field application and it was prevailed by AC electric field rather than DC fields. In our studies the exfoliation was not achieved and in addition a small increase of basal spacing was observed for sample exposed to the DC fields not AC fields. Several other samples (results not shown here) of PP/Cloisite®C20A composites were studied at higher and lower temperatures, different frequencies and strengths of an AC electric fields and the results show also no exfoliation. Possibly the composite

preparation is very important and may explain the differences in clay behaviours measured by our group and these reported by Kim and Park[11,12].

3.2. SAXS – development of anisotropy

Application of an external electric field makes clay particles polarized. If the resulting electric forces overcome thermal interactions particles rotate and align normal to the electric field lines in respect to their stacking direction. The alignment of particles can be monitored by means of electron or neutron diffraction.[21,22]In order to quantify the degree of anisotropy of the system, i.e. how well the clay platelets aligned, one needs to integrate radially over a narrow *q*-range of the 2-D SAXS patterns (see Figure 7) and fit the obtained 1-D azimuthal plot (see Figure 8) to a Maier-Saupe function(for details see [23,24,25,26]). The fitting parameter is related to the full width at half maximum (smaller value means higher degree of anisotropy) and can be expressed using the standard nematic order parameter (S_2). In short, the fitting parameter is related to the full width at half maxima and can be expressed as the nematic order parameter S_2, ranging from -½ to 1, where 1 indicates perfectly oriented particles in the nematic configuration, 0 states no orientation, and finally –½ indicates perfectly oriented particles in the anti-nematic configuration. It is expected here that the nematic order parameter should be in range between 0 and -1/2, since the clay particles align in the anti-nematic fashion, i.e. the direction of the clay stacks, are perpendicular to the field, without any preferred azimuthal direction.

Figure 7 shows 2-D SAXS images of PP/organoclay composite in melted state (around 195°C) under DC electric field of 1 kV/mm. The anisotropy starts to build up (left) in a direction perpendicular to the direction of the electric field lines. Very strong anisotropy can be seen (right) after 55 min of *E*-field application. The direction of the DC *E*-field is horizontal.

[21] Z Rozynek, K D Knudsen, J O Fossum, Y Meheust, B Wang and M Zhou, *J. Phys.: Condens. Mat.***22**, 324104 (2010)
[22] K D Knudsen, J O Fossum, G Helgesen and M W Haakestad, *Physica B: Condens. Mat.***352**, 247 (2004)
[23] I Dozov, E Paineau, P Davidson, K Antonova, C Baravian, I Bihannic and L J Michot, J. Phys. Chem. B 115, 7751–7765 (2011)
[24] Y Méheust, K D Knudsen andJ O Fossum,*J. Appl. Cryst.* **39,** 661 – 670(2006)
[25] H Hemmen et al., *Langmuir* **25**, 12507–12515 (2009)
[26] M Engelsberg and E N de Azevedo, *J. Phys. Chem. B***112**, 7045–7050(2008)

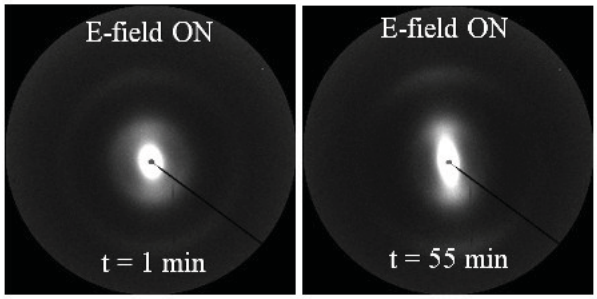

Figure 7.2-D SAXS images of PP/clay composite in melted state (around 195 °C) under DC electric field of 1 kV/mm. Very strong anisotropy can be seen (right) after 55 min of *E*-field application. The direction of the DC *E*-field is horizontal.

Azimuthal plots of the first Bragg peak amplitude (q_1, polymer intercalation) are shown in Figure 8.The degree of anisotropy grows clearly, starting immediately after the application of the electric field.The first collected data was taken within the first minute (black circles) of the X-ray exposure. The value of the nematic order parameter was calculated to be around S_2=-0.19. The next integrated image is plotted using orange diamonds, and it can be seen that the full width at half maximum becomes smaller when compared to that of the first integrated plot. This reflects in the increase of the nematic order parameter which is around S_2=-0.28. The further development of the degree of anisotropy is no longer evident via direct observation of the azimuthal plots in Figure 8, in particular comparison of data plotted using blue stars and green crosses.

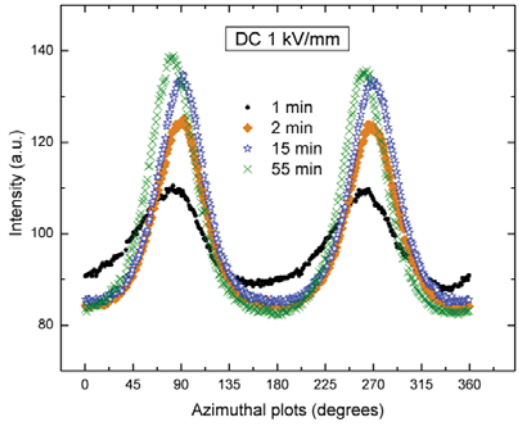

Figure 8. Azimuthal plots of the first Bragg peak amplitude (q_1, polymer intercalation) for PP/Clay sample under DC electric field of 1 kV/mm. The degree of anisotropy grows starting immediately after the application of the electric field.

Similar azimuthal plots (Figure 8) were obtained for Sample 2 exposed to the AC electric fields. These are not included here, but the calculated results for the nematic order parameters are presented in Figure 9 together with those obtained for Sample 1 (DC).

The calculated values of the nematic order parameter are shown in Figure 9. The values of the S_2 for the sample without the *E*-fields applied were ascribed as zero by default. It can be seen that (for both sample) the degree of anisotropy develops with time and in addition it depends on the temperature, and more precisely, the phase of the polymer matrix (melted vs. crystalized). The time for the rotation of clay particles in directly proportional to the viscosity of the hosting medium and depends on the electric field strength that scales as $1/E^2$.[27]

For Sample 1 (DC), the highest value of the S_2 is around -0.31 and it was achieved approximately 15 min after the application of the DC *E*-field (1 kV/mm), whereas the S_2 is around -0.3 calculated for the last data collected before cooling started. The polymer crystallization prevents better particle orientation, and the values of the nematic order parameter decreased. The final value of the S_2 was found to be around -0.26, for the sample cooled down to about 70 ºC .

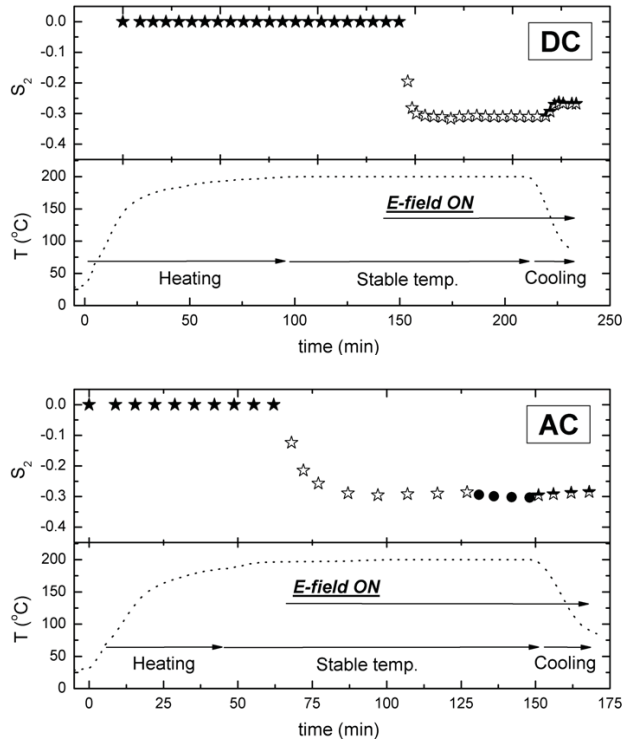

Figure 9.Development of the degree of anisotropy as function of time and the phase of the polymer matrix (melted vs. crystalized). A DC electric field was applied to Sample 1 (top) and an AC electric field was applied to Sample 2 (bottom).

For Sample 2 (AC), the highest value of the S_2 is around -0.3 and it was achieved approximately 25 min after the application of the AC *E*-field (1 kV/mm). The degree of

[27] R Castberg, Z Rozynek, J O Fossum, K J Måløy, E Flekkøy, *"Rotation of Clay Particles in E-fields"*, manuscript in preparation

anisotropy increases slightly (ΔS_2~0.005) when the strength of the electric field is increased to 2kV/mm (filled circles). The polymer crystallization prevents better particle orientation, and the values of the nematic order parameter decreases. The final value of the S_2 was found to be around -0.285, for the sample cooled down to about 70 ºC.

4. Conclusions

The primary objective of this research was to investigate the structural changes and time evolution of the alignment of the layered silicates under different *E*-field strengths. Development of the basal spacing as a function of time, temperature and *E*-field presence was measured by means of small angle X-ray scattering. The electric field was found to have noticeable but little effect on the clay particle structure and the basal spacing has increased by around 5 %. However, despite many efforts, no clay particle exfoliation was observed, and it seems to be more challenging than described by other authors.

While monitoring changes of the degree of anisotropy, it was found that the polymer crystallization prevented better particle orientation, and the values of the nematic order parameter decreased when comparing to those from the sample being at melted state. Application of either DC or AC electric fields resulted in very similar particle alignment and none of them should be considered as privileged.

Acknowledgement

The authors acknowledge assistance from D. Haase and C. B. Hansen while performing experiments at the beamline I711 at Max-Lab, Sweden, and also the staff at the LNLS during the initial experiments. A. P. Hammersley the creator of the Fit2D program is acknowledged. This work was supported by the Research Council of Norway through the FRINAT Program: NFR project number 171300.

References

[1] J Wang, S J Severtson and A Stein, *Adv. Mater.***18**, 467 1585-1588 (2006)

[2] T Sun and J M Garces, *Adv. Mater*. **14**, 128 (2002)

[3] X Liu and Q Wu, *Polymer***42**, 10013 (2001)

[4] P H Nam, P Maiti, M Okamoto, T Kotaba, N Hasegawa and A Usuki, *Polymer***42**, 9633 (2001)

[5] D H Kim, J U Park, K S Cho, K H Ahn and S J Lee, *Macromol. Mater. Eng*. **291**, 1127–1135 (2006)

[6] J Collister, in *"Polymer nanocomposites: synthesis, characterization, and modelling*" by R A Vaia and R Krishnamoorti, London: Oxford university press; Ch.2. (2002)

[7] M Okamoto, P H Nam, P Maiti, T Kotaka,T Nakayama, M Takada, M Ohshima, A Usuki, N Hasegawa and H Okamoto, *Nano Lett*. **1**, (2001)

[8] M Okamoto, P H Nam, P Maiti, T Kotaka, N Hasegawa and A Usuki, *Nano Lett*. **1**, (2001)

[9] Z Rozynek, R Castberg, J O Fossum and A Mikkelsen, *manuscript in preparation*.

[10] D H Kim, J U Park, K H Ahn and S J Lee, *Macromol. Rapid***24**, 388 (2003)

[11] J U Park, Y S Choi, K S Cho, D H Kim, K H Ahn and S J Lee, *Polymer***47**, 5145–5153 (2006)

[12] D H Kim, K S Cho, T Mitsumata, K H Ahn and S J Lee, *Polymer***47**, 5938-5945 (2006)

[13] Supplier web-page: http://www.scprod.com/product_bulletins/ [accessed: 14.06.2011], Southern Clay Products, Inc.

[14] B U Nam and Y Son, *Polym. Bull.***65**, 837–847 (2010)

[15] A Riva, M Zanetti, M Braglia, G Camino and L Falqui, *Polym. Degrad. Stab*. 77, 299 (2002)

[16] J T Yoon, W H Jo, M S Lee and M B Ko, *Polymer***42**, 329-336 (2001)

[17] T Mandalia and F Bergaya, J. Phys.Chem. Sol. 67, 836-845 (2006)

[18] J Zhang, D D Jiang and C A Wilkie, Thermochim. Acta 430, 107-113 (2005)

[19] S M L Silva, M A Lopez-Manchado and M Arroyo, J. Nanosci. Nanotechnol. 7, 4456 (2007)

[20] L Priya and J P Jog, J. Polym. Sci. B 41, 31 (2003)

[21] Z Rozynek, K D Knudsen, J O Fossum, Y Meheust, B Wang and M Zhou, *J. Phys.: Condens. Mat.***22**, 324104 (2010)

[22] K D Knudsen, J O Fossum, G Helgesen and M W Haakestad, *Physica B: Condens. Mat.***352**, 247 (2004)

[23] I Dozov, E Paineau, P Davidson, K Antonova, C Baravian, I Bihannic and L J Michot, *J. Phys. Chem. B***115**, 7751–7765 (2011)

[24] Y Méheust, K D Knudsen and J O Fossum, *J. Appl. Cryst.***39**, 661 – 670 (2006)

[25] H Hemmen, N I Ringdal, E N de Azevedo, M Engelsberg, E L Hansen, Y Meheust, J O Fossum and K D Knudsen, *Langmuir* **25**, 12507–12515 (2009)

[26] M Engelsberg and E N de Azevedo,*J. Phys. Chem. B***112**, 7045–7050(2008)

[27] R Castberg,Z Rozynek, J O Fossum, K J Måløy, E Flekkøy, *"Rotation of Clay Particles in E-fields"*, manuscript in preparation

Paper VI

Characterisation of Paraffin/Clay Composites.

Z Rozynek, R Castberg, J O Fossum, and A Mikkelsen

In preparation.

Characterisation of Paraffin/Clay Nanocomposites

Zbigniew Rozynek[1], Rene Castberg[2], Jon Otto Fossum[1], Alexander Mikkelsen[1]

[1]Department of Physics, NTNU, Trondheim, Norway
[2]Department of Physics, UiO, Oslo, Norway

Abstract

This report is concerned with the behaviour of fluorohectorite synthetic clay particles dispersed in paraffin-wax. Firstly, information about pure paraffin-wax have been collected by means of rheometry (η vs. T), and microscopy observations. Secondly, the time evolution of the one-to-zero/zero-to-one water layer transition in fluorohectorite clay galleries was measured. The third part of the work using wide angle X-ray scattering (WAXS), is related to electric field (E) induced alignment from clay particles as a function of the E-field, and also to observations of system anisotropy during melting and crystallization of clay/paraffin nanocomposites.

Keywords: Clay, alignment, electric field, paraffin, composite

1. Introduction

Clay particles are expected to change and often also to improve many physical properties, i.e. mechanical strength, thermal stability, conductivity, etc. of the medium they are suspended in.[1,2,3] Some of these properties can be enhanced if the particles are deliberately orientationally aligned in the hosting medium. As an example, such particle organization can be utilized as a molecular barrier, i.e. permeability of gas molecule in polymer/clay composite is significantly reduced in direction normal to clay's platelet surfaces, whereas no change is expected for molecules propagating along the clay surfaces. Yano et al.,[4] showed that only 2 wt.% addition of montmorillonite clay particles into polyimide brought gas permeability down to a value less than half of that of polyimide alone. This result was explained by an increase in the tortuosity factor, [5] i.e. longer path that the diffusing molecule must travel in the presence of filler, since it needs to go around clay particles.[6] The alignment of the clay

[1] H J Walls, M W Riley, R R Singhal, R J Spontak, P S Fedkiw and S A Khan, *Adv. Funct. Mater.* **13**, 710-717 (2003)
[2] S H Kim, J Eun-Ju, Y Jung, M Han and S J Park, *Colloid. Surface.* **313**, 216-219 (2008)
[3] D Ratna, S Divekar, A B Samui, B C Chakraborty and A K Banthia, *Polymer* **47**, 4068-4074 (2006)
[4] K Yano, A Usuki, A Okada, T Kurauchi and O Kamigaito, *J. Polym. Sci. A* **31**, 2493–2498 (1993)
[5] L Nielsen, *J. Macromolecules Sci. Chem*. **A1**, 929 (1967)
[6] R K Bharadwaj, Macromolecules 34, 1989–1992 (2001)

particles can be induced by planar shearing,[7] extrusion,[8] gravity,[9] magnetic or electric fields.[10] An electric field is often used to produce anisotropic structures in order to obtain desirable physical properties. When coupled to the field or field gradient, either alternate-current (AC) or direct-current (DC), induced dipoles will result in a rotational or translation force on the particles in accord with the Clausius–Mossotti relation.[11] The alignment of particles can be monitored by means of electron or neutron diffraction[12,13], and the degree of anisotropy can be quantified and expressed in terms of a nematic order parameter (S_2) (see Section 3.3).[9,12] In previously studied clay/silicone oil suspensions, Rozynek et al.[12] showed that the values of the nematic order parameter did not depend on the *E*-field strength (within measured range of *E*-field strengths, namely 350-750 V/mm). Since the viscosity of the silicone was low (100 mPa.s) and the electric field high, the clay alignment was very rapid and therefore its development was difficult to monitor.

In the present work, the average clay orientational distribution is measured in a melted paraffin-wax. There are few major differences between these two types of system. The viscosity of paraffin-wax is significantly higher, their molecules are longer and the clay alignment is achieved at higher temperatures, i.e. between 65 and 100 ºC. The paraffin molecule thermal motions cannot be neglected here, and as it shown in this report, they are competing with electrical forces.

The layout of the report is as follows. Firstly, the sample preparation is explained in section 2. The wide angle X-ray scattering results are presented in section 3 and these include: time dependent one-to-zero water layer transition (section 3.1); zero-to-one water layer transition (section 3.2); alignment of clay particles as a function of the *E*-field strength (section 3.3), and finally the development of the system anisotropy during melting and crystallization (section 3.4). Conclusions and suggestions for further work are presented at the end in section 4.

[7] M Okamoto, P H Nam, P Maiti, T Kotaka,T Nakayama, M Takada, M Ohshima, A Usuki, N Hasegawa and H Okamoto, *Nano Lett*. **1**, (2001)
[8] X He, J Yang, L Zhu, B Wang, G Sun, P Lv, I Y Phang and T Liu, *Appl. Polym. Sci*. **102**, 542–549 (2006)
[9] H Hemmen, N I Ringdal, E N De Azevedo, M Engelsberg, E L Hansen, Yves Meheust, J O Fossum and K D Knudsen, *Langmuir* **25**, 12507–12515 (2009)
[10] J O Fossum, Y Méheust, K P S Parmar, K D Knudsen, K J Måløy and D M Fonseca*, Europhys. Lett.* **74**, 438-444 (2006)
[11] Y P Huang, M J Lee, M K Yang and C W Chen, *Appl. Clay Sci.* **49**, 163-169 (2010)
[12] Z Rozynek, K D Knudsen, J O Fossum, Y Meheust, B Wang and M Zhou*, J. Phys.: Condens. Mat.* **22**, 324104 (2010)
[13] K D Knudsen, J O Fossum, G Helgesen and M W Haakestad, *Physica B: Condens. Mat.* **352**, 247 (2004)

2. Sample preparation and characterisation

Lithium fluorohectorite (Li-Fh) was purchased from Corning Inc., New York in form of a white powder. Li-Fh is a synthetic 2:1 smectite clay having the nominal chemical formula $Li_{0.6}Mg_{2.4}Li_{0.6}S_4O_{10}F_2$ per half unit cell, where Li^+ is an interlayer exchangeable cation. Li-Fh has a surface charge of 1.2 e^-/unit cell and is a polydisperse clay with platelet diameters ranging from a few hundred nm up to several μm.[14] A *single* particle consists of about 80–100 platelets (crystalline sheets)[15] that stack on top of one another forming a "deck of card" structure. Since the thickness of such a stack is approximately 0.1 m, the resulting particle has a diameter-to-height ratio close to 50:1 on average. However, the *single* particles tend to agglomerate when dispersed into a non-polar medium (e.g. oils, polymeric matrices), unless chemically treated.[16] Both a shape and a size of aggregated structures may vary, and in general they depend on clay type and sample preparation.[17,18] The Li-Fh clay takes up water which results in its expendability. The swelling of layered 2:1 smectite clay particles consists of a change in the interlayer repetition distance between crystalline sheets (*d*-spacing), which depends on temperature and humidity, and this behaviour can be monitored by means of X-ray diffraction.[19]

The paraffin-wax normally refers to a mixture of *n*-alkanes (chemical formula C_nH_{2n+2}) with *n* in range between 20 and 40 determining molecules' characteristic length and also the melting temperature of paraffin matrix. The material used for composite preparation was obtained from Sigma-Aldrich (ASTM D 127, batch: MKBC6750). This particular type of paraffin wax, with its melting point around 65 ºC, was chosen due to the following reasons: (i) the X-ray peak positions related to the characteristic molecule dimensions should not overlap with clay reflections related to the interlamellar distance, i.e. space between clay crystalline sheets; (ii) optimal melting and crystallization temperatures providing both the ease of composite preparation and appropriate stiffness of the composite when in solid form at room temperature; (iii) relatively non-polar and non-conductive material that can be used as an electrorheological suspension when in the melted state.

---

[14] P D Kaviratna, T J Pinnavaia and P A Schroeder, *J. Phys. Chem. Solids* **57**, 1897 (1996).
[15] H Hemmen, L R Alme, J O Fossum and Y Meheust, *Phys.Rev. E* **82**, 036315 (2010)
[16] B Wang, M Zhou, Z Rozynek and J O Fossum, *J. Mater. Chem.* **19**, 1816 (2009)
[17] Z Rozynek, T Zacher, M Janek, M Čaplovičová and J O Fossum, *Electric Field Induced Structuring and Rheological Properties of Kaolinite and Halloysite Clays,* **to be submitted**
[18] Z Rozynek, B Wang, J O Fossum and K D Knudsen, *E-field Induced Alignment from Organically Modified Fluorohectorite Clay Particles*, **submitted to** *Eur. Phys. J. E*
[19] G J Silva, J O Fossum, E DiMasi and K J Måløy, *Phys.Rev. B* **67**, 094114 (2003)

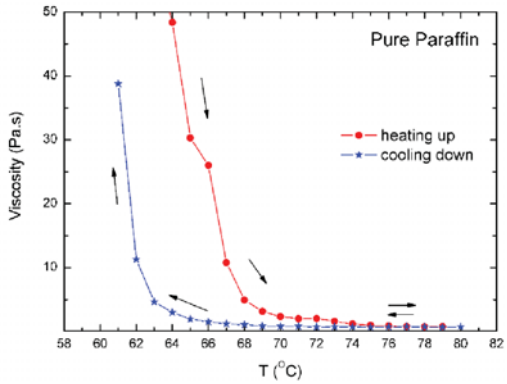

Figure 1. Rheological data showing both the melting and the crystallization transition temperatures for pure paraffin wax.

Prior the composite preparation a melting point of the pure paraffin-wax was measured employing rheometry Physica MCR 300 Rotational Rheometer equipped with a coaxial cylindrical cell C27/ERD. The crystalline melting temperature was found to be around 65 °C, as shown in Figure 1. The temperature range where crystallization occurs, and consequently, also the range of melting during the subsequent heating are broad. The observed hysteresis width is in addition broadened by fast heating rate of 1 °C/min. The complementary information about pure paraffin is provided by wide angle X-ray diffraction measurements, where diffractograms were collected for the sample during the solid-to-liquid transition.

In the solid form, the paraffin-wax has a crystal structure that is composed of stacked layers of the disentangled molecules, each layer being assembled of chain molecules with identical helical conformations.[20] However, when heated up they take on coiled conformations, just like polymers, and the regular structure is lost. Figure 2 shows the X-ray diffractograms of pure paraffin-wax during heating from 25 to 85 °C. The characteristic peaks attributed to the lengths of the oligomer molecules start shifting and decreasing at temperature range between 60 and 75 °C. They vanish completely for higher temperatures indicating a loss of crystallinity. These results coincide with our optical microscopy observations (see supporting Figure S1) and our rheological data. For more details about paraffin-waxes, their different structural phases, solid-liquid phase transitions, positional and orientational order, viscoelastic behaviour, etc. the reader is referred to the literature.[21,22,23,24]

[20] G Strobl, *The Physics of Polymers*, 2nd ed., Springer, p.143-144 (1997)
[21] E Sirota, H King, D. Singer and H. Shao, *J. Chem.Phys.* **98** 5809 (1993)
[22] G Ungar, *J. Phys. Chem.* **87** 689 (1983)
[23] M J Nowak and S J Severtson, *J. Mater. Sci.* **36** 4159 – 4166 (2001)
[24] A E Smith, *J. Chem. Phys.* **21**, 2229-2231 (1953)

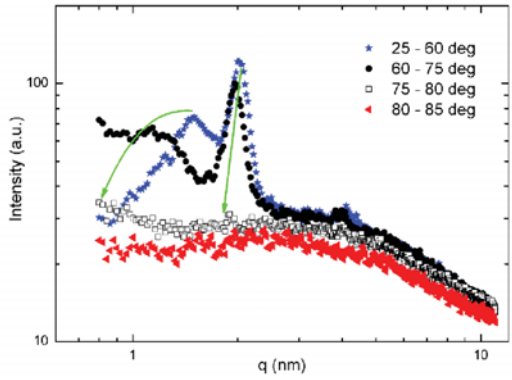

Figure 2. X-ray diffractograms of pure paraffin-wax during heating from 25 to 85 °C. The characteristic peaks attributed to the lengths of the oligomer molecules start shifting and decreasing at temperature range between 60 and 75 °C. They vanish completely for higher temperatures indicating a loss of crystallinity.

The first set of paraffin/clay composites were prepared as following: 1.4 g of Li-Fh clay powder with intercalated one water layer (1WL) was added slowly into 7 g of already pre-melted paraffin wax. After 10 min of stirring, the solution was set at rest for 3 min to let the biggest aggregates to sediment, and then the top part (80 %) was poured into a new 10 ml glass phial. The solution was kept at temperature around 120-130 °C while stirring. Every hour around 0.5 ml of a solution was taken out to make a solid cast. The X-ray diffractograms were collected immediately after each composite had solidified in order to investigate the time-dependent changes in clay's water content. The same samples (kept in a solid form at RT and 55 % RH) were re-examined by X-ray scattering again 6 months later in order to monitor the water content (Set1-Temp).

The second set of samples was prepared similarly to the first one. However, the first sample was collected after 12 h of stirring at temperature between 120 and 130 °C. Around 0.5 ml of a solution was used to make six samples. Electric field (AC, square wave, 100 Hz) of the following magnitudes 30, 60, 120, 240 and 480 V/mm were applied to five samples during their crystallization inside a custom-made mold equipped with electrodes at a gap of 6.5 mm. The X-ray diffractorgrams were collected after each composite had solidified in order to find the clay particle's orientational distribution of particles in an *E*-field (Set2).

The last batch was prepared to monitor the dynamic alignment of clay during the composite melting and crystallization inside a custom-made heating cell. The batch was prepared similarly to the procedure used for preparation of the first set with exception of temperature. The solution was kept at temperature around 80-90 °C while stirring for 2h. Then the solution was cooled down, cut into a small pieces that could fit inside the sample holder, then sealed inside the glass phial and stored until the experiment. The X-ray

diffractograms have been collected during heating and cooling in order to investigate changes in the clay particle's orientational distribution in an applied *E*-field (Set3-Dyn).

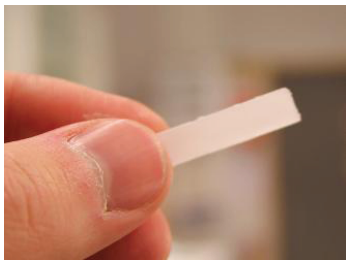

Figure 3. Paraffin/clay composite with dimensions of 30 x 6.5 x 1.5 mm^3.

The dimensions of all composites are 30 x 6.5 x 1.5 mm^3 and the example of a solid cast is shown in Figure 3.

3. Results

Two sample sets (Set1-Temp and Set2) were measured at our home laboratory (NTNU, Norway) using a NanoSTAR from Bruker AXS, setup in a wide-angle X-ray scattering (WAXS) configuration during the present experiments. This instrument is equipped with a CuKα source emitting X-rays at wavelength of 1.5418 Å; and a 2-D detector, which collects Bragg diffraction rings that allow investigating the orientational distribution of the clay platelet stacks embedded in the paraffin-wax matrix. The beamsize at the sample is about 0.4x0.4 mm^2. The sample-to-detector distance was calibrated using a silver behenate standard. The available scattering *q*-range for the setup used here, was 0.08 – 1 $Å^{-1}$.

Investigations of the dynamic alignment of clay particles (Set3-Dyn) were performed the European Synchrotron Radiation Facility (ESRF) in Grenoble, France. An X-ray beam with a wavelength of 0.9 Å and a 0.3x0.3 mm^2 beam size at the sample was used. The beamline BM01A is equipped with a two-dimensional MAR345 image plate detector with diameter of 345 mm. The available scattering *q*-range was 0.03 – 1.6 Å. The custom-made sample cell from NTNU (see supporting Figure S2) enabled precise heating and cooling in temperature range between 20 – 100 °C.

3.1. One-to-zero water layer transition

Water can intercalate in between each platelet causing the clay to swell. For Li-Fh the intercalation process, which is temperature and relative humidity dependent[6], yields four

stable hydration states.[25] The structures, referred to as having 0, 1, 1.5 or 2 intercalated water layers, are quite well ordered along the stacking direction. The unit cell along the stacking direction is given by the distance between the stacked platelets, and is around 1.0, 1.2, 1.38 and 1.5 nm for the case of 0WL, 1WL, 1.5WL and 2WL, respectively.

The first set of samples was measured in order to investigate the time-dependent changes in water content intercalated between the clay's crystalline sheets. The recorded X-ray data allowed monitoring the evolution of one-to-zero water layer transition.

Figure 4 shows radially integrated two-dimensional WAXS patterns from six samples prepared at different times, namely 0, 2, 3, 5, 7 and 10 h of stirring at elevated temperature around 120-130 °C. Initially, the clay particles (kept in room temperature and humidity, in form of powder) were in the pure 1WL hydration state (first measurement - blue dotted curve). The corresponding 100 Bragg peak was located at 1.21 nm. After some time (2 h) the intensity of the peak related to 1WL state has decreased and the new broad and not yet clear peak appeared at distance close to corresponding 0WL hydration state. Those two peaks are asymmetric in respect to their intensities and widths, and both of them are shifted from their initial d_{100}^{1WL}=1.21 nm and final d_{100}^{0WL} =1.03 nm positions towards lower and higher values (d_{100}^{1WL} =1.19 nm and d_{100}^{0WL} =1.07 nm), respectively. As time passes, the intensity of the peak related to 0WL state increases and becomes sharper. After 5 h a large number of clay particles in the scattering volume contain a significantly higher proportion of 0WL spacings over those from 1WL. It took nearly 10 h for the clay particles to reach nearly pure 0WL hydration final state (red curve with triangles). A minor population of clay particles possessing the intercalated water still exists, but is hardly detectable by the instrument used.

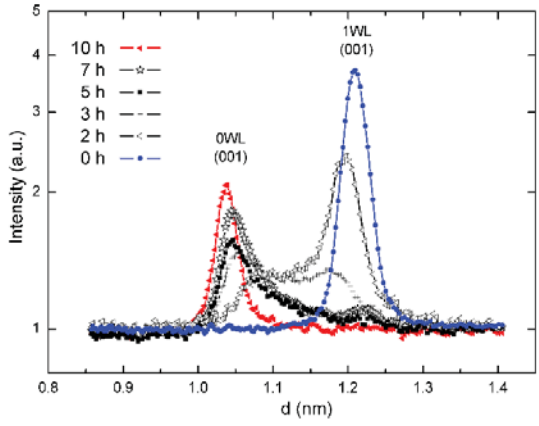

Figure 4. Time evolution of the 1-to-0 water layer transition (S1-Temp).

[25] R P Tenorio, M Engelsberg, J O Fossum and G J da Silva, *Langmuir* **26**, 9703 (2010)

"Traditionally" the interlayer hydration complexes occurring in smectite clays are considered as pure water layers states, i.e.: 0WL, 1WL, (1.5WL) and 2WL for the case of fluorohectorite clays.[26,27] The transitions between those states are "traditionally" considered to be rather sharp,[28] unlike the present case. However, recently Hemmen et al.[2] have thoroughly mapped systematic changes in the d-spacing values (before a discrete transition occurs) as a function of relative humidity (see reprinted Figure 5). Hemmen et.al.[2] investigated the 1-to-2 WL transition, whereas in the present case the 1-to-0 WL transition was monitored. The maximum values of the smooth changes in the d-spacing, respect to both the initial and the final state (1WL→0WL), are on the order of approximately 0.3 Å for deviation from 1WL and 0.5 Å for deviation from 0WL. These values are similar to what Hemmen et al. [2] reported.

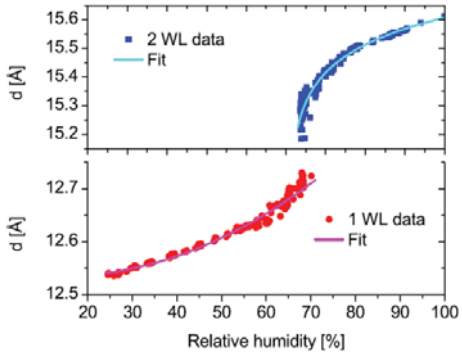

Figure 5. The *d*-spacing as a function or relative humidity (reprinted with permission from Hemmen et al. [2]).

3.2. Zero-to-one water layer transition and paraffin intercalation

The same samples (kept in a solid form) were investigated 6 months later in order to monitor the water content. The time it takes for 2:1 clays to become hydrated depends on relative humidity, temperature and size and charge of the exchangeable cation in the interlayer space. For powder samples this time evolution is in order of magnitude of hours.[29,30,31,32] However, as it could be expected, the time needed for whole clay population (being kept inside the paraffin-wax) to absorb 1WL is considerably longer. The effective RH around

[26] G J da Silva, J O Fossum, E DiMasi, K J Måløy and S B Lutnæs, *Phys.Rev. E* **66,** 011303 (2002)
[27] E N de Azevedo, M Engelsberg, J O Fossum and R E de Souza, *Langmuir* **23**, 5100 (2007)
[28] Y Meheust, B Sandnes, G Løvoll, K J Måløy, J O Fossum, G J da Silva, M S P Mundim, R Droppa and D M Fonseca, *Clay Science* **12**, 66 (2006)
[29] E DiMasi, J O Fossum and G J da Silva, Proceedings of the 12th International Clay Conference, Argentina (2003) *"Synchrotron X-ray Study of Hydration Dynamics in the Synthetic Swelling Clay Na-Fluorohectorite"*
[30] N Wada, D R Hines and S P Ahrenkiel, *Phys. Rev. B* **41**, 12895 (1990)
[31] R W Mooney, A G Keenan and L A Wood, *J. Am. Chem. Sot.* **74**, 1371 (1952)
[32] G Løvoll, B Sandnes, Y Méheust, K J Måløy, J O Fossum, G J da Silva, M S P Mundim, R Droppa Jr. and D M Fonseca *Physica B: Condensed Matter* **370**, 90 (2005)

embedded clay particles is low, since the water penetration through the oligomer matrix may be hindered.

Figure 6 shows ratios $I_1/(I_1+I_2)$ between magnitudes of 0WL and 1 WL peak intensities for 6 samples from the Set1-Temp. Their values are in range 0-1, where 0 indicates pure dehydrated state, 0.5 is obtained when the number of clay particles in two populations are equal, whereas 1 depicts the pure mono-hydrated state. Black squared data points were acquired from the sample investigated just after their preparation (as shown also in Figure 4). Red star data points were obtained from the same samples but measured 6 months later. It can be seen that for all samples (S1-0h omitted in this discussion), water molecules intercalated into clay galleries. However, the complete recovery from partially dehydrated state (0WL) to a mono-hydrated state (1WL) was accomplished by only one sample labelled S2-2h. By comparison of the values of the intensity ratio, it can be concluded that the remaining four samples absorbed comparable amount of water. The two lines in Figure 6 were obtained by fitting those four data points to a linear function $y=a+bx$ and the calculated values of the slope b were very similar, i.e. -0.047±0.011 and -0.055±0.018 for orange and olive curves, respectively.

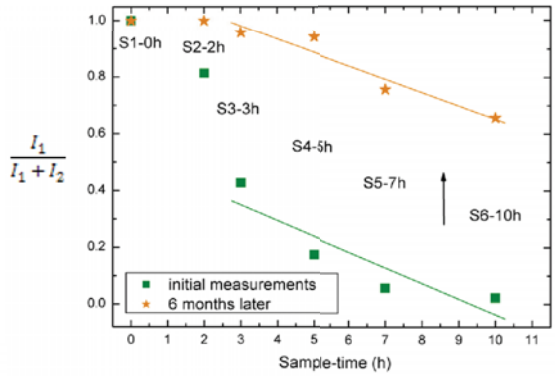

Figure 6. The ratios $I_1/(I_1+I_2)$ between magnitudes of 0WL and 1 WL peak intensities for 6 samples (Set1-Temp). Their values are in range 0-1, where 0 indicates pure dehydrated state, 0.5 is obtained when the number of clay particles in two populations are equal, whereas 1 depicts the pure mono-hydrated state.

3.3. Electric field induced alignment of clay particles

Figure 7 shows the two-dimensional WAXS patterns from paraffin/clay composites without (left) and with (right) an external electric field applied. The outer most ring originates from the Bragg 100 reflection that corresponds to the distance between clay's crystalline layers. It becomes anisotropic in presence of the E-field, which indicates that clay particles are aligned with their stacking direction perpendicular to the E-field lines.

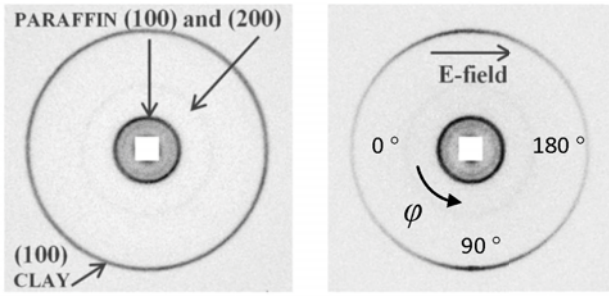

Figure 7. Two-dimensional WAXS patterns from paraffin/clay composites without (left) and with (right) an *E*-field of 240 V/mm applied. The outer most ring from clay becomes anisotropic indicating that clay particles are aligned with their stacking direction perpendicular to the *E*-field lines.

In order to quantify the degree of anisotropy of the system, i.e. how well the clay platelets aligned in respect to the *E*-field direction, one needs to integrate radially over a narrow *q*-range of the 2-D WAXS patterns (corresponding to the width of the 100 clay peak) and fit the obtained azimuthal plot to a Maier-Saupe function.[7] The result of such integration is presented in Figure 8. Intensities of the anisotropic Bragg 100 rings are plotted as a function of the azimuthal angle φ. The peaks at around 90 and 270 ° indicate a stacking direction being perpendicular to the *E*-field lines.

The quantification of the degree of anisotropy was achieved by fitting the azimuthal plots to the Maier-Saupe function (for details see [7,33,34]). In short, the fitting parameter is related to the full width at half maxima (smaller value, i.e. higher degree of anisotropy) and can be expressed as the nematic order parameter S_2, ranging from -½ to 1, where 1 indicates perfectly oriented particles in the nematic configuration, 0 states no orientation, and finally –½ indicates perfectly oriented particles in the anti-nematic configuration. It is expected here that the nematic order parameter should be in range between 0 and -1/2, since the clay particles align in the anti-nematic fashion, i.e. */consider a spherical coordinate system/* the direction of the clay stacks, are perpendicular to the field */zenith direction/*, without any preferred */azimuthal/* direction.

Figure 8 shows the azimuthal plots of the first Bragg peak amplitude under different *E*-field strengths for samples from the Set2. The scattered points are the experimental data, whereas the fully drawn lines are the Maier-Saupe fits. As can be seen, the width of the peaks decreases when the strength of the *E*-field increases indicating better particle alignment. The calculations of averaged nematic order parameters (five measurements at different sample position) for clay particles aligned in paraffin at different *E*-field strengths are presented in

[33] I Dozov, E Paineau, P Davidson, K Antonova, C Baravian, I Bihannic and L J Michot, J. Phys. Chem. B 115, 7751–7765 (2011)
[34] Y Méheust, K D Knudsen and J O Fossum, *J. Appl. Cryst.* **39,** 661 – 670 (2006)

Table 1. The S2 values are between -0.15±0.02 and -0.37±0.01, for E-field strengths from 30 to 480 V/mm.

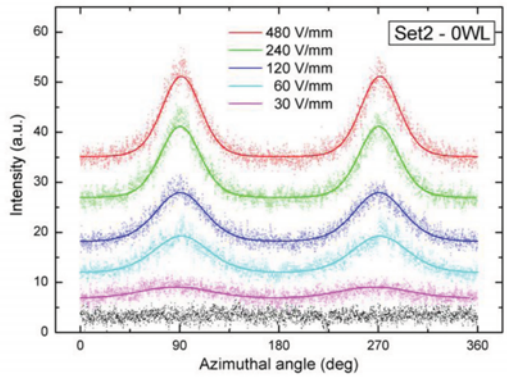

Figure 8. Azimuthal plots of the first Bragg peak amplitude at different E-field strengths.

E-field [V/mm]	30	60	120	240	480
S_2 [Set2]	**-0.15** ± 0.02	**-0.18** ± 0.06	**-0.28** ± 0.05	**-0.34** ± 0.02	**-0.37** ± 0.01

Table 1. Calculated nematic order parameters for clay particles aligned in paraffin matrix at different electric field strengths.

Unlike the previously studied alignment in clay/silicone oil suspension (at room temperature), the particle orientations in the melted paraffin-wax are clearly E-field dependent. It is suggested that thermal fluctuations play important role here, as the mechanism preventing particle alignment. At this high temperature (above 65 °C) there will be a significant contribution to the clay particle rotation opposing the electrical force ($\sim k_B T$ vs. pE, where k_B is a Boltzmann constant and p is the induced dipole moment). When cooling, the particles may still have significant rotational energy left when the paraffin solidifies (below 65 °C), and will thus be immobilized with a certain randomness in the orientation. However, when higher E-fields are used (above 175 V/mm), the orientation distribution is increasingly dominated by the electric field, overcoming the "randomizing" effect of temperature upon solidification. At some saturating field (here around 480 V/mm), it is likely that the E-field dominates completely.

Extending this discussion to already mentioned clay/silicone oil system: Silicone oil used had lower viscosity than the paraffin wax and in addition the measurements were conducted at room temperature. The clay particles had lower rotational energy ($k_B T$-dependent), and one could expect that the effect of the E-field would be close to maximum already at RT, and therefore a small or no effect on E-field amplitude was observed.

3.4.Alignment of clays during paraffin melting and crystallization

In order to find out whether the alignment of clay particles may be disrupted during the paraffin crystallization, the state of the nanoparticles dispersion was monitored during heating and cooling of the sample cell. Collection of the X-ray diffractograms started for samples at room temperature with no preferential orientation. The electric fields (125 and 250 V/mm) were applied from the beginning, and they have no impact on the system when sample in solid form. This is shown in Figure 9, where the nematic order parameter S_2=0 (in fact the zero value for frames 1-29 was ascribed by default, since it was not possible to converge the 1-D azimuthal plots with the fitting curve). The degree of anisotropy in the system increases when the paraffin starts melting (frames ~30-43), and the S_2 reaches it maximum values -0.26 and -0.36, for E–field strengths 125 and 250 V/mm, respectively. Interestingly, when time passes the nematic order values decrease slightly and the average value measured for frames 50-65 (paraffin is completely melted, kept ~100 °C) dropped by ~8 % and ~15 %, respectively. We suggest that the better particle alignment is achieved before individual particles start forming chain-like structures. After frame 65 the sample was let to cool down. It took around 5-7 frames for paraffin to start crystalizing. A small drop of the value of S_2 was observed between frames 72 and 76, but only for the sample at higher E-field. This might be caused by the paraffin crystallization. However, to be more conclusive on these two points, more measurements are needed. The final values of nematic order parameter (last frames - solid sample) are -0.28 and -0.32 for E-field strengths of 125 and 250 V/mm, respectively; and are in range of values obtained for samples from the Set2.

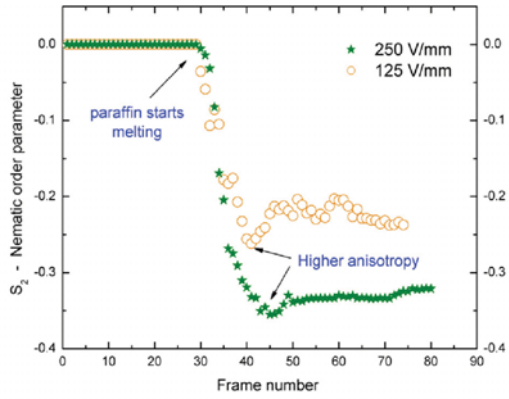

Figure 9. Development of the anisotropy in the system expressed by changes in the nematic order parameter S_2.

4. Conclusions

The primary objective of this research was to investigate the electric field induced alignment of fluorohectorite clay particles in oligomeric matrix. The degree of anisotropy dependence on the *E*-field strength was quantified and presented as the nematic order parameter S_2. It is suggested that thermal fluctuations play important role, as the mechanism preventing good particle organisation . It was found that at low *E*-fields (below 75 V/mm) the clay alignment is less than half of its maximum possible value. Therefor strong electric fields are required to dominate the thermal effects and achieve a successful alignment.

The development of the system anisotropy was observed during melting and crystallization of samples. Interestingly, it was found that, in average, the final clay particle orientation (i.e. after heating, aligning for long time in *E*-field, and solidifying) was not of the highest order. It is believed that particles lose their most optimal arrangement as a cost of chaining.

In addition, the dehydration of clay particles as a function of time was studied. It took nearly 10 h for the clay particles to reach nearly pure 0WL hydration final state, when sample in melted state. However, the zero-to-one water layer transition for clay particles being embedded in crystalized paraffin was very slow. This is due to very low water penetration through the oligomer matrix, and even after 6 months of exposure to air with 55 % of RH there is a population of clay particles possessing no or very little intercalated water.

Acknowledgement

The authors would like to thank Kennedth Dahl Knudsen for his comments that help improve the manuscript, and also D. Chernyshov for his assistance while performing experiments at the Swiss-Norwegian Beam Lines at ESRF.Yves Meheust and Henrik Hemmen are acknowledged as creators of the script for fitting the data to the Maier-Saupe function. The 2-D WAXS diffractograms were analysed using Fit2D created by A. P. Hammersley. This work was supported by the Research Council of Norway through the FRINAT Program: NFR project number 171300.

References

[1] H J Walls, M W Riley, R R Singhal, R J Spontak, P S Fedkiw and S A Khan, *Adv. Funct. Mater*. **13**, 710-717 (2003)
[2] S H Kim, J Eun-Ju, Y Jung, M Han and S J Park, *Colloid. Surface.* **313**, 216-219 (2008)
[3] D Ratna, S Divekar, A B Samui, B C Chakraborty and A K Banthia, *Polymer* **47**, 4068-4074 (2006)
[4] K Yano, A Usuki, A Okada, T Kurauchi and O Kamigaito, *J. Polym. Sci. A* **31**, 2493–2498 (1993)
[5] L Nielsen, *J. Macromol. Sci. Chem*. **A1**, 929 (1967)

[6] R K Bharadwaj, *Macromolecules* **34**, 1989–1992 (2001)
[7] M Okamoto, P H Nam, P Maiti, T Kotaka,T Nakayama, M Takada, M Ohshima, A Usuki, N Hasegawa and H Okamoto, *Nano Lett.* **1**, (2001)
[8] X He, J Yang, L Zhu, B Wang, G Sun, P Lv, I Y Phang and T Liu, *Appl. Polym. Sci.* **102**, 542–549 (2006)
[9] H Hemmen, N I Ringdal, E N De Azevedo, M Engelsberg, E L Hansen, Yves Meheust, J O Fossum and K D Knudsen, *Langmuir* **25**, 12507–12515 (2009)
[10] J O Fossum, Y Méheust, K P S Parmar, K D Knudsen, K J Måløy and D M Fonseca, *Europhys. Lett.* **74**, 438-444 (2006)
[11] Y P Huang, M J Lee, M K Yang and C W Chen, *Appl. Clay Sci*. **49**, 163-169 (2010)
[12] Z Rozynek, K D Knudsen, J O Fossum, Y Meheust, B Wang and M Zhou, *J. Phys.: Condens. Matter* **22**, 324104 (2010)
[13] K D Knudsen, J O Fossum, G Helgesen and M W Haakestad, *Physica B: Condens. Mat*. **352**, 247 (2004)
[14] P D Kaviratna, T J Pinnavaia and P A Schroeder, *J. Phys. Chem. Solids* **57**, 1897 (1996)
[15] H Hemmen, L R Alme, J O Fossum and Y Meheust, *Phys.Rev. E* **82**, 036315 (2010)
[16] B Wang, M Zhou, Z Rozynek and J O Fossum, *J. Mater. Chem.* **19**, 1816 (2009)
[17] Z Rozynek, T Zacher, M Janek, M Čaplovičová and J O Fossum, *Electric Field Induced Structuring and Rheological Properties of Kaolinite and Halloysite Clays*, **to be submitted**
[18] Z Rozynek, B Wang, J O Fossum and K D Knudsen, *E-field Induced Alignment from Organically Modified Fluorohectorite Clay Particles*, **submitted to** Eur. Phys. J. E
[19] G J Silva, J O Fossum, E DiMasi and K J Måløy, *Phys.Rev. B* **67**, 094114 (2003)
[20] G Strobl, *The Physics of Polymers*, 2nd ed., Springer, p.143-144 (1997)
[21] E Sirota, H King, D. Singer and H. Shao, *J. Chem.Phys.* **98** 5809 (1993)
[22] G Ungar, *J. Phys. Chem.* **87** 689-695 (1983)
[23] M J Nowak and S J Severtson, *J. Mater. Sci.* **36** 4159 – 4166 (2001)
[24] A E Smith, *J. Chem. Phys*. **21**, 2229-2231 (1953)
[25] R P Tenorio, M Engelsberg, J O Fossum and G J da Silva, *Langmuir* **26**, 9703 (2010)
[26] G J da Silva, J O Fossum, E DiMasi, K J Måløy and S B Lutnæs, *Phys.Rev. E* **66**, 011303 (2002)
[27] E N de Azevedo, M Engelsberg, J O Fossum and R E de Souza, *Langmuir* **23**, 5100 (2007)
[28] Y Meheust, B Sandnes, G Løvoll, K J Måløy, J O Fossum, G J da Silva, M S P Mundim, R Droppa and D M Fonseca, *Clay Sci.* **12**, 66 (2006)
[29] E DiMasi, J O Fossum and G J da Silva, *Synchrotron X-ray Study of Hydration Dynamics in the Synthetic Swelling Clay Na-Fluorohectorite,* Proceedings of the 12th International Clay Conference, Argentina (2003)
[30] N Wada, D R Hines and S P Ahrenkiel, *Phys. Rev. B* **41**, 12895 (1990)
[31] R W Mooney, A G Keenan and L A Wood, *J. Am. Chem. Soc.* **74**, 1371 (1952)
[32] G Løvoll, B Sandnes, Y Méheust, K J Måløy, J O Fossum, G J da Silva, M S P Mundim, R Droppa Jr. and D M Fonseca, *Physica B: Condensed Matter* **370**, 90 (2005)
[33] I Dozov, E Paineau, P Davidson, K Antonova, C Baravian, I Bihannic and L J Michot, *J. Phys. Chem. B* **115**, 7751-7765 (2011)
[34] Y Méheust, K D Knudsen and J O Fossum, *J. Appl. Cryst*. **39**, 661-670 (2006)

5. Supporting materials

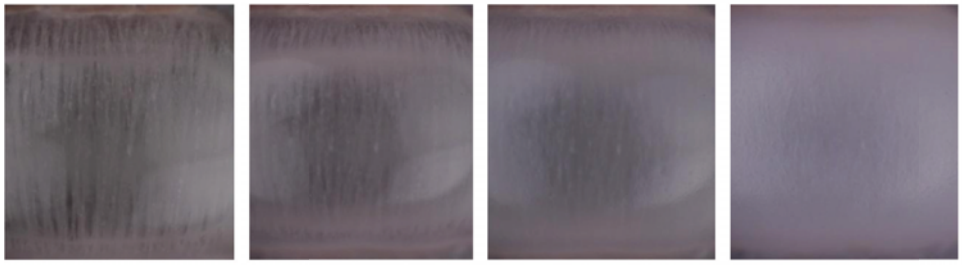

Figure S1. Optical microscopy images of clay/paraffin during paraffin crystallization.

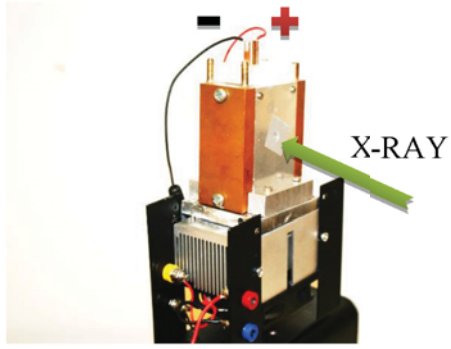

Figure S2. Experimental set-up for studying of dynamic alignment of clay particles during melting and crystallization of clay/paraffin-wax composites.

Paper VII

Electric Field Induced Structuring and Rheological Properties of Kaolinite and Halloysite Clays

Z Rozynek, T Zacher, M Janek, M Čaplovičová and J O Fossum

In preparation.

Electric Field Induced Structuring and Rheological Properties of Kaolinite and Halloysite Clays

Zbigniew Rozynek[a], Tomáš Zacher[b], Marián Janek[b,c] Mária Čaplovičová[d] and Jon Otto Fossum[a]

[a] Department of Physics, NTNU, Høgskoleringen 5, NO-7491 Trondheim, Norway

[b] Department of Physical and Theoretical Chemistry, Faculty of Natural Sciences, Comenius University, Mlynská dolina CH1, SK-84215 Bratislava, Slovakia

[c] Institute of Technology, Slovak Academy of Sciences, Dúbravská cesta 9, SK-84513 Bratislava, Slovakia

[d] Department of Geology of Mineral Deposits, Faculty of Natural Sciences, Comenius University, Mlynská dolina CH2, SK-84215 Bratislava, Slovakia

Abstract

Electric-field (E) induced structuring from two types of clay particles belonging to the kaolin group of minerals, namely kaolinite and halloysite, were studied in relation to the electrorheological response of silicone oil and paraffin dispersions of both clays. Firstly, the structural and morphological properties of both types of clays were probed in detail by means of XRD and FTIR techniques. The second part of the work was related to the E-field induced structuring from both types of clay particles, and this was investigated by means of WAXS with a support of SEM, TEM and optical microscopy techniques. Finally, the electrorheological response of the samples was measured. Well-structured kaolinite particle dispersions were found to have an improved response relative to dispersions of the less-structured halloysite particles. Results of electrical current measurements indicated that the improved current response of halloysite vs. kaolinite arises from involvement of small amount of surface adsorbed water molecules as the applied potentials are far above the water oxidation/reduction electrode over-potentials.

Keywords: kaolinite, halloysite, clay minerals, WAXS, XRD, FTIR, TEM, SEM, TGA, rheology, electrical current

1. Introduction

Kaolin is one of the most important industrial mineral ores in world markets used in paper coating and filling, ceramics, paint, plastics, textiles, gaskets, adhesives, sealants, caulks, fertilizers, rubber, ink, fiberglass, cracking catalysts and many other areas.[1] Easily accessible clay ore has always played an important role in human life.[2,3] Similarly, the traditional utilisation fields of halloysite include ceramic industry, cosmetics and catalysis. In addition, each of these minerals are used as an industrial filler.[4,5] The specific surface area of halloysite particles is very high (typically between 50-80 m^2/g)[6,7] compared to that of kaolinite (typically between 3-7)[8,9], which makes halloysite potentially suitable for the accommodation of a range of guests molecules for new applications, for example small pharmaceutical molecules, or for e.g. immobilization of large-sized enzymes such as serum albumin and conalbumin.

Halloysite nanotubes could also be combined with a polymer matrix to form low-density nanocomposites, replacing larger quantities of macro- or microcounterparts such as glass or carbon fibers. Halloysite tubes can also be used as nanoreactors to host reactants for biomimetic synthesis.[10] The halloysite microtubules can act as a time-release capsule, dissolving over time, and can be filled with different functional additives such as pharmaceuticals, herbicides, pest repellents, or halloysite nanotubes can be coated with metallic and other substances to achieve a wide variety of electrical, chemical and physical properties, ideal for use in electronic fabrication and other high-tech ceramic composite applications.[11]

Both kaolinite and halloysite belong to the kaolinite group of minerals having essentially similar chemical composition with the nominal formula $Al_2Si_2O_5(OH)_4$ per half unit cell, but have important structural layer stacking differences. Kaolinite is a 1:1 naturally occurring clay

---

[1] Murray H. H. (1991) *Appl. Clay Sci.*, **5**, 379-395.
[2] Konta J. (1995) *Appl. Clay Sci.*, **10**, 275-335.
[3] Beneke K. (1995) Zur Geschichte der Grenzflächenerscheinungen – mit ausgesuchten Beispielen – Beiträge zur Geschichte der Kolloidwissenschaften IV. Mitteilungen der Kolloid-Gesellschaft, Verlag Reinhard Knof, Kiel: p81 (in German).
[4] Jasmund K. and Lagaly G. (1993) Tonminerale und Tone. Struktur, Eigenschaften, Anwendung und Einsatz in Industrie und Umwelt. Stenkopff, Darmstadt: 490p (in German).
[5] Harvey C.C. and Murray H.H. (1997) *Appl. Clay Sci.*, **11**, 285-310.
[6] Zheng-Hong H., Aiping W., Feiyu K. and Xiuyun C. (2010) *Mater. Lett.,* **64** 2444-2446
[7] Mellouk S., Belhakem A., Marouf-Khelifa K., Schott J. and Khelifa A. (2011) *J. Colloid. Interf. Sci.,* **360** 716-724
[8] Zhang X., Lin S., Chen Z., Megharaj M. and Naidu R., (2011) *Water Res.,* **45** 3481-3488
[9] Li W., Lu K. and Walz J. Y. .(2011) *J. Am. Ceram. Soc.,* **94** 1256-1264
[10] Yuan P., Southon P.D., Liu Z., Green M.E., Hook M.J., Antill S.J. and Kepert C.J. (2008) *J. Phys. Chem.,* **112**, 15742-51.
[11] Joussein E., Petit S., Churchman J., Theng B., Righi D. and Delvaux B. (2005) *Clay Miner.*, **40**, 383-426.

mineral with a layer structure consisting of siloxane and gibbsite-like sheets. The siloxane sheet is composed of SiO_4 tetrahedra linked in a hexagonal array. The base of the tetrahedral sheet is approximately coplanar and the apical oxygens are linked to a second sheet containing the octahedra – the gibbsite type sheet – forming basic structural layers. The OH groups of the gibbsite sheet interact via hydrogen bonds to the siloxane surface of the neighbouring layer. Natural kaolinites have various degree of structural disorder or "crystallinity", which is often related to the conditions of genesis of the particular mineral.[12,13,14] Therefore, kaolinites are classified as either low defect or high defect kaolinites depending on their varying degrees of order in the crystal structure.[15] The structural disorder or "crystallinity" of kaolinite was in the past proposed to be quantified by the empirical Hinckley index, useful for well-ordered kaolinites.[16] Poorly ordered kaolinites were better characterized by the empirical crystallinity indices according to Hughes & Brown.[17]

Halloysite differs intrinsically from the kaolinite in its layer stacking sequence. It can intercalate a monolayer of water molecules between the aluminosilicate layers and therefore the existence of two different mineral species of halloysite have been reported, namely the anhydrous 7 Å form and its hydrated 10 Å form, marked also as *halloysite* (*7Å*) and *halloysite* (*10Å*), respectively. The stoichiometry of halloysite (10Å) follows approximately the formula $Al_2Si_2O_5(OH)_4 \cdot 2H_2O$ per half unit cell. This hydrated form converts easily into the dehydrated form at atmospheric pressure, when dried at temperatures above 60 °C, or in vacuum at room temperature. The anhydrous form with a basal spacing near 7.2 Å is metastable, and can recover its interlayer water in a wet environment. Particles of halloysite consist of tubes, rolls and cylinders, as well as irregular or spheroidal particles. Halloysite presents a highly disordered structure, with random dislocations and shifts in both the *a* and *b* crystallographic directions.[18] The reason for the curvature of the layers is usually attributed to the lateral misfit between the octahedral and tetrahedral sheets in the structure of halloysite.[19] It was postulated that stacking disorder plays an important role for hydration of kaolinite and formation of halloysite.[20,21] Because the 1:1 layers in hydrated halloysite are separated from each other by a

---

[12] Brindley G. W., Kao C. C, Harrison J. L., Lipsicas M. and Raythatha R. (1986) *Clay Clay Miner.* **34**, 239-249.
[13] Giese R. F. (1988) In: Bailey S.W. (Ed.) *Rev. in Mineral.*, **19**, Mineral. Soc. Amer., Washigton, D.C., 29-66.
[14] Madejová J., Kraus I., Tunega D. and Šamajová E. (1997) *Geologica Carpathica- Series Clays*, **6**, 1, Bratislava, 3-10.
[15] Brindley G. W. and Robinson K. (1947) *Brit. Ceram. Soc. Trans.,* **46**, 49-62.
[16] Hinckley D. N. (1963) *Clay Clay Miner.,* **11**, 229-235.
[17] Hughes J. C. and Brown G. (1979) *J. Soil Sci.*, **30**, 557-563.
[18] Brindley, G. W. and Robinson, K. (1946) *Trans. Faraday Soc.,* **42B**, 198-205.
[19] Bates T., Hildebrand F. A. and Swineford A. (1950) *Amer. Miner.,* **35**, 463-484.
[20] Costanzo P. M., Giese R. F. and Clemency C. V. (1984) *Clay Clay Miner.,* **32,** 29-35.
[21] Costanzo P. M., Giese R. F. and Lipsicas M. (1984) *Clay Clay Miner.,* **32,** 419-428.

layer of water molecules, and due to higher structural disorder, halloysite have usually a larger cation exchange capacity and surface area than kaolinite.[22,23,24,25]

With respect to the chemical identity but differing morphology of kaolinite and halloysite particles, the effect of an electric field on electrorheological properties of silicone oil dispersions of both clays have been tested. Chassagne at al.[26] presented an extended study of the electrophoretic mobility of kaolinite suspensions for different types of salt, various pH and ionic strengths. They presented a new analytical theory for electrophoresis, including extra conductance, hence indicating that the electrokinetic response of kaolinite cannot be fitted without the inclusion of a Stern layer conductance. Additionally, Rowlands and Wyndham[27] investigated the dynamic mobility and dielectric response of kaolinite particles. They concluded that information about the particle size, electrokinetic charge or zeta potential can be obtained from the dynamic mobility spectrum. However, to our knowledge, there are no data published yet for halloysite particles regarding electrokinetic response in non-polar media. Therefore, the aim of the present study was focused on the comparison of electro-rheological response of natural kaolinite and halloysite particles having different morphology and particle size distributions, but almost identical chemical composition.

2. Samples and experimental techniques

2.1. Sample preparation

A German kaolin from a primary deposit in Bayern-Oberpfalz (referred as KBO) was used in this study. The purified sample received from Hirschau, Germany, was washed with distilled water (conductivity ~1.0 μS), dried at 65 °C, and crushed in an agate mortar before the characterization measurements. The halloysite sample was from a Slovak primary deposit located at Michalovce - Biela Hora (referred as HBH). Soluble phases of iron oxide/hydroxides were removed according to the procedure of Tributh and Lagaly.[28,29] This procedure includes removal of carbonates, iron oxohydroxides, organic matter such as humic material and size fractionation. The fine fraction of halloysite particles was prepared by a sedimentation method using Stoke´s equation to calculate the time required to separate

[22] Gardolinski J. E., Filho H.P.M. and Wypych F. (2003) *Quim. Nova,* **26**, 25–30.
[23] Costanzo P. M. and Giese J. R. F. (1985), *Clay Clay Miner.,* **33**, 415–423.
[24] Cheng H., Frost R. L., Yang J., Liu Q. and He J. (2010) *Thermochim Acta*, ***511,*** 124–128.
[25] Nicolini K.P., Fukamachi C.R.B., Wypych F., Mangrich A.S. (2009) *J.Colloid Interf. Sci.,* **338**, 474-479.
[26] Chassagne C., Mietta F. and Winterwerp J. C. (2009) *J. Colloid Interf. Sci.*, **336**, 352-359.
[27] Rowlands W. N. and Wyndham O´Brien R. (1995) *J. Colloid Interf. Sci.*, **175**, 190 – 200.
[28] Tributh H. and Lagaly G. (1986) *GIT Fachz.,* Lab. 30, 524 (in German).
[29] Tributh H. and Lagaly G. (1986) *GIT Fachz.* Lab. 30, 771 (in German).

particles having <2μm equivalent diameter. Collected fine particles were centrifuged, washed with distilled water (conductivity ~1.0 μS), dried at 65 °C, and crushed in an agate mortar before performing the characterization measurements.

For rheological measurements dispersions of KBO and HBH in silicone oil (~5 wt.%) were prepared by mixing in an orbital shaker for minimum 12 h and applying 30 minutes of ultrasonication prior to each rheological and current measurement.

For wide-angle X-ray scattering (WAXS) experiments, it was decided to prepare KBO/ paraffin, and HBH/paraffin composites, since (from our previous observations) the position of a diffuse Bragg diffraction peak from silicone oil overlaps with the 001 Bragg reflection from both clays. The composites were prepared as following: 1.4 g of each clay powder was slowly added into 7g of already pre-melted paraffin-wax (120-130 °C). After vigorous stirring, the suspensions were left undisturbed for 5 minutes to let the largest particle aggregates sediment and then the top portion (80 %) was poured into a new 10 ml glass vial. The dispersions were kept at ~125 °C under stirring. After 2 h four samples were prepared and these included: KBO/paraffin and HBH/paraffin composites cast with and without *E*-field present. After the samples solidified, having a form of stripes (~15 x 6.5 x 1.5 mm), the WAXS measurements were performed.

Optical microscopy measurements were done using low concentration (below 0.5 wt.%) clay dispersions (for observation clarity). All high quality scanning electron microscopy (SEM) images were taken from carbon-coated clay particles.

2.2. Experimental techniques

2.2.1. XRD

X-ray diffraction patterns from kaolinite and halloysite powders were obtained using a Stoe Stadi-P transmission X-ray powder diffractometer equipped with a curved Ge(111) primary beam monochromator and Co radiation ($CoK\alpha_1$ λ=0.178896 nm). The patterns were scanned in the range of 3-60° in 2θ with a step size of 0.02° and a counting time of 1.5 s/step.

2.2.2. FTIR

Infrared spectra of the KBO and HBH samples were obtained using a Nicolet Magna 750 Fourier transform IR spectrometer, equipped with a KBr beam splitter, and a DTGS KBr detector for MIR measurements. The KBr pressed disc technique (0.2 mg of sample and 200 mg of KBr) was used. The discs were heated in a furnace overnight at 130 °C to minimize the water adsorbed on KBr and the clay mineral sample. Spectra were recorded over the range

4000-400 cm^{-1}, accumulating 128 spectral scans, with a resolution of 4 cm^{-1} in the absorbance mode.

2.2.3. TEM/SEM

Transmission electron microscopy (TEM) images of KBO and HBH were recorded on a JEOL JEM-2000FX transmission electron microscope with an accelerating voltage of 160 kV. For this characterization the samples were prepared as follows: suspensions of samples KBO and HBH with ethanol was kept under ultrasound for 5 minutes. Then a drop of the sample was spilled on a copper reticle coated colloidal film with a layer of carbon and finally the sample was dried at room temperature.

Scanning electron micrographs were acquired using a field emission scanning electron microscope (Zeiss Ultra, 55 Limited Edition, accelerated voltage 10-15kV). For the SEM samples, a suspension of a small amount (<0.01 wt.%) of sample was dispersed in de-ionized water and ultrasonicated for 1 h, and then pipetted onto a SEM stub. Before images were collected, all samples were carbon-coated.

2.2.4. WAXS

The WAXS experiment was carried out at the European Synchrotron Radiation Facility (ESRF) in Grenoble, France. An x-ray beam with a wavelength of 0.9 Å and a 0.5 × 0.5 mm^2 beam size at the sample was used. The Swiss-Norwegian beamline (SNBL) BM01A is equipped with a two-dimensional MAR345 image plate detector with a diameter of 345 mm. The sample to detector distance was set to 350 mm, enabling the detection of scattering in a *q*-range of approximately 0.65 – 17 nm^{-1}, which corresponds to the real space d-range of 0.37 – 10 nm.

2.2.5. Rheometry and current measurements

The rheological properties of the clay suspensions were measured under DC electric fields using a Physica MCR300 Rotational Rheometer equipped with a coaxial cylinder (Physica ERD CC/27). All the rheological measurements were performed at constant temperature of 23°C. These included controlled shear rate tests for measuring shear stress as a function of shear rate and bifurcation measurements. In the former experiment the so-called flow curves were collected in the shear rate range between 0.1 and 1000 s^{-1} and fitted to Herschel–Bulkley model in order to obtain the static yield stresses for samples at different *E*-field strengths, namely 250, 500, 750, 1000, 1500 and 2000 V/mm, respectively. The bifurcation tests were performed as a complementary method to verify the values of the yield stresses. In this method samples were forced to flow under a constant stress, and then let to evolve in the

presence of an *E*-field (see details in the Result section 3.6). In addition, current measurements were performed (in the same rheological cell) using an Agilent 34401A multimeter.

2.2.6. TGA/DTG

Thermal gravimetric analysis (TGA) was performed on a TGA/SDTA851^e instrument (Mettler Toledo As.) with a heating rate of 2 ºC/min up to 800°C under static air conditions. About 20 mg of sample was supplied to the Alumina crucible.

3. Results and discussion

Since both types of clays are natural minerals, it is very important to begin the experimental part with sample characterizations considering structural and morphological properties, and perform cross-check measurements to verify the successful sample purification. Therefore the various complementary techniques described above were used: X-ray powder diffraction (XRD), Fourier transform infrared spectroscopy (FTIR), electron microscopy micrographs (TEM/SEM) and thermogravimetry (TGA/DTG). After the initial characterization, the electric field induced structuring from clay particles was investigated by means of synchrotron X-ray scattering, followed by the measurements of electrorheological and electrical properties.

3.1. XRD analysis

The structural and morphological properties of layered compounds such as kaolinite and halloysite clay minerals can be non-directly deduced from their diffraction patterns, because they reveal the variety of order-disorder structural effects. Measured X-ray powder diffraction patterns of both samples are shown in Figure 1, where the transition from the sharp diffraction peaks in KBO to the mainly diffuse and "tailed" reflections in the pattern of HBH are shown, indicating decreased layer stacking order of the HBH sample. The *d*-spacing of the first basal reflections of KBO is 0.71 nm and of HBH 0.74 nm, hence anhydrous forms of halloysite was *practically* used in the experiments (see TGA/DTG analysis in section 3.7). The group of reflections from (020) to (002) particularly reflects the change of crystallinity. In this region the clearly resolved doublet $(1\bar{1}\bar{1})$ and $(1\bar{1}\bar{1})$ of the KBO sample yields a single broadened reflection for the HBH sample. This represents evidence for the decrease in crystallinity.[30]

[30] Grim R. E. (1968) *Clay Mineralogy*, 2nd Ed., McGraw-Hill Book Company, New York, USA.

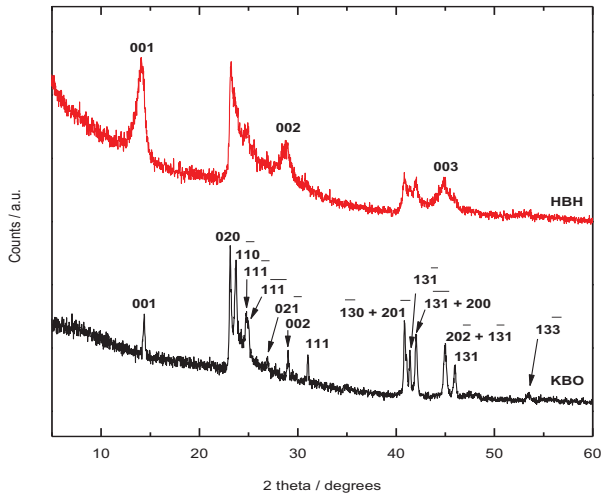

Figure 1. The XRD patterns of KBO and HBH samples with indicated reflections.

3.2. IR spectroscopy.

Infrared spectroscopy (FTIR) was used as a complementary method to X-ray diffraction to investigate possible mineral admixtures in the samples. IR spectra serve as a fingerprint pattern for mineral identification and gives unique information about the mineral structure. Well-ordered KBO samples revealed four clearly-resolved absorption bands in the OH stretching region 3693-3620 cm^{-1} (Figure 2). Inner hydroxyl groups, located in ditrigonal cavities of kaolinite, give the stretching absorption band at 3620 cm^{-1}. The other OH groups located at the external surface of the octahedral sheets interact via weak hydrogen bonds with the basal oxygens of the tetrahedral sheet. A strong band at 3696 cm^{-1} is related to the in-phase symmetric stretching vibration, two weak absorptions at 3668 and 3652 cm^{-1} are assigned to out-of-plane stretching vibrations.[31,32] These four clearly resolved bands and the higher intensity of the band at 3652 cm^{-1} observed for KBO compared to HBH reflect also the higher structural order of the KBO sample. Thus, the KBO can be classified as well-ordered kaolinite. In contrary, the IR spectrum of HBH shows intensive absorption bands only at 3696 and 3621 cm^{-1} in the OH stretching region (Figure 2). The very low intensity of OH stretching bands at 3671 and 3652 cm^{-1} reflect a poorly ordered structure typical for halloysite samples.[4] (Madejová et al., 1997).

[31] Farmer V. C. (2000) *Spectrochim. Acta A*, **56** 927.
[32] Madejová J. (2003) *Vib. Spectrosc.*, **31**, 1–10.

The Si–O stretching and bending as well as OH bending absorption bands are in the region 1300–400 cm^{-1} (Figure 2). Differences in layer stacking arrangement of the basic layers are reflected in the positions and shape of the bands. Clear differences between KBO and HBH can be seen in the 1300-400 cm^{-1} region. The Si–O stretching vibrations of KBO show well-resolved bands at 1114, 1031 and 1007 cm^{-1}. Broadened bands appear for Si-O stretching bands of HBH at 1101, 1034 and 1011 cm^{-1}. The AlAlOH bending bands at 937 and 912 cm^{-1} for KBO are detected as a shoulder near 939 cm^{-1} and as a distinct band at 913 cm^{-1} for HBH. The absorption bands corresponding to Si-O-Al and Si-O-Si deformation vibrations are present at about 538 and 469 cm^{-1}, respectively. The band at 430 cm^{-1} was observed in both KBO and HBH spectra and belongs to Si-O deformation vibrations.[33] The insert in Figure 2 (region 3700-3600 cm^{-1}) shows also stretching bands typical for kaolinite in the HBH sample at 3654 and 3649 cm^{-1}, indicating that kaolinite-like particles are present in the halloysite. However, no other mineral admixtures or impurities were detected by the FTIR technique.

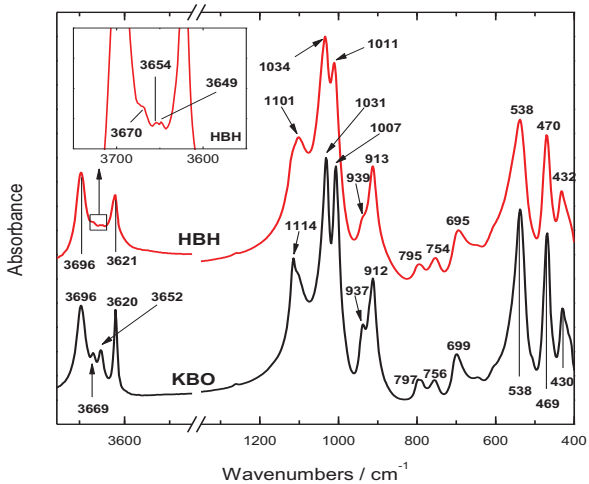

Figure 2. FTIR spectra of kaolinite (KBO) and halloysite (HBH) samples.

[33] Madejová J., Keckes J., Pálková H. and Komadel P. (2002) *Clay Miner.,* **37**, 377–388.

3.3. TEM/SEM

The basic difficulty in classifying kaolinites and halloysites according to a scheme of progressive layer disordering is in the various kinds and degrees of disorder which can be present in the structure. Crystal size and shape are important variables because layers can be planar, curved, rolled, cylindrical or quasi-spherical.[34] TEM images of the KBO sample (Figure 3) show the well-crystallized mineral with platy particles of hexagonal and/or pseudohexagonal symmetry and a lateral size ranging from 0.2 to 4.0 μm. The aspect ratio (lateral length/height) of the KBO particles was estimated to be about 5.[35] TEM images of the HBH sample (Figure 4) show that the morphology of our halloysite particles is significantly different from that of our kaolinite samples. Halloysite show irregular particles with flake shape and a high portion of tubular particles. The outer diameters of rolled halloysite tubes are roughly in the range 0.05 - 0.10 μm.

For comparison, SEM images show the general morphology of aggregated particles (right panel of Figure 3 and Figure 4). The SEM image of KBO shows a typical aggregated structure made out of a few *single particles* with their edges pointing out of the image (other particles in the image lay flat on the SEM stub). The *single particle* is defined here as a "deck of cards" structure consisting of tens of crystalline basic layers stacked on top of one another. The HBH particles are much smaller than KBO and hence tend to form aggregates in a not clearly defined fashion. Most of the SEM micrographs of HBH showed randomly oriented aggregates formed from many particles of different shapes as demonstrated also on the TEM images.

---

[34] Brindley G.W. (1980) *Order-disorder in clay mineral structures: in Crystal Structures of Clay Minerals and their X-ray Identification* (G.W. Brindley and G. Brown, Ed.), **5**, Mineralogical Soc., London

[35] Janek M, Emmerich K, Heissler S, Nüesch R (2007) *Chem. Mater.*, **19**, 684-693.

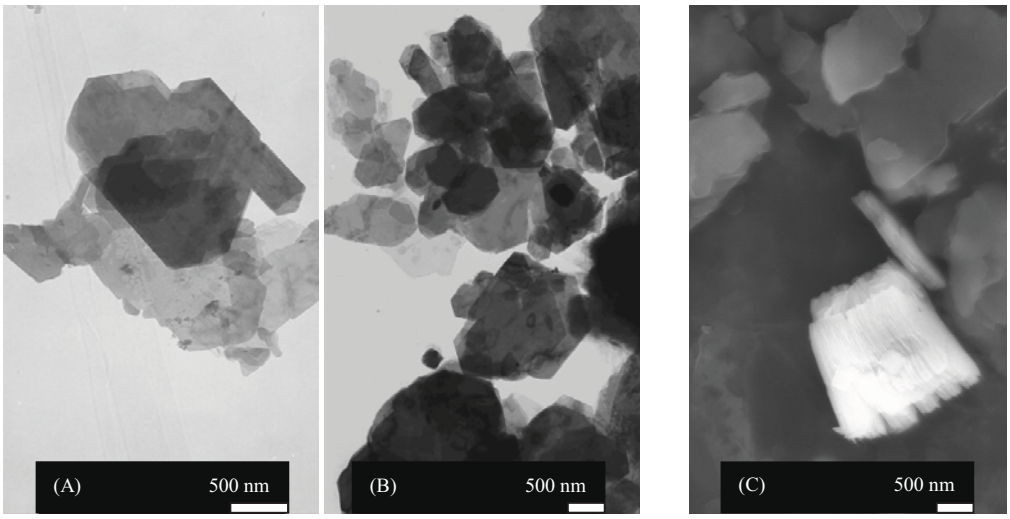

Figure 3. The KBO clay particles' shape and size distribution can be determined from TEM (A,B) micrographs. The SEM (C) image show the KBO typical aggregated structure made out of few single particles.

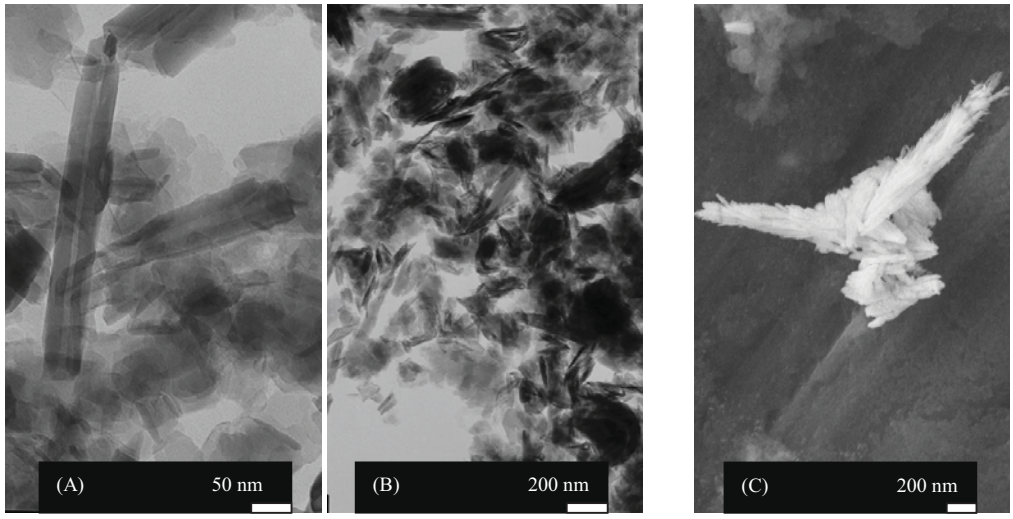

Figure 4. The HBH clay particles' shape and size distribution can be determined from TEM (A,B) micrographs. The SEM (C) image show the HBH undefined aggregated structure made out many small tubular single particles.

3.4. WAXS

Paraffin-wax (hydrocarbons with a general chemical formula C_nH_{2n+2}) is an electrically non-conductive and non-polar material with a low dielectric constant. It is used here as an alternative material to silicone oil being used as a carrier for electrorheological (ER) suspensions (see Section 3.6). Since the position of the diffuse Bragg diffraction peak from the silicone oil overlaps with the 001 Bragg reflection from both clays, its use is limited. The melting temperatures of paraffin-waxes are relatively low, which make them easy to handle during the preparation of composites. In general, the solid-to-liquid transition temperature $T_{s\text{-}l}$ depends on n, which also determines the characteristic length of the paraffin chain L when in crystalline form (see Figure 5A - the strong inner ring near to the beamstop). Hence, it is important to choose an appropriate paraffin type, because the characteristic Bragg peaks from clay can overlap with those from paraffin.

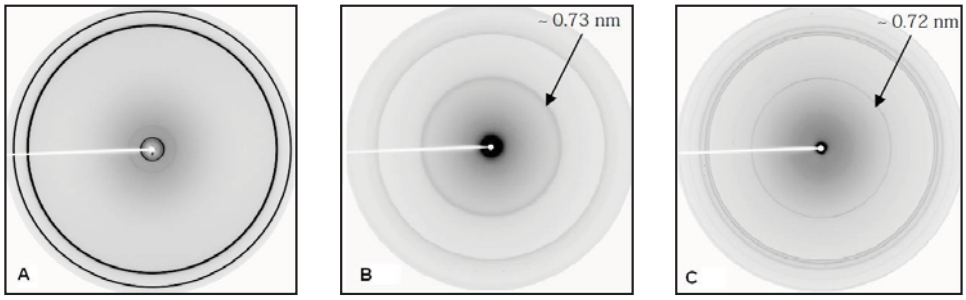

Figure 5. WAXS 2-D images. (A) pure paraffin-wax (B) HBH powder (C) KBO powder

Figure 5B and Figure 5C show 2-D WAXS diffractograms from HBH and KBO powders respectively. The distance $d = 2\pi / q$ between basic clay layers was found to be 0.734 nm and 0.718 nm for HBH and KBO, respectively. These basal spacing are in very good agreement with those identified in the XRD experiment (see section 3.1). As expected, different behaviour was observed for the KBO and HBH paraffin-wax composites prepared under applied strong electric field equal to 500 V/mm. The isotropic Bragg 001 ring shown in Figure 6A, points to a random orientation of KBO particles distributed in the paraffin wax without *E*-field. However, a strong anisotropy was clearly seen in Figure 6B with the *E*-field applied during preparation of the samples. The electric field direction was horizontal and normal to the direction of the X-ray beam. This indicates that kaolinite particles were preferentially arranged with their basal planes being parallel to the electric field direction. The quantification of the degree of anisotropy is normally achieved by fitting the azimuthal plots (Figure 7) to a Maier-Saupe function. The fitting parameter is related to the full width at half

maximum (smaller value means higher degree of anisotropy) and can be expressed using the standard nematic order parameter.[36,37,38,39] The initial KBO composite made without *E*-field present shows a slightly anisotropic arrangement (S_2= -0.05). This might be caused by the sample preparation procedure, since particles can align to some extent while the solution was being poured into the mould / sample cell. However, the degree of anisotropy significantly increased (7 times) after the application of electric field (S_2= -0.35).

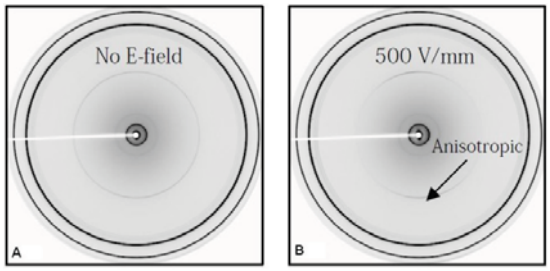

Figure 6. WAXS 2-D images of KBO/paraffin composite without (A) and with (B) *E*-field of ~ 500 V/mm.

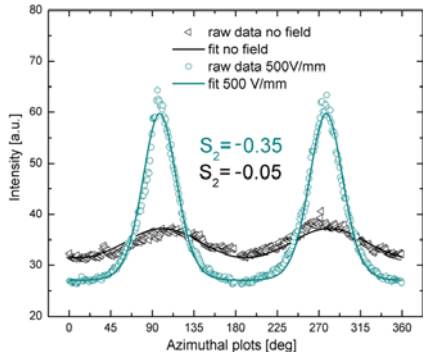

Figure 7. Azimuthal plots with order parameter (A) KBO/paraffin composite (B) KBO/paraffin composite in *E*-field of ~ 500 V/mm

In contrary to the behaviour of kaolinite particles, the situation is very much different for HBH paraffin-wax composites. The WAXS results shown in Figure 8 indicate no particle alignment at all. Both the initial HBH composite and the *E*-field treated sample present an isotropic arrangement of clay particles and the fitted order parameter is the same for both samples (S_2=-0.003, i.e. essentially zero).

---

[36] Méheust Y., Knudsen K.D. and Fossum J.O. (2006) *J. Appl. Cryst.,* **39**, 661 – 670.
[37] Hemmen H, Ringdal N. I., de Azevedo E. N, Engelsberg M., Hansen E. L., Meheust Y., Fossum J. O. and Knudsen K. D. (2009) *Langmuir,* **25**, 12507–12515.
[38] Engelsberg M. and de Azevedo E. N. (2008) *J. Phys. Chem. B*, **112**, 7045–7050.
[39] Dozov I., Paineau E., Davidson P., Antonova K., Baravian C., Bihannic I. and Michot L. J. (2011) *J. Phys. Chem. B*, **115**, 7751–7765.

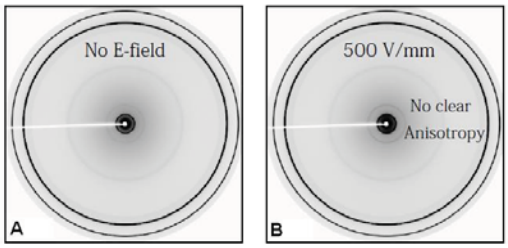

Figure 8. WAXS 2-D images of HBH/paraffin composite without (A) and with (B) *E*-field of ~ 500 V/mm.

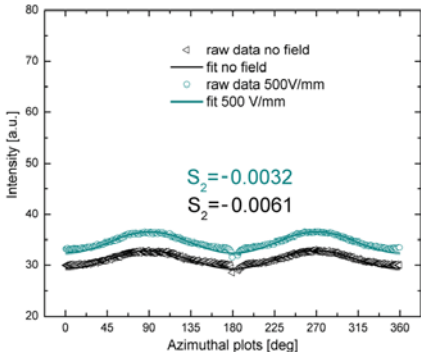

Figure 9. Azimuthal plots with order parameter (A) HBH/paraffin composite (B) HBH/paraffin composite in *E*-field of ~ 500 V/mm

There are three possible explanations for not observing any anisotropy from halloysite particles under the influence of *E*-field and these are: (i) particles are of different and irregular shapes, i.e. kinked tubes; (ii) large agglomerations are made from many particles having random orientations; and finally (iii) halloysite particles in their present form become non-ER species, i.e. they do not re-orient, even though they become polarized under an electric field (for introduction of the non-ER concept etc., see a review on ER suspensions by T. Hao[40]). The two former reasons are believed to apply here, and the justification is provided by electron microscopy images shown in Figure 3 and Figure 4. The particles may orient along the electric field direction, but due to their very irregular shapes, no basal plane parallel orientation (as in the case of kaolinite particles) can be achieved. Since it is not possible to observe structuring from halloysite particles being embedded into the paraffin-wax, optical observations of clay particles suspended in silicone oil were performed.

[40] Hao T, (2002) *Adv. Coll. Interf. Sci.*, **35**, 1-35.

3.5. Optical microscopy observations

The optical microscopy observations aided to exclude the hypothesis that halloysite particles make a non-ER fluid. Figure 10 shows 2 images of both the KBO and the HBH particles suspended in silicone. Randomly dispersed particles can be seen on the left panel of Figure 10, whereas two images of the particles experiencing an *E*-field of 500 V/mm are presented on the right side. The formation of chain-like structures aligning parallel to the field is clearly observed. In the case of kaolinite ER suspension, many thin chains are visible (~10-50 μm). The particles in the halloysite ER fluid retain larger agglomerates of particles reaching nearly 200 μm. The optical observations indicate that the electrorheological properties may differ for each clay suspension, and these are presented in the next section together with the electrical current measurements.

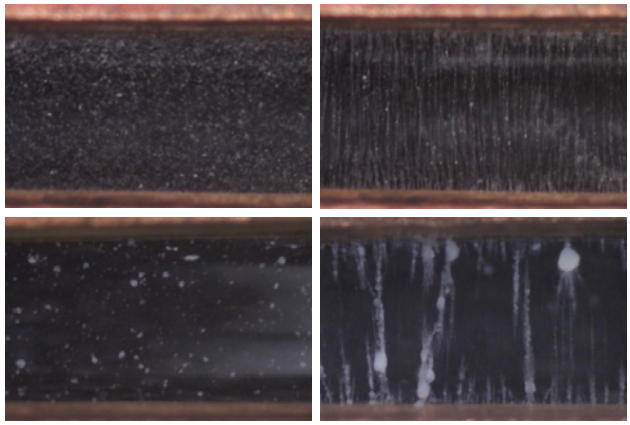

Figure 10. Optical microscopy images of KBO/silicone oil (top) and HBH/silicone oil (bottom) without (left) and with *E*-field present (right). The gap between electrodes is 1 mm.

3.6. Rheology and current response measurements

The flow curves were measured using the controlled shear rate mode for both clay/silicone oil suspensions. In the absence of an *E*-field, the ER fluids behave as a Newtonian fluid, i.e. their viscosities η stay constant independently of values of the shear rate $\dot{\gamma}$ (note: two grounding brushes connected to the measuring bob induce an artificial yield stress τ of ~0.7 Pa). When a DC electric field of strengths 250, 500, 750, 1000 and 2000 V/mm were applied, the behaviour of both ER fluids changed and resembled that of a Bingham fluid, i.e. a viscoelastic material that behaves as a rigid body at low stresses but flows as a viscous fluid at high stresses. This behaviour can be described by the Bingham fluid model or its expanded form (includes the power-law index) described by the Herschel-Bulkley rheological model: $\tau=\tau_y+b\cdot\dot{\gamma}^{p}$, where τ_y, b, p are constants named the yield stress, the consistency index, and the

power-law index, respectively. The values of the static yield stress are presented in Table 1. It can be seen that the ER response from the KBO sample is significantly better and the yield stresses are nearly 3 times higher than those observed for the HBH sample.

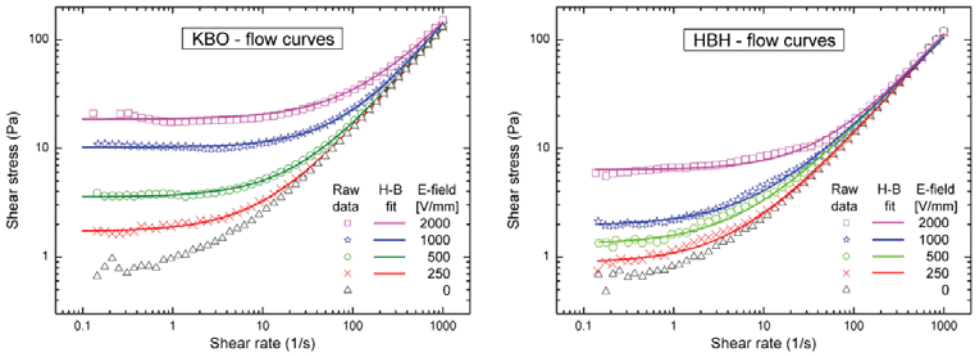

Figure 11. Log-log plot of the flow curves of KBO (left) and HBH (right) ER suspensions with particle concentration of Φ~5 wt.%. Experimental data are represented by symbols and the corresponding H-B fits are drawn using solid lines. (Measurements taken at 750 are not shown for sake of clarity, but the results are included in Table 1)

So-called bifurcation tests[41,42,43,44] were performed as a cross-check on the yield stresses determined from the controlled shear rate measurements. Two examples of such tests are shown in Figure 12. If a constant shear stress is applied to a sample, then a bifurcation in the flow curves may occur at the yield stress τ_y, indicating that microstructure re-build up is dominant if the applied stress $\tau_{ap}<\tau_y$. At high values of the applied stress on the other hand, particle re-structuring fails, e.g. $\tau_{ap}>3.35$ and $\tau_{ap}>0.8$ Pa for KBO and HBH, respectively in the example below.

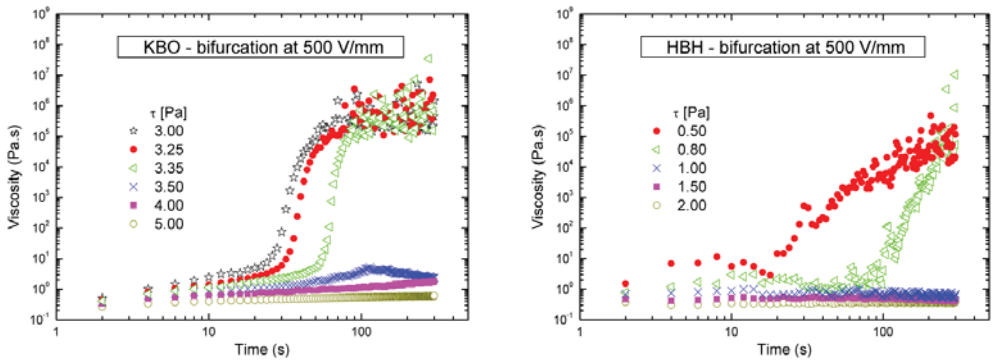

Figure 12. Example of bifurcation in the rheology of KBO (left) and HBH (right) suspensions in presence of *E*-field strength of 500 V/mm. Here the yield stresses are 3.3±0.1 and 0.9±0.1 Pa for KBO and HBH, respectively.

---

[41] Meheust Y., Parmar K., Schjelderupsen B. and Fossum J. O. (2011) *J. Rheol.* **55**, 809.
[42] Khaldoun A, Moller P., Fall A., Wegdam G., de Leeuw B., Meheust Y, Fossum J. O. and Bonn D. (2009) *Phys.Rev.Lett.*, **103**, 188301.
[43] Parmar K., Meheust Y., Schjelderupsen B. and Fossum J. O. (2008) *Langmuir*, **24**, 1814.
[44] Bonn D., Tanase S., Abou B., Tanaka H. and Meunier J. (2002) *Phys. Rev. Lett.*, **89**, 015701.

Table 1 compares the yield stresses for KBO and HBH samples measured at different electric field strengths using both mentioned methods. As can be seen, the values obtained from bifurcation tests coincide very well with those estimated from Herschel-Bulkley fits within the frame of experimental errors.

E-field [V/mm]		250	500	750	1000	2000
τ_y [Pa]	KBO (CSR)	1.7	3.6	5.2	10.2	18.5
τ_y [Pa]	KBO (bif.)	1.5	3.3	5.5	9.5	16.5
τ_y [Pa]	HBH (CSR)	0.9	1.3	1.6	1.9	6.3
τ_y [Pa]	HBH (bif.)	0.6	0.9	1.5	1.5	7.5

Table 1. Comparison of the yield stresses for KBO and HBH suspensions measured at different *E*-field strengths employing constant shear rate (CSR) and bifurcation (bif.) methods.

The values of the yield stress for the KBO are considerably higher than those for the HBH. This behaviour can be connected to either the differences in dielectric properties of the samples or dispersion conductivity. The dielectric constant of halloysite is supposed to be in general slightly higher than that of kaolinite[45], however, our investigations on micaceous clays using THz-TDS showed that despite significant variation in chemical composition of selected micas, the dielectric behaviour for this group of clay minerals is rather similar with the same magnitude of refractive and absorption indexes (e.g. at about 1 THz)[46,47] Taking into consideration either the polarization model or the dielectric loss model (see ref. [37] for detailed description of those mechanisms) one would expect the ER response from the KBO sample to be similar or lower. However, this is clearly not the case here. The possible validity of the conduction model, in which the conductivity mismatch between particle and liquid medium (rather than the dielectric constant mismatch) is thought to be a dominant factor for DC and low frequency AC excitation[37], was therefore tested.

Figure 13 shows the results of conductivity measurements where HBH showed higher conductivity than KBO with increasing voltage applied. The scaling factors observed are different, and these are: $I_H \propto E^{4.1}$ and $I_K \propto E^{2.0}$ for halloysite and kaolinite, respectively. Since the magnitude of the DC electric conductivity I_H is significantly higher than I_K, and the conductivity mismatch HBH/silicone oil is also higher than that of KBO/silicone oil, the conductivity model[37] has no direct application here. Additionally, for each electric field strength two data points are plotted for each sample. These are the readings taken just after the application of the *E*-field, and 30 s later. The arrows on the plot indicate the direction of magnitude of the changes in the electrical currents; I_K is seen to decrease between the initial

[45] Churchman G. J. and Carr R. M. (1975) *Clay Clay Miner.,* **23**, 382-388.
[46] Janek M., Bugár I., Lorenc D., Szöcs V., Velič D. and Chorvát D. (2009) *Clay Clay Miner.,* **57**, 416-424.
[47] Janek M., Matejdes M., Szöcs V., Bugár I., Gaál A., Velič D. and Darmo J. (2010) *Philos. Mag.*, **90**, 2399–2413.

measurement and the measurements taken after 30 s, whereas I_H increases (Figure 13). This behaviour is supposed to be connected with electrochemical behaviour of the suspensions and consumption of electrochemical species mediating the current flow in used non-polar medium. We suppose that the main conducting species in silicon-oil dispersions of KBO and HBH are the physically adsorbed water molecules present at external surfaces of KBO and on external and internal surfaces of HBH. The recent application of water oxidation/reduction species was tested to remove organic pollutants from aqueous environment.[48,49,50] In our case we suppose that water molecules are involved in the current conduction as used potentials are far above the water oxidation/reduction electrode over-potentials. Additionaly presence of different quantities of water was proved by TGA/DTG experiments (section 3.7).

It is well known from voltamperometric studies on e.g. ideally polarised electrodes, that current flow on the electrode after application of a certain potential results in a time dependent response connected to the consumption of electrochemical species in the close proximity to the electrode surface in electrochemical reaction (kinetic factor of diffusion rate of electrochemical species towards electrode surface).[51] In our case of a highly non- conducting medium and a low concentration of conduction species from autoprotolysis of surface adsorbed water molecules, different magnitudes of electrical currents changes were found. However, this does not explain why, in the case of KBO, the current after 30 s observation time decreases, whereas for HBH it increases and why the response of the HBH current grows faster than for KBO. Another significant factor affecting the conductivity must be hence the generation of interparticle structures after voltage application to the measuring cell. In the case of KBO, highly ordered columnar structures and regular arrangement of particles can be seen in Figure 10. We argue that this must enable hopping of protons and hydroxyl anions on the kaolinite particle surface covered with water molecules towards the electrodes, and subsequently a fast consumption of current conducting species observable in the drop of current intensity observed after 30 s. On the contrary, the halloysite did not form regular columnar structures such as kaolinite, and additionally has more water adsorbed on external and internal surfaces. Hence after some columns are formed, more conducting species result in higher currents observation than in the case of KBO. The higher conductivity is possibly related to water content. It was found from TGA/DTG experiment that halloysite particles have roughly a double amount of water compared to kaolinite. Thus it is believed that the way

---

[48] Mohana N., Balasubramanian N. and Basha C. A. (2007) *J. Hazard. Mater.* **147**, 644-651.
[49] Lissens G., Pieters J., Verhaege M., Pinoy L. and Verstraete W. (2003) *Electrochim. Acta* **48**, 1655-1663.
[50] Kraft A., Blaschke M., Kreysig D., Sandt B., Schröder F. and Rennau J. (1999) *J. Appl. Electrochem.* **29**, 895-902.
[51] Li P. W. and Chyu M. K. (2003) *J. Power Sources* **124**, 487-498.

in which these two types of clay make structures during the "chain/column" formation, as well as the concentration of available conducting species, are more important factors than the small differences between dielectric constants or material conductivity of the samples.

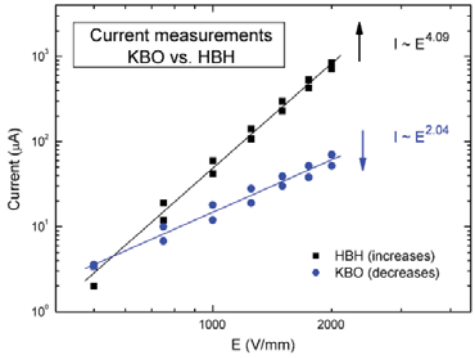

Figure 13. Electric current measurements of KBO and HBH.

3.7. TGA/DTG

Thermal gravimetric analysis was conducted mainly to prove the mineral purity and water content in both minerals. Figure 14 shows typical TGA/DTG behaviour of both the KBO and the HBH samples in the temperature window 50-800 °C.

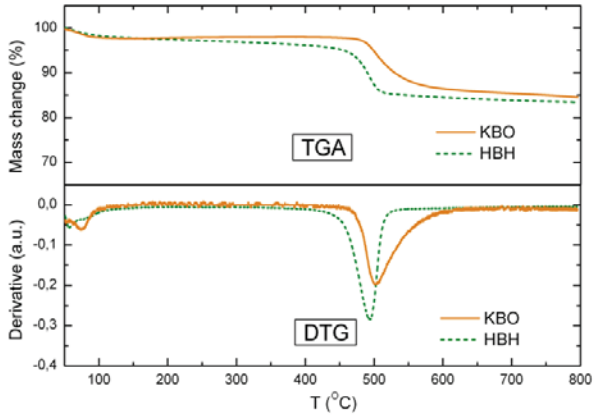

Figure 14. TGA and DTG traces (50-800 °C) of kaolinite (solid) and halloysite (dashed) samples.

The first significant change in the mass ratio can be seen in temperature range up to 200 °C, and is attributed to the loss of physisorbed water molecules, i.e. located at micropores of the clay aggregate surfaces,[52] observable for both the KBO and the HBH samples on the level of about 3%. However, with the temperature increase up to 400 °C, a continuous mass drop of about 3% is noted only for HBH. This is attributed to the loss of water molecules present on

[52] Nicolini K. P., Budziak Fukamachi C. R., Wypych F. and Mangrich A. S. (2009) *J. Colloid Interf. Sci.*, **338**, 474-479.

the internal surfaces, hence the intercalated water molecules. As far as the XRD data revealed the characteristic distance for basal diffraction of HBH at 7.4 Å, this confirms the presence of some small amount of intercalated water molecules.[53] The main mass loss corresponding to structural dehydroxilation of the samples occurs at ~490 °C for halloysite and at ~510 °C for kaolinite, which is in agreement with previously published results.[43,54] The TGA/DTG analysis showed also that excess thermal reactions connected to any impurities present in the samples were not detected.

4. Conclusions

Wide angle X-ray scattering was used to investigate the electric field induced structuring from two types of clay particles belonging to the kaolin group of minerals, namely kaolinite and halloysite. It was found that the overall alignment in *E*-field of the polarized kaolinite particles was significantly better compared to that of polarized halloysite particles. The authors believe that this is mainly a result of the different kind of aggregates each type of particles formed, although similar columnar final structures were made out of these aggregates in the presence of an external *E*-field. The disc-like kaolinite particles stack one another each other (in a coarse approximation) if immersed in a non-polar medium, and when an external *E*-field is applied such a stacked particle aligns with the *E*-field direction perpendicular to the stacking direction, which was evident in observed 2-D WAXS diffractograms. The halloysite samples were found to give no rise to anisotropy on the 2-D WAXS diffraction patterns, indicating no basal plane preferential orientation for this system. SEM and TEM images confirmed that the kaolinite sample is a well-crystallized mineral with platy particles of hexagonal symmetry, whereas the morphology of halloysite particles was found to be very different, consisting of irregular shape particles including flakes and tubular particles. Optical microscopy was used to observe the particle alignment in the presence of the *E*-field. In addition, the structural and morphological properties of both types of clays were probed in detail by means of XRD and FTIR techniques. The electrorheological response was considerably stronger for kaolinite suspensions compared to that of the halloysites. The validity of commonly used models describing the mechanisms of the electrorheological effects, namely polarization model and conduction model, was tested and it was found that they have no direct application here. In addition, electric currents at different

---

[53] Moore D. M. and Reynolds R. C. Jr. (1997) *X-ray Diffraction and the Identification and Analysis of Clay Minerals,* Oxford University Press, Oxford.
[54] Horvath E., Frost R. L., Mako E., Kristof J. and Cseh T. (2003) *Thermochim. Acta*, **404**, 227-234.

electric field strengths were measured and they scale as: $I_K \propto E^{4.1}$ and $I_H \propto E^{2.0}$ for kaolinite and halloysite, respectively. It is believed that the way in which these two types of clay make structures during the "chain/column" formation, as well as the concentration of available conducting species, are more important factors than the small differences between dielectric constants or material conductivity of the samples.

Acknowledgments

We wish to thank to Prof. I. Kraus (CU Bratislava, Slovakia) for his kind support of halloysite sample as well as to Mr. R. Kräuter (bene_fit Hirschau, Germany) for his kind support of kaolinite sample, which were used in presented study. The assistance of Mrs. I. Macková (Institute of Inorganic Chemistry Slovak Academy of Sciences Bratislava, Slovakia) during XRD determination is greatly acknowledged. The authors would also like to thank Elisabeth Lindbo Hansen for her comments that helped to improve the manuscript, and A. P. Hammersley, creator of the Fit2D program. The financial support of the Slovak Grant Agency for Science VEGA (grant No. 1/4457/07), Slovak Research and Development Agency APVV (grants APVV-0491-07, VMSP-P-0110-09) and of Student Grants of CU No. UK/144/2009 is greatly appreciated. This work was supported by the Research Council of Norway through the FRINAT Program: NFR project number 171300.

References

[1] Murray H. H. (1991) *Appl. Clay Sci.*, **5**, 379-395.
[2] Konta J. (1995) *Appl. Clay Sci.*, **10**, 275-335.
[3] Beneke K. (1995) Zur Geschichte der Grenzflächenerscheinungen – mit ausgesuchten Beispielen – Beiträge zur Geschichte der Kolloidwissenschaften IV. Mitteilungen der Kolloid-Gesellschaft, Verlag Reinhard Knof, Kiel: p81 (in German).
[4] Jasmund K. and Lagaly G. (1993) Tonminerale und Tone. Struktur, Eigenschaften, Anwendung und Einsatz in Industrie und Umwelt. Stenkopff, Darmstadt: 490p (in German).
[5] Harvey C.C. and Murray H.H. (1997) *Appl. Clay Sci.*, **11**, 285-310.
[6] Zheng-Hong H., Aiping W., Feiyu K. and Xiuyun C. (2010) *Mater. Lett.*, **64,** 2444-2446.
[7] Mellouk S., Belhakem A., Marouf-Khelifa K., Schott J. and Khelifa A. (2011) *J. Colloid. Interf. Sci*., **360**, 716-724.
[8] Zhang X., Lin S., Chen Z., Megharaj M. and Naidu R., (2011) *Water Res*., **45**, 3481-3488.
[9] Li W., Lu K. and Walz J. Y. .(2011) *J. Am. Ceram. Soc.*, **94**, 1256-1264.
[10] Yuan P., Southon P.D., Liu Z., Green M.E.R., Hook M.J., Antill S.J. and Kepert C.J. (2008) *J. Phys. Chem.*, **112**, 15742-15751.
[11] Joussein E., Petit S., Churchman J., Theng B., Righi D. and Delvaux B. (2005) *Clay Miner.*, **40**, 383-426.
[12] Brindley G. W., Kao C. C, Harrison J. L., Lipsicas M. and Raythatha R. (1986) *Clay Clay Miner*. **34**, 239-249.
[13] Giese R. F. (1988) In: Bailey S.W. (Ed.) *Rev. Mineral.*, **19**, Miner. Soc. Amer., Washigton, D.C., 29-66.
[14] Madejová J., Kraus I., Tunega D. and Šamajová E. (1997) *Geol. Carpath.- Series Clays*, **6**, 1, Bratislava, 3-10.
[15] Brindley G. W. and Robinson K. (1947) *Brit. Ceram. Soc. Trans.*, **46**, 49-62.
[16] Hinckley D. N. (1963) *Clay Clay Miner.*, **11**, 229-235.
[17] Hughes J. C. and Brown G. (1979) *J. Soil Sci*., **30**, 557-563.
[18] Brindley, G. W. and Robinson, K. (1946) *Trans. Faraday Soc*., **42B**, 198-205.

[19] Bates T., Hildebrand F. A. and Swineford A. (1950) *Am. Miner.*, **35**, 463-484.
[20] Costanzo P. M., Giese R. F. and Clemency C. V. (1984) *Clay Clay Miner*., **32**, 29-35.
[21] Costanzo P. M., Giese R. F. and Lipsicas M. (1984) *Clay Clay Miner.*, **32**, 419-428.
[22] Gardolinski J. E., Filho H.P.M. and Wypych F. (2003) *Quim. Nova*, **26**, 25–30.
[23] Costanzo P. M. and Giese J. R. F. (1985), *Clay Clay Miner.*, **33**, 415–423.
[24] Cheng H., Frost R. L., Yang J., Liu Q. and He J. (2010) *Thermochi. Acta*, **511**, 124–128.
[25] Nicolini K.P., Fukamachi C.R.B., Wypych F., Mangrich A.S. (2009) *J. Colloid and Interf. Sci*, **338**, 474-479.
[26] Chassagne C., Mietta F. and Winterwerp J. C. (2009) *J. Colloid and Interf. Sci*, **336**, 352-359.
[27] Rowlands W. N. and Wyndham O´Brien R. (1995) *J. Colloid and Interf. Sci.*, **175**, 190 – 200.
[28] Tributh H. and Lagaly G. (1986) *GIT Fachz. Lab*. **30**, 524 (in German).
[29] Tributh and Lagaly G. (1986) *GIT Fachz. Lab*. **30**, 771 (in German).
[30] Grim R. E. (1968) *Clay Miner.*, 2nd Ed., McGraw-Hill Book Company, New York, USA.
[31] Farmer V. C. (2000) *Spectrochim. Acta A*, **56**, 927.
[32] Madejová J. (2003) *Vib. Spectrosc*., **31**, 1–10.
[33] Madejová J., Keckes J., Pálková H. and Komadel P. (2002) *Clay Miner.,* **37**, 377–388.
[34] Brindley G.W. (1980) *Order-disorder in clay mineral structures: in Crystal Structures of Clay Minerals and their X-ray Identification* (G.W. Brindley and G. Brown, Ed.) **5**, Mineralogical Soc., London.
[35] Janek M, Emmerich K, Heissler S, Nüesch R (2007) *Chem. Mater.,* **19**, 684-693.
[36] Méheust Y., Knudsen K.D. and Fossum J.O. (2006) *J. Appl. Cryst*., **39**, 661 – 670.
[37] Hemmen H, Ringdal N. I., de Azevedo E. N, Engelsberg M., Hansen E. L., Meheust Y., Fossum J. O. and Knudsen K. D. (2009) *Langmuir*, **25**, 12507–12515.
[38] Engelsberg M. and de Azevedo E. N. (2008) *J. Phys. Chem. B* **112**, 7045–7050.
[39] Dozov I., Paineau E., Davidson P., Antonova K., Baravian C., Bihannic I. and Michot L. J. (2011) *J. Phys. Chem. B*, **115**, 7751–7765.
[40] Hao T, (2002) *Adv. Coll. Interf. Sci*., **35**, 1-35.
[41] Meheust Y., Parmar K., Schjelderupsen B. and Fossum J. O. (2011) *J. Rheol.* **55**, 809.
[42] Khaldoun A, Moller P., Fall A., Wegdam G., de Leeuw B., Meheust Y, Fossum J. O. and Bonn D. (2009) *Phys.Rev.Lett*. **103**, 188301.
[43] Parmar K., Meheust Y., Schjelderupsen B. and Fossum J. O. (2008) *Langmuir*, **24**, 1814.
[44] Bonn D., Tanase S., Abou B., Tanaka H. and Meunier J. (2002) *Phys. Rev. Lett*., **89**, 015701.
[45] Churchman G. J. and Carr R. M., (1975) *Clay Clay Miner.*, **23**, 382-388.
[46] Janek M., Bugár I., Lorenc D., Szöcs V., Velič D. and Chorvát D. (2009) *Clay Clay Miner.,* **57**, 416-424.
[47] Janek M., Matejdes M., Szöcs V., Bugár I., Gaál A., Velič D. and Darmo J. (2010) *Philos. Mag.*, **90**, 2399–2413.
[48] Mohana N., Balasubramanian N. and Basha C. A. (2007) *J. Hazard. Mater.* **147**, 644-651.
[49] Lissens G., Pieters J., Verhaege M., Pinoy L. and Verstraete W. (2003) *Electrochim. Acta* **48**, 1655-1663.
[50] Kraft A., Blaschke M., Kreysig D., Sandt B., Schröder F. and Rennau J. (1999) *J. Appl. Electrochem*. **29**, 895-902.
[51] Li P. W. and Chyu M. K. (2003) *J. Power Sources* **124**, 487-498.
[52] Nicolini K. P., Budziak Fukamachi C. R., Wypych F. and Mangrich A. S. (2009) *J. Colloid Interf. Sci*., **338**, 474-479.
[53] Moore D. M. and Reynolds R. C. Jr. (1997) *X-ray Diffraction and the Identification and Analysis of Clay Minerals*, Oxford University Press, Oxford.
[54] Horvath E., Frost R. L., Mako E., Kristof J. and Cseh T. (2003) *Thermochim. Acta*, **404**, 227-234.

5. Supporting materials

5.1. SEM

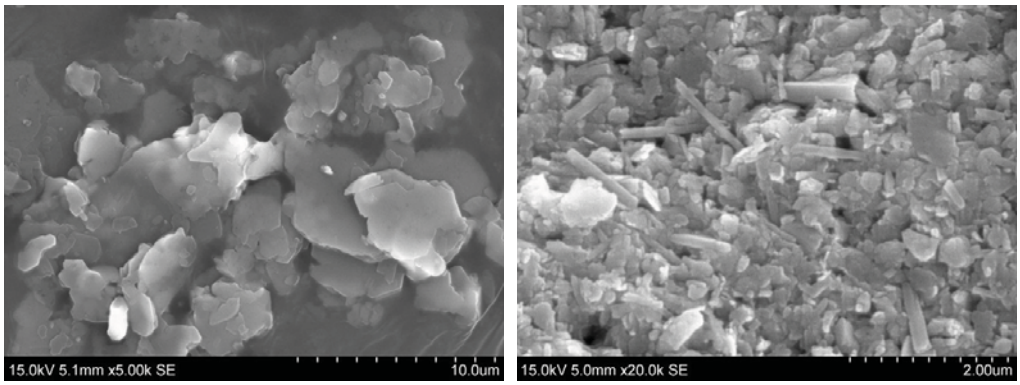

Figure 15. Additional SEM images of KBO (left) and HBH (right) samples.

5.2. Electric current measurements – table.

E-field [V/mm]	250	500	750	1000	1250	1500	1750	2000
I [μA] KBO	< 1	3.6 – 3.4	10 – 6.8	18 – 12	28 – 19	39 – 30	52 – 38	70 – 52
I [μA] HBH	< 1	2.0 – 3.4	12 – 19	42 – 60	107–141	227–298	426–529	711–846

Table 2 Comparison of DC currents for KBO and HBH suspensions measured at different *E*-field strengths. Recordings were taken immediately after the *E*-field was applied (left values) and 30 s later (right values). Note: KBO current values decrease with time, whereas HBH current values increase.

Zbigniew Rozynek
Department of Physics, NTNU
Hoegskoleringen 5
7491 Trondheim
Norway
E-Mail: rozynek@ntnu.no
Phone: +47 735 91858

Tomáš Zacher
Department of Physical and Theoretical Chemistry
Faculty of Natural Sciences, Comenius University
Mlynská dolina CH1,
SK-84215 Bratislava
Slovakia
E-Mail: zacher@fns.uniba.sk
Phone: +421 2 60296244
Fax: +421 2 65429064

Appendix I

Structuring from nanoparticles in oil-based ferrofluids

Z Rozynek, A Józefczak, K D Knudsen, A Skumiel, T Hornowski, J O Fossum, M Timko, P Kopčanský and M Koneracká

Eur. Phys. J. E 34 (2011) 28

Eur. Phys. J. E (2011) **34**: 28
DOI 10.1140/epje/i2011-11028-5

THE EUROPEAN PHYSICAL JOURNAL E

Regular Article

Structuring from nanoparticles in oil-based ferrofluids

Z. Rozynek[1,a], A. Józefczak[2], K.D. Knudsen[3], A. Skumiel[2], T. Hornowski[2], J.O. Fossum[1], M. Timko[4], P. Kopčanský[4], and M. Koneracká[4]

[1] Department of Physics, NTNU, Høgskoleringen 5, NO-7491 Trondheim, Norway
[2] Institute of Acoustics, Faculty of Physics, UAM, Umultowska 85, 61-614 Poznań, Poland
[3] Physics Department, IFE, 2027 Kjeller, Norway
[4] Institute of Experimental Physics, SAV, Watsonova 47, 040 01 Košice, Slovakia

Received 10 October 2010 and Received in final form 1 February 2011
Published online: 18 March 2011

Abstract. The effect of magnetic field on the structure formation in an oil-based magnetic fluid with various concentrations of magnetite particles was studied. The evaluation of the experimental data obtained from small-angle X-ray scattering and ultrasonic attenuation indicates the formation of chain-like aggregates composed of magnetite particles. The experimental data obtained from ultrasonic spectroscopy fit well with the recent theoretical model by Shliomis, Mond and Morozov but only for a diluted magnetic fluid. In this model it is assumed that a dimer is the main building block of a B-field–induced chain-like structure, thus the estimation of the nematic order parameter does not depend on the actual length of the structure. The scattering method used reveals information about the aggregated structure size and relative changes in the degree of anisotropy in qualitative terms. The coupling constant λ, concentrations ϕ, average particle size d and its polydispersity σ were initially obtained using the vibrating sample magnetometry and these results were further confirmed by rheometry and scattering methods. Both the particles' orientational distribution and the nematic order parameter S were inferred from the ultrasonic measurements. The investigation of SAXS patterns reveals the orientation and sizes of aggregated structures under application of different magnetic-field strengths. In addition, the magnetic-field–dependent yield stress was measured, and a relationship between the yield stress and magnetic-field strength up to 0.5 T was established.

1 Introduction

Magnetic fluids (ferrofluids) are colloidal suspensions containing magnetic nanoparticles dispersed in an organic or inorganic liquid carrier. Due to their small core diameters, d, of 4–200 nm, the particles generally form a single domain of uniform magnetization with a magnetic moment μ given by $\mu = M_b V$, where M_b denotes the bulk magnetization of the particle material and $V = \pi d^3/6$ is the volume of the core of the particle. Many applications of magnetic fluids require structural stability, *i.e.* no formation of aggregates even in strong magnetic fields. The aggregation of nanoparticles can be avoided by covering particles with a single or double layer of surfactant. However, large values of the coupling constant, $\lambda = \mu_0 \mu^2 / 4\pi {d_h}^3 k_B T$ [1], and volume fractions of magnetic grains ϕ lead to the formation of magnetic aggregates in the form of chain-like structures. In the expression for λ, d_h is the hydrodynamic diameter of the particle which is greater than the size of the magnetic core, d, by twice the thickness of protective surfactant layer [2]. Detecting the particle aggregation is possible only by indirect experimental methods based on magnetorelaxometry [3], viscosity [4,5], ultrasound attenuation measurements [6], or SANS/SAXS [7–9] performed in external magnetic field.

Ferrofluids exhibit special properties that make them suited for many technical and medical applications. Some of these properties are determined by the particular physics of small-sized magnetic nanoparticles. Therefore it is important to search for better methods and theories describing the physical behaviour of these liquids, and in particular, the magnetic-field–induced structuring from magnetic particles. Concerning the measurements of the ferrofluid degree of anisotropy, typically scattering methods such as small-angle X-ray/neutron scattering (SAXS/SANS) are used and several approaches for the calculation of the nematic order parameter are common [10,11]. It can be seen that the value of the order parameter changes drastically when different methods of calculations are chosen. If for example the so-called "wide angle diffuse ring" approach is used (suggested by Leadbetter *et al.* [12]), several assumptions need to be applied and those normally tend to overestimate the value of the order parameter. The derivation of the

[a] e-mail: zbigniew.rozynek@ntnu.no

orientational distribution functions from scattering data is generally complicated by the coupling between the orientational and positional orders of the scattering moieties. Therefore it is suggested here to employ a different measurement technique, *i.e.* ultrasonic spectroscopy and the theory described by Shliomis, Mond and Morozov [13] as an alternative approach to scattering methods.

The layout of this work is as follows. The sample preparation is first described briefly, followed by the first major part that focuses on the sample characterization. This includes determination of a particle average diameter, volume concentration and estimation of a coupling constant employing VSM (see below), rheology and SAXS. The second part covers the investigation of the B-field–induced structuring from magnetic particles. The average dimensions of the aggregated structures, their preferred orientation and nematic order parameter are studied with SAXS and ultrasonic spectroscopy measurements.

2 Sample preparation

The magnetic liquids composed of mineral oil ITO 100 and Fe_3O_4 particles coated with oleic acid were prepared in the Institute of Experimental Physics in Košice. Magnetic particles were obtained by chemical precipitation of ferrous and ferric salts in alkali medium. The appropriate amounts $FeSO_4$ and $FeCl_3$ solution were mixed and precipitated by a 25% (v/v) solution of NH_4OH. Magnetite was formed as a black precipitate. To remove impurities formed during chemical reaction, the obtained magnetite particles were washed several times by magnetic decantation. After the last washing, the oleic acid (as surfactant to prevent irreversible aggregation of magnetic particles) and mineral oil ITO 100 (as carrier liquid) were added at 70 °C in the volume ratio 1:1. Subsequently ITO 100 was added dropwise during stirring and heating in order to obtain the appropriate volume concentration of magnetite nanoparticles [14].

Samples with four different nanoparticle concentrations were prepared. The initial ferrofluid FF was diluted with mineral oil in the following proportions: FF:4, FF:64 and FF:128, respectively. The exact concentration value for the initial ferrofluid FF was obtained by means of the VSM method (see sect. 3.1).

3 Experimental techniques and results

3.1 VSM—vibrating sample magnetometry

A vibrating sample magnetometer (VSM) measures the magnetic hysteresis loop of the magnetic fluid studied. Volume concentrations of magnetite particles in the magnetic liquids, the average diameter of magnetite particles and the corresponding standard deviation were determined by VSM measurements.

The resulting magnetization curve is shown in fig. 1a. The magnetization of the diluted magnetic fluid can be

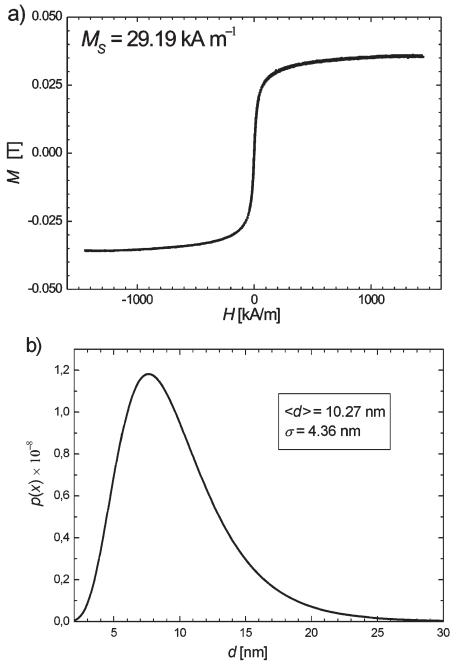

Fig. 1. Magnetization curve (a) and the particle size distribution function (b) for the mineral oil-based magnetic fluid obtained by means of the VSM method.

expressed as a superposition of the Langevin functions [2]

$$M = M_s \int_0^\infty L(\xi) p(x) \mathrm{d}x, \tag{1}$$

where M_S is the saturation magnetization, $L(\xi) = \coth(\xi) - 1/\xi$ is the Langevin function with $\xi = \mu_0 \mu H / k_B T$, μ_0 is the magnetic permeability of vacuum, H is the magnetic-field strength, k_B is the Boltzmann constant and T is the absolute temperature. For the description of the dispersion of the magnetite particle size, the lognormal distribution is usually employed [2]

$$p(x) = \frac{1}{xs\sqrt{2\pi}} \exp\left(-\frac{\ln^2(x/D)}{2s^2}\right), \tag{2}$$

where D and s are the parameters determined from the magnetization curve. On the basis of these parameters the mean diameter, $\langle d \rangle$, and standard deviation of particle size σ, can be determined from the formulae:

$$\langle d \rangle = D \exp\left(\frac{s^2}{2}\right), \tag{3}$$

$$\sigma = D \exp\left(\frac{s^2}{2}\right) \sqrt{\exp s^2 - 1}. \tag{4}$$

The particle size distribution function $p(x)$ extracted from VSM measurements using eq. (1) with the parameter values of $M_S = 29.19\,\mathrm{kA/m}$, $D = 9.48\,\mathrm{nm}$, and $s = 0.407$ is

shown in fig. 1b. From the saturation magnetization M_S the volume fraction of the magnetic phase can be determined via the expression

$$\phi = \frac{M_s}{M_b}, \tag{5}$$

where $M_b = 446\,\mathrm{kA/m}$ is the spontaneous magnetization of magnetite grains. In the case of the initial ferrofluid (FF) studied here, eq. (5) leads to a value $\phi = 6.6\%$ (v/v). The particle size average value, $\langle d \rangle = 10.27\,\mathrm{nm}$, obtained from VSM data using eq. (3), and hydrodynamic diameter $d_h = 14.27\,\mathrm{nm}$, calculated on the assumption that the length of the oleic acid molecule equals 2 nm, leads to a coupling constant $\lambda = 0.54$. In conventional ferrofluids like maghemite (γ-Fe_2O_3) or magnetite (Fe_3O_4), with typical particle size 5–10 nm, the magnetic interaction is generally weak ($\lambda < 1$), mainly reinforcing the vdW attraction [15]. Although the coupling constant $\lambda = 0.54$ is relatively small and the studied fluid magnetic dipole interaction is rather weak, it is still possible for nanoparticles to form chain-like structures. This was confirmed by the rheological studies described in the next section and the chain-like structuring observed via SAXS investigation reported in the next paragraphs.

From the VSM data, the mean-spherical and the high-temperature approximation models give the same lognormal distribution of magnetite particle diameters [16,17].

3.2 Rheology

3.2.1 Experimental method

The magneto-rheology (MR) of the ferrofluid was measured under different magnetic fields using an Anton Paar Physica MCR 300 rotational rheometer equipped with a thermostat unit MRD 180 and measuring system PP20/MR, specially designed for plate-plate–type MR measurements. All rheological measurements were undertaken at constant temperature (21 °C) and a gap of 0.2 mm. The shear stress τ as a function of a shear rate γ was measured by means of controlled shear rate (CSR) tests. For the samples in this study, and under application of a magnetic field, this dependence is well described by the Herschel-Bulkley rheological model: $\tau = \tau_y + b\dot{\gamma}^p$, where τ_y, b, p are constants named yield stress, consistency index, and power law index, respectively. The effective viscosity of the Herschel-Bulkley fluids upon deformation is not constant but follows a power law type behaviour in contrast to the constant viscosity found in Bingham fluids [18,19].

3.2.2 Rheology results

In general, the yield stress values for ferrofluids are low in comparison with those of magnetorheological fluids constituting bigger particle (sizes in the range of μm), since the maximum dipolar attraction (if two dipoles in head-to-tail configuration are considered) scales as $V_m \propto d^3$, where d is the core diameter, including the surfactant shell if it is present [20]. As suggested by Zubarev and Iskakova [21], the saturated magnitude of the yield stress (considering thin-film ferrofluids with thickness significantly smaller than 1 mm) can be estimated using the equation

$$\tau_y^{\mathrm{sat}} = 0.162\mu_0 M_b^2 \psi \cdot \left[\frac{\phi_h}{(1+2d_s/d)^3}\right]^2, \tag{6}$$

where ϕ_h is the hydrodynamical concentration, ψ is the concentration of particles that are big enough ($> 18\,\mathrm{nm}$) and able to form large domains, d_s is the thickness of the surface shell on the particle, and finally d is the diameter of the magnetic core of the particle. When employing the following values: $d_s = 2\,\mathrm{nm}$, $\phi_h = 0.5$ (both assumed as typical values), $d = 10.27\,\mathrm{nm}$ and ψ varying from 0.001 to 0.002 (both provided by the VSM measurement, see fig. 1b), the calculated value of τ_y^{sat}, based on eq. (6), lies between 1.4 and 2.8 Pa, which encompasses the results presented below.

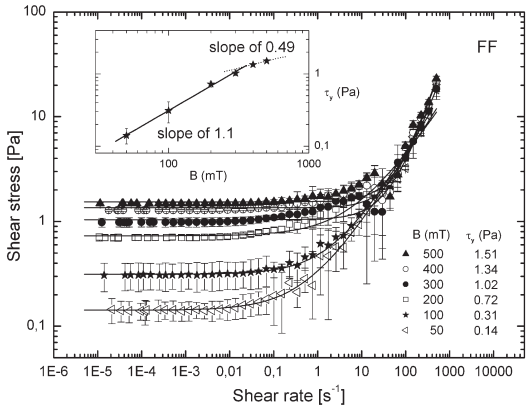

Fig. 2. A log-log plot of the flow curves of the initial ferrofluid (FF). The inset shows the yield stress τ_y dependence on the applied magnetic-field strength.

Figure 2 shows a log-log plot of the flow curves for our samples, fitted with the Herschel-Bulkley model. The yield stress values obtained from CSR measurements by fitting with this model are 0.14, 0.31, 0.72, 1.02, 1.34 and 1.51 Pa for the magnetic-field strengths of 50, 100, 200, 300, 400 and 500 mT, respectively. The dependence of the yield stress τ_y on the applied magnetic-field strength is presented in the log-log plot in the inset of fig. 2. From the fit (black solid line) a nearly linear power law was derived for the dependence on the magnetic-field strength ($B < 300\,\mathrm{mT}$) and the yield stress τ_y scales as $\tau_y \propto B^\kappa$, with the power law exponent $\kappa = 1.1$. However, for higher values of the magnetic-field strength the power law exponent κ decreases sharply below 1 (dotted line). Further increase of the magnetic field would make the saturation yield stress appear.

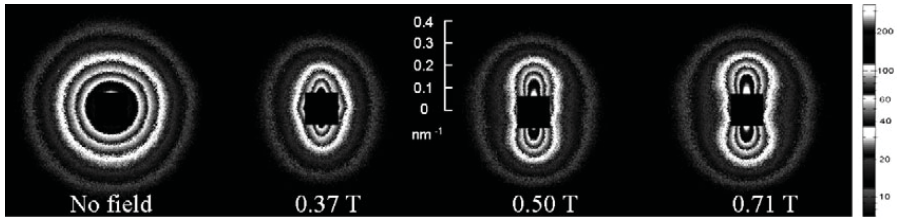

Fig. 3. Scattered intensity from FF:128 without and with horizontally applied magnetic field. Images were taken at the q-range corresponding to the distance $2\pi/q$ of around 9–90 nm.

3.3 Small-angle X-ray scattering

3.3.1 Experimental method

Small-angle X-ray scattering is a useful technique to study shape and size of macromolecules, characteristic distances of partially ordered materials, disordered structures and porous media. In a SAXS experiment, the dependence of the scattered intensity on the scattering angle is controlled by the size of the colloidal particles, their tendency to aggregate, the concentration of the dispersed system, the magnitude of the specific surface area, and more generally, by the inhomogenieties characterizing the structure of the disperse system. The scattered intensity $I(q)$, as a function of the momentum scattering vector q, given as $q = 4\pi \sin(\theta/2)/\lambda$, where λ is the wavelength of the incident beam and θ is the scattering angle, is proportional to the Fourier transform of the geometric correlation function of the electron density. The scattering vector q has the dimension of the inverse length (*i.e.* Å^{-1}), so that the length in real space corresponding to a certain q-value equals $2\pi/q$ [22,23]. The X-ray scattering experiments were performed employing synchrotron radiation (ESRF, France). The experiment was conducted at the Dutch-Belgian Beamline (DUBBLE) at ESRF [24]. In order to induce alignment of the ferrofluid, different magnetic-field strengths, 0 to 0.71 T, were employed. The beam was pointed along the radial direction of a 1 mm capillary whose cylindrical axis was vertical, and the magnetic field was applied horizontally, perpendicular to the X-ray beam. An X-ray beam with a wavelength of 1.033 Å was used. The sample-to-detector distance was calibrated and set to 7 m, enabling the scattering detection in a q-range of approximately 0.007–0.07 Å^{-1}. For the SAXS measurements in a magnetic field, samples were prepared in capillaries and placed between the poles of a permanent magnet. The gap of the latter can be continuously varied between 20 and 3 mm, which allowed changing the field strength from 0.37 to 0.71 T.

3.3.2 SAXS results

When the dipolar interactions are much stronger than the thermal energies (*i.e.* $\lambda \gg 1$ or when an external magnetic field is applied), the fluid develops clusters (dimers, trimers, etc.) and longer chains. Particles of arbitrary shape would exhibit statistically isotropic scattering if they are randomly oriented, *i.e.*, the measured intensity depends only on the magnitude of the scattering vector q, whereas oriented anisometric particles result in anisotropic scattering patterns [25].

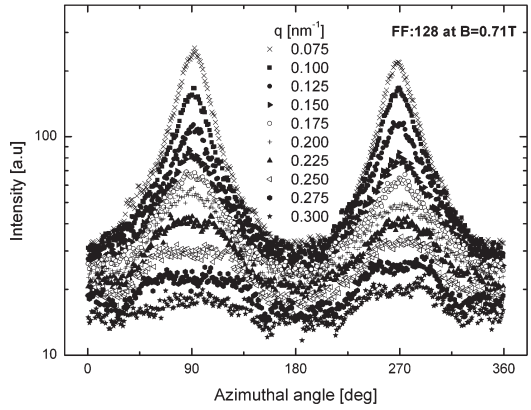

Fig. 4. Azimuthal plots of SAXS intensities at different q-ranges.

Figure 3 shows the 2D SAXS patterns with and without a horizontally applied external magnetic field. For $B = 0$ the intensity pattern is isotropic and it does not depend on the direction of the scattering vector q. However, when the magnetic field is applied, anisotropy develops and the scattering intensity is both radially and azimuthally dependent. In particular, the intensity perpendicular to, the field direction increases, while it decreases in the parallel direction. Since the particles have a diameter starting at about 5 nm (see fig. 1b), or ca. 9 nm when including the surfactant layer, the observable anisotropy caused by the smallest aggregated structure, namely a dimer, can be seen for the q-range starting from around 0.35 nm^{-1} and lower, which corresponds to $2\pi/q > 18$ nm in real space. This is observed in fig. 3, where the application of an external field changes the pattern from being circular at no field to elliptical when the field is present. The anisotropy is more pronounced when approaching the lower q-range (down to $q = 0.09\,\text{nm}^{-1}$ for sample FF:128 at $B = 0.71$ T). This is clearly shown in the azimuthal plots in fig. 4. Interestingly, the anisotropy reaches a maximum at a certain q-value (q_{an}) and then the isotropy

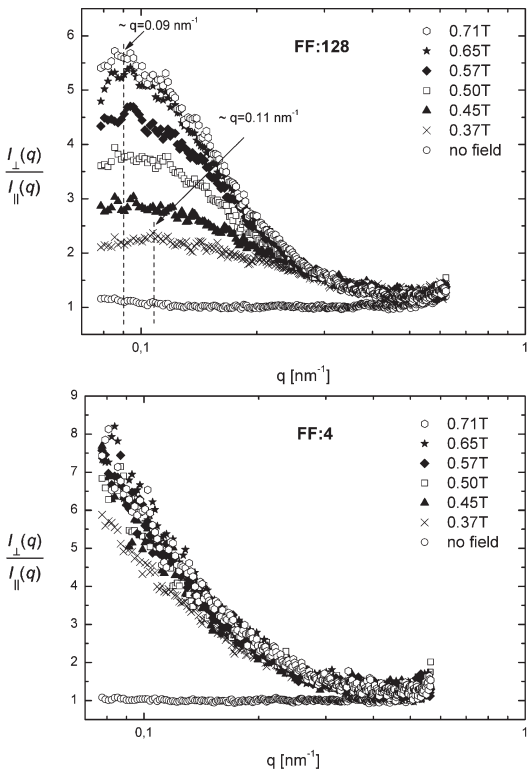

Fig. 5. Ratio of intensities normal and parallel to the magnetic-field direction as a function of wave vector q for samples FF:128 (top) and FF:4 (bottom), respectively.

starts to recover leaving a long and H/kT-dependent tail. This, however, is not readily observed form either fig. 3 or fig. 4, but can be revealed by plotting the ratio of the intensities $I_\perp(q)/I_\parallel(q)$ (perpendicular and parallel to the B-field direction) as a function of the wave vector q shown in fig. 5 (top). The ratio displays maxima shifting from $q_{\rm an} \sim 0.11\,{\rm nm}^{-1}$ to $q_{\rm an} \sim 0.09\,{\rm nm}^{-1}$ for sample FF:128 at magnetic-field strengths of 0.37 T and 0.71 T, respectively. The peak's broadening decreases when the magnetic field strength increases indicating gradually more well-defined ordering. In the thermodynamic limit at the lowest values of q the scattering approaches an isotropic behaviour, while at the highest q isotropy is recovered because we have reached the size of the primary particles in the aggregates, which are spherical. Such behavior suggests that the aggregates are non-spherical assemblies of primary particles that become oriented in the magnetic field: as B increases the radius of gyration (of the aggregated structure) in the parallel direction increases, while that in the perpendicular direction decreases (or remains the same) [26]. If the position of the peak centers (marked with dashed lines) is used as an estimate of the aggregate radius of gyration (as proposed by Teixeira *et al.* [26]), *i.e.*

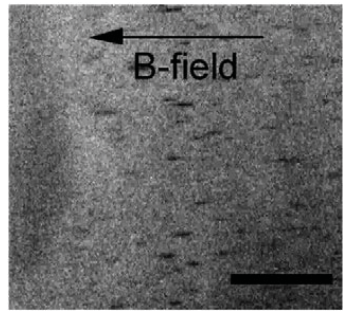

Fig. 6. Optical microscope image of FF:4 at approximately 0.5 T. The length of the bar corresponds to 10 μm.

$R_g \sim 2/q_{\rm an}$, one obtains overall aggregate sizes $2R_g$ from about 115 to 140 nm for FF:128, depending on the field strength. There is however no peak present in the probed q-range when the intensity ratio is plotted for a sample with high particle concentration (FF:4), see fig. 5 (bottom). This indicates that larger structures are formed for samples with high particle concentration (above 1%) in comparison with those formed in diluted samples. In addition, it can be seen that a significant anisotropy starts building up already at a lower value of the B-field. The influence of polydispersity on the structural behaviour cannot be neglected. In particular for highly concentrated samples the formation of both chain-like structures with higher-order oligomers and other forms of aggregates are expected. It can thus be assumed that in the low q-range direction (outside our SAXS q-range) the $I_\perp(q)/I_\parallel(q)$ ratio has a long tail reaching $q \sim 0.03\,{\rm nm}^{-1}$ or lower (see also ref. [26]). One may even expect some of the sub-μm clusters to appear in the presence of high magnetic field. This was in fact observed for the sample with high particle concentration (FF:4) using optical microscopy, as shown in fig. 6. Note that the size of the aggregates cannot be precisely retrieved, since the image was captured with a certain exposure time during particle motion and was also enhanced by adjusting contrast and brightness.

The derivation of the orientational distribution functions from scattering data is generally complicated by the coupling between the orientational and positional orders of the scattering moieties. In the field of liquid crystals, the nematic order parameter S is usually calculated either by considering single-molecule scattering, so that positional correlations are irrelevant, or by assuming ideal positional correlations within a small group of molecules [27]. The situation in our system is not trivial, since there might be no positional correlations within the q-range probed. The azimuthal intensity variations (and thus the nematic order parameter S that depends on the azimuthal peak width) are also q-dependent as shown in fig. 4. In addition, if one assumes the formation of a rod-like structure, a further broadening of the azimuthal peak width is expected due to the rod diameter variations and the structure's finite size in general. Therefore only an analysis in qualitative terms can be presented here and relative changes between the

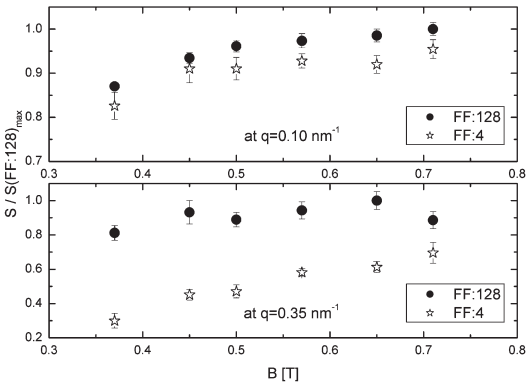

Fig. 7. Normalized order parameter for samples FF:4 (with high particle concentration) and FF:128 (diluted sample) calculated at different q-ranges.

order parameter values for samples FF:4 and FF:128 are illustrated in fig. 7. The order parameter was calculated according to the so-called "wide-angle diffuse ring" approach, where azimuthal plots (examples shown in fig. 4) were fitted using the classical Maier-Saupe distribution function $g(\beta)$, and the order parameter S is given as

$$g(\beta) \sim \exp(m \cos^2 \beta), \tag{7}$$

$$S_n = \frac{1}{2} \left\langle 3 \cos^2 \beta - 1 \right\rangle_g , \tag{8}$$

where m is a parameter that controls the width of the distribution and β is the angle between the major chain axis and the nematic director (along the B-field). Along the whole detectable q-range, the order parameter values for the sample with high particle concentration FF:4 were found to be lower than those from the diluted sample FF:128. The order parameter values shown in fig. 7 for FF:4 and FF128 at $q = 0.1$ and $q = 0.35\,\mathrm{nm}^{-1}$ (top and bottom panels, respectively) have been normalized to the maximum value of S for FF:128. Normally the thermal motion as well as the interaction between the magnetic moments of the particles leading to more complex structure formation (such as rings, clusters, etc.) will prevent a perfect alignment. The latter effect is more pronounced for samples with higher particle concentration and it can explain a lower degree of anisotropy for FF:4 in comparison to FF:128.

3.4 Ultrasonic spectroscopy

3.4.1 Experimental method

In the ultrasonic measurements a broad-band transducer (Optel) with centre frequency of 5 MHz was used. The power spectrum of the echo signal was determined by using a Fast Fourier Transform algorithm. The measuring cell (made of brass) with fixed distance between transducer and reflector was used. The path length (back and forth) traversed by the ultrasonic pulse inside the medium was 12 mm. The attenuation coefficient measured in excess to that of reference medium (water) can be expressed as

$$\alpha(f) = -\frac{1}{2L} \ln \frac{P_\mathrm{m}(f)}{P_\mathrm{w}(f)} + \frac{1}{2L} \ln \frac{R_\mathrm{mb}}{R_\mathrm{wb}} , \tag{9}$$

where $P_\mathrm{m}(f)$, $P_\mathrm{w}(f)$ are the power spectrums of the echo signal reflected from the wall of the measuring cell filled with magnetic liquid and water, respectively, $R_\mathrm{mb} = 0.9319$ is the acoustic power reflection coefficient at the inner side of the measuring cell containing magnetic liquid, and $R_\mathrm{wb} = 0.8314$ is the acoustic power reflection coefficient at the inner side of the measuring cell containing water. The accuracy of the ultrasonic measurements described above amounted to about ±2–5%. For the angular-dependence experiment the magnetic field was rotated by ten degrees each time, while the measuring cell remained stationary in the gap between pole pieces of an electromagnet which produced a field of 75 mT. The magnetic-field strength was measured with a Resonance Technology RX21-type teslameter to within 0.5%.

3.4.2 Ultrasonic anisotropy—results

The compression or stretching of the chain-like aggregates under the influence of the ultrasonic wave results in a magnetic restoring force which leads to forced oscillations of the aggregates. This mechanism was first proposed by Taketeomi [28] and later reconsidered by Pleiner and Brand [29] and Shliomis, Mond and Morozov [13]. The structural changes are manifested by a dependence of the ultrasonic wave absorption on the direction of the wave with respect to the magnetic field. According to Shliomis, Mond and Morozov [13], two-particles chains (dimers) oscillations in the ultrasonic field lead to additional dissipation of ultrasonic wave energy with the coefficient of absorption given by

$$\alpha_\mathrm{dim} = \frac{\eta \phi_d}{2 \rho c^3} \frac{\langle r^2 \rangle}{d^2} \frac{\omega^4 \tau^2}{1 + \omega^2 \tau^2} F(\varphi), \tag{10}$$

where c is the velocity of the ultrasonic wave propagating with angular frequency ω, τ is the relaxation time of the dimer oscillations scaled by the Brownian diffusion time $\tau_B = 3\eta V / k_B T$ for a single particle ($\tau \approx \tau_B$), ρ is the mass density and η the shear viscosity of the magnetic liquid, respectively, ϕ_d is the volume fraction the dimers, and $\langle r \rangle$ is the average distance between magnetic particles in the dimer. The anisotropy function $F(\varphi)$ can be expressed by a field-induced nematic order parameter $S(\lambda, \xi) = 1/2(3\langle \cos^2 \beta \rangle - 1)$, β being the angle between the dimer axis and the applied magnetic field H (similarly as eq. (8)), through the relation

$$F(\varphi) = \left[1 + S(3 \cos^2 \varphi - 1) \right]^2 , \tag{11}$$

where φ is the angle between the wave vector and the direction of the external magnetic field. The upper graph in

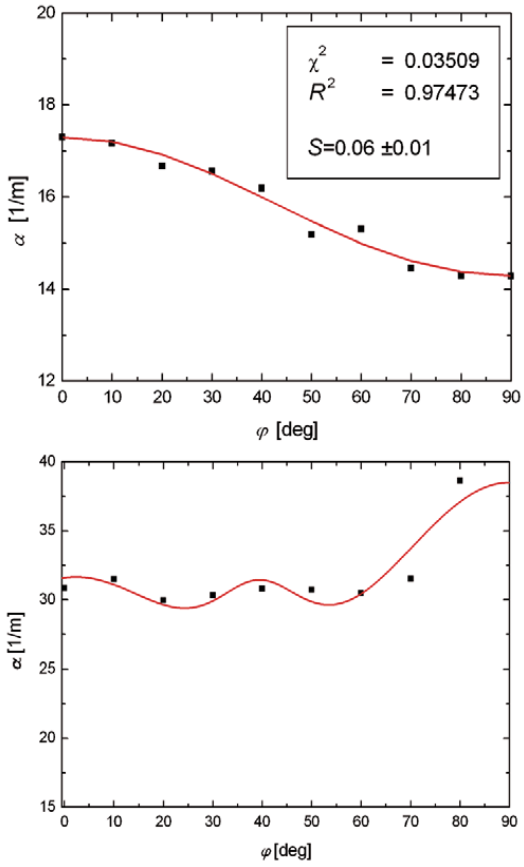

Fig. 8. Angular dependence of the ultrasonic attenuation $\alpha(\varphi)$ for a wave of frequency $f = 5\,\mathrm{MHz}$ in mineral oil-based magnetic liquid in an external magnetic field of $B = 75\,\mathrm{mT}$. Upper graph shows the results for a diluted magnetic fluid (FF:64) and lower graph for a concentrated fluid (FF:4). The solid line on the upper graph was calculated using eq. (12).

fig. 8 shows the results of the ultrasonic anisotropy data $\alpha_{\mathrm{dim}}(\varphi)$ for the diluted mineral oil-based magnetic liquid with concentration (FF:64) subjected to a constant magnetic field of $B = 75\,\mathrm{mT}$. The solid line was obtained by fitting the expression

$$\frac{\alpha(\varphi) - \alpha(\pi/2)}{\alpha(0) - \alpha(\pi/2)} = \frac{2(1-S)\cos^2\varphi + 3S\cos^4\varphi}{2+S}, \qquad (12)$$

following from the Shliomis, Mond and Morozov [13] theory to the experimental data. The observed dependence of α_{dim} on φ is characteristic of short-chains aggregates that are formed as a result of the pair interparticle magnetic dipole-dipole interaction. More specifically, there is a monotonic decrease of the ultrasonic attenuation with increasing φ, and the attenuation is maximal when the field is applied parallel to the direction of the sound propagation and minimal when the field is applied perpendicularly. It should be noted that this behaviour is characteristic only to the weakly concentrated magnetic fluids with predominant presence of two-particle chains. In a more concentrated magnetic fluids (FF:4), lower graph in fig. 8, the structure of the aggregates and angle dependence of the ultrasound coefficient become much more complicated and cannot be explained using the mechanism suggested in the Shliomis, Mond and Morozov theory [30]. This conclusion is supported by the analysis of the SAXS data already discussed in the previous section. The value of the nematic order parameter $S = 0.06 \pm 0.01$ calculated from the best fit of eq. (10) to ultrasonic data is in agreement with the theoretical value of S calculated for $\lambda = 0.54$ and $\xi = 5.43$ [13].

Table 1. Characteristic particle features—summary.

Volume fraction ϕ	6.6	(%)
Mean diameter $\langle d \rangle$	10.27	(nm)
Hydrodynamic diameter d_h	14.27	(nm)
Coupling constant λ	0.54	
Saturated yield stress τ_y^{sat}	1.4–2.8	(Pa)
Order parameter S	0.06	

4 Conclusions

This study has been focused on the magnetic-field–induced structuring from nanoparticles. A considerable part also covers particle characterization without field, since it is important to know in advance the particle average size d and the size distribution σ in order to estimate the coupling constant λ and predict the particle behavior in the colloidal system. Those initial parameters were obtained using the VSM method, giving an average particle diameter $d = 10.27\,\mathrm{nm}$ and a hydrodynamic diameter $d_h = 14.27\,\mathrm{nm}$. In table 1 the characteristic parameters of the system studied are summarized. The list includes the volume fraction ϕ, the average particle diameter, the value of the coupling constant λ, the yield stress, and finally the order parameter acquired from ultrasonic spectroscopy.

The nematic order parameter found by means of ultrasonic spectroscopy converges well with the theoretical values only for low concentrated magnetic fluids. This is due to the structure-size distribution independence of the Shliomis, Mond and Morozov method, since it is assumed that the main building block of the system is a dimer, and larger structures (N-particle oligomers) may be considered as short flexible chains (with $3N - 6$ oscillatory degrees of freedom) represented also as a single dimer (see ref. [13]).

The analysis of the two-dimensional SAXS showed a development of the anisotropy starting from a q-range of around $0.35\,\mathrm{nm}^{-1}$ (corresponding to the size of a dimer).

The anisotropy was more pronounced when approaching a lower q-range (down to $q_{\rm an} = 0.09\,{\rm nm}^{-1}$ for sample FF:128 at $B = 0.71\,{\rm T}$) and interestingly, the anisotropy reached its maximum value and peaks at $q_{\rm an}$ and then the isotropy started to recover leaving a long and H/kT-dependent tail. This was revealed by plotting the ratio of the intensities $I_\perp(q)/I_\parallel(q)$ (perpendicular and parallel to the B-field direction) as a function of the wave vector q shown in fig. 5 (top). The ratio displayed maxima shifting from $q_{\rm an}^{0.35T} \sim 0.11\,{\rm nm}^{-1}$ to $q_{\rm an}^{0.71T} \sim 0.09\,{\rm nm}^{-1}$ for sample FF:128 at magnetic-field strengths of 0.37 T and 0.71 T, respectively. The aggregate radius of gyration changed from 115 to 140 nm for FF:128, depending on the field strength. There was however no peak present at the detectable q-range for a sample with high particle concentration (FF:4). This indicates that larger structures were formed for samples with high particle concentration (above 1%) in comparison with those formed in diluted samples. The relative values of the nematic order parameter were calculated via fits to azimuthal plots of the SAXS data. It was found that along the whole detectable q-range, the relative order parameter values for the sample with high particle concentration FF:4 were lower than those from the diluted sample FF:128. The lower degree of anisotropy for FF:4 in comparison to FF:128 was caused by the formation of more complex structure formations (such as rings, clusters, etc.) that prevented a better alignment. This was also confirmed by the ultrasonic spectrometry.

In addition, the magnetic-field–dependent yield stress was measured, and a relationship between the yield stress and the magnetic-field strength up to 500 mT was obtained. Based on the results from VSM, the value of the saturated magnitude of the yield stress $\tau_y^{\rm sat}$ was estimated to be between 1.4 and 2.8 Pa, which converged well with the results obtained from rheometry. These results provide once more the experimental confirmation of the recently described theory by Zubarev and Iskakova.

This work was supported by the Research Council of Norway through the FRINAT Program: NFR project number 171300. We are grateful for beam time at the Dutch-Belgian Beamline at the European Synchrotron Radiation Facility, Grenoble. The studies were supported by Slovak Academy of Sciences VEGA 2/0077/09, Nanofluid, Centre of Excellence, projects APVV 0509-07, MNT-ERA Net and SK-PL-0069-09/8158/2010. The authors acknowledge A.P. Hammersley, author of the Fit2D program.

References

1. S. Odenbach, J. Phys.: Condens. Matter **16**, 1135 (2004).
2. M. Raşa, Eur. Phys. J. **2**, 265 (2000).
3. D. Eberbeck, F. Wiekhorst, U. Steinhoff, L. Trahms, J. Phys.: Condens. Matter **18**, 2829 (2006).
4. S. Odenbach, K. Raj, Magnetohydrodynamics **36**, 312 (2000).
5. H. Shahnazian, S. Odenbach, J. Phys.: Condens. Matter **20**, 204137 (2008).
6. A. Józefczak, A. Skumiel, J. Phys.: Condens. Matter **18**, 1869 (2006).
7. F.L.O. Paula, R. Aquino, G.J. da Silva, J. Depeyrot, F.A. Tourinho, J.O. Fossum, K.D. Knudsen, J. Appl. Cryst. **40**, 269 (2007).
8. F.L.O. Paula, G.J. da Silva, J.O. Fossum, K.D. Knudsen, G. Helgesen, R. Aquino, F.A. Tourinho, J. Depeyrot, Braz. J. Phys. **39**, 163 (2009).
9. H. Shahnazian, S. Odenbach, Phys. Rev. B **67**, 094206 (2003).
10. P. Davidson, D. Petermann, A.M. Levelut, J. Phys. II **5**, 113 (1995).
11. L.M. Pop, S. Odenbach, J. Phys.: Condens. Matter **18**, 2785 (2006).
12. A.J. Leadbetter, E.K. Norris, Mol. Phys. **38**, 669 (1979).
13. M. Shliomis, M. Mond, K. Morozov, Phys. Rev. Lett. **101**, 074505 (2008).
14. F. Herchl, P. Kopčanský, M. Timko, M. Koneracká, K. Marton, I. Kolcunová, L. Tomčo, Acta Phys. Pol. A **113**, 569 (2008).
15. C. Holm, J.J. Weis, Curr. Opin. Colloid Interface Sci. **10**, 133 (2005).
16. A. Skumiel, Int. J. Thermophys. **31**, 546 (2010).
17. A. Skumiel, T. Hornowski, A. Józefczak, Int. J. Thermophys. DOI 10.1007/s10765-010-0799-4 (2011).
18. K.P. Vishwanath, A. Kandasamy, Appl. Math. Mod. **34**, 219 (2010).
19. A.N. Alexandrou, T.M. McGilvreay, G. Burgos, J. Non-Newtonian Fluid Mech. **100**, 77 (2001).
20. M. Klokkenburg, B.H. Erné, A. Wiedenmann, A.V. Petukov, A.P. Philipse, Phys. Rev. E **75**, 051408 (2007).
21. A.Y. Zubarev, L.Y. Iskakova, Physica A **365**, 265 (2006).
22. O. Glatter, O. Kratky, *Small-Angle X-ray Scattering* (Academic, New York, 1982).
23. P. Linder, T. Zemb, *Neutrons, X-rays and Light: Scattering Methods Applied to Soft Condensed Matter* (North Holland, 2002).
24. W. Bras, I.P. Dolbnya, D. Detollenaere, R. van Tol, M. Malfois, G.N. Greaves, A.J. Ryan, E. Heeley, J. Appl. Cryst. **36**, 791 (2003).
25. F. Dobrich, A. Michels, R. Birringer, J. Magn. & Magn. Mater. **316**, 779 (2007).
26. A.V. Teixeira, I. Morfin, F. Ehrburger-Dolle, C. Rochas, P. Panine, P. Licinio, E. Geissler, Compos. Sci. Technol. **63**, 1105 (2003).
27. B.J. Lemaire, P. Panine, J.C.P. Gabriel, P. Davidson, Europhys. Lett. **59**, 55 (2002).
28. S. Taketomi, J. Phys. Soc. Jpn. **55**, 838 (1986).
29. H. Pleiner, H.R. Brand, J. Magn. & Magn. Mater. **85**, 125 (1990).
30. V.V. Sokolov, Acoust. Phys. **56**, 972 (2010).

Appendix II

Wide angle scattering study of nanolayered clay/gelatin electrorheological elastomer

B Wang, Z Rozynek, M Zhou and J O Fossum

J. Phys.: C.S. 149 (2009) 012032

Journal of Physics: Conference Series **149** (2009) 012032 doi:10.1088/1742-6596/149/1/012032

Wide Angle Scattering Study of nanolayered Clay/gelatin Electrorheological Elastomer

B Wang, Z Rozynek, M Zhou and J O Fossum

Department of Physics, Norwegian University of Science and Technology, Høgskoleringen 5, NO-7491, Trondheim, Norway

E-mail: baoxiang.wang@ntnu.no and jon.fossum@ntnu.no

Abstract: In the general context of self-assembly of nanolayered clay, we have studied both kaolinite and montmorillonite guided assembly into chain-like structures in gelatin hydrogel. The electrorheological (ER) elastomers, containing clay particles which dispersed in gelatin/water matrix, were prepared with or without the applied DC electric field and cross-linked polymerized with the help of formaldehyde. The experimental techniques include synchrotron X-ray scattering, atomic force microscopy, optical microscopy. The aim is to produce a water-based, low-cost and environmentally friendly ER hydrogel. The wide-angle x-ray scattering (WAXS) patterns observed from clay/gelatin ER elastomers curing in the DC field are highly anisotropic and show differences clearly compared to that without curing in the field. Both clay nanolayers have preferential orientation in gelatine hydrogel along the direction of electric field.

1. Introduction

The physical properties of stimuli-responsive soft materials dramatically change corresponding to the external stimuli such as temperature, pH, electric and magnetic fields [1-3]. These materials are called as intelligent materials and have been harnessed in novel systems, for example, sensors, actuators, and biomedical applications [4, 5]. Electrorheological (ER) effects refer to the change of rheological properties of a material upon application of an electrical field [6-11]. When an ER fluid, a suspension of polarizable particles in an insulating medium (such as mineral oil or silicone oil), is subjected to an electric field, the particles polarize, which results in an anisotropic structure of aligned chains of particles along the direction of the uniaxial electrical field. ER fluids exhibit drastic changes in their rheological properties, including a large enhancement in apparent viscosity and yield stress under an applied electric field. An obvious problem with ER fluids is sedimentation of the particles [12-13]. Because of the fluidity, ER fluids must be sealed to prevent leakage, which can complicate the design. Another design problem with fluids is the electrodes, which must be fully supported by the container for the fluid, yet electrically insulated to resist high voltage. Recently, ER elastomers, cross-linked polymer gels with dispersed polarizable particles–have attracted attention. The dispersed phases filled with particles responsive to an applied electric or magnetic field include intercalated or exfoliated platelets obtained from clays, mica, or graphite, nanocages, nanotubes, dual fillers, porous particles, and nanocatalysts etc. Comparing with ER fluid, the liquid medium of ER elastomer is cross linked polymerized after particle alignment, so the anisotropic arrangement of polarisable particles is "frozen". In the gel network, as matrix's solid-like nature, particles are restricted and the congregation of particles is eliminated. Consequently, the instability of the ER effect, which is caused by the particles' congregation in ER fluid, is improved. At the same time, the interaction among the polarized particles under the applied electric field induces the elasticity change of the ER elastomer, and then the elasticity change induces a notable ER effect. The advantages of ER elastomers over ER fluids include no leakage, no sedimentation of particles and possibility to produce custom-made ER objects of exactly the right shape and size for the application (Because the shape and size of ER elastomer can be designed for the practical requirement) [14,15]. In present work, montmorillonite (MMT) and kaolinite guided assembly into chain-like structures in gelatin hydrogel

under the external electric field are studied using synchrotron X-ray scattering, AFM and optical microscopy. There are several green chemistry concepts in our present strategy: the choice of friendly solvent, the selection of friendly benign and non-toxic matrix, the one-step reaction. Gelatin is a water-soluble natural polymer with a long and soft polypeptide backbone and its individual monomer contains an amino acids group. It is a commercially available and inexpensive material. In our approach, firstly water is used as a based component. The second concept is the choice of the low-cost and benign clay and gelatin. The third one is the simple and reproducible syntheses. The aim is to produce a water-based, low-cost and environmentally friendly ER hydrogel.

2. Materials and characterization methods

Gelatin and formaldehyde solution (A.R. 37%, diluted to 5% when used) were purchased from Merck Schuchardt OHG, Germany. Kaolinite is a 1:1 dioctahedral clay mineral with the ideal composition of $Al_2Si_2O_5(OH)_4$. It was used without further purification. Montmorillonite is a typical 2:1 smectites and was purchased from Southern Clay Products, Inc. as a fine gray powder. In this study, firstly 20% gelatin of aqueous solution was prepared at 70°C for 1h. Then appropriate clay (kaolinite or montmorillonite) particles (such as 1wt%, 5wt%, 10wt% etc.) were added into the gelatin/water matrix to further stir for 6h at 70°C. The clay/gelatin/water mixture will be transferred into a custom-made casting cell (Fig.1) and cured under E=1 kV/mm DC electric field for 1 h. At the same time, the temperature will be retained at 70°C during the curing process. After that the system naturally cooled down to 25°C, the clay/gelatin physical hydrogel is obtained. Then this physical hydrogel was dipped into the chemical crosslinking agent (5wt% formaldehyde solution) over a night. The chemical crosslinking clay/gelatin ER hydrogel can be obtained. For comparison, samples with the same chemical composition but in the absence of an electric field were prepared.

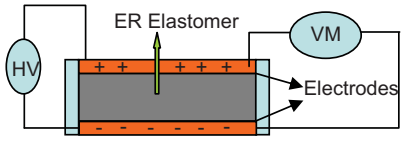

Figure 1. Schematic equipment for curing an elastomer. HV: DC power source, VM: volt meter.

The reaction of the gel chemical crosslinking is described as follows:

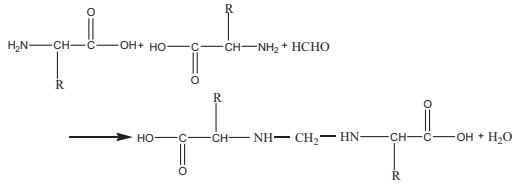

R is amino acid polypeptide macromolecule.

Relative orientations of the clay particles inside the electrorheological elastomers were determined using synchrotron X-ray scattering experiments. These experiments were performed at the Swiss-Norwegian Beamlines (SNBL) at ESRF (Grenoble, France), using the WAXS setup with a 2D mar345 detector at beamline BM01A. The X-ray beam with a wavelength of 0.72 Å and 0.3×0.3 mm^2 beam size were used. The AFM images were taken using a Multi Mode^{TM} Atomic Force Microscope (nanoscope IV) from Veeco Instruments with a contact model.

3. Results and discussion

3.1. 1:1 type clay (kaolinite) assembly in gelatin

The morphology of pure kaolinite is illustrated in Figure 2. It can be seen that kaolinite is composed of stacked small platelets (1~10μm). Furthermore, kaolinite particles are sharing

morphology with well defined hexagonal edges and corner angles (120°) shown in large resolution image. Figure 3 shows the optical image of kaolinite/gelatin hydrogel without curing in the field. Solid-like or gel-like behaviour is observed. Kaolinite have hydroxyl group, which is beneficial for homogeneously dispersing in the gel network.

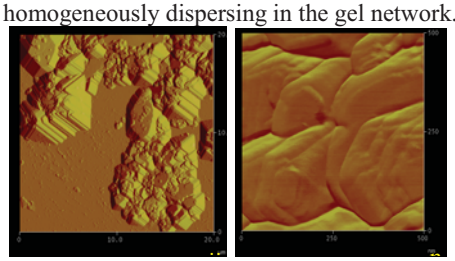

Figure 2. AFM images of pure kaolinite particles, kaolinite/gelatin the scale bar 20×20μm (left) and 500×500nm (right).

Figure 3. Optical images of hydrogel without curing in the field.

Solid kaolinite/gelatin ER elastomer is prepared by arranging suspended kaolinite particles in gelatin with an electric field and crosslinked the obtained structure with the help of formaldehyde to "freeze" the chain. Figure 4(a) shows the micrograph of kaolinite particles in the elastomer cured without the externally applied electric field, and Figure4(b) shows the elastomer cured under the field with E= 1 kV/mm. It is observed that particles are randomly dispersed and aligned dispersed in Figure4 (a) and (b), respectively. By comparing and analyzing the two elastomers, it is obvious that the particles have been assembled by the applied DC field during the curing process.

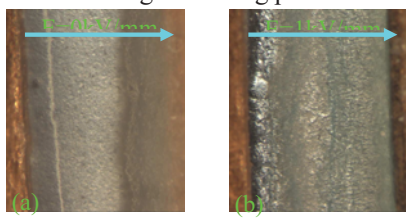

Figure 4. Optical micrographs of the kaolinite/gelatin elastomers cured in the absence/presence of the applied electric field (E=1kV/mm).

Relative orientations of the kaolinite particles inside the electrorheological elastomer were determined using synchrotron X-ray scattering experiments: chain and column formations were observed. The three-dimensional WAXS patterns obtained from kaolinite/gelatin ER elastomer are shown in figure 5.

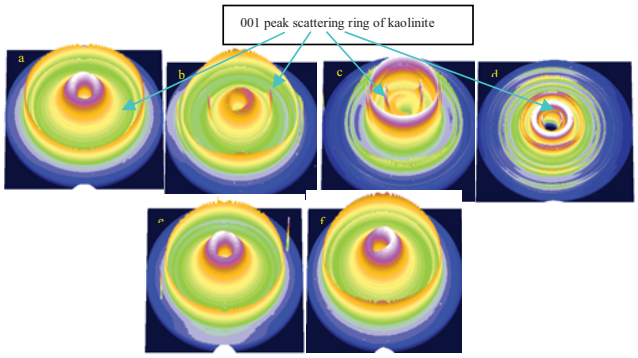

Figure 5. The three Dimensional WAXS patterns obtained from 10wt% kaolinite/gelatin hydrogel curing in a DC external electric field (a) E=0kV/mm, isotropic pattern; (b)(c)(d) E=1kV/mm, anisotropic pattern; the distance between the detector and the sample is different as follow (b) 350mm (c) 200mm (d)110mm, which more scattering rings of kaolinite/gelatin ER hydrogel can be observed; e) pure gelatin hydrogel without curing in a field; f) pure gelatin hydrogel curing in a field E=1kV/mm

The 001 scattering ring of kaolinite is indicated by arrows respectively in figure 5. Clay minerals are sheet silicates or layered silicates, whose primary particles are platelet shape. Each clay platelet is ~1 nm thick (c-direction). Kaolinite is a 1:1 dioctahedral clay mineral with the ideal composition of Al2Si2O5(OH)4. Its structure is composed of AlO2(OH)4 octahedral sheets and SiO4 tetrahedral sheets. Normally, the 001 peak of clay indicates the interlayer spacing between the two basic sheets. For the first strong peak of kaolinite in WAXS patterns represents the diffraction from the (001) crystal surface of the kaolinite, and the associated interlayer d-spacing of this peak is 0.715 nm (In figure 4) [16]. For kaolinite/gelatin hydrogel without curing in the electric field, the kaolinite particles are randomly dispersed into the gelatin matrix, so its WAXS pattern is isotropic shape due to the non-orientation of kaolinite particles (shown in figure 5a). However after curing in the electric field, kaolinite partilces will polarized and assemble or orient to respond with field. Kaolinite particle have preferential orientation in gelatine hydrogel along the direction of electric field and show an anisotropic pattern after the curing of DC electric field compared with the isotropic pattern of kaolinite/gelatin hydrogel without curing in the field (shown in figure 5b, c and d). These two patterns show clearly that the kaolinite particles assemble or orient in the direction of electric field. Likewise, the electric field should be high enough such that the electric force can overcome the effect of the gravitational force acting on the dense kaolinite particles. However□applying a DC field over E=2 kV/mm or much higher can cause the water to hydrolyze and air bubble is observed obviously. The sample will be shrunken during the curing process. The colour of sample will be changed from light gray to green for kaolinite/gelatin hydrogel. Furthermore, too weak electric field strength (below 300V/mm) is difficult to ensure particle polarized for orientation or forming chain-like structure. So we chose a medium electric field strength (E=1 kV/mm) to make sure clay assembling into gelatin matrix and in this case the hydrolyzation is not serious. The multipolar interactions from the highly polarizable particles undoubtedly contribute significantly to the ER response. The result indicates that the orientation of particle chain relative to the field is an important structure factor in the designing of the ER elastomers. Spatial arrangement influences the interparticle forces, especially those within the chains. Furthermore, pure gelatin samples with or without curing in an electric field is prepared and their three-Dimensional WAXS patterns are shown in figure 5 e) and f), respectively. Comparing with kaolinite/gelatin ER elastomer (figure5b), no kaolinite scattering ring, only gelatin scattering ring is shown in the pattern. Furthermore the anisotropic pattern (figure 5f) also indicates that pure gelatin hydrogel can respond with the electric field and oriented along the direction of electric field.

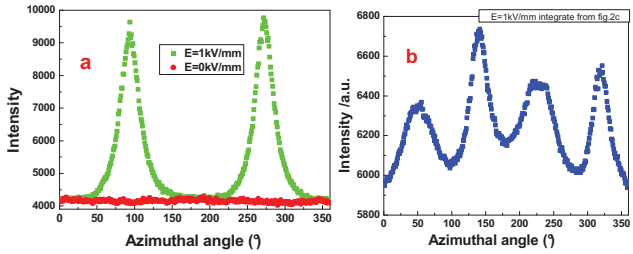

Figure 6. a) Dependence of the intensity of circular scattering rings (only integrating kaolinite 001 peak in figure 4 a and b) on the azimuthal angle for 10wt% kaolinite/gelatin composite at the different electric field; b) Dependence of the intensity of circular scattering rings (kaolinite 001 peak plus the first peak of gelatin in figure 4 c) on the azimuthal angle.

Figure 6 shows how the intensity of circular scattering rings such as those presented in figure4 a) and b) evolve as a function of the azimuthal angle Φ, between 0 and 360°. For the 10wt% kaolinite/gelatin composite, we firstly have considered the first-order Bragg peak of kaolinite (001). The scattered intensity at a given azimuthal angle is proportional to the number of particles that meet the Bragg condition for that angle, so the shapes of the scattered intensities in figure 6a provide the orientation distributions of clay particle orientations inside the chains and columnar structures. For *E*

= 0 kV/mm, the intensities are independent of Φ and the two-dimensional scattering pattern is isotropic because the kaolinite particles is randomly dispersed in gelatin hydrogel. For E =1kV/mm, the azimuthal positions of the maxima along the plots is anisotropic and this demonstrate that the preferred orientation of the kaolinite particles is with the lamellar stacking plane parallel to the direction of the electric field. Secondly, we have considered both the 001Bragg peak of kaolinite and the first peak of gelatin evolve as a function of the azimuthal angle Φ, between 0 and 360°. From figure 6 b), we can see that the azimuthal positions of the maxima along the plots is anisotropic and have 4 maxima. So that means both the visible diffraction rings correspond to the diffraction of kaolinite and gelatin are anisotropic. The reason is probably because the macromolecules of the matrix are polymerized anisotropically under an applied dc electric field for curing. Since the clay particles are platelets with a thickness much smaller than their lateral dimension, this suggests that they are lying in the ER bundles with one of their lateral dimensions parallel to the field; i.e., on average, the clay particles have their directors aligned perpendicular to the direction of applied field [17]. Furthermore, the gelatin matrix polarizes along their macromolecules chain parallel to the direction of the electric field, and hence in figure 5b, c and d we can see that two perpendicular directions for anisotropic rings are observed for kaolinite and gelatin separately.

3.2. 2:1 type clay (MMT) assembly in gelatin

The wide angle X-ray diffraction (WAXS) patterns of a series of MMT/gelatin hydrogel are also studied. The two-dimensional WAXS patterns obtained from MMT chains of particles dispersed in gelatin hydrogel, in the presence (a) 10wt%MMT with field(E=1kV/mm); (b) 5wt% MMT with field (E=1kV/mm) or (c) absence of a DC external electric field are shown in figure 7. The 001 scattering ring of MMT is indicated by arrows respectively in figure 7. The basic structural unit of so-called 2:1 clays (such as MMT) is a 1 nm-thick platelet consisting of two tetrahedral silica sheets sandwiching one octahedral silica sheet. The interlayer d-spacing for the peak of free MMT (001 crystal surface) is near 1nm.

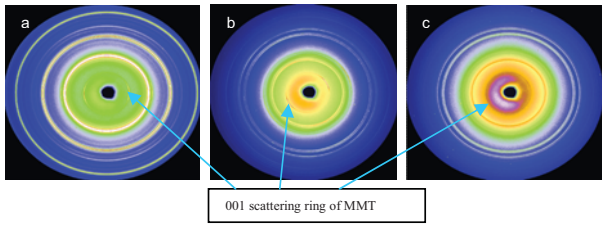

Figure 7. The 2-dimensional WAXS patterns obtained from the MMT/gelatin hydrogel, in the presence (a) 10wt%MMT with field (E=1kV/mm); (b) 5wt% MMT with field (E=1kV/mm); (c) 5wt% MMT without field (E=0kV/mm).

Similarly, the isotropic pattern of 5wt% MMT absence of a DC external electric field in figure 7(c) means that MMT particles are randomly dispersed into gelatin hydrogel and no preferential orientations for the clay aggregates. The two-dimensional WAXS patterns obtained from this MMT/gelatin hyrogel elastomer (figure7 b and c) are clearly anisotropic, reflecting the preferential orientation of the particles in the electric field. Taking advantage of the nano-layered nature of the clay crystallites, we were able to infer MMT particle orientations inside the particle bundles from the anisotropy of two-dimensional WAXS images. This study suggested that the MMT particles polarize along their silica sheets, and hence, that their directors were, on average, perpendicular to the direction of the electric field[18]. Dependence of the intensity of scattering vector for MMT/gelatin hydrogel with and without electric field for 5wt% and 10wt% MMT content are shown in figure 8, respectively. A sharp and strong peak attributable to a low degree of ordering is observed for MMT/gelatin hydrogel elastomer with electric field comparing that of MMT/gelatin hydrogel without electric field (d_{001} =10 Å, $d = 2\pi/q$). This is due to dipolar interaction between polarized MMT particles, which orientate and aggregate to forms chains and then column structures along the direction of applied electric field which also lead to the enhancement of MMT concentration. The intensity of 001 diffraction peak was increased, indicating an increase of MMT particles assembling along the direction of electric field. A

chain-like structure of ER composites enhances their electrostriction response to normal and shear deformations. This makes feasible application of ER composites in stand-alone sensing systems as well as implementation of electrostriction to achieve self-sensing capabilities in ER devices.

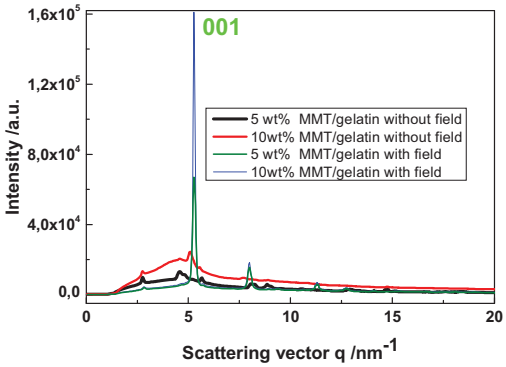

Figure 8. Dependence of the intensity of scattering vector q for 5wt% or 10wt% MMT/gelatin hydrogel with and without curing in an electric field.

4. Conclusions

A serial of clay/gelatin ER elastomers have been synthesized and characterized by wide angle -ray scattering. The resulting materials show different structures compared to uncuring clay/gelatin hydrogel. Two and three-dimensional WAXS images from bundles of clay inside the gelatin matrix exhibits a clear anisotropy, reflecting the preferential orientation of the clay particles in the field. The anisotropy of 2-dimesional diffractogram also provides the angular distribution of clay particles inside the clay assemble into gelatin hydrogel.

Acknowledgements: This work was supported by the Research Council of Norway (RCN) through the NANOMAT Program and the FRINAT Program.

References

[1] Mark J E 2003 *Prog. Polym. Sci.* **28** 1205
[2] Schmidt D F, Clement F and Giannelis E P 2006 *Adv. Funct. Mater.* **16** 417
[3] Giannelis E P 1996 *Adv. Mater.* **8** 29
[4] Gamota D and Filisko F E 1991 *J. Rheol.* **35** 399
[5] Hao T 2001 *Adv. Mater.* 13 1847
[6] Block H, Kelly J P, Qin A and Watson T 1990 *Langmuir* **6** 6
[7] Whittle M and Blullough W A 1992 *Nature* **358** 373
[8] Wen W J, Huang X X, Yang S H, Lu K Q and Sheng P 2003 *Nature Mater.* **2** 727
[9] To K and Choi H J 1998 *Phys. Rev. Lett.* **80** 536
[10] Tetsu M, Kousuke S and Kiyohito K 2004 *Polymer* **45** 3811
[11] Wang B X and Zhao X P 2005 *Adv. Funct. Mater.* **15** 1815
[12] Liu B and Montgomery T S 2001 *J. Rheol.* **45(3)** 641
[13] Martin J E and Anderson R A 1999 *J. Chem. Phys.* **111(9)** 4273
[14] Gao L X and Zhao X P 2007 *J. Appl. Polym. Sci.* **104(3)** 1738
[15] Gao L X and Zhao X P 2004 *J. Appl. Polym. Sci.* **94(6)** 2517
[16] Wang B X and Zhao X P 2002 *J. Mater. Chem.* **12** 1865
[17] Meheust Y, Knudsen K D and Fossum J O 2006 *J.Appl.Cryst.* **39** 661
[18] Fossum J O et al 2006 *Europhys. Lett.* **74** 438